ANL-7679
RETURN TO ANL (IDAHO) LIBRARY.

Argonne National Laboratory

REACTOR DEVELOPMENT PROGRAM PROGRESS REPORT

March 1970

The facilities of Argonne National Laboratory are owned by the United States Government. Under the terms of a contract (W-31-109-Eng-38) between the U. S. Atomic Energy Commission, Argonne Universities Association and The University of Chicago, the University employs the staff and operates the Laboratory in accordance with policies and programs formulated, approved and reviewed by the Association.

MEMBERS OF ARGONNE UNIVERSITIES ASSOCIATION

The University of Arizona
Carnegie-Mellon University
Case Western Reserve University
The University of Chicago
University of Cincinnati
Illinois Institute of Technology
University of Illinois
Indiana University
Iowa State University
The University of Iowa
Kansas State University
The University of Kansas
Loyola University
Marquette University
Michigan State University
The University of Michigan
University of Minnesota
University of Missouri
Northwestern University
University of Notre Dame
The Ohio State University
Ohio University
The Pennsylvania State University
Purdue University
Saint Louis University
Southern Illinois University
University of Texas
Washington University
Wayne State University
The University of Wisconsin

LEGAL NOTICE

This report was prepared as an account of Government sponsored work. Neither the United States, nor the Commission, nor any person acting on behalf of the Commission:

A. Makes any warranty or representation, expressed or implied, with respect to the accuracy, completeness, or usefulness of the information contained in this report, or that the use of any information, apparatus, method, or process disclosed in this report may not infringe privately owned rights; or

B. Assumes any liabilities with respect to the use of, or for damages resulting from the use of any information, apparatus, method, or process disclosed in this report.

As used in the above, "person acting on behalf of the Commission" includes any employee or contractor of the Commission, or employee of such contractor, to the extent that such employee or contractor of the Commission, or employee of such contractor prepares, disseminates, or provides access to, any information pursuant to his employment or contract with the Commission, or his employment with such contractor.

Printed in the United States of America
Available from
Clearinghouse for Federal Scientific and Technical Information
National Bureau of Standards, U. S. Department of Commerce
Springfield, Virginia 22151
Price: Printed Copy $3.00; Microfiche $0.65

ANL-7679
Reactor Technology

ARGONNE NATIONAL LABORATORY
9700 South Cass Avenue
Argonne, Illinois 60439

REACTOR DEVELOPMENT PROGRAM PROGRESS REPORT

March 1970

Robert B. Duffield, Laboratory Director
Alfred Amorosi, Assistant Laboratory Director

Division	Director
Applied Physics	R. Avery
Center for Environmental Studies	L. E. Link
Chemical Engineering	R. C. Vogel
EBR-II Project	M. Levenson
Engineering and Technology	S. A. Davis
Materials Science	P. G. Shewmon
Reactor Analysis and Safety	W. R. Simmons

Report coordinated by
A. Glassner and V. G. Trice, Jr.

Issued April 27, 1970

FOREWORD

The Reactor Development Program Progress Report, issued monthly, is intended to be a means of reporting those items of significant technical progress which have occurred in both the specific reactor projects and the general engineering research and development programs. The report is organized in accordance with budget activities in a way which, it is hoped, gives the clearest, most logical overall view of progress. Since the intent is to report only items of significant progress, not all activities are reported each month. In order to issue this report as soon as possible after the end of the month editorial work must necessarily be limited. Also, since this is an informal progress report, the results and data presented should be understood to be preliminary and subject to change unless otherwise stated.

The issuance of these reports is not intended to constitute publication in any sense of the word. Final results either will be submitted for publication in regular professional journals or will be published in the form of ANL topical reports.

The last six reports issued
in this series are:

September 1969	ANL-7618
October 1969	ANL-7632
November 1969	ANL-7640
December 1969	ANL-7655
January 1970	ANL-7661
February 1970	ANL-7669

REACTOR DEVELOPMENT PROGRAM

Highlights of Project Activities for March 1970

EBR-II

The reactor was operated for 1137 MWd between February 21 and March 20, bringing its accumulated total of operation to 33,498 MWd. Run 40B (February 10-March 1), the longest uninterrupted run in EBR-II history, logged 924 MWd. The test-2 fueled instrumented subassembly (designated as XX02) continues to operate satisfactorily in the reactor.

ZPR-3

The reference critical loading for Assembly 60, the first of a series of configurations to be studied in support of the EBR-II program, contained 222 kg U-235. Radial and axial reaction-rate traverses, isothermal temperature coefficient (-1.26 Ih/°C), and thermoluminescent gamma detector studies were made in this assembly.

Modification to Assembly 61, with a partial nickel-rich radial reflector, is now in progress.

ZPR-9

Relative edge worths of materials at the boundaries of the inner core, outer core, and reflector were determined, and the critical-mass adjustment of Assembly 26, the FTR-3 core, was made. The temperature coefficient of reactivity from 29 to 44°C, corrected for Pu-241 decay, was found to be -3.92 Ih/°C.

The experimental neutron spectrum at the center of FTR-3 was compared with an MC^2 calculation using ENDFB/I data; after correction for a Gaussian window lethargy resolution of the counter, every oscillation in the calculated data corresponded closely in energy, width, and amplitude to a measured oscillation.

ZPPR

The demonstration-plant benchmark core, ZPPR Assembly 2, attained initial criticality this month in a volume of 2498 liters containing 1066 kg Pu-239 and -241. The two-zone core will soon be adjusted to an inner-to-outer zone volume ratio of one, using the edge-worth measurements already performed.

TABLE OF CONTENTS

	Page
I. LIQUID METAL FAST BREEDER REACTORS--CIVILIAN	1
A. Physics Development	1
1. Experimental Reactor Physics	1
2. ZPR-6 and -9 Operations and Analysis	6
3. ZPR-3 and ZPPR Operations and Analysis	11
B. Component Development	25
1. Instrumentation and Control	25
C. Sodium Technology	29
1. Sodium Chemistry	29
2. Sodium Analytical Development	30
3. On-line Monitors	31
4. Fission Product Behavior and Control	32
D. Systems and Plant Development	33
1. Plant and Design	33
E. EBR-II--Research and Development	34
1. Equipment--Fuel Related	34
2. Instrumented Subassemblies	37
3. Coolant Chemistry	40
4. Experimental Irradiation and Testing	48
5. Materials-Coolant Compatibility	50
6. Systems Engineering	53
7. Reactor Analysis, Testing and Methods Development	53
8. Driver Fuel Development	74
9. Operations with Failed Fuel	83
10. Physics Mock-up Studies	92
F. EBR-II--Fuel Fabrication	95
1. Cold Line Operations	95
G. EBR-II--Operations	96
1. Reactor Plant	96
2. Fuel Cycle Facility	97
PUBLICATIONS	105

TABLE OF CONTENTS

	Page
II. OTHER FAST REACTORS--OTHER FAST BREEDER REACTORS--FUEL DEVELOPMENT	107
A. Irradiation Effects, Mechanical Properties and Fabrication	107
1. Neutron Simulation Experiments by Ion Bombardment	107
2. Mechanical Properties of Cladding Materials	107
3. Surface Defects as Failure Sites in Type 304 Seamless Stainless Steel Fuel-clad Tubing	108
PUBLICATION	109
III. GENERAL REACTOR TECHNOLOGY	110
A. Applied and Reactor Physics Development	110
1. Theoretical Reactor Physics--Research and Development	110
2. Nuclear Data--Research and Development	111
B. Reactor Fuels and Materials Development	115
1. Fuels and Claddings--Research and Development	115
2. Radiation Damage on Structural Materials--Research and Development	125
3. Techniques of Fabrication and Testing--Research and Development	125
4. Engineering Properties of Reactor Materials--Research and Development	128
C. Engineering Development--Research and Development	131
1. Instrumentation and Control	131
2. Heat Transfer and Fluid Flow	133
3. Engineering Mechanics	136
D. Chemistry and Chemical Separations	137
1. Fuel Cycle Technology--Research and Development	137
2. General Chemistry and Chemical Engineering--Research and Development	142
PUBLICATIONS	148

TABLE OF CONTENTS

	Page
IV. NUCLEAR SAFETY RESEARCH AND DEVELOPMENT	149
A. LMFBR Safety--Research and Development	149
1. Accident Analysis and Safety Evaluation	149
2. Reactor Control and Stability	151
3. Coolant Dynamics	151
4. Fuel Meltdown Studies with TREAT	152
5. Materials Behavior and Energy Transfer	159
6. Fast Reactor Safety Test Facility Study	160
7. 1000-MWe Safety Analysis Studies	161
8. Post-accident Heat Removal	162
B. Effluent Control--Environmental Studies--Research and Development	164
1. Thermal-Plume Transport in the Great Lakes	164
C. Engineered Safety Features--Safety Features Technology--Research and Development--Containment	170
1. Hydrodynamic Response to High-Energy Excursion	170
PUBLICATIONS	177
PUBLICATION--General	178

I. LIQUID METAL FAST BREEDER REACTORS--CIVILIAN

A. Physics Development

1. Experimental Reactor Physics

a. Fast Critical Experiments--Experimental Support--Idaho

(i) Pulsed, Cross-correlation, and Noise Measurements (W. K. Lehto)

Not previously reported.

A polarity correlation system which utilizes the SEL-840 computer has been implemented to sample the instantaneous sign of the analog signal from each of two detectors and calculates the polarity cross-correlation function. The system is patterned after Cohn's.* Data from each detector are inputted to trigger circuits which sense the level of the input (positive or negative) and output a corresponding logic signal. The logic signals are time sampled by a computer-controlled 24-bit shift register. After input of a set number of 24-bit words, the correlation function is calculated, and displayed as a printout and on the CRT. The dual registers and exclusive-or instructions of the SEL permit a considerable reduction in calculational time over that required in computers not similarly equipped. Two programs are operational. The first calculates the cross-correlation function for 24 delays from 1000 input words sampled at a bit rate of up to 20 μsec/bit, with continuous updating.

The second program can process 50 of 64 input words for 24 delays which vary systematically from 0 to 300 times the interval between bits. The limiting factor in this system will be the data-input time which precludes data-sampling rates greater than 1/20 μsec using only two shift registers. However, data-sampling rates of this order are adequate for the cores to be built in ZPPR.

An alternative system, not based on the computer, has been set up to do on-line experiments at ZPR-3, where a computer is not available. This system uses trigger circuits as above to generate the + or - logic signals. One train of logic signals is delayed with respect to the other, and the two signals are passed to an exclusive-or gate. This logic signal is positive when the inputs are in phase and negative when they are out of phase. The signal is then used to instruct a reversing scaler to count external clock pulses up or down. The net result is proportional to the cross-correlation function for the chosen delay.

*Cohn, C. E., Nucl. Appl. 6, 391 (1969).

These systems are operational, and the computer-based system has been completely checked out. The checkout of the ZPR-3 system will be completed shortly.

The first system was used in a study of the effects of signal-to-noise (S/N) ratio on the results of polarity correlation experiments. Analog data from a detector (phototube and plastic scintillator) driven by a neutron source was low pass filtered to simulate fast reactor data and passed into each channel of the polarity correlator, the data being the signals. The noise signal for each channel was derived from separate detectors and superimposed on the signal through an isolation network. The polarity correlation function was calculated for systematically varying S/N ratios.

The limit as established in these studies for this equipment was a S/N ratio of 0.2 as opposed to a minimum value of 0.1 in a measurement of the full-amplitude cross power spectral density.

b. Fast Critical Experiments--Experimental Support--Illinois

(i) Development of Experimental Techniques (E. F. Bennett)

Last Reported: ANL-7640, p. 17 (Nov 1969).

(a) Signal-transmission Line with Low Attenuation and Wide Frequency Passband (K. G. Porges)

In nuclear experiments with either accelerators or reactors, there are occasions when very fast signals must be transmitted over considerable distances, possibly through shielding. The transmission properties of standard commercial cable have been thoroughly investigated.* As a result of the findings, UCRL developed a stiff transmission line (2-in.-OD) pieces of Styrofoam threaded by a copper tube and wrapped in copper foil) which outperforms any standard cable by a considerable margin. The UCRL design is also somewhat better than special semiflexible pulse cables, a number of which were investigated.* On the other hand, these Styrofoam lines are easily damaged, difficult to accommodate in restricted space, and difficult to match to existing connectors at each end. A rigid transmission line has been developed here in an effort to overcome these problems while maintaining the superior properties of the UCRL line.

The transmission line uses an outer conductor made from 1-in.-OD, 0.032-in.-wall tubing and an inner conductor of 0.375-in.-OD tubing (both of which are readily available). Tapered matching pieces at each end accommodate GR-874 connectors. The space between inner and

*Kerns, Q., et al., Counting Note CC2-1, in UCRL-3307 (Rev.).

outer conductor is filled with Styrofoam, which may be cut to size on a lathe or foamed in place. To allow disassembly, one end of the inner conductor is attached to the central pin of the GR-874 connector by means of a bayonet joint, while the other end is threaded (see Fig. I.A.1). Several such lines were fabricated in 10-ft lengths. To provide desirable mechanical properties, brass was used for the outer conductors; the inner surfaces of these were subsequently silverplated to cut down attenuation (which was very noticeable on some unplated units).

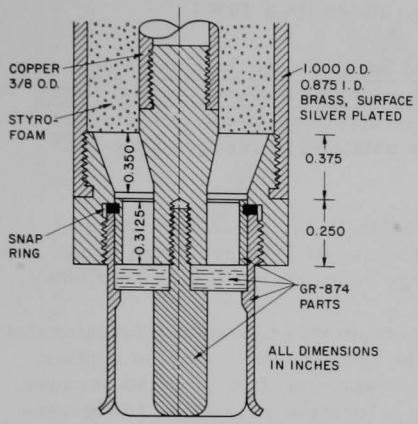

Ω Fig. I.A.1. 50-Ω Tapered Matching Connection to 1-in.-OD Styrofoam Transmission Line for GR-874 Connectors

The performance of these lines may be judged from Fig. I.A.2, which was obtained with a relay pulser and a sampling oscilloscope, the arrangement being equivalent to dc transmission through 40 ft of line. The response of an equivalent length of RG-8-U is also shown. With the equipment available, which has an overall risetime of 420 ps, no significant difference in risetime was noticeable between the leading edge (direct input into the sampling scope) and the trailing edge (transmitted through 40 ft of line); attenuation amounted to a few percent.

Fig. I.A.2

Pulse Transmission. The pulse with steeper rise was transmitted through 40 ft of Styrofoam line; the other pulse, shown for comparison, through RG-8-U cable.

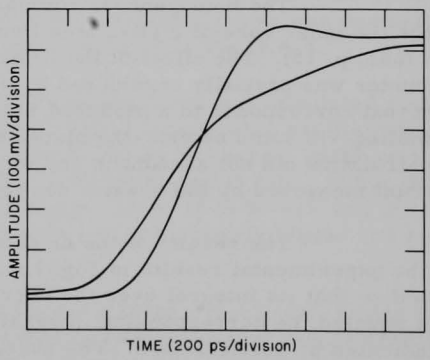

The use of stiff lines becomes awkward when such lines must be inserted in existing ducts; however, it is often possible to locate such lines in the shielding wall before the concrete is poured. To the advantage of low attenuation and preservation of risetime, one should add the further advantage of virtual freedom from noise and pickup, which is often a problem when flexible braided cable is used.

c. FFTF Critical Assembly Experiments--Planning and Evaluation (A. Travelli)

Last Reported: ANL-7669, pp. 17-25 (Feb 1970).

(i) Calculation of the Neutron Spectrum at the Center of ZPR-9/FTR-3, and Comparison with Experimental Data.

A preliminary calculation of the neutron spectrum as measured at a location near the center of ZPR-9/FTR-3 was obtained by means of the MC^2 code.

The calculation used the ENDFB/I nuclear data and an ultrafine group structure which included the use of 1980 groups of equal lethargy width and spanning over the energy range from 10 MeV to 0.68 eV.

The calculation of the spectrum was based on a fundamental-mode model in the P-1 approximation. The simple model may be applied with some confidence to the analysis of the experiment in question because (1) the neutron spectrum was measured at a location very close to the center of the inner zone of the core; (2) the size of the inner core zone is such that it may be safely assumed that the spectral perturbations arising from the inner-core/outer-core interface do not extend to the center of the core; (3) the material buckling of the inner core zone is relatively small (1.06×10^{-3} cm^{-2}); (4) the measurement was performed in an assembly that was very close to critical ($k = 0.979$), so that the excitation of higher-order modes could be neglected.

The homogeneous composition used in the calculation was that for the inner core of FTR-3 (see Progress Report for January 1970, ANL-7661, p. 15). The effect of the heterogeneous structure surrounding the counter was partially considered by using the heterogeneous MC^2 option that corresponds to a modified Bell approximation for a structure resembling--to some extent--the plate arrangement around the counter. The calculation did not account in any way for the effect on the neutron spectrum measured by the counter due to the presence of the counter itself.

The results of the direct MC^2 calculation are compared with the experimental results in Fig. I.A.3. The continuous curve was normalized so that its integral over the energy range considered in the experiments equaled the corresponding integral of the experimental data, which are indicated by vertical bars. The average energy of the measured spectrum is in good agreement with the calculation, and so is the location of the main oscillations of the spectrum. These oscillations, which correspond to resonances in the cross sections, have much wider amplitudes in the calculation than in the experiments. The effect is due to the finite energy resolution of the counter.

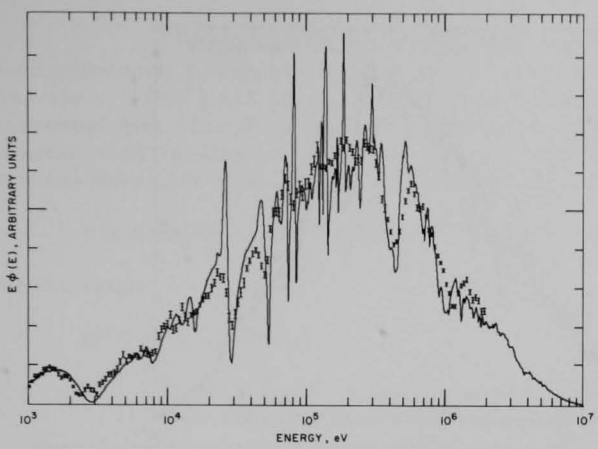

Fig. I.A.3
Comparison of Neutron Spectrum Measured at Center of ZPR-9/FTR-3 with Result of a 1980-group MC^2 Calculation

If the counter is tentatively assumed to have a lethargy resolution corresponding to a Gaussian window with a standard lethargy deviation of 0.15, the energy response f(u) of the counter can be calculated easily on the basis of the following expression:*

$$f(u) = \frac{\sqrt{2}}{0.15\sqrt{\pi}} \int_0^\infty \phi(u') \exp\left[-2\left(\frac{u-u'}{0.15}\right)^2\right] du',$$

where $\phi(u')$ is the MC^2 spectrum. Figure I.A.4 shows a comparison of the measured spectrum with the calculated MC^2 spectrum smoothed by the Gaussian window mentioned above. The calculated curve was normalized by the same method used for the normalization in Fig. I.A.3.

The agreement between measured and calculated counter responses in Fig. I.A.4 is very good. Every measurable oscillation in the calculated curve is found to correspond closely in energy, width, and amplitude to a similar oscillation of the experimental data. Minor discrepancies are found in the energy ranges from 15 to 50 keV and from 1.5 to 2 MeV, where the calculated results are respectively higher and lower than the experimental data.

A more accurate analysis of the experiment, taking into account the energy-dependence of the counter resolution and, possibly, more detailed heterogeneity effects, will be reported in the future.

*Travelli, A., "A Comment on the Comparison of Theoretical with Experimental Neutron Spectra in Fast Critical Assemblies," Proceedings of the Int. Conf. on Fast Critical Experiments and their Analysis, ANL-7320 (1966), p. 481.

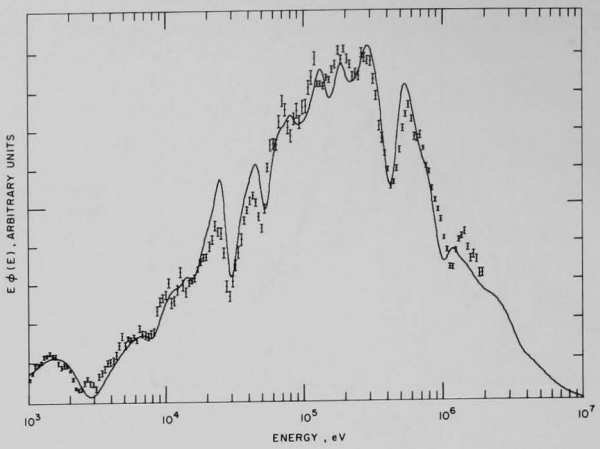

Fig. I.A.4. Comparison of the Neutron Spectrum Measured at Center of ZPR-9/FTR-3 with Result of a 1980-group MC^2 Calculation Smoothed by a Gaussian Lethargy Window with a Standard Deviation of 0.15

2. ZPR-6 and -9 Operations and Analysis

a. Mockup Experiments (J. W. Daughtry)

Last Reported: ANL-7669, pp. 27-30 (Feb 1970).

(i) FTR-3 Temperature Coefficient (R. M. Fleischman)

The temperature coefficient of reactivity for ZPR-9 Assembly 26, FTR-3, was determined by an analysis of data taken during the edge worth measurements. Repeated observations of the control-rod configuration in the reference core provided information regarding the reference excess reactivity as a function of the average core temperature.

The data for each point consisted of the average position of a previously calibrated control rod required to maintain a specified subcritical power level, the readings of 21 copper-constantan thermocouples located throughout the reactor core region, and the time elapsed since the first reference measurement. Although the average of the thermocouple readings does not truly represent the core average temperature, it does give a consistent sampling of the temperature distribution and provides a relative gauge of changes of core temperature. Since the reference measurements were spread over several days, the elapsed time since the first reference measurement was recorded to allow for the correction for ^{241}Pu decay.

Since the reactivity effect due to the decay of ^{241}Pu had not been calculated or measured for FTR-3, an estimated value of -0.17 Ih/day* was used. Table I.A.1 summarizes the basic reference and ^{241}Pu-decay-corrected data. Least-squares analysis of the corrected data yielded an equation representing the available excess reactivity at the specified subcritical power level as a function of average thermocouple reading:

$$\rho \pm 0.48(\text{Ih}) = -3.92 \pm 0.03(\text{Ih}/^\circ\text{C})\ T(^\circ\text{C}) + 196.97 \pm 1.13(\text{Ih}) \qquad (1)$$

for the range

$$25^\circ\text{C} < T < 45^\circ\text{C}.$$

TABLE I.A.1. Summary of FTR-3 Reference Excess Reactivity Measurements

Loading Run	Measured Excess Reactivity[a] (Ih)	Time from Initial Ref Critical (hr)	Temp (°C)	Excess Reactivity[a] Corrected for ^{241}Pu Decay (Ih)
18-1	85.77	0	28.78	85.77
18-2	87.4	18.33	28.05	87.53
21-1	61.43	47.87	34.68	61.77
25-1	52.27	215.75	36.78	53.80
28-1	43.03	238.63	39.08	44.72
31-1	24.5	260.05	43.67	26.34
34-1	21.73	329.93	44.50	24.07

[a]The actual excess reactivity of the core for each run is given by the values listed in the table minus 0.99 Ih.

All measurements listed in Table I.A.1 were made at the same reactor power level. At this power level, the reactor (as determined by inverse kinetics method) was subcritical by 0.99 ± 0.08 Ih. Thus the actual excess reactivity of the core at any temperature is given by ρ of Eq. (1) minus 0.99 ± 0.08 Ih. In performing the analysis the following assumptions were made: (1) all uncertainty in a data pair was concentrated in the reactivity measurement, and (2) the weight of each point equaled the square root of the number of data sets used in calculating the average reactivity and temperature for that reference (Run 18-2, $\omega = \sqrt{2}$; all others, $\omega = \sqrt{3}$). The root-mean-square deviation of the reactivities about the fitted line equaled ±0.48 Ih. The temperature coefficient of reactivity over

*Calculations for the reactivity effect arising from ^{241}Pu decay in FTR-2 and ZPR-3 Assembly 56B (see Progress Report for December 1969, ANL-7655, pp. 13-14) and ^{241}Pu atom densities were used to arrive at an estimated value for FTR-3.

the temperature range of these measurements is the slope of the fitted line; (3.92 ± 0.03 Ih/°C). Systematic error due to the ^{241}Pu-decay correction and error in the rod calibration are not included in the above considerations.

(ii) FTR-3 Core Edge Worth and Adjustments of Critical Mass (R. M. Fleischman)

The worths of outer-core drawers relative to radial reflector material and the worths of inner core drawers relative to outer core material were measured at selected locations along the outer core-reflector and inner core-outer core boundaries of FTR-3.

Each worth was measured by determining the position of a previously calibrated control rod necessary to maintain a specified subcritical power level. The temperature of the core was measured by averaging the readings of 21 copper constantan thermocouples located throughout the core region. The measured excess for each configuration was corrected by an estimated -0.17 Ih/day* for the ^{241}Pu-decay reactivity effect. The excess reactivity of the reference core for that temperature [see Eq. (1) above] was then subtracted and the result divided by the net gain or loss of fissile mass (^{239}Pu + ^{241}Pu + ^{235}U). The basic data and results of the analysis are summarized in Table I.A.2. The estimated error

TABLE I.A.2. Summary of Measurements of Drawer Exchange Worth in FTR-3

Type of Drawer Removed	Type of Drawer Added	Matrix Position	Radius (cm)	Temp (°C)	Time (hr) from Initial Reference Critical	Measured Excess Reactivity[a] (Ih)	Excess Reactivity[a] Corrected for ^{241}Pu Decay (Ih)	Worth of Exchange[b] (Ih)	Specific Worth[c] (Ih/kg)
Inner Core A	Outer Core C	M-19-28	35.41	28.38	22.98	125.8	126.04	39.24	124.38
Inner Core A	Outer Core C	M-17-26	37.1	34.6	42.25	99.45	99.89	37.41	118.58
Outer Core C	Inner Core A	M-18-28	39.11	36.09	212.17	16.73	18.94	-38.27	121.30
Outer Core C	Inner Core A	M-16-26	42.12	42.55	377.98	-5.2	-1.26	-33.69 ±0.96	106.79 ±3.04
Inner Core B	Outer Core C	M-17-23	33.19	41.92	358.75	52.43	56.17	21.33	96.25
Inner Core B	Outer Core C	M-18-27	35.41	38.37	234.13	66.0	68.44	20.10	90.70
Outer Core C	Inner Core B	M-20-29	37.1	39.0	236.32	63.2	65.66	19.78	89.26
Outer Core C	Inner Core B	M-18-28	39.11	34.11	72.0	43.23	43.98	-20.52	92.60
Outer Core	Radial Reflector	M-23-33	55.31	41.30	359.3	7.33	11.07	-26.19	31.84
Outer Core	Radial Reflector	M-16-31	58.79	40.97	261.92	13.77	16.50	-21.74	26.43
Radial Reflector	Outer Core	M-23-34	60.84	39.22	240.28	57.0	59.5	14.47	17.59
Radial Reflector	Outer Core	M-23-34	60.84	40.43	335.25	50.77	54.26	13.66	16.60
Radial Reflector	Outer Core	M-15-31	62.51	47.37	257.88	27.27	29.96	16.82	20.45
Boron Control 0-10 in.	Radial Reflector 0-10 in.	S 20-11 S 20-12 S 21-11 S 21-12	-	41.62	332.62	122.87	126.33	90.41	-

[a]The actual excess reactivity of the core is equal to the value listed in the table minus 0.99 Ih.
[b]The estimated error equals ±0.68 Ih unless otherwise stated.
[c]The estimated error equals ±2.16 Ih/kg, ±3.07 Ih/kg, and ±0.83 Ih/kg for ICA-OC, ICB-OC, and OC-RR types of exchange, respectively, unless otherwise stated.

*See footnote on p. 7.

is based on the assumption that the ±0.48 Ih* random error resulting from the least-squares analysis of the reference excess reactivity [see Sect. I.A.2.a.(i)] is representative of the random error in measurements of excess reactivity using this technique. Since the core temperature generally increased with time, uncertainty in the worth due to error in the ^{241}Pu-decay correction was essentially cancelled when the difference of the excess reactivities was taken. The estimated uncertainty in the worth does not include uncertainties due to inaccuracy in the calibration of control rods.

The specific worths of drawer exchanges were analyzed as a function of radius (core center to drawer center) using a linear least-squares analysis. Each point was weighted by the inverse of its uncertainty. At the outer core-radial reflector boundary the specific worth can be represented by:

$$\rho \pm 3.54(\mathrm{Ih/kg}) = -2.05(\mathrm{Ih/kg\text{-}cm})\ r(\mathrm{cm}) + 144.88(\mathrm{Ih/kg})$$

for the range 55 cm $< r <$ 63 cm. Evaluating this at the average outer core radius (60.27 cm) gave 21.33 ± 3.54 Ih/kg for the conversion factor from outer-edge fissile mass to reactivity. (The average radius is the radius of a cylinder having the cross-sectional area of the core.)

At the inner core-outer core boundary the fissile-mass normalization did not completely account for the difference between A- and B-type drawers. It was assumed, however, that the slopes of the curves of specific worth versus radius were the same for both sets of data. A fit to the data was made by carrying an additive normalization constant through the weighted least-squares analysis. The root-mean-square deviation of the normalized specific worths about the fitted line was minimized with respect to the normalization constant. The fitted slope and weighted average specific worth and radius were then used to determine fitted lines for both sets of data. An average of these two lines weighted by the total number of A or B drawers in the inner core is the best representation of the average specific worth function across the boundary:

$$\rho \pm 4.05(\mathrm{Ih/kg}) = -1.624(\mathrm{Ih/kg\text{-}cm})\ r(\mathrm{cm}) + 165.27(\mathrm{Ih/kg})$$

for the range 33 cm $< r <$ 43 cm. Evaluating this at the average inner core radius (37.58 cm) gave 104.24 ± 4.05 Ih/kg for the conversion factor from inner-boundary fissile mass to reactivity.

*The inner core A exchange at M-16-26 had an estimated random uncertainty in the measured excess reactivity of $\sqrt{3}$ x 0.48 Ih due to the subcriticality of the system and the technique used to infer the degree of subcriticality.

The large uncertainty in the fitted lines may be due in part to the variation in azimuthal angle at which the exchanges were made. An example in support of this is the ~6% difference in the measured worth of fueled control rods No. 6 and 9, which are located at the same radius and separated by 180°.

The final entry at the bottom of Table I.A.2 gives the results of a substitution of radial-reflector material for peripheral boron control material. This substitution was made in a cluster of four drawers of one peripheral control zone. The volume in which the substitution was made extended 10 in. into the stationary half from the midplane of the assembly.

The FTR-3 critical mass is summarized in Table I.A.3. The average specific worth of fissile-mass exchange at the two boundaries was used to determine the fissile-mass adjustment for fully inserting control rod No. 9 and correcting for the fact that the core was subcritical at the reference power level. Adjustment at the inner core-outer core boundary effectively increases the inner core radius. Adjustment at the outer core-radial reflector boundary effectively decreases the outer core radius. It should be noted that the corrected critical mass includes no corrections for smoothing of the boundaries, for the reactivity effect of the interface gap between assembly halves, or for the effect of core heterogeneity. It should be noted that the core-average thermocouple reading (30°C) is not a true representation of the core-average temperature.

TABLE I.A.3. Critical Mass of ZPR-9 Assembly 26 (FTR-3)

Reference Configuration	FTR-3 As Built Fissile-mass Inventory
1) Temp. 30°C 2) No. 9 Control rod withdrawn 57.18 cm (all others fully inserted) 3) All ^{10}B blades fully withdrawn 4) Subcritical by 0.99 Ih	541.948 (kg of ^{239}Pu, ^{241}Pu, ^{235}U)

Adjustment for:	Reactivity effect of adjustment[a] (Ih)	Fissile-mass adjustment at outer core-inner core boundary (kg of ^{239}Pu + ^{241}Pu + ^{235}U)	Fissile-mass adjustment at outer core-radial reflector boundary (kg of ^{239}Pu, ^{241}Pu, ^{231}U)
Control rod No. 9 partially withdrawn	-80.27 ± 0.48	-0.771 ± 0.031	-3.768 ± 0.626
Reference core subcritical at reference power level	+0.99 ± 0.08	+0.010 ± 0.001	+0.046 ± 0.009
Critical mass of unsmoothed, heterogenous cylinder		541.19	538.23

[a] 1% $\Delta k/k$ = 1064 Ih.

(iii) Doppler Experiments in FTR-3 (J. W. Daughtry)

In preparation for measurements of the ^{238}U and ^{239}Pu Doppler effects in FTR-3, the Doppler oscillator and autorod were installed in ZPR-9. The oscillator is located in the central tube, 23-23. The autorod is at matrix location 24-16. (See the Progress Report for February 1970, ANL-7669, p. 28, for a matrix map of the FTR-3 assembly.) Both the Doppler oscillator and the autorod extend through both halves of the reactor. A 1/4-in.-thick stainless steel "filter" has been loaded into the drawers surrounding the Doppler oscillator to reduce the hot sample-cold environment resonance interaction effect. Adjustments in the core loading were made to compensate for the reactivity change caused by the installation of the oscillator, autorod, filter, and Doppler samples. The ^{238}U Doppler measurement has been completed. The ^{239}Pu measurement is not yet complete.

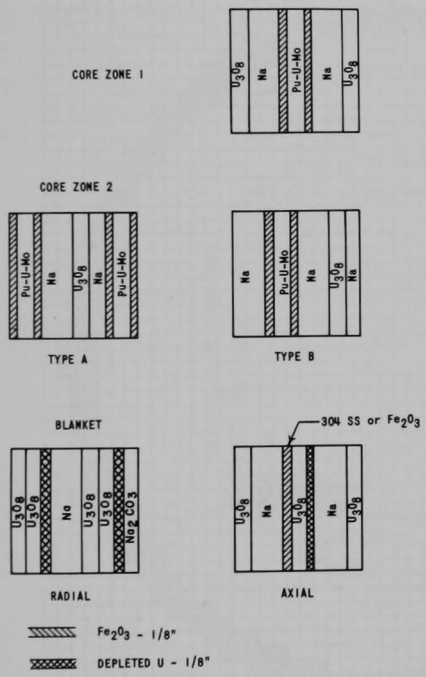

Fig. I.A.5
Drawer Configurations for ZPPR Assembly 2

3. ZPR-3 and ZPPR Operations and Analysis

a. Clean Critical Experiments (P. I. Amundson)

Last Reported: ANL-7669, pp. 30-36 (Feb 1970).

(i) ZPPR Assembly 2 (R. E. Kaiser)

ZPPR Assembly 2, the demonstration-plant benchmark core, went critical in early March. The assembly has a two-zone core with approximately equal zone volumes surrounded by a sodium-uranium oxide blanket. The inner core zone has a one-drawer unit cell, and the outer zone has a two-drawer cell, which includes blanket drawers as well (see Fig. I.A.5). The ratio of zone enrichments (outer zone to inner zone) was intended to be approximately 1.5, with an approximate core composition of 32% oxide fuel equivalent, 40% sodium, 19% steel, and 9% void.

The entire core was preloaded to a total volume of 2600 liters, 1300 liters per zone, with U_3O_8 or depleted uranium in place of the fuel plates. In this configuration, the core drawers were quite similar,

in total material content, to the blanket drawers. The approach to critical was then conducted by replacing the U_3O_8 or depleted uranium with ZPPR Pu-U-Mo alloy fuel plates. Criticality was initially achieved with a total of 2498 liters containing 1066.3 ± 4.8 kg of Pu-(239 + 241). At this point, there were 35 preloaded drawers per half which had not had fuel added to them. After rod calibrations were completed, those drawers were replaced with blanket material, resulting in a net reactivity change, for the 70 drawers, of -40.8 Ih. The core outline thus achieved has been designated the initial-critical core and is shown in Fig. I.A.6.

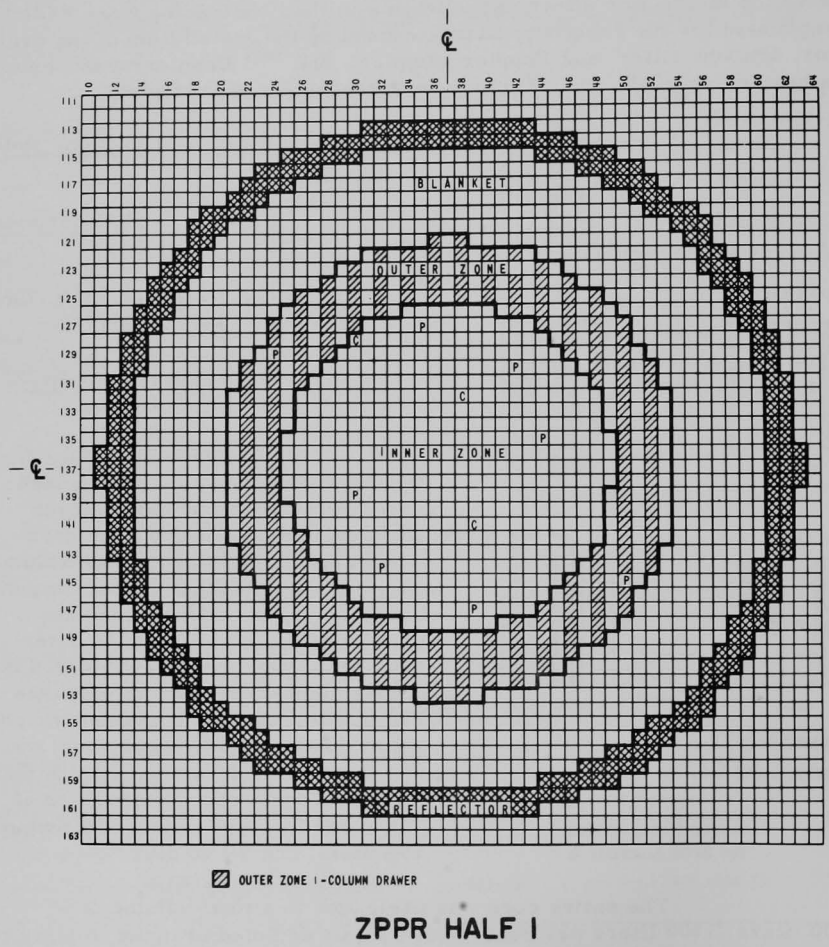

Fig. I.A.6. Interface Diagram for Initial Critical Configuration of ZPPR Assembly 2

Control-rod worth in the initial-critical configuration was quite small, equivalent to approximately 8 kg of edge fuel or 140 Ih. It was therefore decided to spike two of the six control rods with an extra column of fuel in order to provide greater capability for control. With this done, the total control-rod worth was 210 Ih, which was satisfactory for continued operation. Total safety-rod worth was determined by conducting measurements for four of the sixteen rods and extrapolating by means of symmetry to obtain the total rod worth. Past experience has shown this to be a valid procedure. The results indicated a total worth of 1.88% $\Delta k/k$ for the safety rods, as shown in Table I.A.4.

TABLE I.A.4. Worths of Poison Safety Rods in ZPPR Assembly 2

Rod Measured (position)	Worth (% $\Delta k/k$)	Additional Symmetric Rods	Total Worth (% $\Delta k/k$)
139-30	0.148	3	0.592
144-32	0.146	3	0.584
147-39	0.135	3	0.540
144-50	0.041	3	0.164
		Total worth of 16 rods	= 1.880% $\Delta k/k$

The initial critical configuration had a zone-volume ratio (inner to outer) of 52 to 48; it will be adjusted in the near future to 1 to 1. The cylindrical dimensions of the core with the 52-to-48 ratio are shown in Figs. I.A.7 and I.A.8 for Half 1 and Half 2 respectively. The dimensions

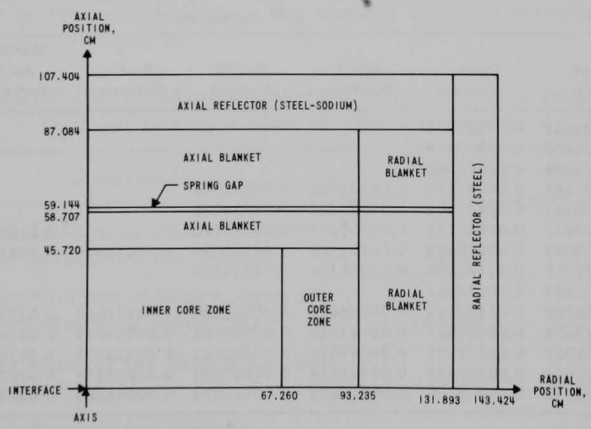

Fig. I.A.7. Initial Criticality Configuration of Half 1 of ZPPR Assembly 2

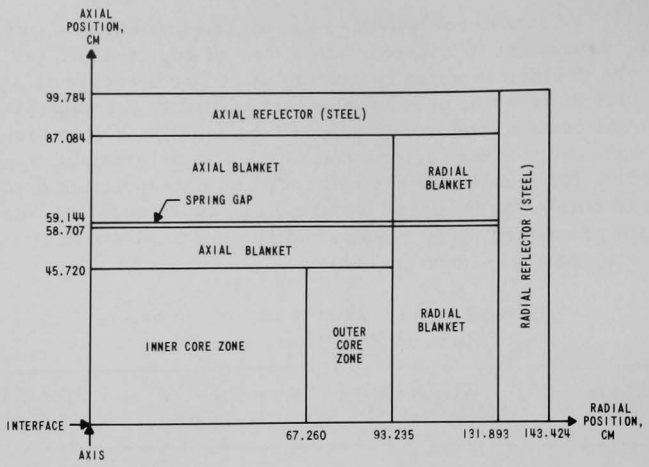

Fig. I.A.8. Initial Criticality Configuration of Half 2 of ZPPR Assembly 2

do not include the 0.06-in. interface gap. The atom densities in the various regions for the as-built core are presented in Table I.A.5. The values in the core zones and radial blanket and reflector include the interface gap volume and its stainless steel content, homogenized with the rest of the materials in the respective zones. The spring gap, which includes the

TABLE I.A.5. Atom Densities for the As-built Initial-critical Core of ZPPR Assembly 2

	10^{24} Atoms/cc						
Isotope	Inner Core	Outer Core	Axial Blanket	Radial Blanket	Radial Reflector	Na-Steel Axial Reflector	Steel Axial Reflector
Pu-239	0.00084688	0.00127960					
Pu-240	0.00011450	0.00017310					
Pu-241	0.00001694	0.00002592					
U-235	0.00001244	0.00001165	0.00001506	0.00002376			
U-238	0.00556942	0.00521791	0.00693322	0.01101575			
Na	0.00809837	0.00844749	0.00859637	0.00565222		0.01019209	
C	0.00000687	0.00000699	0.00001486	0.00100286	0.00053979	0.00030174	0.00054046
O	0.01316710	0.01181889	0.01376330	0.02011209			
Mo	0.00021587	0.00032662					
Fe	0.01204720	0.01402619	0.00954698	0.00705480	0.07172669	0.04933243	0.07279654
Ni	0.00127074	0.00127927	0.00123316	0.00100584	0.00059039	0.00162752	0.00073335
Cr	0.00255229	0.00257191	0.00247898	0.00202443	0.00120005	0.00325986	0.00148517
Mn	0.00021672	0.00021839	0.00021034	0.00017158	0.00059358	0.00055495	0.00061849
Si	0.00014058	0.00014169	0.00013623	0.00011039	0.00006364	0.00018029	0.00007905

holding spring at the back of the front drawers and the adjoining end pieces of the front and back drawers, has been similarly included in the calculation of atom densities in the axial and radial blankets. The actual enrichment ratio for the as-built core (outer zone to inner zone) is 1.51.

The total content of fissile material in the core zones is given in Table I.A.6. The U-235 that will be present as part of the U_3O_8 and depleted uranium plates in the blanket regions is not included.

TABLE I.A.6. Inventory (kg) of Fissile Material in Core Zones of ZPPR Assembly 2

Material	Plate	Inner Zone	Outer Zone	Total
Pu-239	Fuel	437.80	607.20	1045.00
Pu-241	Fuel	8.87	12.46	21.33
U-235	Fuel	2.74	3.79	6.53
U-235	U_3O_8	3.53	1.63	5.16
Total		452.94	625.08	1078.02

The critical mass quoted herein has not yet been corrected for core excess reactivity, irregular boundary effects, interface-gap worth, or control-rod spiking. These corrections will be applied later.

Preliminary measurements of edge worth have been performed at the interface between core zones and at the outer zone-blanket interface; the values will serve as a guide to adjust zone volumes to achieve a 50-to-50 configuration. The results of these measurements are summarized in Table I.A.7.

TABLE I.A.7. Measurements of Edge Worth in Initial Critical Configuration of ZPPR Assembly 2

Substitution	Worth (Ih)	r (cm)
Single Column of Outer Core for Single Column of Inner Core	+2.58	65.63
Double Column of Outer Core for Single Column of Inner Core	+24.19	66.56
Radial Blanket for Single Column of Outer Core	-9.42	90.00
Radial Blanket for Double Column of Outer Core	-16.08	93.03

b. Doppler Experiments (R. E. Kaiser)

Last Reported: ANL-7669, p. 37 (Feb 1970).

A safety document for the ZPPR Doppler-reactivity experiments has been written, including a description of the new axial system and the open- and closed-loop control systems. Specifications for the SEL 840 MP computer programs for these systems have been written; programing is under way.

c. Mockup Critical Experiments (W. P. Keeney, R. O. Vosburgh, and D. Meneghetti)

Last Reported: ANL-7669, p. 37-39 (Feb 1970).

(i) Experiment Status. Experiments with ZPR-3 Assembly 60, the first configuration in the current series of criticals in support of the EBR-II reactor program, have been concluded. The modification to form Assembly 61, with a partial nickel-rich radial reflector, is in progress.

(ii) As-built Compositions of ZPR-3 Assembly 60. The as-built compositions of Assembly 60 (see Table I.A.8), correspond to the zones of Fig. I.A.29, p. 39, Progress Report for February 1970, ANL-7669.

TABLE I.A.8. Compositions (Units: 10^{+24} atoms/cc) for ZPR-3 Assembly 60

Element	Core: Half 1	Core: Half 2	Core[a] Average	Control and Safety Rods[a]	(R1) Upper Gap	(R2) Upper Reflector[b]	(R3) Lower Gap	(R4) Lower Reflector[b]	(R7) Radial Blanket: Half 1[b]	(R7) Radial Blanket: Half 2[b]
U-235	0.005578	0.005613	0.005594	0.005594	-	-	-	-	0.000055	0.000054
U-238	0.004571	0.004568	0.004570	0.004570	-	-	-	-	0.026505	0.026548
Na	0.01017	0.01052	0.01033	0.01033	0.01480	0.01029	0.01199	0.00898	0.00457	0.00455
Fe	0.01323	0.01353	0.01337	0.01462	0.01844	0.02802	0.02332	0.03175	0.00964	0.00963
Cr	0.00340	0.00347	0.00343	0.00364	0.00480	0.00762	0.00622	0.00881	0.00254	0.00253
Ni	0.00148	0.00151	0.00149	0.00159	0.00209	0.00331	0.00271	0.00382	0.00111	0.00110
Mn	0.000171	0.000174	0.000172	0.000152	0.000260	0.000501	0.000379	0.000626	0.000146	0.000145
Si	0.00013	0.00013	0.00013	0.00017	0.00015	0.00012	0.00014	0.00007	0.00007	0.00007
Mo	-	-	-	-	0.00001	0.00003	0.00002	0.00004	-	-
O	0.002137	0.002132	0.002135	0.002135	-	-	-	-	-	-

[a]This represents a core average weighed in terms of the geometric arrangement, with a weight of 0.538 for Half 1 and of 0.462 for Half 2.
[b]Spring gap (0.66 cm wide) is located 21.03 in. from interface in Half 1 and core region of Half 2, and is 15.03 in. from interface in radial blanket of Half 2. Its composition is (10^{24} atoms/cc): Fe, 0.01685; Cr, 0.00419; Ni, 0.00184; Mn, 0.000175; and Si, 0.00020. This composition includes the spring, the back of the front drawer, and the front of the back drawer.

(iii) Critical Loading of ZPR-3 Assembly 60. The reference critical loading contained 221.93 kg of U-235 (see ANL-7669, p. 30). Table I.A.9 gives the type and number of fuel-bearing core drawers contained in the critical configuration. At critical, the excess reactivity due to the control rod in 1-T-16 being withdrawn 6.311 in. was determined to be +0.187% $\Delta k/k$.

TABLE I.A.9. Fissile Mass in Reference Loading (60-12) of ZPR-3 Assembly 60

Drawer Type	No. Loaded	Fissile Mass (kg U-235)
Core-half 1	90	107.204
Core-half 2	90	92.535
Control and Safety Rods, Half 1	5	5.956
Control and Safety Rods, Half 2	5	5.141
Half Drawers in Half 1[a]	5 pairs	5.956
Half Drawers in Half 2[a]	5 pairs	5.141
		Total 221.933

[a]The "half drawers" are loaded such that a pair is identically equal to one core drawer plus one radial reflector drawer. The plates in in these "half drawers" are loaded horizontally.

At 19.1°C, Control Rod No. 6 was 6.311 in. from full insertion. This corresponds to an excess reactivity of 0.187% $\Delta k/k$.

The delayed-neutron fraction (β) used in the kinetics code for the calibration of this control rod are listed in Table I.A.10. These values of β were derived from calculations supplied by the EBR-II Project (see Progress Report for January 1970, ANL-7661, p. 75). These were MACH-1 spherical diffusion calculations using the 22-energy-group cross-section set 238. For core radii of 27.65 and 30.19 cm both a depleted uranium-reflected and axial-reflector reflected case were calculated. These calculations indicated β_{eff} was not significantly affected by the radius. By use of the 27.65-cm cases, the calculations for axial reflector and radial depleted-blanket refector were equally weighted to produce the listed β values. The value of β_{eff} is considered to be preliminary until the values are available from the two-dimensional calculations from the ARC System, which is currently being modified to provide the group values.

TABLE I.A.10. Delayed-neutron Data for ZPR-3 Assembly 60 (Core radius of 27.65 cm)

	Effective Delayed-neutron Fractions (Units 10^{-3}) for Group						
Isotope	1	2	3	4	5	6	Total
U-235	0.2226	1.2478	1.1014	2.3844	0.7499	0.1523	5.8584
U-238	0.0154	0.1619	0.1914	0.4586	0.2660	0.0886	1.1819
Total	0.2380	1.4097	1.2928	2.8430	1.0159	0.2409	7.0403
	434.0 Ih/% $\Delta k/k$.						

(iv) Experimental Results for ZPR-3 Assembly 60

(a) Measurements of Edge Worth. The measurements of edge worth in Assembly 60 were confined to those needed for reactor operations. The half-core drawers in matrix positions 1- and 2-U-18 and 1- and 2-U-14 were individually replaced by blanket material, Zone 7 composition. The worths given in Table I.A.11 were obtained.

TABLE I.A.11. Measurements of Edge Worth in ZPR-3 Assembly 6

Matrix Position	Fissile Mass Removed (g U-235)	Worth of Blanket versus Core
1- and 2-U-14	985.21	-0.106% $\Delta k/k$
1- and 2-U-18	1,234.08	-0.150% $\Delta k/k$

(b) Temperature Coefficient of Reactivity. All reactivity measurements are corrected using a temperature coefficient of -1.26 Ih/°C obtained by elevating the reactor cell temperature.

(c) Modification of Upper Reflector. The worth of replacing the upper reflector, Zone R2, of the central 9 matrix elements with the composition of the 6-in. upper gap, Zone R1, was measured. This substitution is referred to as the "upper reflector modified configuration." To this modified reflector configuration, one inch of enriched B_4C was added at the axial extreme. The composition of this B_4C addition was B-10, 0.05997; B-11, 0.00613; and C, 0.02457 in units of 10^{24} atoms-cm^{-3}. The stainless steel composition remained unchanged at 10.6 vol %. The worths of these changes are given in Table I.A.12.

TABLE I.A.12. Axial-reflector Substitutions

From	To	Worth (% $\Delta k/k$)
Normal Axial Reflector	Modified Axial Reflector	-0.024
Normal Axial Reflector	Modified Axial Reflector + 1 in. B_4C	-0.023

(d) Radial Reaction-rate Traverses. Radial reaction-rate traverses were made at the core axial center from flat to flat of the quasi-hexagon, with U-238(n,f) and U-235(n,f) counters. The U-235 counter was traversed radially in two geometries. The first traverse measurements, made at only a few selected radial positions, were through a 1 x 2 x 2-in. void constructed by moving all of the plates back from the front of the drawers at the interface of the assembly. The second configuration, which

was also used for the U-238 counter, was one in which the plates of the drawers in the P-row were rotated through 90° and a 1/2 x 1 x 2-in. void was formed for placement of the traverse tube. Results of the radial reaction-rate traverses are given in Table I.A.13.

TABLE I.A.13. Radial Reaction-rate Traverses in ZPR-3 Assembly 60

Matrix Position[a]	U-235 (1 x 2 x 2-in. Void) Relative Count	U-235 (1 x 2 x 2-in. Void) Error (%)	U-235, Plates Horizontal Relative Count	U-235, Plates Horizontal Error (%)	U-238, Plates Horizontal Relative Count	U-238, Plates Horizontal Error (%)
1-P-22			0.5170	0.28	0.2244	1.09
21/22			0.5838	0.27	0.3763	0.89
21			0.6377	0.26	0.5211	0.80
20/21			0.6984	0.25	0.6160	0.76
20			0.7541	0.25	0.6990	0.73
19/20			0.8071	0.24	0.7714	0.71
19			0.8573	0.24	0.8393	0.69
18/19			0.8985	0.24	0.8889	0.68
18			0.9316	0.23	0.9205	0.67
17/18			0.9607	0.23	0.9515	0.67
17			0.9843	0.23	0.9809	0.66
16/17			0.9940	0.23	0.9930	0.66
16	1.0000		1.0000		1.0000	
15/16			0.9946	0.23	0.9943	0.66
15			0.9822	0.23	0.9836	0.66
14/15			0.9630	0.23	0.9462	0.67
14			0.9343	0.23	0.9240	0.67
13/14			0.9012	0.24	0.8681	0.69
13			0.8591	0.24	0.8346	0.69
12/13			0.8136	0.24	0.7736	0.71
12			0.7588	0.25	0.7019	0.73
11/12			0.6984	0.25	0.6130	0.76
11	0.6367	0.53	0.6355	0.26	0.5129	0.80
10/11			0.5710	0.27	0.3695	0.90
10			0.4866	0.28	0.2193	0.78
9/10			0.4094	0.30	0.1459	0.93
9	0.3552	0.64	0.3423	0.32	0.0873	1.17
8	0.2430	0.74	0.2323	0.38	0.0366	1.11
7			0.1553	0.45	0.0159	1.68
6			0.0982	0.55	0.0074	2.45
5			0.0612	0.68	0.0037	3.45
4			0.0360	0.88	0.0017	5.10
3	0.0223	2.24	0.0177	1.25	0.0008	7.23
2			0.0094	1.71	0.0005	9.40

[a]Positions indicate matrix location of center of counter, with 1-P-16 being radial horizontal center of core. Center-to-center distance of matrix tubes is 2.1755 in.

(e) Axial Reaction-rate Traverses. Axial reaction-rate traverses at the core-blanket interface, the center of 1- and 2-P-11, and in 1- and 2-P-16 with U-238(n,f), U-235(n,f), and B-10(n,α) counters were made. The U-238 counter used in all of the traverses was No. IC 24-4; the U-235 Counter No. J contains a loading of 5.1 mg which is 93.2 wt % U-235, 6 wt % U-238, and 1 wt % U-234. The U-238 counter and a plutonium traverse counter, identical in construction to Counter J, are described in the Progress Report for May 1968, ANL-7457, p. 13. In all data, the count rates listed as "U-235" and "U-238" are the sum reaction of Counter J or Counter IC 24-4. The central axial traverses in 1- and 2-P-16 were done with four different top axial reflector configurations: the normal upper gap and reflector composition, the modified upper reflector composition, and with the 1 in. of enriched B_4C added at the top axial extreme for both the normal and modified reflector cases. These data are tabulated in Tables I.A.14 through I.A.18.

TABLE I.A.14. Axial Reaction Rates in P-11, Normal Compositions for ZPR-3 Assembly 60

	U-235		U-238	
Position (in.)	Relative Count	Error (%)	Relative Count	Error (%)
-28.56	0.1287	1.27	0.0014	7.58
-24.56	0.2744	0.92	0.0041	4.53
-20.56	0.4235	0.79	0.0109	2.78
-18.56	0.5055	0.74	0.0183	2.15
-16.56	0.5826	0.71	0.0318	1.64
-14.56	0.667	0.68	0.0546	1.27
-13.56	0.6986	0.67	0.0700	1.13
-12.56	0.7342	0.66	0.0944	0.98
-11.56	0.7566	0.65	0.1237	0.87
-10.56	0.7823	0.65	0.1555	1.11
-9.56	0.7928	0.64	0.2058	0.99
-8.56	0.8055	0.64	0.2658	0.89
-7.56	0.8175	0.64	0.3567	0.79
-6.56	0.8306	0.64	0.5169	0.70
-5.56	0.8485	0.63	0.6969	0.63
-4.56	0.9021	0.62	0.8196	0.60
-3.56	0.9308	0.62	0.8989	0.59
-2.56	0.9672	0.61	0.9457	0.58
-1.56	0.9911	0.61	0.9815	0.58
-0.53	1.0059	0.60	0.9890	0.58
0.0[a]	1.0000		1.0000	
+0.50	0.9988	0.61	1.0040	0.57
+1.50	0.9865	0.61	0.9819	0.58
+2.50	0.9658	0.61	0.9474	0.58
+3.50	0.9372	0.62	0.9002	0.59
+4.50	0.8887	0.62	0.8267	0.60
+5.50	0.8515	0.63	0.7159	0.63
+6.50	0.8277	0.64	0.5466	0.68
+7.50	0.8155	0.64	0.3850	0.77
+8.50	0.8132	0.64	0.2921	0.86
+9.50	0.7807	0.65	0.2289	0.94
+10.50	0.7778	0.65	0.1810	1.04
+12.50	0.7378	0.66	0.1160	1.26
+14.50	0.6688	0.68	0.0783	1.07
+16.50	0.5945	0.70	0.0420	1.44
+20.50	0.4402	0.78	0.0150	2.38
+24.50	0.2838	0.91	0.0061	3.71
+28.50	0.1372	1.24	0.0022	6.18

[a]Zero position is core centerline, which lies 0.53 in. from reactor interface. Positive numbers are in Half 1, negative numbers are in Half 2.

TABLE I.A.15. Axial Reaction Rates in P-16, Normal Reflector Composition, for ZPR-3 Assembly 60

	U-235		U-238	
Position (in.)	Relative Count	Error (%)	Relative Count	Error (%)
-28.56	0.1860	0.87	0.0013	6.51
-24.56	0.3928	0.65	0.0040	3.70
-20.56	0.5965	0.56	0.0103	2.30
-18.56	0.6977	0.54	0.0138	1.76
-16.56	0.7777	0.52	0.0317	1.32
-14.56	0.8457	0.51	0.0531	1.46
-13.56	0.8690	0.51	0.0717	1.27
-12.56	0.8854	0.50	0.0960	1.11
-11.56	0.8871	0.50	0.1284	0.97
-10.56	0.8887	0.50	0.1616	1.24
-9.56	0.8838	0.50	0.2113	1.11
-8.56	0.8619	0.51	0.2836	0.99
-7.56	0.8278	0.51	0.3733	0.89
-6.56	0.8331	0.51	0.5222	0.79
-5.56	0.8589	0.51	0.6893	0.72
-4.56	0.8340	0.50	0.8057	0.69
-3.56	0.9317	0.50	0.8881	0.67
-2.56	0.9675	0.49	0.9503	0.66
-1.56	0.9918	0.49	0.9699	0.66
-0.53	0.9971	0.49	0.9895	0.66
0[a]	1.0000	0.49	1.0000	
+0.50	0.9999	0.49	0.9991	0.65
+1.50	0.9911	0.49	0.9919	0.66
+2.50	0.9638	0.49	0.9391	0.67
+3.50	0.9276	0.50	0.8806	0.68
+4.50	0.8810	0.50	0.8068	0.69
+5.50	0.8376	0.51	0.6917	0.72
+6.50	0.8123	0.51	0.5302	0.79
+7.50	0.8152	0.51	0.3915	0.87
+8.50	0.8242	0.51	0.2939	0.97
+9.50	0.8202	0.51	0.2292	1.07
+10.50	0.8198	0.51	0.1813	1.18
+11.50	0.8199	0.51	0.1404	0.93
+12.50	0.8196	0.51	0.1122	1.03
+13.50	0.8087	0.52	0.0870	1.16
+14.50	0.7961	0.52	0.0668	1.31
+16.50	0.7448	0.53	0.0392	1.69
+18.50	0.6726	0.54	0.0236	2.16
+20.50	0.5872	0.57	0.0140	2.80
+24.50	0.4022	0.64	0.0049	3.34
+28.50	0.1987	0.85	0.0019	5.32

[a]Zero position is core centerline, which lies 0.53 in. from reactor interface. Positive numbers are in Half 1, negative numbers are in Half 2.

TABLE I.A.16. Axial Reaction Rates in P-16, Normal Reflector Composition + 1 in. B_4C, for ZPR-3 Assembly 60

	U-235		U-238	
Position (in.)	Relative Count	Error (%)	Relative Count	Error (%)
-28.56	0.1854	0.88		
-24.56	0.3909	0.66		
-20.56	0.5900	0.57		
-18.56	0.6915	0.54		
-16.56	0.7806	0.52		
-14.56	0.8496	0.51		
-13.56	0.8727	0.51		
-12.56	0.8915	0.51		
-11.56	0.8901	0.51		
-10.56	0.8923	0.51		
-9.56	0.8804	0.51		
-8.56	0.8687	0.51	0.2743	1.00
-7.56	0.8654	0.51		
-6.56	0.8445	0.51	0.5159	0.79
-5.56	0.8454	0.51		
-4.56	0.8806	0.51	0.8164	0.69
-3.56	0.9241	0.50		
-2.56	0.9623	0.50	0.9557	0.66
-1.56	0.9894	0.49		
-0.53	1.0014	0.49	0.9972	0.65
0[a]	1.0000	-	1.0000	-
+0.50	1.0031	0.49	1.0001	0.65
+1.50	0.9855	0.49		
+2.50	0.9625	0.50	0.9523	0.66
+3.50	0.9248	0.50		
+4.50	0.8742	0.51	0.8156	0.69
+5.50	0.8277	0.52		
+6.50	0.8055	0.52	0.5430	0.78
+7.50	0.8095	0.52		
+8.50	0.8162	0.52	0.2988	0.96
+9.50	0.8125	0.52		
+10.50	0.8224	0.52	0.1817	0.83
+11.50	0.8203	0.52		
+12.50	0.8190	0.52	0.1160	1.01
+13.50	0.8071	0.52		
+14.50	0.7923	0.52	0.0676	1.30
+16.50	0.7466	0.53	0.0402	1.18
+18.50	0.7000	0.55	0.0241	1.51
+20.50	0.5852	0.57	0.0143	1.96
+24.50	0.4055	0.65	0.0054	3.16
+28.50	0.1889	0.87	0.0019	5.31

[a]Zero position is core centerline, which lies 0.53 in. from reactor interface. Positive numbers are in Half 1, negative numbers are in Half 2.

TABLE I.A.17. Axial Reaction Rates in P-16, Upper Reflector Modified, No. B_4C, for ZPR-3 Assembly 60

	U-235		U-238	
Position (in.)	Relative Count	Error (%)	Relative Count	Error (%)
-28.56	0.1848	0.89		
-24.56	0.3930	0.66		
-20.56	0.5843	0.57		
-18.56	0.6951	0.54		
-16.56	0.7816	0.53		
-14.56	0.8521	0.51		
-13.56	0.8769	0.51		
-12.56	0.8884	0.51		
-11.56	0.9011	0.51		
-10.56	0.8873	0.51		
-9.56	0.8762	0.51		
-8.56	0.8709	0.51	0.2749	1.00
-7.56	0.8554	0.51		
-6.56	0.8428	0.52	0.5171	0.79
-5.56	0.8418	0.52		
-4.56	0.8816	0.51	0.8038	0.69
-3.56	0.9297	0.50		
-2.56	0.9655	0.50	0.9428	0.66
-1.56	0.9927	0.49		
-0.53	1.0006	0.49	0.9973	0.65
0[a]	1.0000	-	1.0000	-
+0.50	1.0015	0.49	0.9954	0.66
+1.50	0.9821	0.50		
+2.50	0.9582	0.50	0.9421	0.66
+3.50	0.9221	0.50		
+4.50	0.8769	0.51	0.8185	0.69
+5.50	0.8327	0.52		
+6.50	0.8047	0.52	0.5409	0.78
+7.50	0.8107	0.52		
+8.50	0.8082	0.52	0.2970	0.97
+9.50	0.8176	0.52		
+10.50	0.8148	0.52	0.1809	0.84
+11.50	0.8114	0.52		
+12.50	0.8012	0.52	0.1144	1.02
+13.50	0.7874	0.53		
+14.50	0.7760	0.53	0.0713	1.27
+16.50	0.7160	0.54	0.0439	1.13
+18.50	0.6497	0.56	0.0287	1.39
+20.50	0.5692	0.58	0.0176	1.76
+24.50	0.3966	0.66	0.0071	2.78
+28.50	0.1986	0.86	0.0028	3.95

[a]Zero position is core centerline, which lies 0.53 in. from reactor interface. Positive numbers are in Half 1, negative numbers are in Half 2.

TABLE I.A.18. Axial Reaction Rates in P-16, Upper Reflector Modified + 1 in. B_4C, for ZPR-3 Assembly 60

Position (in.)	U-235 Relative Count	U-235 Error (%)	U-238 Relative Count	U-238 Error (%)
-28.56	0.1854	0.91		
-24.56	0.3936	0.67		
-20.56	0.5934	0.59		
-18.56	0.6891	0.56		
-16.56	0.7874	0.54		
-14.56	0.8532	0.53		
-13.56	0.8732	0.52		
-12.56	0.8942	0.52		
-11.56	0.8946	0.52		
-10.56	0.8901	0.52		
-9.56	0.8862	0.52		
-8.56	0.8721	0.52	0.2815	0.98
-7.56	0.8623	0.53		
-6.56	0.8471	0.53	0.5242	0.78
-5.56	0.8437	0.53		
-4.56	0.8849	0.52	0.8024	0.69
-3.56	0.9320	0.51		
-2.56	0.9650	0.51	0.9533	0.66
-1.56	0.9894	0.51		
-0.53	0.9981	0.51	0.9924	0.65
0[a]	1.0000	-	1.0000	-
+0.50	1.0002	0.51	1.0050	0.65
+1.50	0.9920	0.51		
+2.50	0.9608	0.51	0.9457	0.66
+3.50	0.9219	0.52		
+4.50	0.8795	0.52	0.8172	0.68
+5.50	0.8324	0.53		
+6.50	0.8072	0.54	0.5408	0.77
+7.50	0.8083	0.54		
+8.50	0.8176	0.53	0.2989	0.96
+9.50	0.8137	0.53		
+10.50	0.8105	0.53	0.1781	0.83
+11.50	0.8148	0.53		
+12.50	0.8002	0.54	0.1115	1.03
+13.50	0.7919	0.54		
+14.50	0.7704	0.54	0.0714	1.26
+16.50	0.7177	0.55	0.0443	1.12
+18.50	0.6491	0.57	0.0280	1.39
+20.50	0.5770	0.59	0.0174	1.57
+24.50	0.3916	0.68	0.0071	2.45
+28.50	0.1924	0.89	0.0028	3.90

[a]Zero position is core centerline, which lies 0.53 in. from reactor interface. Positive numbers are in Half 1, negative numbers are in Half 2.

(f) Irradiations. A series of irradiations of thermoluminescent gamma detectors and foil packets for neutron activation studies was made throughout the assembly.

B. Component Development

1. Instrumentation and Control

a. Instrumentation Development for Instrumented Subassembly

(i) Instrumented Fuel Subassembly Flowmeters (G. A. Forster)

(a) Procurement of Mark-III (Sodium Calibratable) Flowmeters

Last Reported: ANL-7669, p. 40 (Feb 1970).

Close contact is being maintained with both contractors to ensure adherence to quality-assurance provisions of their contract specifications and to quickly resolve apparent conflicts in specifications or definitions of terms.

One contractor is considerably behind in his original schedule for developing a detailed quality-assurance plan and a manufacturing plan. This is not expected to affect final delivery of the flowmeters, since development of both plans is concurrent with procurement of long-delivery items such as the permanent magnets.

(b) Calibration of Mark-III Flowmeters

Last Reported: ANL-7669, p. 40 (Feb 1970).

Calibration data for the Mark-III flowmeter (Serial 010) has been analyzed. This flowmeter was calibrated in the ANL Sodium Flowmeter Calibration Loop and subsequently installed in EBR-II Instrumented Subassembly Test XX02 (PNL-17). The results indicate that if the flowmeter sensitivity (in mV/gpm) is a function of the flowrate, the variation in sensitivity will be less than 1%. The effect of minor variations of flowrate on sensitivity will be determined in future calibrations of other Mark-III flowmeters.

The calibration test plan called for initial runs at nominal temperatures of 600, 700, and 800°F, cooling to below 400°F, followed by repeat runs at 600 and 800°F. As shown in Table I.B.1, the repeat runs agree within 0.03% and 0.2% of the initial runs at nominal 600 and 800°F, respectively, indicating that the flowmeter was adequately stablized for 800°F.

Sensitivity is a decreasing function of temperature. At 700°F, a linear approximation is

$$0.3167 - [5.7 \times 10^{-5}(F-700)] \text{ mV/gpm.}$$

TABLE I.B.1. Out-of-pile Calibration of Mark-III Flowmeter (Serial 010)

Initial Runs						Repeat Runs			
585°F		700°F		800°F		590°F		800°F	
gpm	mV/gpm	gpm	mV/gpm	gpm	mV/gpm	gpm	mV/gpm	gpm	mV/gpm
22.8	0.3237	7.2	0.3170	6.5	0.3132	9.7	0.3234	12.2	0.3128
30.7	0.3227	14.7	0.3159	13.0	0.3126	18.4	0.3244	23.7	0.3121
42.8	0.3237	23.2	0.3167	19.5	0.3121	27.6	0.3242	34.8	0.3125
48.3	0.3271	31.5	0.3165	25.8	0.3120	36.8	0.3263	43.5	0.3115
		38.9	0.3168	31.9	0.3115	46.4	0.3259	60.1	0.3128
		46.0	0.3173	38.8	0.3118	55.2	0.3252		
				45.2	0.3111				
				49.0	0.3112				
				57.3	0.3114				
Avg	0.3248		0.3167		0.3117		0.3249		0.3123

From small-sampling theory, this calibration constant is within 0.13% of true value, with 90% confidence; however, this does not account for systematic errors in the calibration flow loop. A more reasonable estimate of total error would be 1/2%.

A Mark-II flowmeter is being calibrated in the calibration flow loop. This flowmeter has the same magnetic characteristics and flow tube design as the Mark-III. Therefore, the data will aid in understanding the performance of the Mark III and in analyzing the performance of two Mark-II flowmeters that have been operated in the EBR-II Instrumented Subassembly.

(ii) Fuel-pin Thermocouples (A. E. Knox)

(a) In-pile Tests in EBR-II Instrumented Subassembly

Last Reported: ANL-7669, pp. 40-41 (Feb 1970).

Four of the seven fuel-pin thermocouples in the Test XX02 Instrumented Subassembly appear to be functioning properly; two thermocouples (FCTC 2 and FCTC 17) have low output indications at the recorders, and one (FCTC 3) has an erratic output due to an opening in its thermoelements. FCTC 2 and FCTC 17 are being examined with a time-domain reflectometer (TDR) to determine the cause of the low outputs.

The low output of FCTC 1, as reported in ANL 7669, was due to a faulty voltage-to-current transmitter, which has since been repaired.

At zero power (during shutdowns), the indicated fuel temperatures for capsules 7 and 10 have been less than the indicated spacer-wire temperatures for these capsules. On January 13, 1970, February 10, 1970, and March 5, 1970, the output of FCTC 7 averaged 355 ± 4°C, whereas that of SWTC 7

averaged 370 ± 2°C. Also, for the same three shutdowns, the output of FCTC 10 was 368 ± 5°C, that of SWTC 10 being 371 ± 2°C. The output of each thermocouple showed no drift at shutdown during the period from January 13, 1970, to March 5, 1970.

In contrast, prior to irradiation and during the first shutdown, the temperature indications from the thermocouples at the fuel center for capsules 7 and 10 were higher than those of the associated spacer-wire thermocouples. The reason for this reversal is not evident and is being investigated.

b. EBR-II In-Core Instrument Test Facility (E. Hutter)

(i) Design, Development, and Fabrication of the Facility (O. S. Seim and R. H. Olp)

Last Reported: ANL-7669, pp. 45-46 (Feb 1970).

A full-scale mockup of portions of the small rotating plug of EBR-II, as shown in Fig. I.B.1, has been installed in the access opening of the lower-level walkway area of the D-331 building.

The dimensional requirements for the INCOT terminal-box assembly, which accepts the sensor leads extending upward from the reactor core, have been determined through operating tests performed in the mockup. The spatial and mechanical relationships for the signal-lead bundle, the multiple-sensor connectors, and the sensor-tube assembly, which are located within the terminal-box assembly, have been studied.

Other tests using a mockup of the terminal-box assembly have successfully demonstrated the remote insertion and removal of a 34-ft-long thermocouple sensor (including the end-termination connector) into one of the sensor guide tubes in the sensor-thimble assembly of the mockup.

The interface relationships between the top of the terminal box and the handling-container system that provides the remote-removal capability for irradiated sensors have been developed. The necessary dimensional relationships have been established between the shielded-coffin section of the handling container, which holds the sensors, and the terminal box attached to the thimble assembly.

Studies have resulted in a practical system for the selective withdrawal of an individual sensor from a multiple (19-sensor) thimble assembly into the handling container.

Various types of handling containers also have been studied in the mockup in an attempt to simplify the procedure for removing and

inserting sensors when the INCOT facility is operating in the No. 2 control-rod-drive location on the small rotating plug. Because of the space limitations inherent in this location and around the adjacent control-rod-drive assemblies on the small rotating plug, realistic dimensional limitations in this area must be used to develop a proper sensor-handling system. Space limitations, therefore, determine the complexity and size of the equipment necessary for inserting and removing individual experiments from the reactor without removing the entire INCOT facility each time.

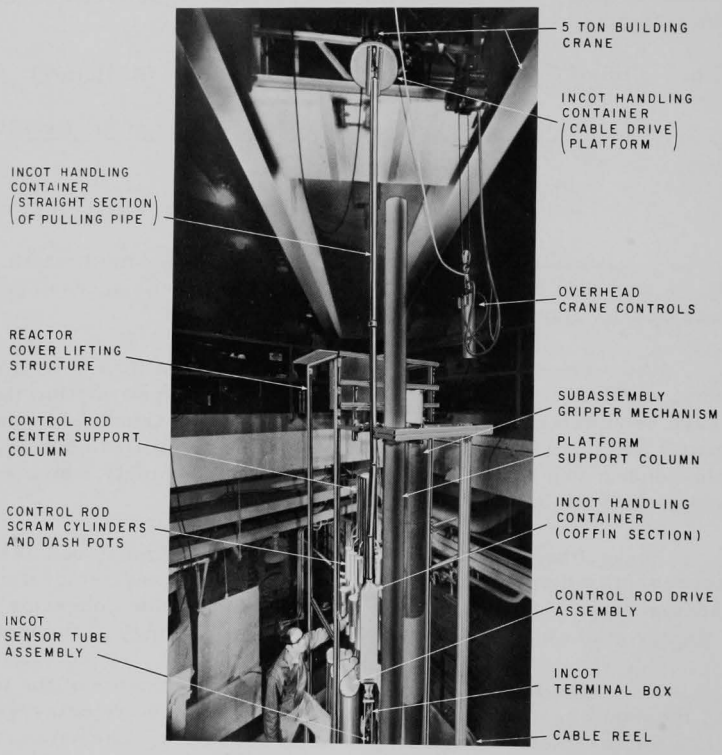

Fig. I.B.1. Mockup to Study Spatial Relationships for INCOT. ANL Neg. No. 104-70.

An analysis was made of the requirements for positioning the handling container (pulling pipe plus the coffin and drive apparatus) over the terminal box when using the five-ton building crane in the mockup area. These requirements include making the attachment of the coffin section to the thimble assembly and terminal box located in the No. 2 control-rod opening of the mockup. As a result of the tests, special guidance devices were developed to permit a smooth and positive positioning of the coffin section to the top of the terminal box in preparation for removal of the sensor-tube assembly.

Additional studies in the mockup have led to the development of an alternative to the straight handling container design to provide greater flexibility in positioning and moving the container system over the control-rod opening in the small rotating plug. This approach utilizes an offset handling container to permit the positioning and final location of the handling container over the control-rod opening without the necessity for disassembling and removing the support frame for the reactor-cover drive motor, as would be required with the straight type of container. This approach permits a significant reduction in the effort required to arrange the overhead equipment on the small rotating plug so as to accommodate the positioning of the handling container for sensor removal. Other mockup tests are being made to select or confirm the design approaches used for the INCOT.

C. Sodium Technology

1. Sodium Chemistry

a. Determination of the Solubility of Gases in Liquid Sodium (F. Cafasso and E. Veleckis)

Last Reported: ANL-7655, p. 49 (Dec 1969).

(i) Xenon Solubility in Sodium. The inclusion of isotopic mixtures* of xenon in gas-bonded fuel elements is being evaluated at EBR-II as a means of locating fuel failures in LMFBRs. Xenon escaping from failed fuel passes through the sodium coolant and enters the cover gas, which can be analyzed by a mass spectrometer. Accordingly, the solubility of xenon in liquid sodium is of importance and is being measured. The technique involves saturating liquid sodium with xenon gas at a preselected temperature and pressure, stripping the dissolved xenon from sodium with a helium sparge, trapping the stripped xenon on liquid-nitrogen-cooled silica gel, heating the gel to remove the xenon, transferring it to a bulb, and finally assaying it. Previous work (see ANL-7655, p. 49) showed that a Beckman GC-5 gas chromatograph equipped with an ionization detector could detect nanomole concentrations of xenon in the final gas samples.

Recent effort has been devoted to determining whether xenon is completely recovered from the sodium by the helium sparging and subsequent steps. This was done by introducing into the system helium mixed with approximately 100 nmol of xenon, the amount expected to dissolve. The gas mixture was circulated through sodium for 2 hr, and then the steps from stripping to analysis were carried out, as would be done in a typical solubility experiment. Recoveries of 90-100% of the added xenon were obtained.

*Chemical Engineering Division Annual Report--1968, ANL-7575, pp. 105-111 (April 1969).

The requisite analytical and operational capability having been established, an exploratory solubility experiment was run. At 500°C, the solubility of xenon in sodium was about 5 ppb/atm.

2. Sodium Analytical Development

a. Analytical Methods for Metallic and Halide Impurities in Sodium (R. Meyer and H. Edwards)

Last Reported: ANL-7655, pp. 50-51 (Dec 1969).

Complete characterization of the metallic impurities in a sodium system is time consuming when individual atomic-absorption determinations are performed, as is done at EBR-II.* It would be desirable to have a rapid survey method that determines several impurities simultaneously, possibly with less accuracy than provided by the individual determinations. If this aim is not reasonably achievable, it would be valuable to have a monitoring system that at least showed if a significant change in impurity level had occurred. A literature search has been made for methods that might be used for on-line analysis of flowing molten sodium, methods for examination of aqueous solutions of a sodium sample, and methods that employ a preconcentration of the metallic impurities. Consideration is being given to several of these methods; some are being evaluated experimentally.

One approach to the direct measurement of trace impurities in sodium is suggested by two recent papers by Fassel and Dickinson.** By ultrasonic nebulization they produced a metal aerosol which then was passed through an induction-coupled plasma, and the resultant spectrum was analyzed by emission spectroscopy. Working curves for impurities in the metal-dust aerosols extended down to about 50 ppm. Subsequently, aqueous solutions were treated with an improved plasma source, and the emission spectrographic detection limits for all elements investigated fell in the range of nanograms to fractional milligrams per milliliter. This improved technique should also be applicable to the metal aerosols. Because the combination of ultrasonic agitation and total consumption of the metal sample should counteract sampling inaccuracies due to segregation of impurities (a cause for concern in most other methods), this approach to the determination of metallic impurities in sodium is very attractive. An experimental evaluation of the method is planned.

---

*Ramachandran, T. P., and Hareland, W. E., The Determination of Trace Metallic Impurities in Reactor Sodium, presented at the 13th Conference on Analytical Chemistry in Nuclear Technology, Gatlinburg, Tennessee (Sept. 30-Oct. 2, 1969).

**Fassel, V. A., and Dickinson, G. W., Anal. Chem. 40, 247 (1968); Dickinson, G. W., and Fassel, V. A., Anal. Chem. 41, 1021 (1969).

For methods requiring dissolution of the sodium sample, at least three detection methods are under consideration: emission spectroscopy, spark-source mass spectroscopy, and X-ray fluorescence. (1) As noted above, the application of emission spectroscopy to the analysis of aqueous aerosols is feasible. (2) Spark-source mass spectroscopy has outstanding sensitivity, but it is a microsampling method and is of doubtful reliability for solid metallic sodium, in which impurities segregate. However, the technique* of analyzing a conductive electrode formed by freezing a mixture of high-purity graphite and an aqueous solution might be applicable to reactor sodium. (3) We are currently investigating the suitability of X-ray fluorescence spectroscopy for determination of impurities in a NaCl matrix. Emphasis has been on devising a suitable way of localizing and mounting the sample for analysis, and on determining the interfering effect of the relatively large amount of NaCl. Our measurements to date indicate that 1 μg of nickel is detectable, but the signal/background ratio changed from 2/1 to 1/1 when the amount of NaCl was increased from 1 to 5 mg. Even with the larger amount, however, the net counting rate (32 cpm) was high enough to indicate that the method is reasonably sensitive. Similar checks will be made with elements of widely varying atomic number (e.g., Ca, Sn, and Pb) to determine general trends in sensitivity of the X-ray fluorescence technique.

For methods requiring preconcentration of the trace metal impurities, vacuum distillation is being evaluated. This step would be followed by emission spectrographic or X-ray fluorescence examination of the residue. A still based on an EBR-II design is being assembled and will be used in checking out the entire analysis.

3. On-line Monitors

a. Evaluation and Improvement of Oxygen-activity Meter (J. T. Holmes)

Last Reported: ANL-7655, pp. 51-53 (Dec 1969).

A complete monitoring station for oxygen impurities in sodium, including up to four electrochemical oxygen meters and means for testing the meter response and calibration, has been scheduled for installation on the Radioactive Sodium Chemistry Loop (RSCL) at EBR-II by December 1970. The field-test program at EBR-II will examine the operability of station components and on-line procedures for testing meter response and calibration, and will determine how stable and accurate meter operation is in radioactive sodium.

As reported in ANL-7655, the oxygen meter being given prime consideration is being developed at Brookhaven National Laboratory (BNL);

*Cherrier, C., and Nalbantoglu, M., Anal. Chem. 39, 1640 (1967).

however, oxygen meters developed at Westinghouse will also be tested. The electrochemical cells in both types of meter employ a reference electrode containing oxygen gas. A response test being considered at ANL involves the periodic changing of the reference gas to one of a different oxygen activity. The meters will be calibrated periodically by the equilibration and analysis of refractory-metal wires. Design of the wire-exposure device for the RSCL is under way.

Performance and quality specifications for oxygen meters have been submitted with purchase orders to BNL and Westinghouse. Delivery from both sources is expected by mid-1970. Apparatus is being readied at ANL-Illinois to calibrate these meters by on-line distillation analysis, equilibration and analysis of refractory-metal wires, and, possibly, determination of the oxidation rate of uranium metal foils. If both types of oxygen meters perform well in these tests, two of each type may be installed on the RSCL, since there is space for four meters.

4. Fission Product Behavior and Control

a. Source-rate Calculational Model (W. E. Miller)

Not previously reported.

A major objective of fuel-failure detection is to differentiate between innocuous leaks (that release only fission product gases) and serious cladding ruptures (that permit the sodium to contact the fuel). Such contact by sodium may cause fuel washout or may lead to blockage of the coolant channel and thus propagate the damage.

A detection system that distinguishes between innocuous and serious fuel failures might be based on the detection of specific fission product isotopes dissolved in the sodium coolant. Criteria for selecting such isotopes would include the following: (1) the chemical state of the isotope must be relatively nonvolatile and readily soluble in sodium; (2) any gaseous or volatile precursors must be short-lived, so that little of the precursor escapes into the sodium and decays there to the isotope to be detected; (3) preferably, the isotope should migrate to the fuel-cladding interface, where it could concentrate and be promptly dissolved by inleaking sodium. It appears that certain cesium and rubidium isotopes may have these qualifications. Therefore, evaluation studies are in progress, and experimental work is planned to determine whether they do, in fact, satisfy the above criteria.

D. Systems and Plant Development

1. Plant and Design

a. Contract Management, Technical Review and Evaluation (L. W. Fromm and K. A. Hub)

Last Reported: ANL-7661, p. 34 (Jan 1970).

(i) Evaluation of 1000-MWe Follow-on Study Task Reports. Drafts of Volume II (Plant Design, Parts 1 and 2), Volume III (Research and Development), and Volume IV (Backup and Contractual Material) for the 1000-MWe LMFBR Follow-on Study evaluation reports have been completed and transmitted to RDT for review. Comments on the evaluation reports have been received from Atomics International, Babcock & Wilcox, Combustion Engineering, and Westinghouse. Comments from General Electric are expected soon.

E. EBR-II--Research and Development

1. Equipment--Fuel Related (E. Hutter)

a. Handling of Subassemblies Containing Failed Fuel (C. Divona)

Not previously reported.

During operation of EBR-II, the fuel-handling equipment has successfully handled all fuel subassemblies, including some which contained fuel elements that had become defective. Although the need is remote for handling subassemblies containing more severe fuel failures, including those in which the subassembly itself may fail, a number of methods for handling such subassemblies are being studied to reduce potential reactor downtime should such a failure occur.

One method, still under preliminary development, makes use of a dipper and an emergency coffin. With this scheme, the subassembly with the failed fuel is removed from the reactor and placed on the transfer arm in the standard manner. The subassembly is then deposited into an elongated dipper having a closed bottom. The dipper functions as a removable storage basket. The subassembly can be stored in it in the reactor for removal of decay heat, or the dipper and failed subassembly can be removed from the primary tank into an emergency coffin on the operating floor.

The dipper approach makes use of a spare fuel-transfer penetration--the X nozzle--in the cover of the primary tank. This nozzle is approximately 10 in. in diameter and is located directly above the fuel-subassembly catch basin. The transfer arm passes directly beneath the nozzle when traveling between the storage basket and the fuel-transfer port.

There are two advantages of using the X nozzle rather than the normally used fuel-transfer port: (1) The nozzle is directly above the deepest part of the subassembly basin, and therefore there is sufficient depth below the subassembly to position the dipper, which is long enough to accept the full length of the subassembly while it is suspended from the transfer arm. (2) The larger diameter of the X nozzle (10 in. as compared to the usual 3.5 in.) allows insertion and removal of the dipper.

In the proposed removal system, an elongated dipper fastened to a long extension is lowered through the X nozzle into the sodium in the primary tank. View A in Fig. I.E.1 shows the dipper in its lowest position. The subassembly containing the failed fuel has been brought directly over the mouth of the dipper by the transfer arm. The dipper then is raised until

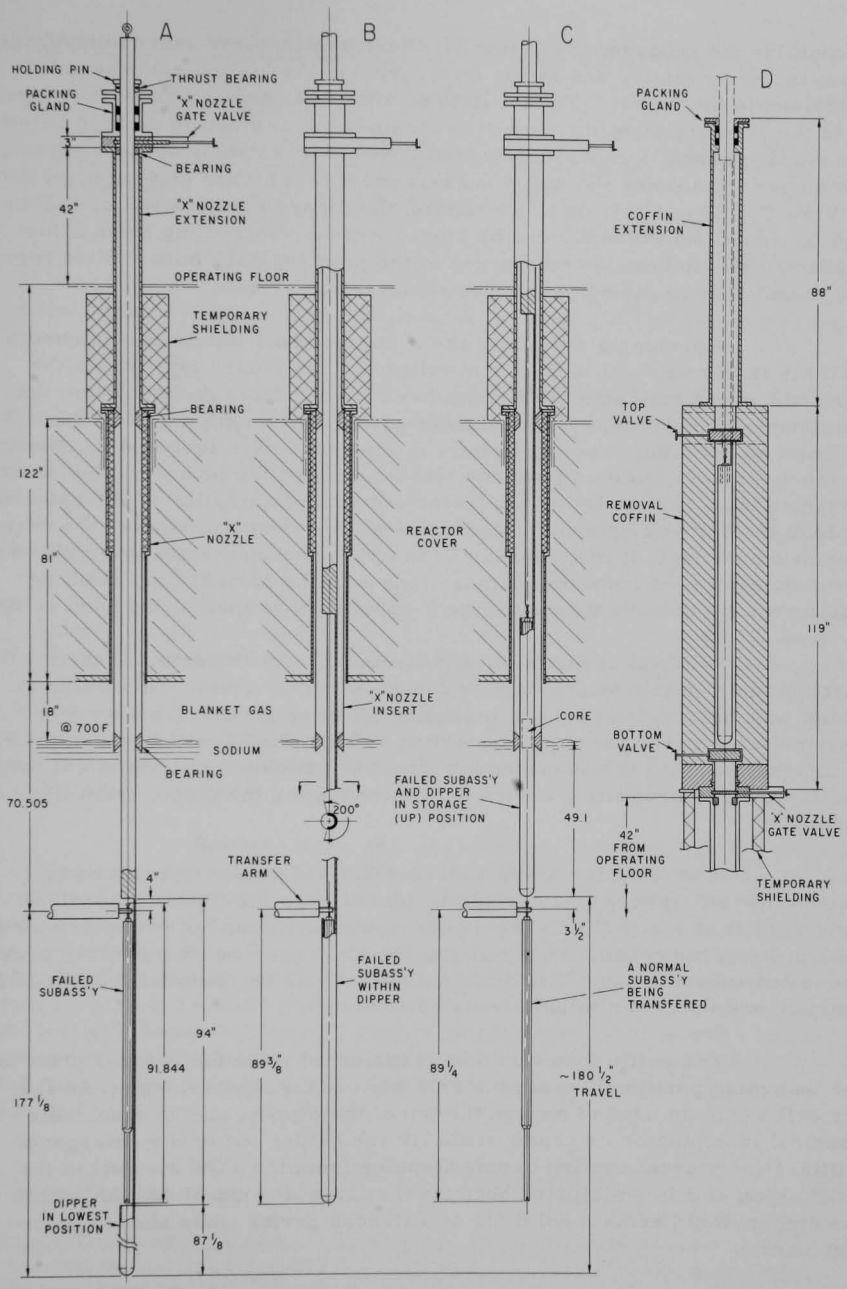

Fig I.E.1. Scheme for Handling EBR-II Subassembly Containing Failed Fuel

it contains the subassembly (View B). Next, the transfer arm is disengaged from the subassembly and swung away, leaving the "failed subassembly" contained in the dipper. To facilitate normal fuel handling while the dipper is in the primary tank, the path of the transfer arm must be cleared between the storage basket and the fuel-transfer port. This can be done by raising the dipper (containing the failed subassembly) to a higher elevation, as shown in View C of Fig. I.E.1. In this position, the dipper remains full of sodium, and the failed subassembly can be stored without obstructing normal fuel handling. Decay heat is transferred to the primary-tank bulk sodium through the bottom half of the dipper, which remains submerged.

A packing gland above the X nozzle seals the dipper extension while it allows vertical motion. In addition, a stationary tube within the X nozzle is extended into the sodium to create a region isolated from the remainder of the primary-tank blanket gas. When the dipper is in the storage (up) position, the atmosphere in this stationary tube and the sodium in the dipper are isolated from the blanket gas and the primary-tank sodium, respectively. This isolation suggests the possible sampling of the gas and sodium to verify or determine the extent of subassembly failure. On evaluation of the damage, it may be decided to either return the subassembly to the reactor, remove it from the primary tank with the normal fuel-handling equipment, or remove it through the X nozzle into a special shielded coffin.

Removal of the failed subassembly from the primary tank through the X nozzle would require a lead-shielded coffin. This coffin would be a bottom-loading, top-unloading type designed to transfer subassemblies between the reactor building and the Fuel Cycle Facility (FCF). A means of cooling the subassembly would be provided, and the top of the coffin would incorporate a device for disconnecting the dipper from its extension.

Whenever the failed subassembly and dipper were to be removed, the emergency coffin would be placed over the dipper extension (see View D of Fig. I.E.1). The dipper would be raised out of the primary tank and into the coffin, and the sodium in the dipper would be frozen around the failed subassembly. Finally, the dipper would be removed from its extension, and the coffin would be sealed.

The coffin then would be transferred from the reactor plant to the unloading position beneath the FCF air cell. A special tool from the air cell would be used to engage the top of the dipper, and an electromechanical manipulator or crane would lift the dipper out of the emergency coffin. No external cooling during transfer from the FCF air cell to the FCF argon cell is anticipated because the large amount of sodium within the dipper would remain solid for an extended period, thus absorbing decay heat.

2. Instrumented Subassemblies (E. Hutter and A. Smaardyk)

a. Test One and Two

(i) Operation and Performance of Test 2 (R. Dickman)

Last Reported: ANL-7661, pp. 36-37 (Jan 1970).

Outputs from 23 sensors in instrumented subassembly XX01 (Test 2) have continued to provide information and records about in-reactor performance of the sensors, the in-reactor environment, and the instrumented subassembly itself.

The report in ANL-7661 was for EBR-II reactor run 39A.* During EBR-II Runs 39B and 39C, between January 14 and January 29, all sensors were functional, and measured values, except for those from the fuel-centerline thermocouples, were in good agreement with the values previously reported. The outputs of the fuel-centerline thermocouples showed a small downward shift. Each sensor remained consistent in its operation during these runs.

During EBR-II reactor run 40A, between February 1 and February 10, the subassembly continued to perform well and to provide much useful information. One outlet-coolant thermocouple initially gave zero output, but recovered completely after about 150 MWd of operation. Throughout Run 40A, one fuel-centerline thermocouple gave zero output, and the other fuel-centerline thermocouples continued to drift slightly and gradually downward. Otherwise, all sensors remained functional and consistent.

Between Runs 40A and 40B, three fuel-centerline thermocouples ceased giving output signals. Run 40B started on February 10 and continued until March 2. Following the startup of Run 40B, one of the three fuel-centerline thermocouples recovered immediately, one was operative but erratic for about three days and then recovered, and the third recovered after 10 days of full-power operation. After 13 days of operation, one spacer-wire (or cladding) thermocouple and one fuel-centerline thermocouple both began to generate erratic output signals. Four days later, the spacer-wire thermocouple once again read steady, expected values, but the fuel-centerline thermocouple remained erratic in its signal throughout Run 40B.

Run 41A started on March 5. The fuel-centerline thermocouple that was erratic at the end of Run 40B continues to be erratic. A

*On p. 35 of ANL-7661, the statement "Fission-gas Pressure at Tops of Four Fuel Capsules" should have read "Total Gas Pressure in Top Plenums of Four Fuel Capsules." Also, on the same page, the statement "~24 psia" should have read "~24 psig (= ~36.2 psia)."

second fuel-centerline thermocouple has been giving erratic signals since the startup of Run 41A. A third fuel-centerline thermocouple began producing an erratic output after one day of the run, and a spacer-wire (or cladding) thermocouple started to give an erratic output after the third day of the run. The output of a fourth fuel-centerline thermocouple became erratic after 10 days of the run, but recovered two days later. On the eleventh day of the run, still another fuel-centerline thermocouple began to show a low, erratic output.

As of March 20, one fuel-centerline thermocouple was inoperative, two were quite erratic in their outputs, and one was slightly erratic; and one spacer-wire (or cladding) thermocouple was showing an oscillating, erratic output. The remaining 18 of the 23 sensors have functioned properly and consistently during Run 41A, through March 20--about 700 MWd of operation.

Table I.E.1 gives representative measurements from the subassembly sensors during Runs 39B through 41A.

TABLE I.E.1. Representative Measurements from Sensors of Instrumented Subassembly XX01[a]

	Run No.			
	39B and 39C (600 MWd)	40A (443 MWd)	40B (924 MWd)	41A (~700 MWd as of 3/20/70)
Fuel-centerline Temperatures (°C)				
In fuel element closest to core center	1350	1325	1300	1300 (?) (erratic)
In two fuel elements next closest to core center	1210 and 1300	Zero output and 1275	1172 and 1272	1180 (?) (erratic) and 1220 (?) (often inoperative and/or erratic)
In fuel element farthest from core center	1140	1115	1100	430 (malfunctioning)
Spacer-wire (or cladding) Temperatures (°C)				
Closest to core center and also at periphery of capsule bundle	418	418	420	422
Center of capsule bundle	442	442	440	440
Coolant-inlet Temperature (°C)	365	368	367	367
Coolent-outlet Temperature (°C)	440	435	435	440
Temperature in Center of Two Structural-materials Test Capsules (°C)	Both 452	Both 452	445 and 452	445 and 452
Coolant Flow through Subassembly (gpm)	~28.3	~27.7	~28.0	~27.5
Total Gas Pressure in Top Plenums of Four Fuel Capsules (psig)	~24 (= ~36 psia)	~24 (= ~36 psia)	~24 (= ~36 psia)	~24 (= ~36 psia)
Fission-gas Pressure in Top Plenums of Four Fuel Capsules (psia)	~0	~0	~0	~0

[a]Measurements are typical and approximate for steady-state operation at 50 MWt.

b. Test Three

Last Reported: ANL-7669, pp. 53-57 (Feb 1970).

(i) Lead-cutting Tests (J. Poloncsik)

The equipment has been assembled for performing tests of cutting the leads for instrumented subassembly XX02 (Test 3). It consists of a sodium-storage container, a cutting container, and a lead-cutting fixture. The cutting fixture is placed in the cutting container, and this container is filled with sodium from the storage container. During the cutting,

the cutting forces are measured by a torque transducer mounted on the motor driving the cutter and are recorded throughout the entire cutting operation.

Cutting tests with typical XX02 leads were performed in 600°F sodium. A maximum torque of 46 ft-lb was required to cut the leads. The cutting action and the torque required to complete the cut are similar to those required for the cuts of the leads of the Test-1 and Test-2 prototypal subassemblies.

The subassembly and extension tube have been assembled and helium leaktested with satisfactory results.

To further verify leak tightness, a second leak test was performed. For this test, the system was charged with argon, and the pressure inside the terminal box was observed. After seven days, the pressure again was observed; there was no perceptible drop in pressure, thus verifying the leak tightness of the system.

c. Test Four

Last Reported: ANL-7669, pp. 56-57 (Feb 1970).

(i) Lead-cutting Tests (J. Poloncsik)

The cutting equipment required to perform tests of cutting of the leads for instrumented subassembly XX03 (Test 4) in air has been assembled. A model of the top end fixture of the subassembly has been fabricated to hold the various sizes of leads to be cut. These leads are considerably heavier than the leads used in previous instrumented subassemblies.

When any lead is being cut, the cutting-tool shaft and the extension tube are subjected to a torsional twist that releases on completion of a lead cut. This twist is about 4° when heavy leads are cut. Sufficient space must therefore be provided between the leads to keep the cutting tool from striking the next heavy lead as the twist releases. This avoids possible impact loads and resultant potential damage of the tool.

Preliminary cutting tests on typical XX03 leads have been performed; the maximum torque observed was 80 ft-lb. Although this torque is greater than the torque required to cut the XX01 and XX02 leads, the leads were cut in a satisfactory manner.

Further cutting tests are under way. These will endeavor to reduce the required torque by rearranging the leads and to determine the capability of the cutting tool to reliably perform repeated cutting operations in sodium.

(ii) Bulkhead Brazing (D. Walker)

Work has been initiated to establish the requirements for brazing the heavy leads into the bulkhead of instrumented subassembly XX03. The large diameter of some of the leads has required that the bulkhead penetrations be placed on a larger-diameter circle than in previous bulkheads so as to accommodate all 20 leads. A layout that appears satisfactory increases the circle diameter from 1.968 to 1.980 in. and reduces the diameter of the braze-powder pocket counterbores wherever possible. The counterbores that were 0.187 in. in diameter on all penetrations in Subassembly XX02 have been reduced to 0.156 in. for the fifteen 0.062-in.-dia penetrations in XX03. The one 0.125-in.-dia penetration will have a 0.187-in.-dia counterbore, and the four 0.187-in.-dia penetrations will have 0.250-in.-dia counterbores. The 30- to 40-mil annulus thus provided is sufficient to permit the use of the stainless steel sleeve procedure developed for Subassembly XX02 and described in ANL-7669, pp. 54-56.

Six single-hole test pieces containing the 0.187-in.-dia hole and the 0.250-in.-dia counterbore have been made for brazing tests on the large-hole penetrations. In addition, three full-size test bulkheads are being machined. Two will be used as test samples for destructive testing, and one will be used as an archive sample.

3. Coolant Chemistry (D. W. Cissel)

a. Sodium Coolant Quality Monitoring and Control (W. H. Olson, C. C. Miles, T. P. Ramachandran, E. R. Ebersole, and G. O. Haroldsen)

Last Reported: ANL-7669, pp. 57-58 (Feb 1970).

(i) Radionuclides in Sodium

(a) ^{137}Cs and ^{131}I. Table I. E. 2 lists the results of analyses for ^{137}Cs and ^{131}I in primary sodium. More samples than usual were analyzed for ^{131}I to support testing of Subassembly C-2250S, which contains an element having an intentional sodium-bond leak.

Preliminary measurements of the residue and distillate of laboratory-distilled primary sodium indicate that ^{131}I codistills with sodium as anticipated. This supports the belief that distillation residues cannot be used in analyses for iodine species.

(b) Tritium. Preliminary results from recent analyses for tritium in primary sodium indicate that tritium and/or tritium compounds segregate during sampling. A sample of primary sodium collected in a 10-ml quartz beaker on 12/11/69 was aliquoted for analysis as follows:

(1) a 1.4-g aliquot of solid sodium was dug from the center of the beaker; (2) a 1.5-g aliquot was dug from near the edge of the beaker; (3) the remaining 8 g was melted and poured from the beaker into the dissolution flask. Table I.E.3 gives the results of the tritium analysis on these aliquots, together with the results from a center aliquot from a primary sample (B) taken 1/20/70.

TABLE I.E.2. ^{137}Cs and ^{131}I in Primary Sodium[a]

Sample Date	Sample Size (g)	Sample Flow (gpm)	Flush Time (min)	Sample Temp (°F)	^{137}Cs ($\mu Ci/g \times 10^2$)	^{131}I ($\mu Ci/g \times 10^4$)
1/20/70	12.5	0.3	18	580	1.3	3.8
1/26/70	13.5	0.4	20	600	1.3	3.7
1/30/70	12.9	0.4	15	600	1.1	3.7
2/4/70	13.4	0.4	18	560	1.3	2.9
2/9/70	13.5	0.3	18	580	1.3	2.8
2/11/70	12.2	0.4	17	580	1.3	2.9
2/12/70	12.8	0.5	15	600	1.3	3.1
2/13/70	11.9	0.5	15	600	1.3	3.8
2/16/70	12.9	0.5	15	580	1.3	5.3
2/18/70	12.7	0.4	18	590	1.3	5.1
2/20/70	12.9	0.4	15	595	1.3	5.4
2/23/70	12.2	0.4	15	560	1.3	6.3
2/25/70	12.1	0.4	15	600	1.3	6.3
3/5/70	12.0	0.3	15	610	1.3	6.8

[a]All samples taken in Pyrex or quartz beaker.

TABLE I.E.3. Tritium Segregation

Sample/Date	Aliquot	Tritium ($pCi/g \times 10^{-3}$)
A/12/11/69	Center (1.4 g)	6.2
A/12/11/69	Edge (1.5 g)	9.2
A/12/11/69	Remainder (8 g)	20.0
B/1/20/70	Center (2.3 g)	6.7

The total tritium in Sample A averages approximately 17×10^3 pCi/g or nearly three times the value measured in the center cut. Further investigation of the extent of segregation of tritium is planned.

Based on this single experiment, the previously reported* values for tritium in primary and secondary sodium are probably

*Progress Report for January 1970, ANL-7661, p. 38; for April 1968, ANL-7445, p. 77; for December 1967,

low by at least a factor of three, since all analyses were made on a center cut from a frozen sample. The relative values with respect to MWd operation are probably reasonably valid, but the absolute magnitude is incorrect. Historical samples will be analyzed to provide correct absolute magnitudes of tritium in both the primary and secondary sodium as a function of MWd of operation as soon as adequate methods of aliquoting are devised. All future analyses for tritium in sodium will be performed only on total samples.

The tritium content of two samples of driver fuel has been determined by dissolving the fissium fuel in nitric acid, passing the off-gases over hot CuO, collecting the tritiated water formed, and analyzing both the dissolver solution and the overhead solution for tritium. The number of tritium atoms remaining in the fuel per fission has been calculated and is given in Table I.E.4. If we assume that the fission yield of tritium in the EBR-II spectrum is approximately the same as the thermal-fission yield from ^{235}U (~8 x 10^{-5} ^{3}H/fission), it appears that ~75-80% of the tritium produced in fission has been lost from this fuel. Additional analyses are planned to confirm these values.

TABLE I.E.4. Tritium in Driver Fuel

Subassembly No./ Row No.	Measured Burnup (at. %)	Tritium (atoms/g U x 10^{-14})	Tritium (atoms/fission x 10^{5})
B-387/6	1.56	7.65	1.92
B-3038/6	1.69	8.1	1.89

(c) Gamma Scan of Original Primary Cold Trap. The sodium cold trap removed from the primary sodium-purification system in June 1968 was qualitatively gamma-ray scanned on March 5, 1970. The activity just outside a plywood box encasing the trap was 200 mR/hr hard gamma. The encased cold trap was analyzed from 8 ft with a Ge(Li) detector through a 1/2-in. collimator in a lead shield and from 30 ft with the lead shield removed. The gamma-ray spectra from the two distances were essentially the same. The only identifiable gamma rays were those of ^{137}Cs, ^{134}Cs, and ^{22}Na.

(ii) Trace Metals in Sodium. Table I.E.5 lists results of routine analyses for trace metals in sodium. The samples were distilled and the impurities determined by atomic-absorption spectrophotometry. The bismuth concentration apparently doubled sometime in the first half of January (2.1 ppm on 12/23/69 to 4.5 on 1/16/70). This coincides with extensive cleaning of the eutectic Sn-Bi alloy seals of the rotating plugs. The primary cold trap has been out of service for investigation of leak alarms on the

Conoseal fittings of the inlet and outlet piping. The bismuth concentration is expected to return to ~2 ppm when the trap is returned to service.

TABLE I.E.5. Trace Metals in Sodium[a] (ppm)

Sample Date	Sample Size (g)	Sample Flow (gpm)	Flush Time (min)	Sample Temp (°F)	Ag	Al	Bi	Ca	Co	Cr	Cu	Fe	In	Mg	Mn	Mo	Ni	Pb	Sn
								Primary Sodium											
1/16/70[b]	55	0.4	15	610	~0.04	<0.6	4.5	<0.01	<0.04	<0.006	0.05	0.1	<0.03	<0.004	<0.005	<0.1	<0.04	11.6	25.0
2/5/70[b]	56	0.6	17	560	~0.04	-	4.4	<0.01	<0.04	<0.007	0.07	0.1	<0.06	<0.007	<0.005	-	<0.04	11.4	22.4
								Secondary Sodium											
1/19/70[b]	54	0.5	15	490	0.02	<0.6	<0.1	<0.006	0.04	2.7	0.06	8.2	<0.03	0.02	0.2	0.15	1.9	0.5	<0.2
2/11/70[c]	~125	0.9	32	560	0.04	<0.3	<0.04	<0.004	<0.01	0.04	0.01	0.1	<0.03	0.02	0.003	<0.03	0.2	0.7	<0.1
2/24/70[c]	~125	0.9	15	540	0.01	<0.3	<0.04	0.05	<0.01	0.08	0.01	0.4	<0.03	0.1	0.03	<0.05	0.04	0.7	<0.03

[a]All samples taken in titanium crucibles.
[b]Laboratory distillation.
[c]In-line distillation.

Variations in Ca, Cr, Fe, Mg, Mn, Mo, and Ni in secondary sodium are believed due to pickup of sediment from the secondary storage tank when the system was drained in late December 1969 (see Progress Report for December 1969, ANL-7655, p. 61, and for January 1970, ANL-7661, p. 40). It is expected that these variations will decrease with continued operation of the secondary cold trap, which is effective as a filter.

(iii) Oxygen in Sodium. Table I.E.6 lists results of routine analyses for oxygen in sodium by the mercury amalgamation method. The samples, of ~15 g, were taken in stainless steel vessels and were extrusion aliquoted for analysis. Flush time was 15 min for all.

TABLE I.E.6. Oxygen in Sodium

Sample Date	Sample Flow (gpm)	Sample Temp (°F)	Number of Aliquots[a]	Average Concentration (ppm)	Oxygen Equivalent of Plugging Run (ppm)
			Primary Sodium		
12/12/69	0.4	600	3	1.3 ± 0.1	<0.5
1/16/70	0.4	600	3	0.7 ± 0.3	<0.5
2/25/70	0.5	590	4	2.6 ± 0.9	<0.5
			Secondary Sodium		
1/15/70	0.9	470	4	1.8 ± 1.1	<0.5
2/4/70	0.8	470	4	2.0 ± 0.8	<0.5

[a]Aliquot size was ~1 g.

The glovebox mercury amalgamation method for the determination of oxygen in sodium was studied further to verify the effect of short-term versus long-term equilibration of the glassware with the glovebox atmosphere. The glassware was vacuum dried at 300°C, transferred into the glovebox, and then removed from the vacuum oven. The data in Table I.E.7 show the effect of short-term and long-term equilibration of the glassware with the glovebox atmosphere. In each case, the sodium sample was added to mercury cooled to near the freezing temperature.

TABLE I.E.7. Effect of Glassware Equilibration on Oxygen Values (ppm) Determined by Mercury Amalgamation

Glassware Equilibration Time	Secondary Sodium (1/15/70)	Primary Sodium (12/12/69)
30 min	4.7	13.2
60 min	5.9	7.7
90 min	3.1	5.0
120 min	2.4	3.1
72 hr	1.0	-
72 hr	1.0	-
72 hr	1.4	-
1 week	-	1.6

The effect of long-term equilibration is obvious. All future samples analyzed for oxygen by mercury amalgamation will be run in glassware equilibrated for several days with the glovebox atmosphere.

The search continues for an analytical method specific for oxygen in sodium. The pitfall encountered in determining oxygen by mercury amalgamation or vacuum distillation is aptly illustrated in Table I.E.8. The sodium remaining in the residue from vacuum distillation of eight samples of secondary sodium was measured by flame-emission spectrophotometry. Some of the samples produced acid-insoluble residues consisting principally of silicates (see Progress Report for December 1969, ANL-7655, p. 61). If it is assumed that all sodium in the residue is present as Na_2O, a very high, and obviously incorrect, value for oxygen is reported. The values of oxygen for samples with no visible acid-insoluble particulate content agree well with recent determinations by mercury amalgamation (1-2 ppm), but are undoubtedly higher than the actual oxygen concentration. Any nonvolatile sodium compound other than Na_2O will cause an error in the reported oxygen value.

TABLE I.E.8. Nonvolatile Sodium in Distillation Residues

Sample Date	Sample Container	Sodium in Residue (ppm)	Oxygen Equivalent If All Na Is Na_2O (ppm)	Oxygen Equivalent of Plugging Run (ppm)	Acid-insoluble Particulate Content (chiefly silica)
10/29/69	Ti	36	24	<0.5	Highest
11/3/69	Ti	21	14	<0.5	Moderate
12/5/69	Ti	3.9	2.6	<0.5	Trace
12/18/69	Ti	2.1	1.4	<0.5	None Visible
2/11/70	Ti	2.5	1.7	<0.5	None Visible
2/12/70	304 SS	2.4	1.6	<0.5	None Visible
2/13/70	Ti	3.0	2.0	<0.5	None Visible
2/24/70	Ti	6.0	4.0	<0.5	Trace

(iv) Carbon in Sodium. Table I.E.9 lists the results of routine analyses for carbon in sodium by the oxyacidic flux method. Flush times all were 15 min.

TABLE I.E.9. Carbon in Sodium

Sample Date	Sample Flow (gpm)	Sample Temp (°F)	Number of Aliquots[a]	Average Concentration (ppm)
		Primary Sodium		
1/16/70	0.4	600	3	0.7 ± 0.3
2/25/70	0.5	590	3	0.5 ± 0.1
		Secondary Sodium		
1/15/70	0.9	470	4	0.5 ± 0.2
2/4/70	0.8	470	4	0.8 ± 0.2

[a]Aliquot size was ~1 g.

A sample of secondary sodium taken on 7/11/69 was extrusion aliquoted in the carbon-analytical glovebox at EBR-II and sent to the Bureau of Standards for carbon analysis by photon activation.* Results have been reported by G. J. Lutz of the Bureau as follows:

Aliquot 1	0.4 ppm carbon
Aliquot 2	0.6 ppm carbon
Aliquots 3-6	<1.0 ppm carbon

A quantitative value was not reported on four of the six aliquots because of difficulties in achieving a suitably clean separation. Four aliquots of the same sample, analyzed by the oxyacidic flux method at EBR-II, yielded the following results:

Aliquot 1	1.5 ppm carbon
Aliquot 2	1.3 ppm carbon
Aliquot 3	0.8 ppm carbon
Aliquot 4	2.0 ppm carbon

Two extrusion vessels identical to those used in routine sampling for carbon analysis at EBR-II were filled with sodium by MSA Corporation. The sodium then was extrusion aliquoted and analyzed for total carbon by the oxyacidic flux method at EBR-II. Table I.E.10 lists information pertaining to loop and sampling conditions, results of total carbon analysis by MSA Corp., and results of total carbon analysis at EBR-II. Both analyses (by MSA and EBR-II) show little or no difference in total carbon content between the "high-carbon" and "high-purity" loops. There is, however, a significant difference in the total carbon values determined by the two methods. No explanation is offered for this discrepancy.

*Lutz, G. J., and DeSoete, D. A., Determination of Carbon in Sodium by Photon Activation Analysis, Anal. Chem. 40, 820-822 (1968).

TABLE I.E.10. Carbon Analysis of Sodium Samples from MSA Corporation

	Loop 1 High-carbon Loop	Loop 3 High-purity Loop
Sampling Time (hr)	21	21
Sodium Flow through Extrusion Vessel (gpm)	0.75	0.75
O_2-meter Reading	1.192	1.135
O_2 Content (ppm)	2.0	1.5
Plugging-indicator Temperature (°F)	835, 485, 330	<225
Cold-trap Temperature (°F)	250	250
Carbon-bed Temperature (°F)	1100	Not Applicable
Sampling Temperature (°F)	1055	1115
Carburization Rate ($\mu g/cm^2$-min) (5-mil Type 304 SS Tabs)	0.036	0.0
Total Carbon Content by Chemical Analyses (by MSA) (ppm)	32	28
Total Carbon by Oxyacidic Flux Method (ppm) (Analyzed at EBR-II)	0.55 ± 0.18 (11 analyses)	0.70 ± 0.4 (9 analyses)

(v) Hydrogen in Sodium. Table I.E.11 lists results of routine analyses for hydrogen in sodium by the isotope-dilution method.

TABLE I.E.11. Hydrogen in Sodium

Primary Sodium		Secondary Sodium	
Sample Date	Duplicate Analyses (ppm)	Sample Date	Duplicate Analyses (ppm)
1/15/70	1.2, <1	1/30/70	<1, <1

(vi) Hydrogen and Nitrogen in Cover Gas. Table I.E.12 summarizes the concentrations of hydrogen and nitrogen in the primary and secondary argon cover-gas systems. Measurements are made with on-stream gas chromatographs.

TABLE I.E.12. Hydrogen and Nitrogen in Primary and Secondary Argon Cover-gas Systems (ppm)

	Primary			Secondary		
	High	Low	Avg	High	Low	Avg
			February			
H_2	100	4	8	4	4	4
N_2	5400	2900	3900	300	200	200
			March			
H_2	108	4	10	4	4	4
N_2	9200	3800	5800	300	150	200

(vii) Plugging Indicator. A plugging-indicator system designed around a micrometallic filter has been assembled and prepared for testing. Figure I.E.2 is a schematic diagram of the system. Sodium flows in through

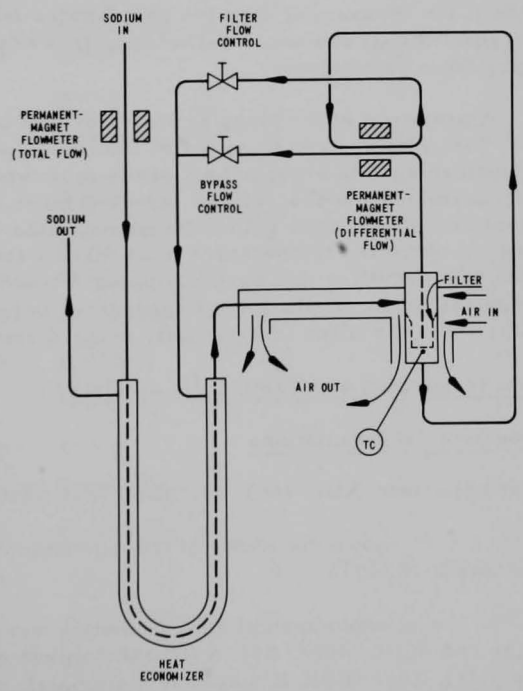

Fig. I.E.2. Plugging Indicator Using Micrometallic Filter

the tube side of a regenerative heat exchanger (heat economizer), is cooled, and enters the filter assembly. Flow then splits, flowing through the filter element or out through a center-tube bypass. Sodium from the filter and the bypass flow in opposite directions through a differential-flow permanent-magnet flowmeter. Each stream then passes through a control valve and leaves the system through the shell side of the regenerative heat exchanger.

The intent of this arrangement is to increase the sensitivity of plugging determinations in very clean sodium with a plugging temperature near the freezing point of sodium. Two features are considered unique. The micrometallic filter should enhance gettering and/or filtering of precipitate and thus produce a more pronounced flow change at the precipitation temperature. The differential flowmeter should produce a compound change in signal (increased bypass flow, decreased filter flow) at the precipitation temperature.

The most serious potential problem with this concept is considered to be the possibility that the filter will plug with precipitate or particulates and not clean up. It is expected, however, that passing hot sodium through the filter bypass will dissolve precipitates from the filter. It is also believed that EBR-II sodium is sufficiently free of particulates to preclude plugging from particulates.

A prototype of the plugging indicator will be tested initially in the secondary sampling system so as not to interrupt operation of the existing plugging indicator. The arrangement of the prototype should facilitate testing in three operational modes: (1) the standard mode, in which the sodium temperature is reduced until a flow change indicates plugging; (2) the oscillating mode, in which the temperature is oscillated about the precipitation temperature with the filter in a partially plugged (seeded) condition; and (3) the continuous mode, in which the temperature is held at the precipitation temperature with the filter in a partially plugged condition.

4. Experimental Irradiation and Testing (R. Neidner)

a. Experimental Irradiations

Last Reported: ANL-7669, pp. 58-60 (Feb 1970).

Table I.E.13 shows the status of the experimental subassemblies in EBR-II as of March 16, 1970.

The following experimental subassemblies were discharged from the reactor at the end of Run 40B: X012A (NUMEC mixed oxide); X021 (PNL structural materials); X063 (EBR-II magnetic materials); and X065B (EBR-II pressurized creep capsules).

Subassembly X042B, a reconstituted subassembly containing PNL poison materials, was loaded into the grid for Run

TABLE I.E.13. Status of EBR-II Experimental Irradiations as of March 16, 1970 (Run 41A in Progress)

Subassembly No. and (Position)	Date Charged	Capsule Content and (Number of Capsules)		Experimenter	Accumulated Exposure (MWd)	Estimated Goal Exposure (MWd)	Burnup[a]
XG03 (7D1)	7/16/65	UO_2-20 wt % PuO_2	(2)	GE	28,148	37,000	7.1
XG04 (7B1)	7/16/65	UO_2-20 wt % PuO_2	(2)	GE	29,344	45,000	7.4
X018B (4E2)	10/2/69	Structural	(3)	GE	3,838	10,000	1.4 + 5.8[b] = 7.2
		Structural	(2)	ANL			1.4 + 5.8[b] = 7.2
		Structural	(1)	ANL			1.4
		Structural	(1)	PNL			1.4
X027 (4B3)	11/21/67	UO_2-25 wt % PuO_2	(18)	GE	16,630	17,600	9.3
		Structural	(1)	PNL			6.5
X034A (2F1)	9/30/69	Structural	(4)	ORNL	3,838	7,500	1.6 + 4.8[b] = 6.4
		Structural	(3)	ORNL			1.6
X035 (7B3)	4/13/68	Structural	(7)	ORNL	16,422	44,800	3.8
X036 (7E1)	7/25/68	UO_2-25 wt % PuO_2	(19)	GE	14,028	43,300	2.2
X038 (7C5)	5/7/68	Structural	(7)	INC	16,004	17,700	3.4
X040A (5B2)	9/30/69	UO_2-20 wt % PuO_2	(18)	ANL	3,838	4,800	1.8 + 3.5[b] = 5.3
		UO_2-25 wt % PuO_2	(16)	GE			1.8 + 3.4[b] = 5.2
X041 (7A3)	7/24/68	Structural	(7)	PNL	14,464	16,700	3.1
X042B (7D5)	3/4/70	Structural	(5)	PNL	500	6,400	0.1 + 2.1[b] = 2.2
		Structural	(2)	PNL			0.1
X043 (4D2)	2/20/69	UO_2-25 wt % PuO_2	(37)	GE	9,744	11,000	5.4
X050 (4C2)	2/23/69	UO_2-20 wt % PuO_2	(4)	GE	9,744	11,900	5.4 + 7.4[b] = 12.8
		UO_2-28 wt % PuO_2	(4)	GE			5.3
		UO_2-20 wt % PuO_2	(5)	ORNL			5.3
		$(U_{0.82}\text{-}Pu_{0.18})C$	(2)	W			5.3
		Structural	(4)	GE			3.7 + 5.3[b] = 9.0
X051 (3A2)	12/16/68	UO_2-25 wt % PuO_2	(37)	PNL	10,289	16,400	2.1
X054 (4E1)	3/31/69	UO_2-25 wt % PuO_2	(37)	PNL	9,144	10,000	4.8
X055 (6A4)	2/23/69	$(U_{0.85}\text{-}Pu_{0.15})C$	(19)	UNC	10,514	20,000	3.3
X056 (5C2)	4/2/69	UO_2-25 wt % PuO_2	(37)	GE	9,144	10,600	4.5
X057 (2B1)	2/23/69	Structural	(7)	PNL	10,514	15,000	4.4
X058 (6F1)	4/24/69	UO_2-25 wt % PuO_2	(37)	GE	8,568	16,000	3.2
X059 (4A1)	4/23/69	UO_2-25 wt % PuO_2	(37)	PNL	8,568	17,500	2.9
X061 (7A5)	4/23/69	Structural	(7)	INC	9,338	18,000	2.0
X062 (6F3)	5/23/69	UO_2-25 wt % PuO_2	(37)	GE	6,665	13,400	3.0
X064 (4F2)	5/28/69	UO_2-25 wt % PuO_2	(19)	GE	7,436	10,700	4.2
X068 (4A3)	1/30/70	Mark IA	(61)	ANL	1,867	6,500	0.6

TABLE I.E.13 (Contd.)

Subassembly No. and (Position)	Date Charged	Capsule Content and (Number of Capsules)		Experimenter	Accumulated Exposure (MWd)	Estimated Goal Exposure (MWd)	Burnup[a]
X069 (4F1)	10/1/69	UO_2-25 wt % PuO_2	(37)	PNL	3,838	20,700	1.3
X070 (3E1)	1/10/70	UO_2-20 wt % PuO_2	(8)	NUMEC	2,467	6,000	1.4 + 6.5[b] = 7.9
		UO_2-20 wt % PuO_2	(7)	GE			1.4 + 5.1[b] = 6.5
		$(U_{0.8}$-$Pu_{0.2})C$	(1)	LASL			1.4 + 1.4[b] = 2.8
		$(U_{0.8}$-$Pu_{0.2})C$	(1)	LASL			1.4
		$(U_{0.8}$-$Pu_{0.2})C$	(1)	W			1.4
		$(U_{0.8}$-$Pu_{0.2})N$	(1)	BMI			1.4
X071 (4C3)	1/30/70	Mark II	(28)	ANL	1,867	5,200	1.0 + 4.3[b] = 5.3
		Mark II	(9)	ANL			0.7
X072 (6B2)	12/12/69	UO_2-20 wt % PuO_2	(18)	ANL	3,238	9,200	1.3
		Structural	(1)	ANL			0.8
X073 (6C3)	12/12/69	UO_2-25 wt % PuO_2	(37)	PNL	3,238	29,600	0.8
X074 (5A2)	1/10/70	UO_2-25 wt % PuO_2	(37)	PNL	2,467	14,500	1.2
X075 (5E4)	1/30/70	$(U_{0.8}$-$Pu_{0.2})C$	(18)	UNC	1,867	5,100	0.9 + 6.2[b] = 7.1
XX01 (5F3)	11/19/69	UO_2	(16)	ANL	3,238	12,200	0.8
		Structural	(2)	ANL			1.1

[a]Estimated accumulated center burnup on peak rod, based on unperturbed flux and without depletion corrections (fuels, at. %; nonfuels, nvt x 10^{-22}).
[b]Previous exposure from another subassembly.

5. Materials-Coolant Compatibility (D. W. Cissel)

a. Evaluation and Surveillance of EBR-II Materials

Last Reported: ANL-7669, pp. 60-62 (Feb 1970).

(i) Substitution of Other Stainless Steels for Type 304 Stainless Steel in EBR-II (S. Greenberg and W. E. Ruther)

The materials under test were removed after 35 days of exposure to sodium cold trapped at 257°F. Table I.E.14 summarizes the weight-change data.

All samples except those of Type 303 stainless steel behaved in a comparable manner. An additional period of exposure will show if corrosion of Type 303 stainless steel may be expected to continue at a relatively high rate or if the rate becomes reduced to a value comparable with that for other stainless steels. It should be noted that Type 303 stainless steel components may be functioning satisfactorily in EBR-II at temperatures as high as ~800°F.

The samples not removed for metallographic examination were returned to the test, together with samples of additional alloys, for continued exposure under the same conditions.

TABLE I.E.14. Weight Change of Stainless Steel Samples Exposed in Sodium

Type of Stainless Steel	Sample No.	Temp (°F)	Sodium Velocity (m/sec)	Weight Change (mg/cm^2)
304	2	700	2.0	-0.0068
304	4[a]	700	1.0	0.00
304	1	1050	2.0	-0.068
304	3[a]	1050	1.0	-0.062
301	2	700	2.0	0.00
301	4	700	2.0	+0.014
301	6[b]	700	1.0	+0.014
301	1	1050	2.0	-0.069
301	3	1050	2.0	-0.082
301	5[b]	1050	1.0	-0.041
303	2	700	2.0	-0.064
303	4	700	2.0	-0.064
303	6[b]	700	1.0	-0.073
303	1	1050	2.0	-0.46
303	3	1050	2.0	-0.45
303	5[b]	1050	1.0	-0.48
304LN	2	700	2.0	+0.022
304LN	4	700	1.0	+0.022
304LN	1	1050	2.0	-0.076
304LN	3	1050	1.0	-0.065
201	2	700	2.0	+0.037
201	4	700	2.0	+0.037
201	6[b]	700	1.0	+0.074
201	1	1050	2.0	-0.15
201	3	1050	1.0	-0.074
201	5[b]	1050	1.0	-0.037

[a]Sample was cut in half. One half was removed for metallographic examination, and the other returned to the subassembly for additional exposure.
[b]Removed from test for metallographic examination.

(ii) Subassembly XA08 (S. Greenberg)

There is a typographical error on page 40 of the Progress Report for January 1970 (ANL-7661). The last sentence should read: "The average midplane fluence was 8.5×10^{22} nvt total."

b. Examination of Materials from EBR-II Surveillance Subassemblies (R. V. Strain and S. Greenberg)

Last Reported: ANL-7669, pp. 62-64 (Feb 1970).

(i) Density Changes from SURV-2. Additional density determinations were made of SURV-2 samples of Type 304 stainless steel, tool steel, and tantalum (all reported in ANL-7669 as showing density decrease), as well as of Stellite 6B and Inconel X-750 (both reported in ANL-7669 as showing density increase). These additional measurements indicate that:

a. The density of the Type 304 stainless steel, within the accuracy of the measurements, did not decrease. The initial measurements probably were in error.

b. The decrease in density of the tool-steel samples ranged from 0.014 to 0.018 g/cm^3. Since there was no consistent relationship between density decrease and sample position, the decrease probably is the result of thermal conditions rather than neutron fluence.

c. The decrease in density of the tantalum ranged from 0.054 to 0.077 g/cm^3 and varied directly with fluence. The maximum decrease in density was equivalent to a swelling of ~0.4%.

d. The increases in densities of the Stellite 6B and Inconel X-750 were confirmed as ~0.013 g/cm^3 and 0.017 g/cm^3, respectively.

There was no discernible difference between the densities of samples which had been exposed to flowing sodium and the densities of samples which had been sealed under helium during irradiation. This indicates that irradiation was responsible for the changes in density.

(ii) Graphite-containing Cans from SURV-2. In discussing the tensile data for the Type 304 stainless steel graphite-containing cans from SURV-2 (see Progress Report for December 1960, ANL-7655, pp. 64-65), the statement was made that "very small changes in tensile properties resulted from the SURV-2 exposure." Actually, as shown in Table I.D.15, the changes were appreciable.

TABLE I.E.15. Tensile Properties of Graphite-can Material from SURV-2

Property	Type 304 Stainless Steel from SURV-2a		Typical[b] Value for Annealed Type 304 Stainless Steel
	Average	Range	
Yield Strength (psi)	42,500	40,900-44,100	30,000
Ultimate Strength (psi)	90,200	87,900-92,400	80,000
Elongation (%)	41	37-44	50
Reduction in Area (%)	50	45-56	60

[a]Values obtained at strain rate of 0.012 min^{-1}.
[b]Tipton, C. R., Jr. (Ed.), Reactor Handbook, 2nd Ed., Vol. 1, p. 568, Interscience Publishers, New York (1960).

It is apparent that appreciable hardening, presumably due to radiation, took place. However, as indicated by the data for elongation and for reduction in area, the material is still very ductile after exposure in SURV-2.

Sections of the cans, taken through the welds, were bent 180° over a 1/2-in.-dia mandrel. The weld joint was parallel to the axis of the mandrel. There was no cracking or other unusual effect.

6. Systems Engineering (B. C. Cerutti)

a. Surveillance, Evaluation, and Studies of Systems

Last Reported: ANL-7655, pp. 65-66 (Dec 1969).

The rate of dross formation in the freeze seals of the rotating plugs has been shown experimentally to be strongly dependent on temperature. Thus, to reduce the rate of dross formation, the operating temperature of the alloy in the full-molten condition was lowered from 380 to 350°F. Operation at 350°F proved satisfactory, so the temperature for the full-molten condition is now being lowered to 325°F.

7. Reactor Analysis, Testing and Methods Development

Last Reported: ANL-7669, pp. 66-86 (Feb 1970).

a. Reactor-physics Calculations for an EBR-II Core with Depleted-uranium and Nickel Reflectors (B. R. Sehgal, R. Rempert, and P. Fullerton)

The methods and results of calculations based on the proposed EBR-II core configuration for extended 62.5-MWt operation and which is reflected with either depleted uranium or nickel are described.

(i) Material Cross Sections. The group cross sections used in the calculations are derived from the ENDF/B revised category-1 data. The code MC²* is used to generate 26 broad-group cross sections (each of half-lethargy width) for the materials in the various compositions in the reactor. The cross sections for the materials in the EBR-II core regions are those derived for the ZPR-3 Assembly 6F at critical buckling, which has approximately the same composition as the EBR-II core. The group cross sections for the depleted-uranium-blanket and the nickel-reflector compositions are derived from the MC² code at $B^2 = 0.0\ cm^{-2}$. The stainless steel-reflected configuration, which is similar to that in EBR-II Runs 25-28, was analyzed similarly as a means of normalization.

(ii) Method of Calculation. The DOT** code, a two-dimensional neutron-transport code, is used to calculate the various physics parameters for a reactor configuration. This code allows both two-dimensional RZ and two-dimensional XY calculations. In the RZ calculations, the composition

---

*Toppel, B. J., Rago, A. L., and O'Shea, D. M., MC², A Code to Calculate Multigroup Cross Sections, ANL-7318 (1967).

**Mynatt, F. R., DOT, A Two-dimensional Discrete-ordinate Code, Report K-1694, Radiation Shielding Information Center, Oak Ridge National Laboratory. Also see Progress Report for October 1968, ANL-7513, p. 50.

of the subassemblies in each reactor row are volume homogenized into a row composition, and the axial variation of compositions (e.g., the axial reflectors) is explicitly represented in each row. In the XY calculation, each subassembly composition is explicitly specified in the central plane of the reactor, the leakage in the Z direction is approximated by a pseudo-absorption equal to DB^2. A constant value of $B^2 = 0.0023\ cm^{-2}$ is chosen for the whole reactor, and the diffusion coefficient D is varied to account for the many types of subassemblies present in the reactor. In these calculations, nine subassembly types (e.g., driver, control, blanket, nickel, and experimental) have been designated for D specifications, and each subassembly in the reactor has been selected (somewhat judiciously) out of these nine types.

It is clear from the above discussion that the two-dimensional RZ calculation represents the reactor in three dimensions, but provides a "homogenized" variation of the neutron-physics parameters over each row. The two-dimensional XY problem gives a detailed picture over each individual subassembly in the central plane of the reactor, but none along the axial direction. Since the Z dependence in the two-dimensional XY representation is approximated rather crudely, the values of the calculated physics parameters (e.g., k_{eff}) are not as reliable as in the two-dimensional RZ problem, and therefore, the results of the two-dimensional XY problem should be used only for the distribution of fluxes or fission rates over individual subassemblies.

The two-dimensional calculations are done in the S_2 approximation with 4 mesh points per subassembly in the XY calculations and 2 mesh points per row in the R direction. A total of 46 points in the Z direction was used in the RZ problems. That this much spatial and angular detail in the calculations may not be adequate and that the S_n ray effect may be present is quite evident; however, these calculations, with the rather detailed energy representation (26 groups), require long computation time. It may be necessary soon to repeat some calculations with more angular and spatial detail so as to gain an understanding of the uncertainties in the results reported here. Meanwhile, two one-dimensional calculations have been done with the SNARG 1D code with the S_2 and S_4 approximation in a cylindrical representation of the depleted-uranium-reflected reactor, with 4 mesh points per row, and a constant axial buckling of $\simeq 0.0023\ cm^{-2}$.

(iii) Reactor Configurations Calculated. The basic core configuration used is the proposed EBR-II core for extended operation at 62.5 MWt (see Fig. I.E.3). In the two-dimensional RZ calculations, a total of 15 rows is represented and the reflectors (blanket) are as follows: (1) depleted-uranium blanket in Rows 7 through 15, and (2) nickel reflector in Rows 7, 8, 9, and 10, and depleted-uranium blanket in Rows 11 through 15.

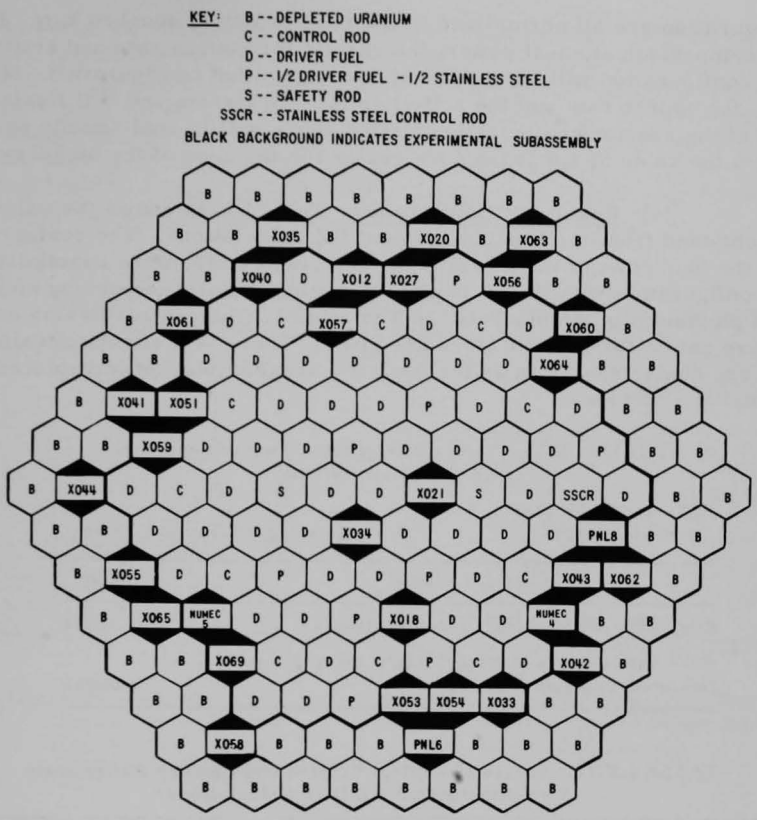

Fig. I.E.3. Configuration of Proposed EBR-II Core for Extended Operation at 62.5 MWt

In the XY calculations, only 11 rows on each side of the core center have been represented. The two RZ calculations have a 180° (twofold) symmetry.

(iv) Normalization for Intercomparison of Results. The RZ DOT calculations (and S_n calculations in general) have a source normalization such that

$$1 = \frac{1}{k_{eff}} \int \nu\Sigma(r,z,E)\phi(r,z,E)\, dE\, 2\pi r\, drdz,$$

which implies that the k_{eff} calculated by the code in the final iteration equals the source rate over the whole reactor and that the edits for source density, fission rate, flux, and activity in the code for a particular

configuration are all normalized to the reactor power equal to k_{eff}. For intercomparison at equal power, the results for source rate and activity for each configuration will be divided by the k_{eff} in that configuration. Moreover, the source rate and the activities for ^{235}U fission and ^{238}U fission for each of the reactor configurations listed above will be individually normalized to the value of 1.0 at the core center for the case of the nickel reflector.

(v) Results of Calculations. Table I.E.16 shows the values of k_{eff} obtained from the two-dimensional RZ calculations. The configuration with the four rows of nickel reflector contributes ~4% more reactivity than the configuration with the all depleted-uranium blanket (assuming no build-up of plutonium in the blanket). In Table I.E.17, the central fission and capture ratios for the two cases are given. There is a slight softening of the core center spectrum as the depleted-uranium blanket is replaced by the nickel reflector.

TABLE I.E.16. Values of k_{eff} from Two-dimensional RZ DOT Calculations

Fissionable material in 6 rows of core: ^{235}U = 193.86 kg; ^{239}Pu = 6.29 kg

Configuration	k_{eff}
Core with All Depleted-uranium Blanket	1.02008
Core with 4 Rows of Nickel Reflector and Rest Depleted-uranium Blanket	1.06045

TABLE I.E.17. Values of Central Fission and Capture Ratios from Two-dimensional RZ DOT Calculations

Configuration	$^{238}U_{fis}$	$^{238}U_{cap}$	$^{239}Pu_{fis}$	$^{240}Pu_{fis}$
Core with All Depleted-uranium Blanket	0.0625	0.1128	1.1734	0.4641
Core with 4 Rows of Nickel Reflector and Rest Depleted-uranium Blanket	0.0612	0.1131	1.1713	0.4532

A series of graphs (Figs. I.E.4-I.E.8) has been prepared to show the spatial variations of source density rate, the ^{235}U fission rate, and the ^{238}U fission rate.* In calculating the activities, ^{235}U and ^{238}U cross sections collapsed over the spectra of the pertinent regions are used. That this makes quite a difference is evident from the axial distribution of ^{235}U

*For normalization to the power level of 62.5 MWt over the whole reactor, the values shown on the graphs should be multiplied by the following numbers: for source density rates--9.23 x 10^{13}; for ^{235}U fission activity/g--1.2827 x 10^{13}; for ^{238}U fission activity/g--7.7518 x 10^{11}.

fission along the core edge, where it is not clear which averaging spectrum is more appropriate. In the radial-distribution plots, the activities of the ^{235}U and ^{238}U pertinent to core, reflector, and blanket regions have been averaged near the interfaces. The results of SNARG-1D calculations, demonstrating the effect of going from the S_2 to the S_4 approximations, show that the difference in k_{eff} obtained with the two approximations is $\simeq -0.61\%$ and that the ^{238}U fissions in the blanket region may be underpredicted up to 50% by the S_2 calculation.

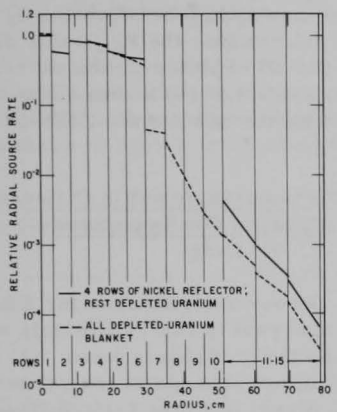

Fig. I.E.4. Relative Radial Source Densities for Depleted-uranium and Nickel-reflector Configurations in RZ Geometry

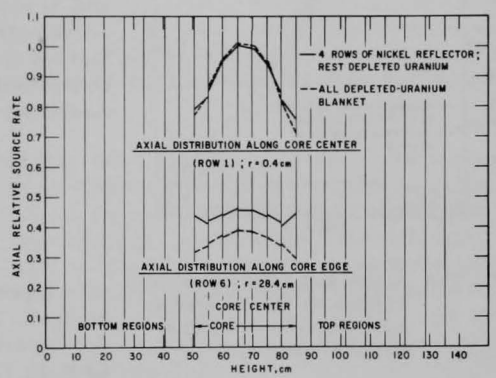

Fig. I.E.5. Relative Axial Source Densities (in Row 1 and Row 6) for Depleted-uranium and Nickel-reflector Configurations

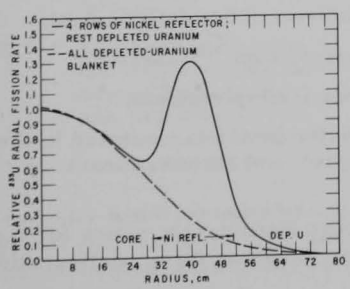

Fig. I.E.6. Relative Radial ^{235}U Fission Distributions for Depleted-uranium and Nickel-reflector Configurations in RZ Geometry

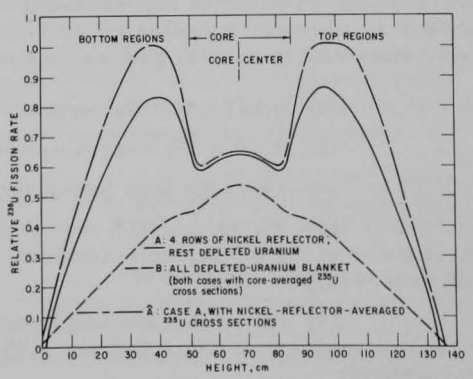

Fig. I.E.7. Relative Axial ^{235}U Fission Distributions along r = 28.4 cm for Depleted-uranium and Nickel-reflector Configurations

Previous calculations for ZPR-3 Assembly 5, using the ENDF/B cross sections and the DOT code in the S_4 approximation (reported in the Progress Report for December 1969, ANL-7655, p. 73), indicate ~1.27% overprediction in k_{eff}, reasonably good agreement with the measured central fission ratios for ^{238}U and ^{239}Pu, very good agreement with the measured ^{235}U axial fission distribution, and ~10 to ~30% underprediction of ^{238}U fission rate in the ^{238}U light blanket region. Noting the ~0.6% difference in k_{eff} between the S_2 and S_4 approximations, the k_{eff} value of 1.0201 for the all depleted-uranium blanket (cf. Table I.E.16) seems to be consistent with the results for ZPR-3 Assembly 5.

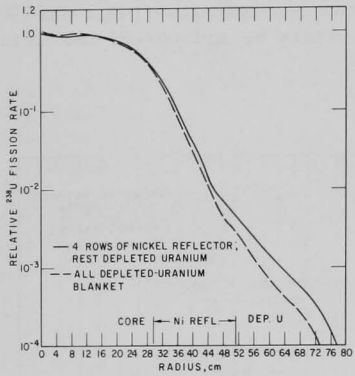

Fig. I.E.8. Relative Radial ^{238}U Fission Distributions for Depleted-uranium and Nickel-reflector Configurations in RZ Geometry

b. Fission Rates with Different Blanket Configurations (J. K. Long)

Power distributions for EBR-II with three different blanket materials were studied. The three blankets were: (1) all depleted-uranium pins, as in the present EBR-II; (2) nickel in Rows 7-10, followed by depleted uranium; and (3) stainless steel in Rows 7 and 8, followed by depleted uranium. The study was based on a set of two-dimensional transport-theory calculations furnished by Sehgal (see Sect. I.E.7.a), and was confined to an interpretation of his RZ calculations. The radial fission-rate distributions were calculated in six annular core regions whose fissile inventories corresponded to those of the first six rows of EBR-II in a projected loading for 62.5-MWt operation. These distributions were converted to reactor power under the following assumptions:

(1) 3.121×10^{16} fissions = 1 MW-sec (200 MeV/fission);

(2) 4.6% of the core power derives from ^{238}U fissions;

(3) 5% of the core power derives from plutonium;

(4) 89, 99, and 97% of total reactor power is produced in the first six rows for the depleted-uranium, nickel, and stainless steel blankets, respectively;

(5) the axial maximum to average fission-rate ratios for the first five rows are 1.106, 1.100, and 1.09 for the same three configurations, respectively;

(6) the axial maximum to average fission-rate ratios for the sixth row are 1.080, 1.024, and 1.046 for the same three configurations, respectively.*

As Sehgal's three examples all had the same mass of fissile material, they differed considerably in their calculated eigenvalues. It was assumed that these could all be corrected to the same eigenvalue by the relationship

$$\Delta k/k = 0.5\ \Delta\rho/\rho,$$

where ρ is the density of fissile atoms in the core. With this correction, Sehgal's calculations were made to correspond approximately to actual EBR-II loadings, which would be adjusted by some kind of distributed change in mass to have a k of about 1.01.

The relative fission rates were processed by the above factors to yield absolute fission rates in the central plane of the reactor at 62.5 MWt. These rates are shown, together with the experimental values from Runs 29C and 29D, in Fig. I.E.9. The increased fission rates in the cores that are reflected by low-density materials are evident, and the peak fission rate in the nickel reflector is conspicuous.

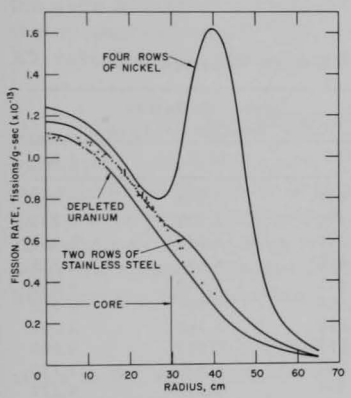

Fig. I.E.9. RZ-calculated ^{235}U Fission Rate at 62.5 MW, Using Three Different Blanket Configurations; Data Points Are Foil-irradiation Values from EBR-II Runs 29C and 29D

It is also apparent from Fig. I.E.9 that the experimentally determined fission rates display a broader shape through the core than is calculated by the RZ depleted-uranium-blanket example. Therefore, although the shapes in Fig. I.E.9 are useful for comparison of parametric variations, they cannot be used for predicting actual fission rates in the EBR-II reactor loaded with the corresponding reflectors.

c. A Study of Power and Temperature Distributions in Variously Reflected Cores (R. A. Cushman)

The power distribution, and subsequently some temperature distributions, were determined for several typical and self-consistent EBR-II cores operating at 62.5 MWt. The results and the method used in arriving at these results are presented here.

*The six ratios cited in items 5 and 6 were derived from numerical integration of the axial fission-rate profiles.

(i) Cores and Reflectors Considered. The basic input data for the study was provided by Sehgal (see Sect. I.E.7.a.), who gives results of a series of RZ calculations on a core (a diagram of which is shown in Fig. I.E.3) which has been shown to be typical of a core for extended EBR-II operation at 62.5 MWt with a depleted-uranium blanket.* The same core then was utilized with (a) a reflector consisting of nickel-reflector subassemblies in Rows 7-10, and (b) a reflector consisting of stainless steel subassemblies in Rows 7 and 8. Subsequently, an additional calculation was made by Sehgal, using the same core but with stainless steel reflector subassemblies in Rows 7 and 8 and nickel-reflector subassemblies in Rows 9 and 10.

The same core layout was used for the four different blanket-reflector cases; consequently, the value of k for the three reflected cases was greater than the assumed just-critical value for the depleted-uranium blanket. To compensate for the greater reactivity provided by the various reflectors, the requirement of fuel uniformity was removed from each of the reflected cores. The values in Table I.E.18 were obtained by using the relationship that 1% excess reactivity could be compensated for by removing 2% of the fuel.

TABLE I.E.18. Effective Subassemblies for Variously Reflected Cores

		Type of Reflector (No. = number of rows)		
Core Position	Depleted-U Blanket	2 SS	2 SS, 2 Ni	4 Ni
1N1	1.000	0.971	0.943	0.925
2N1	3.516	3.414	3.317	3.255
3N1	4.280	4.155	4.037	3.962
3N2	6.000	5.825	5.660	5.555
4N1	6.000	5.825	5.660	5.555
4N2 and 4N3	9.960	9.669	9.395	9.222
5N1	3.350	3.252	3.160	3.101
5N2 and 5N4	10.460	10.155	9.867	9.685
5N3	4.050	3.932	3.820	3.750
6N1	5.700	5.533	5.377	5.277
6N2 and 6N5	10.640	10.330	10.040	9.851
6N3 and 6N4	9.180	8.912	8.659	8.500
Total	74.136	71.973	69.935	68.638
Relative Value	1.000	0.971	0.943	0.925
% Supercritical	0	1.5	3	4

(ii) Input Data for the Normalization. Sehgal performed RZ calculations for the four cores and produced a radial fission-source distribution at the axial midplane of the core. Table I.E.19 gives his values for the radial fission-source distribution.

*Cushman, R. A., et al., Proposal for Operating EBR-II at 62.5 MWt, ANL/EBR-012 (to be published).

TABLE I.E.19. Radial Fission-source Distribution for Variously Reflected Cores

Row	Radius (cm)	Depleted-U Blanket	Type of Reflector		
			2 SS	2 SS, 2 Ni	4 Ni
1	0.779	1.0122	1.0193	1.011	1.000
1	2.337	1.0044	1.012	1.004	0.9931
2	4.398	0.574	0.579	0.5745	0.5686
2	6.961	0.562	0.567	0.563	0.5484
3	9.577	0.812	0.822	0.816	0.8086
3	12.247	0.782	0.793	0.788	0.7815
4	14.924	0.765	0.779	0.774	0.7686
4	17.610	0.709	0.726	0.722	0.7192
5	20.298	0.544	0.561	0.560	0.5587
5	22.989	0.493	0.513	0.515	0.5158
6	25.682	0.437	0.461	0.467	0.4718
6	28.375	0.386	0.420	0.416	0.4559

The core with a depleted-uranium blanket had been used* as the basis for DOT XY calculation. From this calculation, with its discrete, subassembly-by-subassembly power distribution, a curve of average relative radial fission rate versus radius was obtained.** This curve (for the core blanketed with depleted uranium) was used as the additional input for the normalization process, so that similar curves (representing assumed XY calculations) could be produced for the three reflected cores.

(iii) Normalization Procedure. The averaged radial distribution obtained from XY calculations is believed to give an indication of the azimuthal variation in power generation that occurs in various core positions in the outer rows of the core. The results of averaged XY calculations agree with experimentally determined fission rates. A limitation of RZ calculations is that they treat 6N1 positions in the same manner as 6N3, whereas an approximate 20% difference in radial fission rate is possible between the two positions.

Therefore, the effort was made to convert the RZ calculations to the averaged XY case. The normalization was done as follows:

(1) The two data points for each row for each of the cores shown in Table I.E.19 were averaged, producing the values in Table I.E.20A.

(2) The values in each column of Table I.E.20A then were normalized, by columns, to 1.000 at Row 1, producing the values in Table I.E.20B.

(3) The values in each row of Table I.E.20B were then ratioed to the value for that row of a core blanketed with depleted uranium, producing the values in Table I.E.20C.

*Cushman, R. A., et al., Proposal for Operating EBR-II at 62.5 MWt, ANL/EBR-012 (to be published).
**Fig. 3 in ANL/EBR-012.

TABLE I.E.20. Values for Radial Fission Rates Obtained with First Three Steps of Normalization Procedure

Row	Depleted-U Blanket	Type of Reflector		
		2 SS	2 SS, 2 Ni	4 Ni
		A (Step 1)		
1	1.0083	1.0156	1.0075	0.9966
2	0.568	0.573	0.569	0.5585
3	0.797	0.808	0.802	0.7950
4	0.737	0.752	0.748	0.7439
5	0.518	0.537	0.538	0.5372
6	0.412	0.440	0.442	0.4638
		B (Step 2)		
1	1.000	1.000	1.000	1.000
2	0.563	0.564	0.565	0.560
3	0.790	0.796	0.796	0.798
4	0.731	0.740	0.742	0.746
5	0.514	0.529	0.534	0.539
6	0.409	0.433	0.439	0.465
		C (Step 3)		
1	1.000	1.000	1.000	1.000
2	1.000	1.002	1.004	0.995
3	1.000	1.008	1.008	1.010
4	1.000	1.012	1.015	1.021
5	1.000	1.029	1.039	1.049
6	1.000	1.059	1.073	1.137

(4) Values of averaged fission-rate distribution that were obtained by XY calculations for the depleted-uranium-reflected core then were multiplied by the factors in Table I.E.20C to produce the points for corresponding curves of fission rate versus radius that might be expected from averaged XY calculations for the reflected cores. The radii at which the values were applied were the arithmetic averages for the respective row radii given in Table I.E.19. Table I.E.21 shows the radii and resulting relative fission rates.

TABLE I.D.21. Normalized XY Radial Fission-rate Distribution (Obtained from Step 4 of Normalization Procedure)

Row	Radius (cm)	Depleted-U Blanket	Type of Reflector		
			2 SS	2 SS, 2 Ni	4 Ni
1	0	1.000	1.000	1.000	1.000
2	5.680	0.980	0.982	0.984	0.975
3	10.912	0.939	0.947	0.947	0.948
4	16.267	0.863	0.873	0.876	0.881
5	21.643	0.746	0.768	0.775	0.783
6	27.028	0.599	0.634	0.643	0.681

If the data from Table I.E.21 were plotted, a relative radial fission-rate distribution for the axial midplane of the reactor would be obtained. One additional correction of the data was made, however, to arrive at a better radial power distribution. Sehgal showed different axial distributions for the variously reflected cores; in particular, he showed a difference in the axial distribution between the core-reflector interface and the remainder of the core. Therefore, the value of the relative fission rate at the 30-cm radius for the three reflected cores was multiplied by a factor which represented the greater power produced by a subassembly with a lower peak to average axial distribution but with the same peak (i.e., axial midplane) value. This factor was 1.036 for the nickel-reflected core, 1.027 for the core reflected with two rows of stainless steel and two of nickel, and 1.017 for the core reflected with two rows of stainless steel. A straight line was then drawn through the 30-cm point (on each of the curves for the reflected core) and the point of tangency to the curve drawn from the values of Table I.E.21. In Fig. I.E.10 are plotted the four curves of a relative fission rate versus radius resulting from the foregoing normalization process.

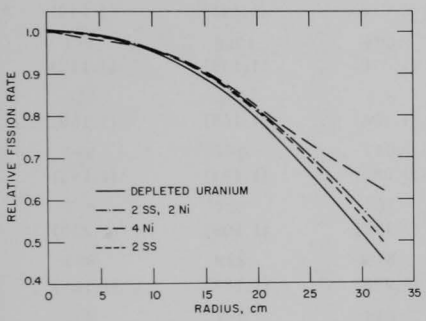

Fig. I.E.10. Normalized Relative Radial Fission-rate Distributions for Variously Reflected Cores

(iv) Power and Temperature Distributions. The data from Fig. I.E.10 and the number of effective subassemblies from Table I.E.18 then were used as input to the POWDIST program to determine the power produced in an effective (i.e., standard driver-fuel) subassembly located in the various core positions of a reactor operating at 62.5 MWt. The variation in reflector, however, introduced an additional variable. For a depleted-uranium-blanketed core, 89% of the total reactor power is produced in the core (Rows 1-6). For a two-row stainless steel reflector, this increased to 95%, and for both cores with four reflector rows the power produced in the core increased to 99%.

The results of the POWDIST calculations are shown in Table I.E.22, which presents the power produced per effective subassembly in the various core positions. Also in Table I.E.22 are the ratios of the power produced for a given subassembly in a reflected core to the value in the depleted-uranium-blanketed core. A subassembly in position 6N1 produces 41% more power in a core reflected with four rows of nickel than in a core blanketed with depleted uranium when both reactors produce 62.5 MWt.

One additional set of calculations was made. The temperature distributions in driver subassemblies in the hottest region of the

various rows of the four types of cores were calculated with HECTIC, using the POWDIST output and the nominal coolant flow rates for the several rows. Table I.E.23 shows the flow rates used.

TABLE I.E.22. Kilowatts Produced per Effective Subassembly for Variously Reflected Cores[a]

Position	Depleted-U Blanket	Type of Reflector		
		2 SS	2 SS, 2 Ni	4 Ni
1A1	984	1053 (1.070)	1119 (1.137)	1106 (1.124)
2N1	966	1035 (1.071)	1101 (1.140)	1085 (1.123)
3N1	916	987 (1.078)	1050 (1.146)	1046 (1.142)
3N2	933	1004 (1.076)	1068 (1.145)	1061 (1.137)
4N1	824	895 (1.086)	956 (1.160)	956 (1.160)
4N2	862	933 (1.082)	994 (1.153)	994 (1.153)
5N1	686	763 (1.112)	820 (1.195)	837 (1.220)
5N2	746	819 (1.098)	878 (1.177)	884 (1.185)
5N3	766	838 (1.094)	897 (1.171)	901 (1.176)
6N1	520	599 (1.152)	658 (1.265)	731 (1.406)
6N2	591	671 (1.135)	728 (1.232)	774 (1.310)
6N3	628	707 (1.126)	764 (1.217)	798 (1.271)

[a]Values in parentheses are ratios of power produced in reflected core to that produced in core blanketed with depleted uranium.

TABLE I.E.23. Flow Rates Used for HECTIC Calculations of Temperature Distribution in Cores with Various Reflectors

Row	Flow Rate (gpm)		Row	Flow Rate (gpm)	
	Depleted-U Blanket	Reflected		Depleted-U Blanket	Reflected
1,2	141	151	5	77	82.6
3	124	133	6	67	71.4
4	91	97.6			

The flow rates for the reflected cores are the same as those previously used for calculations when the stainless steel reflector was in use during EBR-II Runs 25 to 28. They are higher than those with a depleted-uranium blanket because of the reduced flows through reflector subassemblies.

Table I.E.24 presents the results of the HECTIC calculations. The temperatures shown are the maxima that occur in a subassembly in the given row for the given core and blanket-reflector configuration. Also shown in Table I.E.24 are the maximum temperatures for the original 67-subassembly core in ANL-5719 (Addendum). Two sets are presented for that core: one taken from the report, and the other calculated using the same input but present calculational techniques.

TABLE I.E.24. Maximum Temperatures (°F) for Variously Reflected Cores

Reflector or Blanket	Row	Coolant	Cladding ID	Fuel Surface	Fuel Average	Fuel Center
Depleted U	1	919	976	997	1051	1113
2 SS		921	981	1004	1062	1129
2 SS, 2 Ni		935	999	1023	1080	1156
4 Ni		933	997	1020	1082	1153
Depleted U	2	907	961	981	1032	1090
2 SS		910	967	989	1044	1108
2 SS, 2 Ni		923	984	1007	1066	1134
4 Ni		922	983	1005	1064	1132
Depleted U	3	940	996	1016	1066	1123
2 SS		941	1000	1022	1076	1139
2 SS, 2 Ni		956	1019	1042	1100	1167
4 Ni		954	1016	1039	1096	1162
Depleted U	4	1007	1061	1080	1125	1172
2 SS		1008	1066	1086	1135	1188
2 SS, 2 Ni		1028	1090	1112	1164	1220
4 Ni		1028	1090	1112	1164	1220
Depleted U	5	1019	1068	1085	1125	1165
2 SS		1025	1078	1096	1140	1185
2 SS, 2 Ni		1048	1105	1124	1171	1219
4 Ni		1049	1106	1125	1172	1220
Depleted U	6	1015	1057	1072	1106	1140
2 SS		1031	1078	1094	1132	1170
2 SS, 2 Ni		1056	1107	1124	1165	1206
4 Ni		1065	1117	1135	1177	1219
ANL-5719[a] Values						
Book		1037	1087	1108	1161	1213
Using Present Calculational Techniques		1037	1084	1102	1148	1198

[a]Hazard Summary Report Experimental Breeder Reactor II (EBR-II), ANL-5719 (May 1957).

d. Gamma Heating in EBR-II with a Depleted-uranium Blanket (L. B. Miller and R. E. Jarka)

The rate of energy deposition in the EBR-II core, upper-reflector, and radial-blanket regions as a function of radius is shown in Fig. I.E.11. The heat-generation rate, in kW/cm^3, is shown at the core midplane, along the top of the core, and at 18 cm above the top of the core. These results were obtained by first calculating the neutron flux as a function of R and Z for 22 energy groups. The gamma source rate produced by this neutron flux then was calculated and used as the source for a 20-energy-group gamma-transport problem. The two-dimensional multigroup photon flux from the gamma-transport problem was used with gamma-energy absorption coefficients to compute the heat-generation rate shown in Fig. I.E.11. The neutron-transport problem was done with the usual transport approximation for neutron scattering and the S_6 approximation to neutron transport. The photon-transport problem was done with P_3 scattering, using the S_6 approximation. The neutron-transport problem was normalized to a total reactor power of 50 MWt.

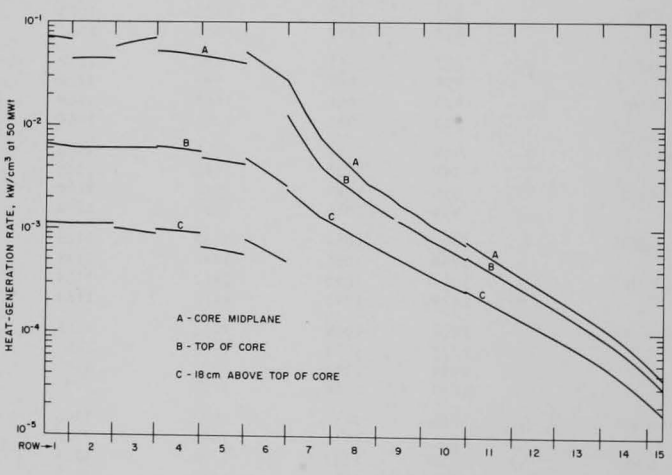

Fig. I.E.11. Rate of Gamma-heat Generation in EBR-II with Depleted-uranium Blanket (S_6P_3 calculations)

The compositions of all the subassemblies in each row were averaged in computing the atomic densities used for each row in the calculations. This results in some variation in atomic density from one row to the next. The discontinuities in heating rate shown in Fig. I.E.11 are due to these variations.

The gamma-heating rates in the core midplane as a function of radius were obtained for EBR-II with a stainless steel reflector in two rows,

with a nickel reflector in four rows, and with a depleted-uranium blanket. For this comparison, it was assumed that the stainless steel-reflected and nickel-reflected cores would have a composition similar to that in EBR-II Run 31F except that a critical configuration would be achieved by placing half-worth subassemblies in Row 5. This adjustment to critical of the nickel-reflected core configuration would result in a 5.5% increase in the power in fully loaded driver subassemblies. The increased power in Row 6 would result in a similar increase in the gamma source rate and the gamma-heating rate. This renormalization to account for the required changes in the core configuration to bring the reactor critical is reflected in the comparison of gamma-heating rates in the cores reflected by nickel, stainless steel, and ^{238}U that is shown in Fig. I.E.12.

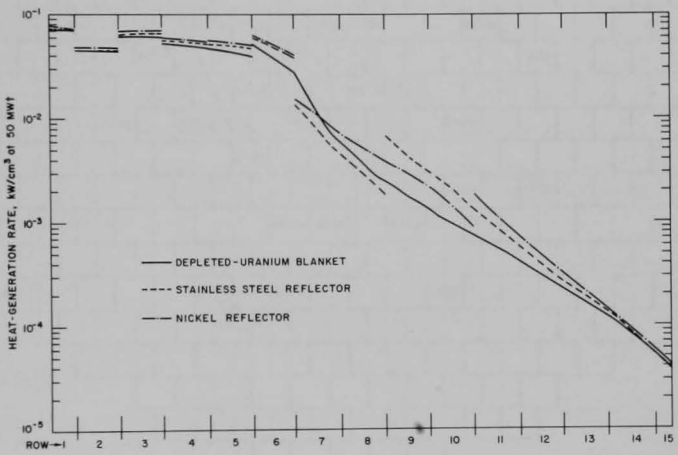

Fig. I.E.12. Rate of Gamma-heat Generation at Midplane of Core of EBR-II with Various Reflectors

e. Fission-rate Distribution in EBR-II Run 39A (L. B. Miller and R. E. Jarka)

Six-group fluxes and fission rates in the core midplane of EBR-II have been computed for Run 39A, using the usual 360° XY representation and the DOT-5 code. Figure I.E.13 shows the core loading for Run 39A. Fission-rate distributions have been plotted along the lines shown on the diagram. Figure I.E.14 is a plot of the ^{235}U fission rate per atom in positions 6A1 through 6D1. The fission rate per atom of ^{235}U is 11% greater in 6A1 than in 6D1. The effect of structural Subassembly X021 to the right of center and X059 to the left of center is clearly shown in the graph.

Figure I.E.15 shows the microscopic ^{235}U fission rate between positions 6E4 and 6B3. The depressions caused by structural

Subassemblies X034 and X057 are evident to the left and the right of the central position. The difference in fission rate per atom of ^{235}U between positions 6E4 and 6B3 is 4%.

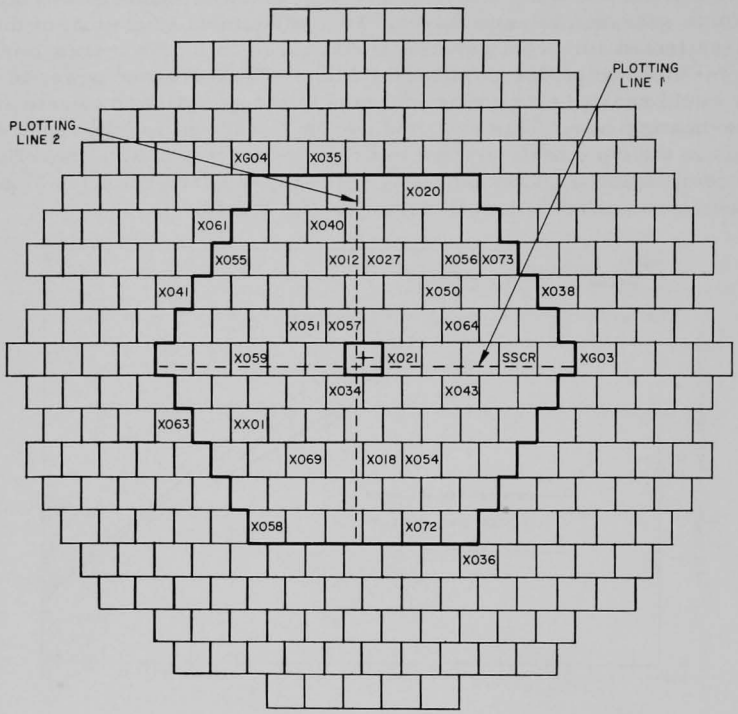

Fig. I.E.13. Core-loading Diagram for EBR-II Run 39A

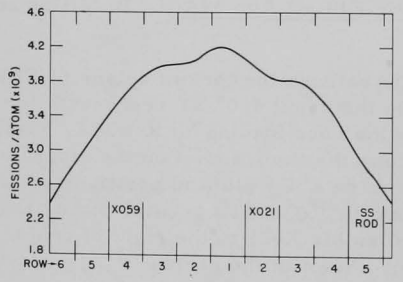

Fig. I.E.14. Fissions per Atom of ^{235}U in EBR-II Run 39A, along Plotting Line 1 in Fig. I.E.13.

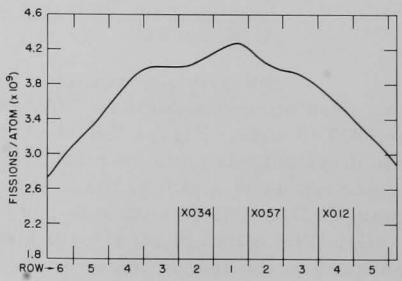

Fig. I.E.15. Fissions per Atom of ^{235}U in EBR-II Run 39A, along Plotting Line 2 in Fig. I.E.13.

Figures I.E.16 and I.E.17 are similar graphs of the ^{238}U microscopic fission rate. The flux-depression effects seen in the graphs for ^{235}U microscopic fission rate are also evident in the graphs for ^{238}U microscopic fission rate, but are much more pronounced because the structural materials with high inelastic-scattering cross sections are much more effective in depleting the high-energy flux responsible for ^{238}U fissions than in depleting the total flux. The high-energy flux tilt also is larger than the total flux tilt, as is evident from the 18% greater ^{238}U microscopic fission rate in 6A1 than in 6D1.

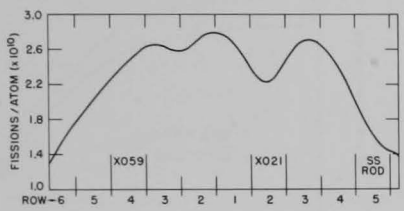

Fig. I.E.16. Fissions per Atom of ^{238}U in EBR-II Run 39A, along Plotting Line 1 in Fig. I.E.13

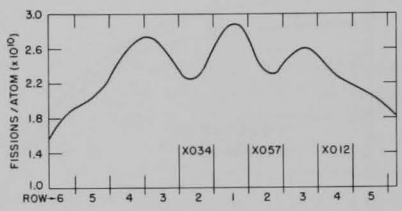

Fig. I.E.17. Fissions per Atom of ^{238}U in EBR-II Run 39A, along Plotting Line 2 in Fig. I.E.13

Figure I.E.18 shows the total fission rate from position 6A1 to position 6D1. The driver in 6A1 produces 12% more power than the driver in 6D1. The peak power occurs in the central driver along its edge adjacent to X057. Figure I.E.19 shows the total fission rate from position 6E4 to position 6B3.

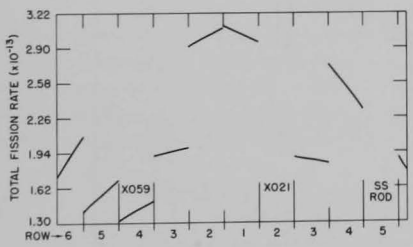

Fig. I.E.18. Total Fission Rate in EBR-II Run 39A, along Plotting Line 1 in Fig. I.E.13

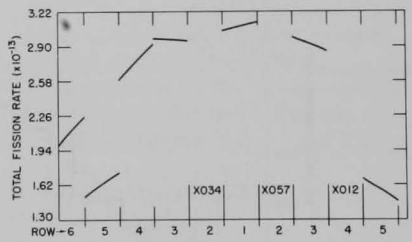

Fig. I.E.19. Total Fission Rate in EBR-II Run 39A, along Plotting Line 2 in Fig. I.E.13

f. Neutron Importance in EBR-II (L. B. Miller and R. E. Jarka)

The adjoint transport problem was solved with the DOT-5 code to obtain the neutron importance in EBR-II as a function of energy, axial position, and radius. The 22-group cross-section set 238, which gives good agreement with experiments in calculations of control-rod worths,

^{235}U fission rates, and ^{238}U fission rates, was used in the calculation. A typical loading, Run 31F, was selected as the basis for the calculation.

Figure I.E.20 shows the importance of high-energy neutrons ($E > 3.68$ MeV) as a function of radius in the core midplane and along the top of the core. Figure I.E.21 shows the neutron importance in an energy region near the peak of the flux spectrum.

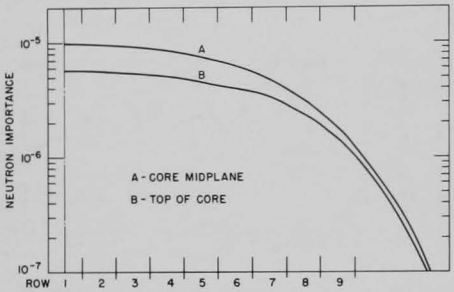

Fig. I.E.20. Neutron Importance vs Radius in EBR-II Run 31F; Neutron Energy > 3.68 MeV

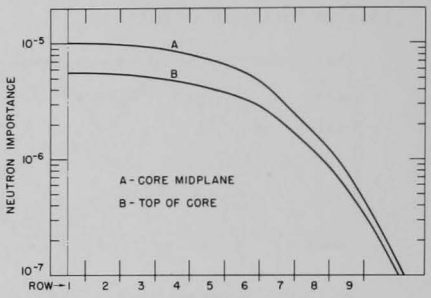

Fig. I.E.21. Neutron Importance vs Radius in EBR-II Run 31F; Neutron Energy, 498-821 keV

Figure I.E.22 shows neutron importance as a function of lethargy at the center of the core.

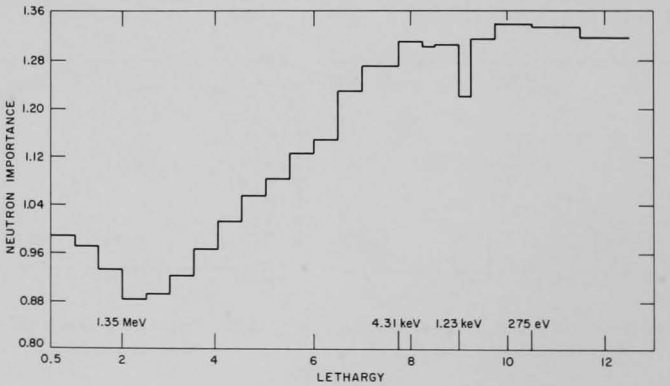

Fig. I.E.22. Neutron Importance vs Lethargy in EBR-II Run 31F; Center of Core

General features of the curves are typical of adjoint flux spectra in fast reactors. One unexpected local minimum in the adjoint spectra occurs in the energy group $0.961 < E < 1.23$ keV. However, careful study of the cross-section curves in BNL-325 reveals that the capture-to-fission ratio in ^{235}U has a local maximum in this group.

g. Analysis of a Mixed Core (J. L. Gillette)

Neutronic and thermal-hydraulic analyses of mixed cores in EBR-II has continued (see Progress Report for February 1970, ANL-7669, pp. 78-81). The method of neutronic analysis, however, has been slightly changed. Rather than doing a series of calculations to obtain group-dependent transverse bucklings, a single problem is done with the transverse buckling given by

$$B_z^2 = \pi^2/H_{ext}^2$$

in all regions and for all energy groups. The value of H_{ext} is determined from previous work and is assumed to be the same for all core loadings. This assumption is consistent with the fact that the axial maximum-to-average power in EBR-II is relatively insensitive to core alignment. It is believed that this method of analysis leads to a more realistic description of the transverse leakage than does the iteration process used previously.

Two additional core configurations have been analyzed: the wet critical loading and an artificial loading in which 25 mixed-oxide-fueled subassemblies are placed in Rows 5 and 6. A radial blanket of depleted uranium was used in each analysis.

The wet critical analysis has a dual purpose. Not only does it provide a base for the mixed-core analysis series, but it is also serving as a check on the steady-state portion of the MELT-II accident code.

Table I.E.25 presents the results of the wet critical analysis. The column entitled T_{Bulk} records the mean temperature of the mixed coolant leaving a subassembly in the row indicated. The column $T_{Cool\ Max}$ represents the maximum coolant-outlet temperature in the subassembly. These temperatures differ because of the effects of the subassembly-can wall on the mass flow rate of the coolant. The columns T_{Clad} and T_{Fuel}

TABLE I.E.25. Calculated Temperatures (°F) at 62.5 MWt with Wet Critical Loading

Row	T_{Bulk}	$T_{Cool\ Max}$	T_{Clad}	T_{Fuel}
1	925.6	983.2	1038.4	1193.4
2	922.0	978.6	1032.3	1182.1
3	930.9	989.8	1039.8	1175.2
4	964.7	1032.2	1076.4	1191.0
5	981.2	1052.8	1092.1	1193.5
6	916.2	971.4	1000.4	1073.7

represent the maximum cladding temperatures and maximum fuel temperatures, respectively.

These temperatures agree very well with those previously reported in ANL-5719 (Addendum)* and will be used as a basis for comparison of future results.

The other core alignment assumes that 10 oxide subassemblies are placed in Row 5 and 15 oxides in Row 6. The uranium in the oxides is assumed to be fully enriched (92.7%), so that the temperatures calculated (and shown in Table I.E.26) represent the most severe situation which can be attained under nominal operating conditions. The assumptions in the thermal-hydraulic analysis are presented in ANL-7669.

TABLE I.E.26. Calculated Temperatures (°F) in Mixed Core at 62.5 MWt

	Drivers				Oxides		
Row	T_{Bulk}	$T_{Cool\ Max}$	T_{Clad}	T_{Fuel}	$T_{Cool\ Max}$	T_{Clad}	T_{Fuel}
1	878.6	924.1	971.5	1102.3	-	-	-
2	878.5	924.0	970.8	1099.2	-	-	-
3	893.9	943.3	988.7	1109.8	-	-	-
4	933.5	993.0	1035.1	1142.8	-	-	-
5	947.7	1010.8	1048.2	1143.1	1026.2	1090.7	3953.3
6	923.2	980.0	1012.0	1092.4	994.0	1049.1	3555.2

These results show that placing of oxide-fueled subassemblies having a fuel enrichment of up to 92.7% into a core configuration described above will cause no adverse thermal-hydraulic effects in the reactor.

h. Temperature of Cladding of Oxide Fuel Element during Postulated Gas Blanketing and Nuclear Excursion (R. K. Lo)

Calculations were made to determine the temperature distribution in the cladding and fuel of an oxide fuel element during postulated gas blanketing and nuclear excursion. The angle of the blanketing arc studied ranged from 10 to 100°. The reactor was assumed to be operated at normal power with full coolant flow. A single control rod was assumed to be driven into the reactor in an uncontrolled manner at a rate of 5 in./min. Figure I.E.23 shows the rate of power increase and change in sodium temperature that would occur with such an event.

The oxide fuel was assumed to have a central void and three fuel regions--columnar, equiaxed, and as sintered. Fuels with theoretical density of 82 and 92% were considered. The power generation of the oxide fuel element was 16 kW/ft. The cladding was 0.290 in. in OD, had a 0.015-in.-thick wall, and contained fuel pellets of 80% UO_2-20% PuO_2. The contact

*Hazard Summary Report for Experimental Breeder Reactor II (EBR-II).

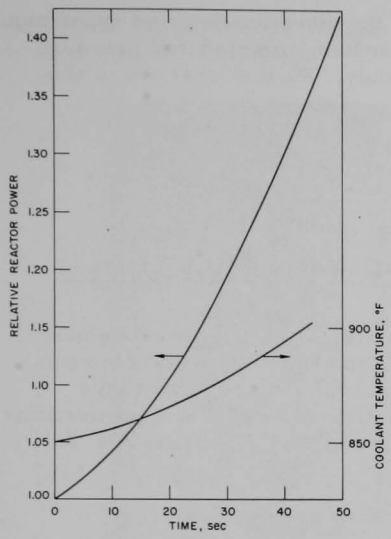

Fig. I.E.23. Increases in Power and Coolant Temperature Following a Postulated Accidental Insertion of a Control Rod into an EBR-II Core at Normal Operating Power

conductance between the fuel and the cladding was assumed to be 1500 Btu/hr-ft^2-°F, and the velocity of the sodium flow used was 12.4 ft/sec. These parameters represent the average conditions for an unencapsulated mixed-oxide fuel element in the EBR-II core.

The general computer code THTB for transient heat transfer was used to determine the temperature of the cladding and the fuel. It was found that the cladding temperature would not reach 2600°F, the melting temperature of the stainless steel, with gas-coverage angles from 10 to 80°. However, with 100° of gas coverage, the maximum temperature of the cladding of the 92%-density fuel would reach 2600°F after 13 sec from the start of the event and that of the cladding of the 82%-density fuel would reach 2600°F in 12 sec. Figure I.E.24 shows the variation of the maximum cladding temperature with time for the two types of fuels blanketed with 100° coverage.

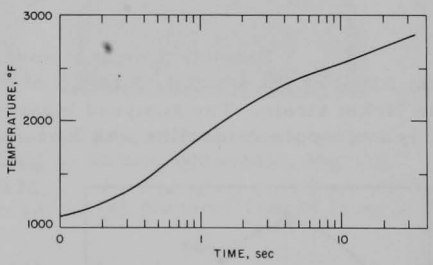

Fig. I.E.24

Variation with Time of Maximum Cladding Temperature of Oxide Fuels Having 82% and 92% Theoretical Density and Blanketed with 100° Arc of Fission Gas

i. Vibration Effects in EBR-II (L. K. Chang)

During operation of EBR-II, a 10-cps vibration of the reactor was experimentally detected by an accelerometer mounted remotely from the reactor. The cause of the vibration and the object which vibrated are unknown at present.

One of the possibilities is parallel-flow-induced vibration of a subassembly cooled by sodium at an average velocity. If a subassembly is simulated by considering a long, hollow cylindrical rod clamped at one end and free at the other, the fundamental nautral frequency of the cylinder is found to be 10 cps, which coincides with the experimentally determined

frequency. It is possible, therefore, that the vibration detected experimentally may be due to vibrations caused by sodium-flow-induced pressure fluctuation on the surface of the subassembly. Further analysis of this problem is being carried out.

8. Driver Fuel Development (C. M. Walter)

a. High Burnup Encapsulated Irradiations

Last Reported: ANL-7669, pp. 86-87 (Feb 1970).

(i) Postirradiation Examination of Encapsulated Mark-II Elements (W. N. Beck)

Subassembly X053, containing 37 encapsulated elements, was removed from reactor position 4B3 at the end of Run 34. Elements from this subassembly are being subjected to a detailed destructive examination. Table I.E.27 gives some preliminary results of postirradiation examination of these elements as well as those (Elements 201, 251, and 212) examined at ~2 at. % burnup.

TABLE I.E.27. Preliminary Results of Postirradiation Examination of Encapsulated Mark-II Elements

Element No.	Element Length (in.)	Restrainer Height above Fuel (in.)	Fuel Enrichment (%)	Max Burnup (at. %)	Max Fuel Temp (°F)	Max Cladding Temp (°F)	Max Cladding ΔD/D (%)	Increase in Fuel Length (in.)	Fission-gas Release (% of theoretical)
201	24	0.19	80	1.7	1220	1025	0.37	0.24	36.6
251	24	0.24	93	2.0	1295	1095	0.21	0.39	36.1
212	24	0.24	93	2.0	1200	1005	0.13	0.24	-
207	24	0.20	80	3.0	1165	950	0.8	0.30	58.0
227	24	0.25	80	3.1	1220	1025	0.6	0.34	-
279	26	0.27	80	3.1	1220	1025	0.3	0.30	-
262	26	0.38	93	3.5	1295	1095	0.3	0.44	-
255	26	0.77	93	3.6	1295	1095	-	0.85	-
213	24	0.32	93	3.6	1200	1005	1.0	0.33	38.3

Diametral measurements of the elements showed a maximum ΔD/D of 1%, which is a result of swelling of the stainless steel rather than jacket strain. The analyzed maximum burnup for the element nearest the reactor-core centerline was 3.61 at. %. Figure I.E.25 shows the burnup profiles for two of the elements (207 and 213) from Subassembly X053.

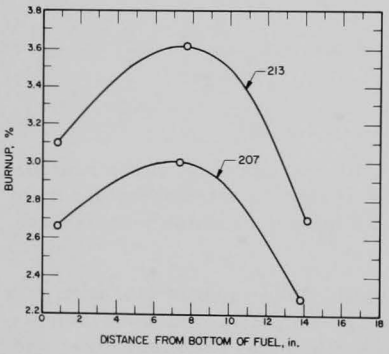

Fig. I.E.25. Axial Burnup Profiles for Encapsulated Mark-II Elements 207 and 213

Metallographic examination of transverse as well as longitudinal sections showed the fuel to be making intimate contact with the cladding. The fuel column had elongated to the restrainers but had not changed appreciably from the fuel column position observed at a burnup of 2 at. %. Figure I.E.26 shows longitudinal sections of two elements taken at the points where the fuel is contacting an indent-type restrainer and a ferrule-type restrainer. The fuel is of uniform texture; intercor

enough to be observed by light microscopy appears at only the extreme ends of the element.

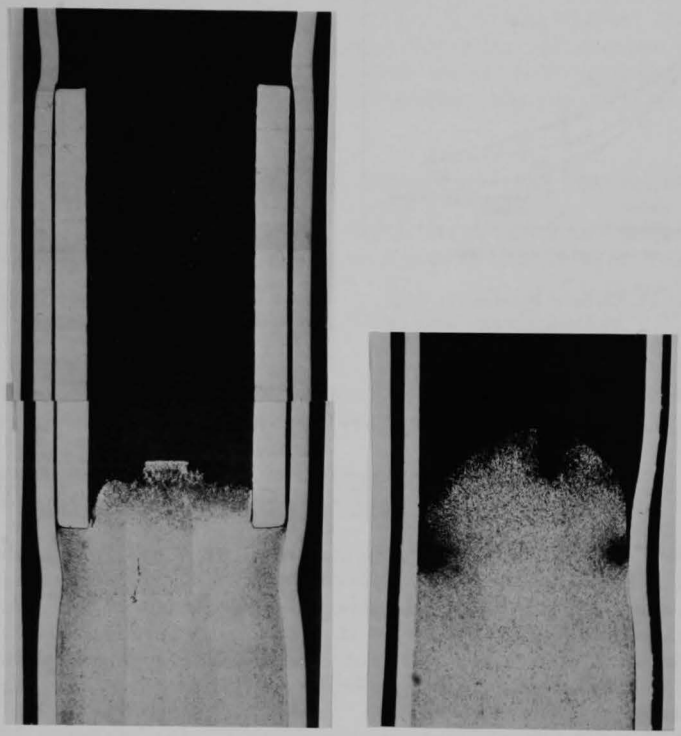

Fig. I.E.26. Longitudinal Section of Element 279 (left), Which Had a Ferrule-type Fuel Restrainer. Element 207 (right) had the indent-type restrainer. Mag. 10X.

Release of fission gas to the plenums ranged from 36 to 58% of theoretical.

The cladding exhibited a sensitized structure (carbide precipitates at the grain boundaries) over the entire length of the pin. This structure is not frequently observed at the bottom of the element because of the low temperature and exposure to low fluences. Diamond indent hardness measurements taken at 13 mean-thickness locations and at different axial positions in the element showed a reduction of hardness from ~240 DPH at the bottom of the element to ~190 at the top (see Fig. I.E.27). Figure I.E.28 shows the mean cladding temperatures for the elements in Fig. I.E.27. It is apparent that irradiation-induced hardening is partially annealed out by the higher cladding temperatures.

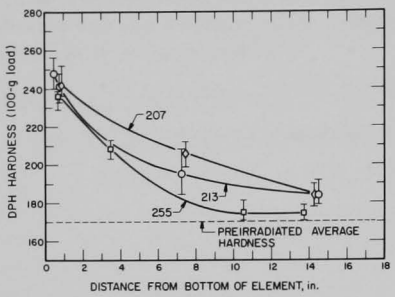

Fig. I.E.27. Cladding Hardness (at Mean Thickness) vs Axial Position for Elements 207, 213, and 255

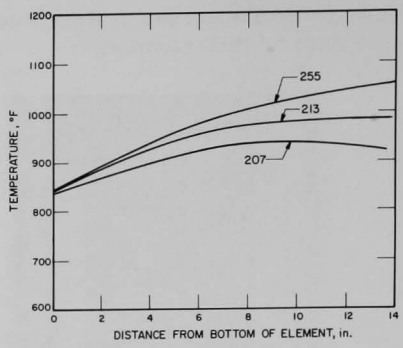

Fig. I.E.28. Axial Mean Cladding Temperatures for Elements 255, 207, and 213

Details specific to the examination of one of the elements (No. 255) from Subassembly X053 are discussed in the following section.

(ii) Metallographic Examination of Samples from Encapsulated Mark-II Fuel Element 255 at ~3.6 at. % Burnup (R. V. Strain)

Optical metallographic examination has been made of ten samples of Element 255 from Subassembly X053. The element was of the Mark-II design, 26 in. long, and contained a 93%-enriched fuel pin. It had been irradiated to approximately 2 at. % burnup in Subassembly X029 and an additional ~1.6 at. % burnup in Subassembly X053, for a total burnup of ~3.6 at. %. The metallographic examination revealed the following information:

(1) The fuel had swollen out to the cladding and up to the restrainer. It contained many large voids near the bottom of the fuel element (up to a height of at least 1/2 in.). The remainder of the fuel pin contained only a few large voids, but contained many small voids having an average diameter of about 2×10^{-4} in. The dimple restrainer appeared to be effectively stopping the axial growth of the fuel pin at this burnup.

(2) There was an interaction band at the fuel-cladding interface, extending from approximately 1/2 in. from the bottom of the fuel pin to 1/8 in. from the top. An interaction zone existed in both the fuel and the cladding over this length. Electron-microprobe examination will be run further to characterize this apparent interaction between the fuel and cladding. A similar zone was seen earlier in an encapsulated Mark-II element irradiated to ~2.0 at. % burnup. Microprobe analysis of this earlier element showed no chemical interaction.

(3) The cladding exhibited a sensitized structure (carbide precipitates at the grain boundaries) over the entire length of the fuel pin. Sensitized structure usually is not observed near the bottom of the element because of the low temperature and low fluence in that region. The sensitization at the bottom of the element may indicate that the element operated at higher than normal temperatures or that the extended irradiation of the element has enhanced the degree of sensitization and caused it to occur at lower than normal temperatures.

The major difference between this fuel element at ~3.6 at. % burnup and Element 251 at 2.1 at. % burnup was the large number of voids at the bottom of the element. It appeared that the fuel had moved out of the lower region and up into the region just below the restrainer. The other apparent change was the widening of the interaction band between the fuel and cladding. Although the band was quite wide on the fuel side of the interface, the change in the cladding structure extended only about 0.0001 in. into the cladding. This metallographic examination revealed sensitization of the cladding but no cracking at the grain boundaries or loss of grains. On the basis of these results, the cladding appears to be sound and suitable for further irradiation.

b. Fuel and Cladding Surveillance

(i) In-pile Creep Studies (L. C. Walters, C. M. Walter, M. A. Pugacz, J. A. Tesk, R. Carlander, and Che-Yu Li)

Last Reported: ANL-7640, pp. 71-73 (Nov 1969).

In the present creep experiment (Subassembly X065, Creep 1), the outer diameters of 18 helium-pressurized, annealed, Type 304L stainless steel capsules that have a 0.290-in. outer diameter and a 20-mil wall, and are 60 in. long are being measured. Type 304 stainless steel filler rods (0.238-in. OD) were used inside each tube to reduce the potential energy release of an unexpected failure. Details of the subassembly constitution are given in ANL-7640.

The subassembly has been through three reactor cycles, and the outer diameters of the capsules have been measured after each cycle. The diameter measurements taken after the first reactor cycle (post 1) are subject to question for the following reasons. All those measurements were consistently larger than the diameter measurements taken after the second cycle (post 2), even from unpressurized dummy capsules. The post-2 diameter measurements were all repeated with good reproducibility. Since no physical reason can account for an apparent shrinkage of the capsules, a consistent measurement error must have been inherent in the post-1 measurements. The diameter measurements after the third

reactor cycle (post 3) show good reproducibility with those of post 2 except in the core region of the higher-stressed tubes, where there appears to be flux-enhanced creep.

Figure I.E.29 shows typical diameter measurements along the length of Capsules 29 and 36 after the second reactor cycle and of Capsule 29 before irradiation. (The relatively large difference between the pre- and postirradiation diameters of Capsule 29 is typical. It can be attributed to immediate yielding as the capsules are brought to temperature in the reactor.) The progressive increase in diameter from the bottom to the top of the capsules is due to a temperature gradient due to radial heat conduction from adjacent subassemblies. A large increase in data scatter also was detected after irradiation. This increase in scatter probably results from variations in tube-wall thickness and material homogeneity.

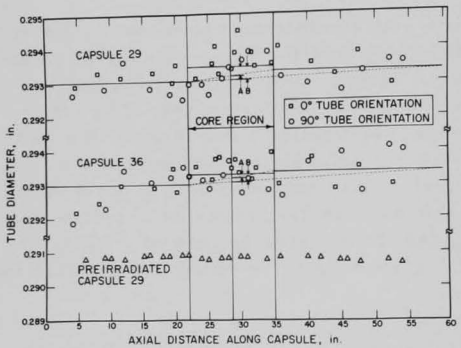

Fig. I.E.29. Postirradiation Measurements (Top Two Plots) of the Diameters of Capsules 29 and 36. The preirradiation measurement (bottom plot) of Capsule 29 is typical of measurements of all capsules before irradiation and demonstrates the precision with which measurements are made.

It is not readily apparent from the results as shown in Fig. I.E.29 that any enhanced creep has occurred in the core region of the capsules. However, a careful examination of the diameter data shows that an enhanced creep does exist in the core region of the higher-stressed capsules. To determine the magnitude of the enhanced creep quantitatively, the following procedure is used. The diameter measurements below the core region, in the core region, and above the core region are averaged to yield a diameter representative of each region. To avoid end effects, measured diameters near the bottom and top of the capsules are excluded in arriving at the averages. The continuous, solid horizontal lines in Fig. I.E.29 represent these averages in each region. These average diameters were then analyzed, using as a basis the assumption that radiation-enhanced creep would cause a diameter increase in the core region. Any diameter increase larger than that which could be explained by deformation from a temperature gradient would positively identify flux-enhanced creep.

Two assumptions must be made at this point because experimental information on the existing temperature profiles was not available. The first assumption is that a linear temperature gradient existed. The second is that the deformation (other than the radiation-enhanced creep)

is linearly related to temperature. The linear temperature profile was allowed to fall between two extremes: (1) that when the temperature increase occurred only in the core region, and (2) that when the temperature increased linearly from the bottom of the core region to the top of the capsules. The broken lines in Fig. I.E.29 represent the deformations that result from the two extremes in linear profiles.

The deformation due to radiation-enhanced creep then was calculated as the difference between the average diameter in the core region and the diameter predicted on the basis of the linear temperature profile. For a linear increase in temperature in the core region, the creep enhancement will be a minimum, as shown by the increment A in Fig. I.E.29. The other case (where the temperature rise is extended to the top of the capsules) will yield a larger value for an enhancement effect, as shown by increment B.

The nine higher-stressed capsules were analyzed according to the above procedure. Table I.E.28 shows the results. Post-2 results refer to the measurements made after the second reactor cycle, when the capsules had accumulated a maximum fast fluence (>0.1 MeV) of approximately 3×10^{21} n/cm^2. Post-3 results refer to the measurements made after the third reactor cycle, when the capsules had accumulated a maximum fast fluence (>0.1 MeV) of approximately 5.3×10^{21} n/cm^2. After the second reactor cycle, the capsules had accumulated a total time at power of 822.5 hr; after the third reactor cycle, the total time at power was 1473 hr. The negative values shown simply mean that there is no significant enhancement and that the average diameter in the core region is below the linear approximation made on the basis of the temperature-gradient considerations.

TABLE I.E.28. Deformation due to Flux-enhanced Creep in Core Region of Higher-stressed Capsules from Creep 1

Capsule No.	44	57	30	29	36	37	45	48	38
Initial Hoop Stress[a] (kpsi)	25.0	25.0	25.0	30.0	30.0	30.0	35.0	35.0	35.0
Final Hoop Stress[b] (kpsi)	22.8	22.8	22.8	24.7	24.7	24.7	27.3	27.3	27.3
Post-2 Enhancement[c] (10^{-4} in.)									
max	-0.5	0	0.3	3.8	2.6	1.0	2.4	4.7	-1.9
min	-1.7	-0.2	-1.2	2.8	1.4	0	2.1	1.2	-3.0
Post-3 Enhancement[c] (10^{-4} in.)									
max	0.7	-1.1	0.6	4.6	5.1	0.9	3.1	6.2	-1.0
min	-0.2	-1.4	-1.1	3.8	4.1	0.4	2.4	3.5	-2.5

[a]The initial hoop stress is referenced to a temperature of 700°F before any deformation.
[b]The final hoop stress is referenced to a temperature of 700°F and corrected for volume expansion due to deformation.
[c]A reasonable estimate of the standard deviation for the enhanced deformation is $\pm 2 \times 10^{-4}$.

The important aspect of the results shown in Table I.E.28 is that five of the six capsules stressed to 30 and 35 kpsi showed an enhanced deformation in the core region. No flux-enhanced creep was detected in capsules stressed to less than 30 kpsi. In all five higher-stressed capsules, this deformation increased between the post-2 and the post-3 examinations.

The subassembly containing these capsules is being prepared for the fourth in-reactor cycle. After further irradiation, a fairly reliable estimate of the flux-enhanced creep rate should be gained from this experiment. At this point in the experiment, only an approximate value of the enhanced creep rate can be calculated. The average enhanced strain for the five capsules from the post-3 measurements that exhibited an enhancement was divided by the total time at power. With this approximation, the creep rate is about $8 \times 10^{-7}\ hr^{-1}$.

To make the above analysis more meaningful, more information must be accumulated concerning the temperatures and temperature gradients existing in the subassembly. An earlier attempt at measuring temperatures with melt wires in the first reactor cycle was unsuccessful. The subassembly in the third reactor cycle contained five capsules with silicon carbide temperature monitors. These monitors are being analyzed. In the fourth reactor cycle, four capsules in the subassembly will contain sodium-expansion temperature indicators. In addition to these point determinations of temperature, a heat-transfer analysis is being initiated to determine the temperature gradients through the subassembly.

(ii) Cladding Surveillance (C. L. Meyers)

A surveillance program is being conducted for the purpose of monitoring the performance of EBR-II fuel-element cladding. The program is concerned primarily with irradiation-induced changes in the mechanical and physical properties of the cladding and with the associated changes in cladding microstructure.

Four creep tests have been conducted within a high-vacuum environment, using the ANL BRATT* in conjunction with a diametral extensometer. The tests were conducted in a temperature range representative of cladding temperature during irradiation in EBR-II, using samples from unirradiated Aerojet-General jackets (Matthey-Bishop tubing lot 20). Two of these samples, tested at 850°F, essentially did not creep (i.e., the creep rate was too low for a practical surveillance test); they ruptured at an internal pressure of 5400 psig of helium in a short-term mode as the applied internal pressure was successively increased from 4600 psig in 200-psig increments. The other two samples, tested at 950°F and at 4870 and 5010 psig internal pressure of helium, respectively, exhibited creep at a rate more of interest for cladding-surveillance tests.

The test results from the sample tested at 950°F and 5010 psig are shown in Fig. I.E.30, in which the variables have been replotted from a continuous test record to show several points along the diametral-increase curve. Diametral increase was measured over three separate regions of the sample by three eddy-current coils that covered most of the freely expanding sample. During initial pressurization of the

*Biaxial rupture-anticipating tubing tester.

sample at a rate of ~500 psig/min, the midlength coil sensed that the outside diameter of the tubing expanded from 0.1737 to 0.1880 in. (point e_1) at a linear rate of 5.1×10^{-2} min^{-1}, or 3.06 hr^{-1}. (Strain at point e_1 is 0.0843.) Beyond an outside diameter of 0.1880 in., the rate of expansion of the tubing diameter decelerated. At an outside diameter of 0.1891 in. (point e_1^i; strain = 0.0886), a sampling of the readings of the top and the bottom coils indicated that the bottom region of the sample had expanded more than the other regions; therefore, the recorder was switched over to monitor the bottom region of the sample. This explains the discontinuity between e_1^i and e_2 in Fig. I.E.30. The sample exhibited a linear secondary creep rate of 4.13×10^{-6} min^{-1} (2.48×10^{-4} hr^{-1}) between e_2 and e_2^i. Between e_2^i and e_3, the creep rate accelerated, passing into the tertiary stage of creep, which would normally terminate in rupture if the test were permitted to continue uninterrupted. Between e_3 and e_3^i, another linear creep rate was recorded: 2.85×10^{-5} min^{-1} (1.71×10^{-3} hr^{-1}). At e_3^i the other two regions of the sample were inspected, with the finding that the top region at that point in the test had expanded more than the other two. Therefore, the recorder was switched over to monitor the top region of the sample, resulting in the discontinuity between e_3^i and e_3^{ii}. The rate of expansion between e_3^{ii} and e_3^{iii} was 8.33×10^{-5} min^{-1} (5.00×10^{-3} hr^{-1}); between e_3^{iii} and e_3^{iv}, 2.00×10^{-4} min^{-1} (1.20×10^{-2} hr^{-1}); between e_3^{iv} and e_3^{v}, 1.44×10^{-4} min^{-1} (8.65×10^{-3} hr^{-1}); and between e_3^{v} and e_3^{vi}, 7.50×10^{-5} min^{-1} (4.50×10^{-3} hr^{-1}). At e_3^{vi}, the pressure was released to terminate the test before the sample could rupture. Final measurements of the sample, made by a precision micrometer, agreed well with final coil outputs at room temperature.

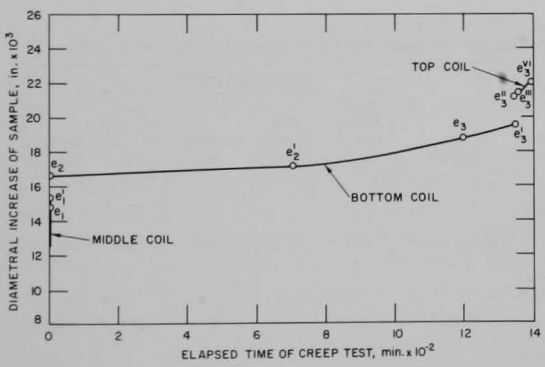

Fig. I.E.30

Results of Creep Test of Sample No. 3, a 5-1/4-in. Length of Type 304L Stainless Steel Tubing from Aerojet-General Fuel-element Jacket No. 58150 (Matthey-Bishop tubing lot 20). Test conditions: temperature, 950 ± 3°F; internal helium pressure, 5010 ± 10 psig; vacuum environment, 4×10^{-6} Torr.

A sample from the midlength section of the jacket of irradiated fuel Element E87 from driver-fuel subassembly C-2191 was tested (without fuel) after being cleaned and decontaminated sufficiently to permit testing in a conventional laboratory area. The element had attained a fuel burnup of ~0.33 at. %, which roughly corresponds to a fluence of ~5×10^{21} n/cm² (E > 0.1 MeV) in the sample tested. The sample was enclosed within a 1-in. pipe capsule to control the spread of any radioactive

contamination that might come off the sample surfaces at rupture. The outside of the sample was held at atmospheric pressure while the internal pressure was raised at a rate which varied between about 300 and 800 psig/min until the sample ruptured at 9870 psig. This burst pressure represents an increase (by irradiation hardening) of ~14% over the mean value of the unirradiated samples from the same tubing lot (Superior Tube, "Box" 4). The spread of contamination from the sample was successfully confined to the interior of the capsule.

Room-temperature biaxial tube-burst tests and uniaxial tensile tests have been made on samples of heat-treated tubing used by Aerojet-General to jacket its fuel elements. These tests are being made to determine the effect of a heat-treat "reclamation" of these centrifugally bonded elements* on the mechanical properties of the jacket. Table I.E.29 gives the results of the tensile tests, and Table I.E.30 those of the burst tests. The results of acceptance tests on the tubing as received from the vendor and of the subsequent tests of the heat-treated tubing are listed on the left and right sides of the tables, respectively, for comparison. Neither the uniaxial strengths nor the biaxial burst pressures are obviously affected by the heat treatments. However, the uniaxial elongation of the heat-treated tubing at fracture is about 30% lower than that of the as-received tubing. The biaxial diametral expansion, though degraded by heat treatment, does not seem to be degraded nearly as much as the unaxial elongation. Thus, the heat treatments do not appear to have compromised the intended service capability of this cladding. During irradiation, the cladding will be subjected predominantly to biaxial (rather than uniaxial) loading.

TABLE I.E.29. Tensile Properties of As-received and Heat-treated Jackets of Aerojet-General (AGC) Fuel Elements[a]

		As-received Properties				Heat-treated Properties				
AGC Jacket No.	MB Tubing Lot No.	Ultimate Tensile Strength (kpsi)	Yield Strength (kpsi)	Elongation (%)	Heat Treatment	Ultimate Tensile Strength (kpsi)	Yield Strength (kpsi)	Elongation (%)	Reduction in Area[b] (%)	Crosshead Rate (ipm)
29879	13	92.7 (Range: 89.0-96.1)	35.8 (Range: 33.9-37.6)	62.0 (Range: 58.0-66.0)	15 min @ 649°C	91.9	34.1	41.7	30.0	0.02
	13A	93.6 (Range: 91.8-96.0)	36.3 (Range: 34.1-44.6)	63.0 (Range: 57.0-68.0)						
31343	14	94.0 (Range: 92.0-95.4)	38.6 (Range: 37.0-40.6)	61.0 (Range: 55.0-65.0)	1 hr @ 646°C	95.3	36.3	38.7	27.5	0.05
32793	14	94.0 (Range: 92.0-95.4)	38.6 (Range: 37.0-40.6)	61.0 (Range: 55.0-65.0)	3 hr @ 672°C	93.4	35.0	41.7	30.1	0.02
35271	15	95.0 (Range: 90.0-99.8)	36.3 (Range: 34.6-38.7)	61.0 (Range: 57.0-65.0)	5 hr @ 656°C	94.6	34.6	44.5	29.5	0.05

[a]Room-temperature tests in air with Instron universal testing unit.
[b]Reduction in area estimated from minimum OD in necked region.

*These elements shortened with irradiation. The reclamation process consists of two heat-treat cycles, one at 660°C and the other at 500°C, with an air quench between them.

TABLE I.E.30. Burst Pressures of As-received and Heat-treated Jackets of Aerojet-General (AGC) Fuel Elements[a]

AGC Jacket No.	MB Tubing Lot No.	As-received Properties: Burst Pressure (kpsig)	As-received Properties: Strain at Fracture (%)	Heat Treatment	Heat-treated Properties: Burst Pressure (kpsig)	Heat-treated Properties: Strain at Fracture (%)
	13	7.94 (Range: 7.75-8.25)	24.2 (Range: 19.2-31.7)			
29879				15 min @ 649°C	7.77	20.8
	13A	7.97 (Range: 7.75-8.13)	22.4 (Range: 17.6-30.7)			
31343	14	8.11 (Range: 7.75-8.75)	23.5 (Range: 15.4-32.7)	1 hr @ 646°C	8.20[b]	22.7[b]
32793	14	8.11 (Range: 7.75-8.75)	23.5 (Range: 15.4-32.7)	3 hr @ 672°C	7.90	20.4
35271	15	7.96 (Range: 7.63-8.25)	23.1 (Range: 14.7-31.3)	5 hr @ 656°C	8.00	22.6

[a]Room-temperature tests in air with ANL biaxial rupture-anticipating tubing tester (BRATT).
[b]Test conducted in two steps. Swagelok fitting blew off during test.

9. Operation with Failed Fuel (R. R. Smith)

a. Studies with the Reactor Cover-gas Monitor (G. S. Brunson)

Last Reported: ANL-7606, pp. 63-66 (Aug 1969).

A general description of the reactor cover-gas monitor (RCGM) and some experimental results with it were reported in ANL-7606. The following material includes figures illustrating some of the earlier remarks and describes the results of subsequent work.

Figure I.E.31 illustrates the troublesome surges in counting rate associated with changes in the bulk-sodium temperature. The three juxtaposed charts cover about an hour during a startup while the reactor was going from approximately 500 kW to 10 MW (power is proportional to ΔT). Temperature fluctuations occur because of the operator's inability to adjust the coolant flow in the secondary system to compensate exactly for the increasing power. Similar surges occur during a scram or a rapid shutdown. Figure I.E.32 illustrates what happened when the bulk-sodium temperature was driven upward on a ramp by reducing secondary-sodium flow while the reactor power was stable at 50 MW. Again there was a marked increase in counting rates, with the trace tending to a flat-topped profile during the ramp as though the relationship were of a time-derivative nature.

In ANL-7606, such surges in counting rate were attributed to the capricious release of ^{23}Ne from the sodium, where it is formed by the $^{23}Na(n,p)^{23}Ne$ reaction. Support for this assumption was obtained in a

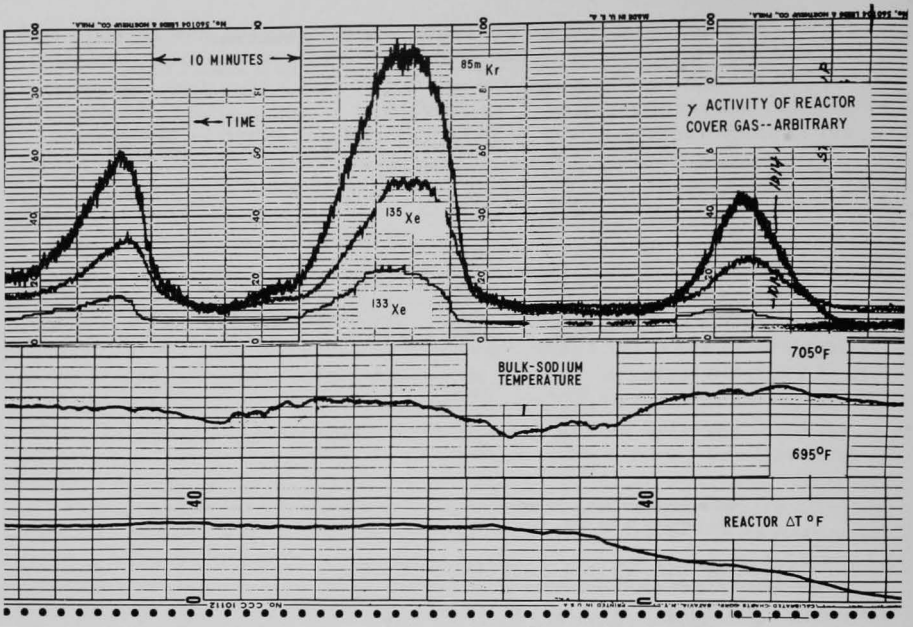

Fig. I.E.31. Spurious Surges in Indicated EBR-II Cover-gas Activity during a Normal Startup. Reactor power is proportional to ΔT (28°F corresponds to approximately 10 MW).

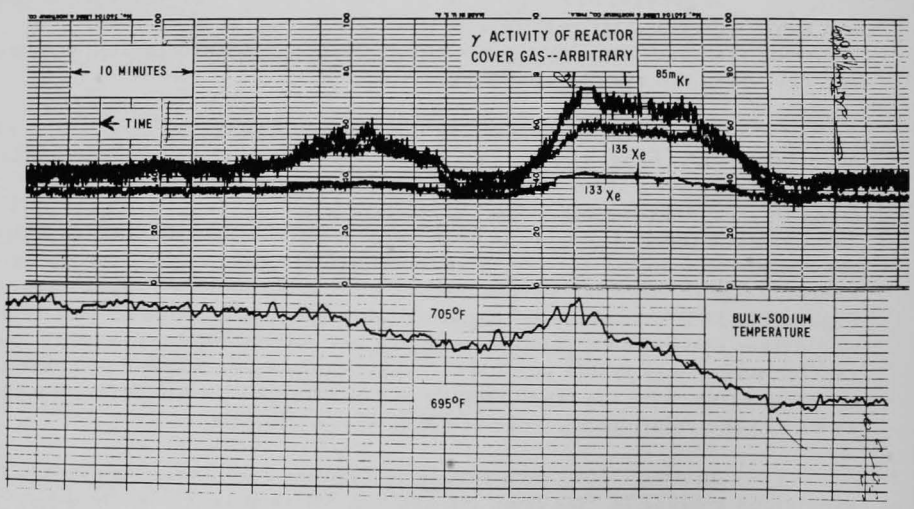

Fig. I.E.32. Spurious Indication of Increase in EBR-II Cover-gas Activity When the Bulk-sodium Temperature Was Deliberately Driven Upward While Reactor Power Was Stable at 50 MW

number of ways. The solid curve in Fig. I.E.33 represents the output of the ^{135}Xe channel; the straight dashed lines represent the power history. Note that during startup and at other times, there are spikes in the data corresponding to such events as are shown on a larger scale in Fig. I.E.31.

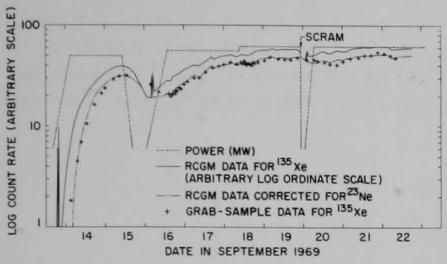

Fig. I.E.33

The Upper Curve Is the Output of the RCGM ^{135}Xe Channel during Several Days in September 1969. The lower curve represents the same data with the effect of interfering short-lived isotopes subtracted. The crosses show results of grab-sample analysis.

Late on the 19th of September 1969, a scram occurred, and the RCGM reading decreased by what is effectively a step function on the time scale of Fig. I.E.33. The height of this step was taken as the ^{23}Ne contribution to the ^{135}Xe channel for a reactor power of 62.5 MW. The ^{23}Ne contribution was taken as proportional at other powers and was subtracted to generate the lower curve of Fig. I.E.33. The crosses represent the results of high-quality determinations obtained from grab samples. Normalization was accomplished by displacement along the logarithmic ordinate scale. The excellent fit indicates that the effect of ^{23}Ne (and possibly of other short-lived isotopes) has been effectively eliminated.

A similar treatment of the data for ^{133}Xe was unsuccessful. The ^{133}Xe gamma is of such low energy that many higher-energy lines interfere. Some of the interfering gamma-emitting isotopes (e.g., ^{135}Xe) are so long-lived that the treatment described above is of no use.

Since ^{23}Ne has a half-life of 38 sec, the effect of the ^{23}Ne could be expected to be reduced by "aging" the gas before it is counted. Accordingly, a coil of stainless steel tubing was inserted in the sample line to delay the gas. Figure I.E.34 shows the RCGM spectrum as a function of

Fig. I.E.34

Gamma Spectrum Seen by the RCGM as a Function of Age of the Sample. Note the progressive reduction of the gamma peak about 440 keV.

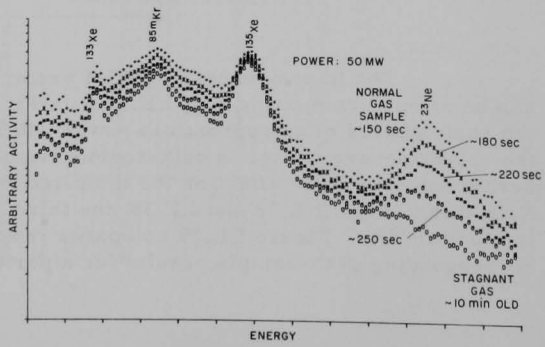

gas age. Age is measured only from the outlet for the cover-gas sample in the reactor vessel to the counter; nothing is implied concerning diffusion from the sodium.

Figure I.E.35 compares a spectrum taken under stable conditions with one taken during a ramp for gas aged approximately 170 sec. Figure I.E.36 makes the same comparison for gas aged approximately 235 sec. Note the greatly reduced effect of the ramp on the ^{135}Xe peak for the older gas sample. The improvement also is apparent for the ^{133}Xe and ^{85m}Kr peaks.

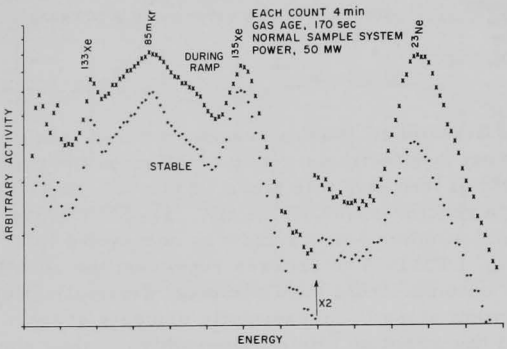

Fig. I.E.35

Comparison of Spectra Showing the Extent to Which a Temperature Ramp Causes Evolution of Extra ^{23}Ne and Its Effect on the Significant Fission-product Peaks

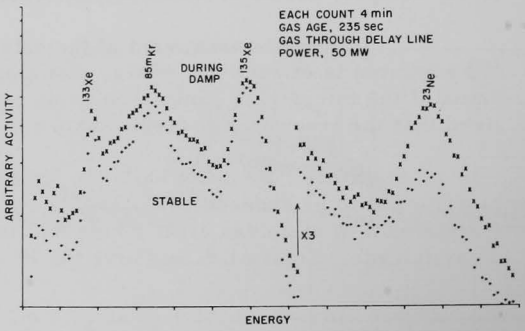

Fig. I.E.36

Pair of Spectra Taken under Stable and Ramp Conditions as in Fig. I.E.35. In this case, the gas has been aged in the delay line, thereby reducing the ^{23}Ne peak and its effect of the fission-product peaks.

The improvement in RCGM performance due to the delay line can be seen by comparing Fig. I.E.37 with Fig. I.E.31, both of which cover the early phases of an approach to power. In Fig. I.E.38, it is seen that the rather severe change in bulk-sodium temperature associated with a scram had very little effect on the indicated levels for ^{135}Xe and ^{133}Xe. Note that in Figs. I.E.37 and I.E.38, the third channel has been redeployed to monitor ^{23}Ne. Figure I.E.39 compares raw RCGM data for ^{135}Xe with the corresponding grab-sample results for a period of about three weeks in

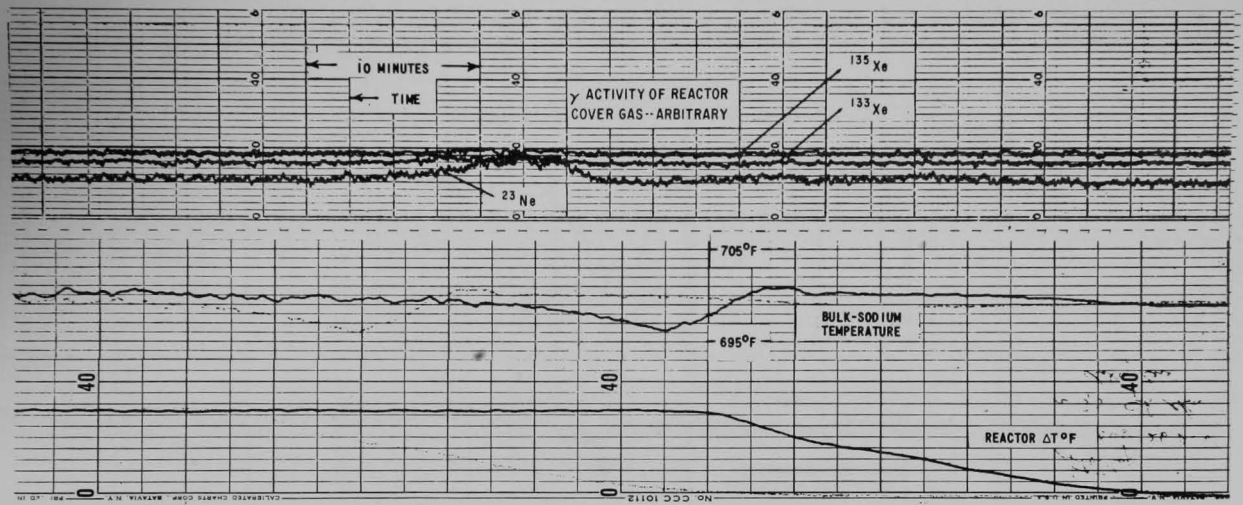

Fig. I.E.37. This Figure Is Directly Comparable with Fig. I.E.31, Covering the Same Stage of a Routine Startup. In this case, the use of the delay line has suppressed the spurious surges in count rate.

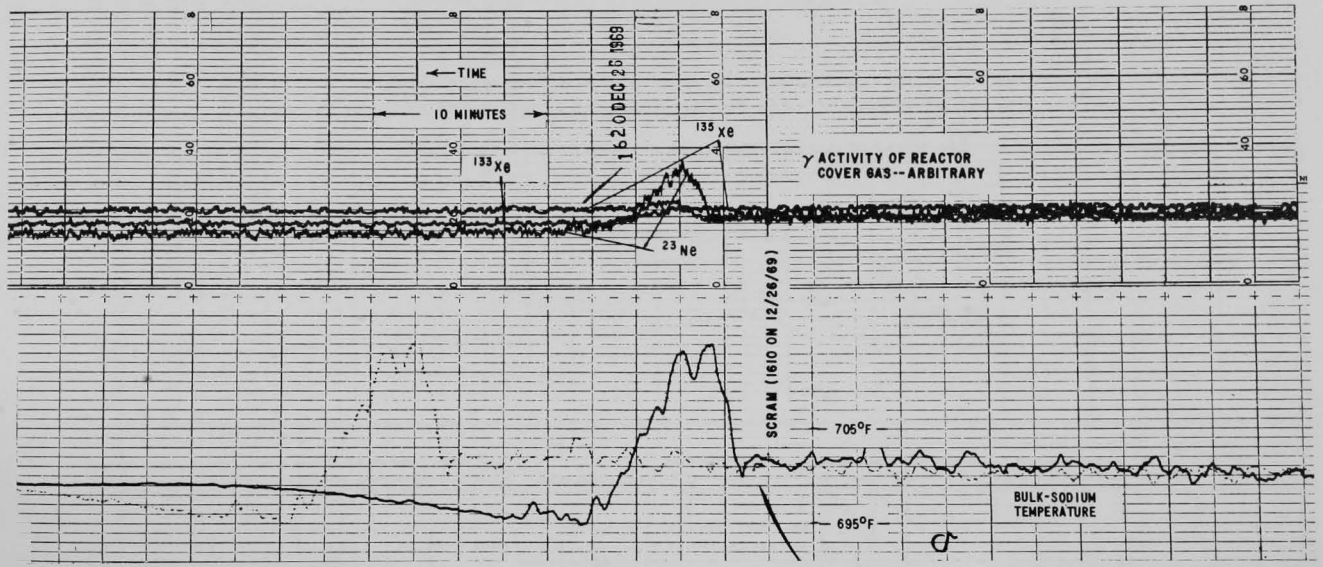

Fig. I.E.38. The RCGM Chart Is Coordinated with the Chart for Bulk-sodium Temperature for an Interval of Time Containing a Scram. Although an unusual change in temperature occurred, there was very little effect on the indications for ^{133}Xe and ^{135}Xe. This is an excellent demonstration of the effectiveness of the delay line in removing spurious surges. ("Ghost" temperature trace is due to inking double print.)

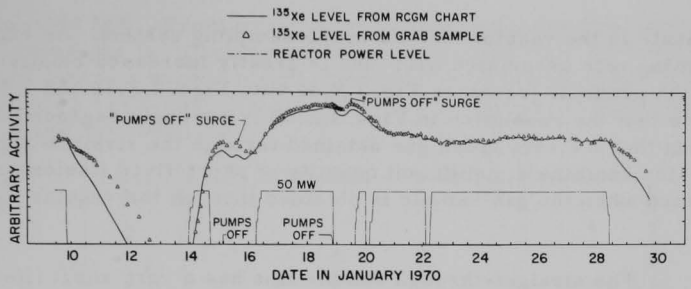

Fig. I.E.39. Comparison of Data for ^{135}Xe from the RCGM Chart with Data from Grab Samples for about Three Weeks in January 1970. During this time, the delay line was in use, and the estimated age of the sample gas was about 230 sec.

January 1970. The delay line was in operation during this time, and the age of the sample gas was estimated as 230 sec. The improvement is apparent when this figure is compared with Fig. I.E.33. The delay line did not bring any substantial improvement in the ^{133}Xe for the reasons discussed earlier.

Despite the improvement obtained through the use of the delay line, one question remained. The path by which the cover gas reaches the RCGM is long and complicated; it includes vapor and aerosol traps whose volumes are large relative to the flow rate of the sample stream. Is it possible that the surges in counting rate might arise from an erratic flow path through one or both traps? A momentary straight-through path would bring much fresher gas (and consequently a higher ^{23}Ne activity) to the counter than would a meandering path.

To investigate this possibility, an unfiltered sample line with minimum volume was installed directly from the reactor to the counter. The age of the gas from this line is estimated as 25 sec. Figure I.E.40 compares the equilibrium spectrum with those obtained during a ramp while the line was in use. This leaves no doubt that the surges in counting rate

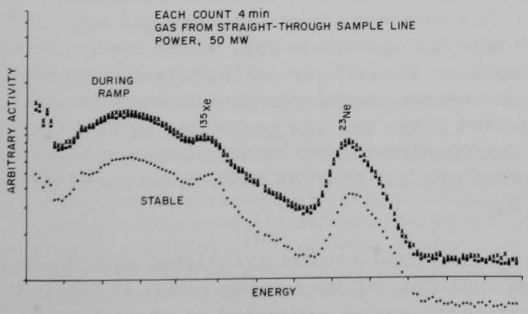

Fig. I.E.40

Spectra of Fresh Gas (~25 sec old) under Stable and Ramp Conditions. This demonstrates conclusively that the surges occur in the reactor, not in the sampling system.

do originate in the reactor and not in the sampling system. As expected, the counting rate associated with ^{23}Ne is greatly increased relative to that for fission products (compare Fig. I.E.40 with Figs. I.E.35 and I.E.36). Note also that the resolution in Figs. I.E.40 is severely degraded, thus indicating that the very fresh gas obtained through the straight-through sample line contains a significant quantity of short-lived fission products not counted when the gas sample is obtained through the regular sample line.

The straight-through sample line has a very short life expectancy because it will inevitably plug with deposited sodium. The line is used only intermittently for brief experimental runs, and it will be removed at the end of this investigation.

It is concluded as a result of these studies that the RCGM, when the delay line is used to increase the sample age to about 4 min, does in fact give a reliable indication of the ^{135}Xe level in the cover gas. The indications for ^{133}Xe and ^{85m}Kr are only qualitative, since the resolution of the sodium iodide crystal is insufficient to reduce adequately the Compton interference from higher-energy lines.

For purposes of operational monitoring, it should be acceptable to increase the travel time of the gas from about 3 to about 4 min. Although this change is in the wrong direction from the standpoint of a prompt alarm, it is relatively small and does increase the reliability of the RCGM.

An analogous but much more sophisticated cover-gas monitoring system based on a high-resolution lithium-drifted germanium detector--designated as the germanium-lithium argon-scanning system (GLASS)--has been designed. The resolution of the detector will be better than that of the RCGM by more than an order of magnitude. Such resolution permits not only cleaner measurement of the isotopes now being counted, but also useful detection of other isotopes.

Figure I.E.41 shows a grab-sample spectrum taken with a detector of the type proposed. The data were taken between gas ages of 300 and 700 min. Comparison with the spectra in Fig. I.E.34 makes obvious the great improvement in resolution. Clearly, an on-line spectrum obtained with a germanium detector would contain numerous gamma lines from short-lived isotopes that are not detected at the gas age pertaining to Fig. I.E.41. It is hoped that the additional information content of the on-line spectra will permit "fingerprinting" of fission-product sources, both in terms of fissionable material and irradiation age.

Following are some numerical results associated with the work just described. From experimental Run 3 (lower curve in Fig. I.E.35), the ^{23}Ne activity in the RCGM counting volume is estimated as about $1.5 \times 10^{-3}\ \mu Ci/cm^3$. This is based on an equilibrium level of $3 \times 10^{-3}\ \mu Ci/cm^3$

for ^{135}Xe at 50 MW. From this and the transit time, the ^{23}Ne activity in the reactor cover gas is calculated to be approximately 33×10^{-3} $\mu Ci/cm^3$. A similar estimate based on experimental Run 12 (lower curve in Fig. I.E.40) yields 26×10^{-3} $\mu Ci/cm^3$. This is excellent agreement considering the quality of the data available.

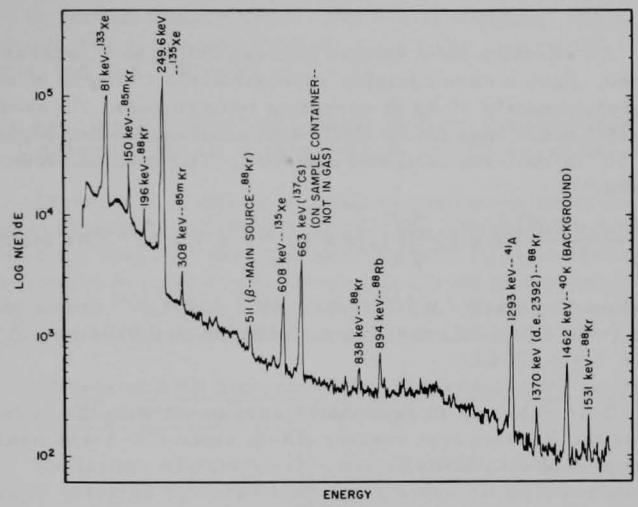

Fig. I.E.41. Cover-gas Spectrum Taken with a Lithium-drifted Germanium Detector. Median gas age was 500 min.

Based on the foregoing numbers (which are for gas at NTP), assume a "round number" ^{23}Ne level of 3×10^{-2} $\mu Ci/cm^3$ in the reactor.* The geometric gas volume in the tank is estimated as 1.85×10^7 cm^3, but this volume contains only about 0.90×10^7 cm^3 of NTP gas. The total number of disintegrations (^{23}Ne) per second in the tank is

$$(0.90 \times 10^7)(3 \times 10^{-2})(3.7 \times 10^4) \cong 1.0 \times 10^{10} \text{ dis/sec.}$$

Ne-23 is generated in the reaction $^{23}Na(n,p)$ by neutrons having energies in excess of ~4 MeV. The core configuration for reactor run 27 was assumed to be reasonably representative; calculations indicated that

*The EBR-II bare-pin experiments furnish data for some useful comparisons. In the most recent of those experiments (November 1968), it was found that an unclad Mark-IA fuel pin, when irradiated in Row 5, contributed fission products amounting to four times the tramp background. Specifically, a bare pin in that position at a reactor power of 50 MW contributes roughly 1.2×10^{-2} $\mu Ci/cm^3$ to the cover-gas activity for each of the xenon isotopes ^{133}Xe and ^{135}Xe. In terms of total production, the fission-product xenon input to the primary system was about 1.1×10^{10} atoms/sec for each of these isotopes. In comparison, the ^{23}Ne production (7×10^{14} atoms/sec) is very high and therefore could be expected to constitute a troublesome background when monitoring noble-gas fission products.

approximately 3% of the flux fell in the uppermost energy group. By assuming, that the flux in this group has the shape of the fission tail, the effective group cross section was calculated to be 11.5 mb from data given in BNL-325. Since the quality of available cross-section and spectral data is questionable, errors in the cross section may be as large as a factor of 2 or more.

An effective core volume corresponding to 91 subassemblies was assumed. Such a core contains approximately 45 liters of sodium weighing approximately 38 kg at operating temperature. An average core flux of 2×10^{15} n/cm^2-sec (at 50 MW), with a corresponding high-energy flux of 6×10^{13} n/cm^2-sec also was assumed. The overall production rate of ^{23}Ne is thus

$$\left(6 \times 10^{13}\right)\left(\frac{3.8 \times 10^4}{23}\right)\left(6 \times 10^{23}\right)\left(11.5 \times 10^{-27}\right) = 7 \times 10^{14}\ {}^{23}\text{Ne atoms/sec.}$$

At equilibrium there are $7 \times 10^{14}/1.82 \times 10^{-2} \cong 4 \times 10^{16}$ atoms of ^{23}Ne in the coolant, or (with a half-life for ^{23}Ne of $0.693/38 = 0.0182\ \text{sec}^{-1}$) $7 \times 10^{14}/3.7 \times 10^{10} = 1.9 \times 10^4$ Ci.

This result is in reasonable agreement with the "over 1000 Ci" reported for the Russian fast reactor BR-5, since BR-5 was operated at 5 MW versus 50 MW in EBR-II.

10. Physics Mock-up Studies

Last Reported: ANL-7669, p. 91 (Feb 1970).

(Experimental results for the ZPR-3 assemblies discussed here are reported in Sect. I.A.3.)

a. Calculated k_{eff} Values for ZPR-3 Assembly 60 (D. Meneghetti and K. E. Phillips)

Table I.E.31 compares the k_{eff} values for ZPR-3 Assembly 60 (the homogeneous-core EBR-II mockup having a depleted-uranium radial reflector)

TABLE I.E.31. Calculated k_{eff} Values for ZPR-3 Assembly 60

Set	Number of Groups	k_{eff}[a]
BENDF	26	1.024
238	22	1.011
23806	6	1.011

[a]Not corrected for thin-plate heterogeneity

calculated with three multigroup cross-section sets: (1) BENDF, a 26-group ENDF/B-based set; (2) the 22-group set 238, dating before ENDF/B; and (3) the 6-group set 23806 collapsed from the 22-group set. Both the 22-group and the 6-group sets frequently have been used in EBR-II studies. The two-dimensional transport code DOT was used in the S_2 approximation in RZ geometry. The dimensions and composition correspond essentially to those of the critical experiment. The quasi-hexagonal radial outline was approximated by an equal circular area. The k_{eff} values listed in the table correspond to a ^{235}U mass of 222 kg.

b. Fine-energy-detailed Central Neutron Spectrum for ZPR-3 Assembly 60 (D. Meneghetti, D. Stenstrom, and K. E. Phillips)

Figure I.E.42 shows the fundamental-mode neutron-flux spectrum for the core composition of ZPR-3 Assembly 60. The calculation of the spectrum was based on the ENDF/B data and used the MC^2 flux-generating code. The peaks and troughs are due to resonance-scattering properties of the sodium, the oxygen, and the stainless steel components. The flux spectrum near the center of the assembly should be essentially the same.

c. Effects of ZPR Slab-geometry Heterogeneities on Parallel Leakage of Neutrons (D. Meneghetti and K. E. Phillips)

Variations of neutron flux within a ZPR critical-assembly drawer are generally obtained by one-dimensional slab-cell calculations. The spatial variations then are used to obtain spatially averaged cross sections by flux weighting. Cell calculations for simulation of the gross effects of fine structure within a system having overall nonzero buckling in a direction parallel to the thin plates have been performed, and their results have been compared with the gross parallel leakages obtained from direct two-dimensional calculations. The latter calculations are for infinitely high layers of disk-shaped binary cells 50 cm in diameter.

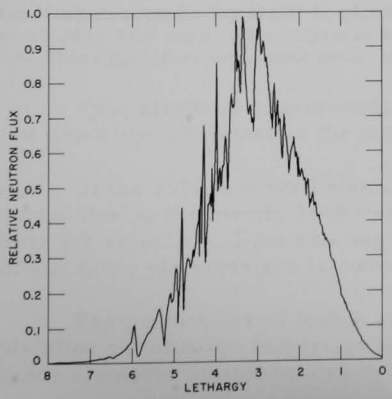

Fig. I.E.42

Fundamental-mode Neutrons Spectrum for ZPR-3 Assembly 60, the EBR-II Type Critical (Calculated by MC^2 Code, using ENDF/B Data)

One-group, applied-source calculations were used in the slab-cell calculations. The single-group cross sections for transport and removal corresponded approximately to those of neutrons above 1.35 MeV in a fuel-plate region and an intervening sodium region. These regions are 0.64 cm and 4.48 cm thick, respectively, and are referred to as heavy material (HM) and light material (LM), respectively. Calculations were also carried out with progressive increases of the density of the heavy material by factors of 2, 4, and 8 to strongly depress parallel leakage out of the heavy regions relative to the light regions. Table I.E.32 compares the overall parallel leakages as obtained by direct calculation with those obtained by cell flux-weighting of cross sections, considering the flat applied source in heavy regions and in light regions separately.

TABLE I.E.32. Parallel Leakages in Thin-cell Plate Arrays

Case	Heavy-material Density Factor			
	1	2	4	8
Exact Heterogeneous (source in light material)	0.375	0.304	0.232	0.179
Homogeneous Simulation of Above	0.374	0.301	0.225	0.166
Exact Homogeneous	0.368	0.287	0.196	0.119
Exact Heterogeneous (source in heavy material)	0.354	0.270	0.180	0.107
Homogeneous Simulation of Above	0.354	0.268	0.177	0.104

It is seen that spatial flux-weighting of cross sections in a cell generally results in leakages that are closely similar to the corresponding direct heterogeneous leakages. Deviations are noted, however, with the fictional increase of heavy-material density if the applied source is located in the light material.

F. EBR-II--Fuel Fabrication

1. Cold Line Operations (D. L. Mitchell)

Last Reported: ANL-7669, pp. 92-93 (Feb 1970).

The cold line is continuing to fabricate nonirradiated subassemblies and to impact bond the unbonded vendor-fabricated elements on hand. The production equipment for postbonding reclamation heat treatment of vendor-fabricated elements is being tested. Table I.F.1 summarizes the production activities for February 16, 1970, through March 15, 1970, and for 1970 to date.

TABLE I.F.1. Production Summary for FCF Cold Line

	2/16/70 through 3/15/70	Totals for 1970
	Mark-IA Fuel	Mark-IA Fuel
Subassemblies Fabricated		
With cold-line elements	4	16
With vendor elements	0	0
Preirradiation Treatment of Vendor Fuel		
Impact bonding of unbonded elements (11,853[a])		
Impact bonded, inspected, and accepted	1,488	5,697[b]
Impact bonded, inspected, and rejected	88	369[b]
Total Elements Available for Subassembly Fabrication as of 3/15/70		
Cold-line fuel: Mark IA	666	
Mark II	234	
Vendor fuel (Mark IA)	22,665[c]	

[a]This is the total number of unbonded vendor fuel elements scheduled for impact bonding by ANL. All unbonded elements have been received at ANL. Ten of them have been set aside as historical samples.

[b]Total includes figures for 1969.

[c]Accepted by FCF verification inspection but not yet approved for general use in the reactor. This figure does not include vendor elements that were impact bonded by ANL.

Four Mark-IA subassemblies containing fuel elements made in the cold line were fabricated in the cold line during the month.

Of the 1576 unbonded elements that were impact bonded and inspected during the month, 1488 were accepted. Void size was the primary cause for rejection. Data relating to receipt, impact bonding, and acceptance of these elements are included in Table I.F.1.

The number (as of March 15) of vendor-fabricated elements available after verification inspection is 22,665. This figure does not include vendor elements impact bonded by ANL.

As reported in ANL-7669, depleted-uranium Mark-I elements were used to test the production equipment and a heat-treatment procedure for reclaiming centrifugally bonded vendor-fabricated fuel elements. For this test, the elements were heated at 660°C for 1/2 hr, air quenched to room temperature, heated again at 500°C for 1/2 hr, and finally air quenched again to room temperature. The eddy-current traces of the heat-treated elements have been compared with those taken of the same elements before heat treatment and evaluated as to bond condition. The rejection of an element for size of voids in the bonds was based on the definition in Revision 6 of Specification FCF-1: Product Specification for the EBR-II Driver Fuel Elements. Of the 100 elements tested, 82 were "accept" elements and 18 "reject" elements before heat treatment. After heat treatment, 80 elements were considered accept elements and 20 were reject elements. Fourteen elements which had acceptable void sizes before heat treatment became reject elements after heat treatment, and 12 which were initially considered rejects because of void size became accept elements. Six elements which were initially rejected because of void size remained reject elements.

The test results indicate that the two-step heat treatment could be done in the production furnace and that about 80% of the heat-treated elements would be accept elements. The heat-treated reject elements may be reclaimable by impact bonding.

During the month, as-fabricated vendor fuel elements were heat treated (using the treatment described above) in two tests. The elements from the first test are being examined to determine if the treatment is oxidizing the cladding and transforming the fuel alloy to the alpha phase with random orientation. The elements (20) in the second test were those that had been accepted by FCF verification inspection but not yet approved for general use in the reactor. After heat treatment, the sodium-bond traces of these elements showed that 75% of them were accept elements. The remaining elements were reject elements on the basis of Revision 6, FCF-1; however, they may be acceptable on the basis of Revision 7 of this specification, which was recently approved and which allows acceptance of larger void sizes than does Revision 6. (The sodium-bond testers may have to be modified to allow testing of elements per Revision 7 of FCF-1. This is being investigated.) If the reject elements are found not to be acceptable on the basis of Revision 7, reclaiming them by impact bonding will be tried.

G. EBR-II--Operations

1. Reactor Plant (G. E. Deegan)

Last Reported: ANL-7669, pp. 93-94 (Feb 1970).

During the period from February 21 through March 20, the reactor was operated for 1137 MWd in Runs 40B and 41A. The accumulated total of EBR-II operation is 33,498 MWd.

Run 40B, which began February 10 and ended March 1, constituted the largest number of megawatt-days (924) yet accumulated by the reactor without a scram. At the end of the run, a test of the evacuation procedures was performed to check their adequacy. Test results were satisfactory, but are being evaluated further to determine possible revisions of the existing procedures.

Fuel handling for Run 41A was completed, and scheduled periodic maintenance was performed. The reactor was started up on March 5, and low-power physics measurements were made. Fifty-megawatt operation was resumed the following day. A brief power reduction was required on March 11 to change the Variac in the secondary-pump control system. On March 15, a scram was caused by a transient in the 138-kV site grid. Reactor power was returned to 50 MWt, and operation continued.

Fuel handling during this period consisted of the loading changes for Run 41A. These changes involved experimental subassemblies (as reported in Sect. I.E.4.a) as well as the following special subassemblies. Three Mark-II fuel-surveillance subassemblies had reached their approved burnup limits and were removed from the grid. One of these will be examined and the other two held in the basket for future irradiation. One vendor-fuel subassembly that had been examined previously and reconstituted completed its planned irradiation and was removed from the grid. One inner-blanket depleted-uranium surveillance subassembly also completed its scheduled burnup and was removed.

One previously irradiated controlled-flow subassembly was reinstalled in the grid for additional irradiation during Run 41A. Six driver subassemblies containing temperature monitors were included among the driver subassemblies installed. The lower-leaky-weld-test subassembly was relocated from Row 1 to Row 5, and a fresh antimony oxide source was installed in a storage thimble.

The EBR-II plant factor for the first quarter of 1970 was 75.3%. This is the highest it has been for any quarter since EBR-II began operation.

2. Fuel Cycle Facility (M. J. Feldman)

a. Surveillance (M. J. Feldman, J. P. Bacca, and E. R. Ebersole)

Last Reported: ANL-7669, pp. 94-95 (Feb 1970).

(i) Postirradiation Analysis of EBR-II Fuel (J. P. Bacca)

(a) Surveillance of Vendor-produced Fuel (A. K. Chakraborty and G. C. McClellan)

(1) Fuel-characterization Studies

(A) Subassembly C-2261. Thirty-one elements from driver subassembly C-2261, which contained 85 fuel elements cast by

the vendor and impact bonded by ANL as well as 6 cold-line elements, were examined after the subassembly had attained a calculated maximum burnup of 0.85 at. % at the end of Run 39. This subassembly is the first of eight (including one controlled-flow subassembly) containing fuel cast by the vendor and impact bonded by ANL which are to be examined following scheduled irradiation so as to qualify the fuel for standard use in the reactor. None of the 31 elements examined showed any axial shortening of the fuel as a result of irradiation. Table I.G.1 summarizes the results of postirradiation examination of those elements. The fuel swelling indicated compares favorably with that observed in the past for ANL-produced Mark-IA fuel after comparable burnup.

TABLE I.G.1. Fabrication and Irradiation Data for Vendor-fuel-qualification Subassembly C-2261[a]

(Calculated Burnup: 0.85 at. % max)

Injection-casting Batch No.	Silicon Content of Fuel (ppm)	Number of Elements	Element Burnup Range (at. %)	Total Volume Fuel Swelling ($\Delta V/V$, %) Average	Range
		Vendor Fuel			
AG 553	560	2	0.80-0.82	3.2	3.2-3.2
AG 559	560	8	0.79-0.85	3.1	2.7-3.4
AG 563	540	10	0.78-0.85	3.1	2.2-3.7
AG 578	450	5	0.79-0.82	2.8	2.6-3.1
AG 584	480	5	0.82-0.84	3.1	2.5-3.8
		ANL Cold-line Fuel			
155 II	388	1	0.79	2.2	-

[a]Contained 85 fuel elements cast by vendor and impact bonded by ANL as well as 6 ANL-produced elements.

(B) Subassembly C-2262. Thirty-two elements from this driver subassembly, which contained 30 vendor-produced elements that had been heat treated at 500°C for one hour prior to centrifugal bonding as well as 61 cold-line elements, were examined. These elements had attained an accumulated burnup of 1.2 at. % at the end of Run 39. The elements previously had been irradiated to 0.35 at. % burnup in Subassembly C-2209. None of the 30 vendor elements and neither of the 2 cold-line elements examined showed any axial shortening. The fuel swelling observed is consistent with that shown in the past for ANL-produced elements. Table I.G.2 summarizes the results of the postirradiation examination of these elements.

TABLE I.G.2. Fabrication and Irradiation Data for Vendor-fuel Driver Subassembly C-2262[a]

(Calculated Accumulated Burnup: 1.20 at. % max)

Injection-casting Batch No.	Silicon Content of Fuel (ppm)	Number of Elements	Element Burnup Range (at. %)	Total Volume Fuel Swelling ($\Delta V/V$, %) Average	Range
		Vendor Fuel			
AG 615	500	10	1.11-1.18	4.5	3.1-5.9
AG 616	420	10	1.10-1.19	5.3	3.8-6.3
AG 620	470	10	1.11-1.19	4.1	1.4-5.0
		ANL Cold-line Fuel			
119 IH	486	1	1.18	5.3	-
122 IH	419	1	1.18	5.0	-

[a]Contained 30 vendor-cast fuel elements subjected to heat treatment for 1 hr at 500°C prior to centrifugal bonding as well as 61 ANL cold-line fuel elements. All elements had been irradiated previously to 0.35 at. % burnup in Subassembly C-2209.

(b) Postirradiation Surveillance (A. K. Chakraborty and G. C. McClellan)

(1) 70%-enriched Driver-fuel Experiments. Sixty-eight of the seventy 70%-enriched fuel elements in reconstituted driver subassembly C-2213S were examined after the subassembly had attained a calculated accumulated maximum burnup of 1.99 at. % at the end of Run 39B. The two elements that were not examined had unreadable sodium levels because of sodium trapped in their upper-plenum regions. All 70 of the 70%-enriched elements in the subassembly had been irradiated previously in Subassemblies C-2175S and C-2193S.

Fuel-swelling data for these elements, summarized in Table I.G.3, are consistent with fuel-swelling rates observed for earlier 70%-enriched experiments at lower burnups.

Measurements of the diameters of 12 of the elements showed increases in cladding diameters which were well within those values to be expected as a result of swelling of the stainless steel cladding

alone (as calculated from the PNL swelling equation*). Eddy-current bond testing showed that there was considerable pin-to-jacket contact in most of the elements.

TABLE I.G.3. Fabrication and Irradiation Data for 70%-enriched Fuel Elements from Fuel Subassembly C-2213S[a]

(Calculated Accumulated Burnup: 1.99 at. % max)

Injection-casting Batch No.	Silicon Content of Fuel (ppm)	Number of Elements	Element Burnup Range (at. %)	Total Volume Fuel Swelling ($\Delta V/V$, %)	
				Average	Range
0700	260	4	1.87-1.92	16.4	16.2-16.6
0701	533	3	1.87-1.94	15.8	15.3-16.3
0702	362	7	1.83-1.97	16.4	15.9-17.0
0703	407	17	1.81-1.99	16.2	15.0-17.7
0704	409	11	1.81-1.97	15.9	13.1-17.1
0705	437	26	1.81-1.99	15.2	11.8-16.9

[a]These elements had been in Subassembly C-2175S (initial burnup of 1.23 at. %) and then in Subassembly C-2193S (additional burnup of 0.31 at. %) before being reconstituted into Subassembly C-2213S.

(2) Product-analysis Surveillance of Driver Fuel
(A. K. Chakraborty and G. C. McClellan)

(A) Subassembly C-2176. The contents of this driver subassembly were examined after the subassembly had attained a calculated maximum burnup of 1.71 at. % at the end of Run 39. The subassembly contained ANL-produced Mark-IA (52% enriched) fuel elements. Table I.G.4 summarizes the fuel swelling observed. The fuel swelling for elements from fuel batches 4295 and 4298 is consistent with that shown in the past for ANL-produced elements, but the swelling of the elements from fuel batch 4297 was higher than expected. Reanalysis of a pin from Batch 4297 showed that the silicon content was high enough (350 ppm) so as not to be responsible for the increased rate of fuel swelling. No explanation for the higher swelling can be offered at this time.

Measurements of the diameters of three elements from the subassembly showed that the diameter increases were well within those values to be expected as a result of swelling of the stainless steel cladding only.

*Claudson, T. T., Pacific Northwest Laboratories, private communication.

TABLE I.G.4. Fabrication and Irradiation Data for Driver-fuel Subassembly C-2176[a]

(Burnup: 1.71 at. % max; 1.45 at. % avg)

Injection-casting Batch No.	Silicon Content of Fuel (ppm)	Number of Elements	Element Burnup Range (at. %)	Total Volume Fuel Swelling (ΔV/V, %)	
				Average	Range
4295	500	10	1.58-1.68	7.43	6.24-8.55
4297	410 and 350[b]	16	1.58-1.64	14.81	11.24-16.73
4298	511	4	1.60-1.62	8.27	7.75-8.60

[a]Contained ANL-produced Mark-IA (52%-enriched) fuel elements.
[b]Two analyses for silicon were made for this batch.

(B) Subassembly C-2100. The contents of this subassembly, ANL-produced Mark-IA elements, were examined after the subassembly had attained a calculated maximum burnup of 1.77 at. % at the end of Run 39. Table I.G.5 summarizes the fuel swelling observed. Average swelling is at the extreme lower end of the range observed in the past for fuel irradiated to this burnup level. The one high-swelling element shown in the table was from Batch 0429, which had a low silicon content. This subassembly was in the EBR-II core for 4970 MWd during operation at 50 MWt and for 770 MWd during operation at 62.5 MWt. It is concluded that no abnormalities in the performance of the elements arose as a result of the higher-power operation of the reactor.

TABLE I.G.5. Fabrication and Irradiation Data for Subassembly C-2100[a]

(Calculated Burnup: 1.77 at. % max)

Injection-casting Batch No.	Silicon Content of Fuel (ppm)	Number of Elements	Element Burnup Range (at. %)	Total Volume Fuel Swelling (ΔV/V, %)	
				Average	Range
4222	250	1	1.69	7.1	-
4223	250	1	1.69	6.8	-
4224	350	21	1.70-1.75	7.4	6.4-8.3
4225	568	5	1.66-1.70	6.6	5.8-6.9
4226	318	2	1.67-1.67	7.2	7.1-7.3
0429	94	1	1.72	17.0	-

[a]This subassembly was in the reactor core for 4970 MWd at 50-MWt operation and for 770 MWd at 62.5-MWt operation. It contained ANL-produced Mark-IA (52%-enriched) fuel elements.

(c) Surveillance of EBR-II Depleted-uranium Radial-blanket Subassemblies (A. K. Chakraborty and G. C. McClellan)

The initial surveillance work carried out on EBR-II depleted-uranium inner-blanket (Rows 6 and 7) subassemblies is summarized in ANL-7597.* This work served to assess the performance (fuel swelling and diametral increases) of blanket elements at low burnups and provided data necessary to establish a conservative peak burnup goal of 0.27 at. % for radial-blanket subassemblies.

In later work, elements from outer-blanket (Rows 9 and 10) subassemblies were examined after a burnup of less than 0.1 at. %. Their performance was found to be in agreement with the results presented in ANL-7597. Several elements from inner- and outer-blanket subassemblies (from Rows 7 and 8) also were examined at burnup levels ranging from 0.17 to 0.26 at. %. These examinations revealed the element performance to be in agreement with that predicted by the earlier work.

Recently, elements from various irradiated blanket subassemblies were examined to compare the performance of blanket elements at 62.5-MWt operation of the EBR-II with that at 50-MWt operation or less. The results of examination of three such subassemblies are summarized here.

(1) Subassemblies A-786 and A-766. Elements from Subassembly A-786 (Row 7), which had experienced approximately 500 MWd of irradiation during 62.5-MWt operation of EBR-II, were subjected to precision diameter measurements. These measurements were then compared with those obtained for elements of comparable burnup (in the range of 0.2 to 0.26 at. %) from another subassembly, A-766 (Row 7), which had been irradiated during 50-MWt operation or less. Based on comparison of these measurements, no apparent differences in the performance of the elements could be concluded. Additional examinations, including neutron radiography and measurements of gas-plenum pressure, are planned to further evaluate the relative performance of these elements.

(2) Subassembly A-785. Blanket subassembly A-785 (Row 7) was examined following irradiation to a peak burnup of 0.30 at. % attained at the end of Run 39C. Precision diameter surveys of six elements from the subassembly indicated diameter increases ($\Delta D/D$) in the range of 0.2 to 0.6%. These increases appear to be wholly attributed to swelling of stainless steel only. The results also are very similar to those obtained for subassemblies examined earlier following a peak burnup of 0.27 at. %. The values of $\Delta D/D$ from that examination ranged from 0.2 to 0.8%.

*Eschen, V. G., Surveillance of the EBR-II Blanket Subassemblies, ANL-7597 (Sept 1969).

Five blanket subassemblies have been approved to accumulate a peak burnup of 0.30 at. % at the end of Run 41. In addition, based on the experimental data obtained to date, a request has been initiated for approval to increase the burnup limit of all blanket subassemblies to 0.30 at. %.

(d) Metallographic Examination of Encapsulated Mark-II Fuel Element 255 from Subassembly X053 (R. V. Strain)

Postirradiation surveillance examinations of this element, which had attained an accumulated burnup of ~3.6 at. %, were performed. These examinations included determination of fuel swelling as well as metallographic examination of the interface between the fuel and element cladding and of the cladding for irradiation-induced changes in microstructure. (The results of the examinations are reported under Sect. I.E.8.a.)

b. Fuel Handling and Transfer (N. R. Grant, W. L. Sales, and K. DeCoria)

Last Reported: ANL-7669, p. 95 (Feb 1970).

Table I.G.6 summarizes the fuel-handling operations performed.

c. Experimental Support (J. P. Bacca, N. R. Grant, R. V. Strain, S. T. Zegler, J. W. Rizzie, C. L. Meyers, and G. C. McClellan)

Last Reported: ANL-7669, pp. 95-97 (Feb 1970).

Subassembly X020 was received from the reactor and disassembled. This Mark-A19 irradiation subassembly contained three UNC mixed-carbide fuel capsules, nine GE mixed-oxide fuel capsules, and seven structural elements (5 PNL and 2 ANL). The UNC and GE fueled capsules had attained calculated maximum burnups of 7.1 and 6.7 at. %, respectively. The structural elements had accumulated a calculated total fluence of 5.0 x 10^{22} nvt. All capsules were weighed and visually examined; the fueled capsules were neutron radiographed, and their diameters were measured. The radiographs indicated that one carbide element had failed and that the other two also may have failed. The carbide capsules and structural elements were returned to the experimenters. The mixed-oxide capsules will be reloaded into a new subassembly.

Subassembly X065B was received from the reactor and disassembled. This Mark-B37 irradiation subassembly contained 21 helium-pressurized structural elements, 5 temperature-monitor elements, and 11 dummy elements. The pressurized elements and temperature-monitor elements had accumulated respective calculated total fluences of 0.7 x 10^{22} and 0.3 x 10^{22} nvt. The diameters of all the pressurized elements were measured, and gross gamma scans were made of six of them. The

temperature-monitor elements will be dismantled later. The pressurized elements and dummy elements will be reassembled into Subassembly X065C. (The results of the diameter measurements are reported under Sect. I.E.8.b.)

TABLE I.G.6. Summary of FCF Fuel Handling

	2/16/70 through 3/15/70	Totals for CY 1970
Subassembly Handling		
Subassemblies received from reactor		
Driver fuel (all types)	15	25
Experimental	2	2
Other (blanket)	0	1
Subassemblies dismantled for surveillance, examination, or shipment to experimenter		
Driver fuel	7	10
Experimental	2	2
Other (blanket)	0	1
Driver-fuel elements to surveillance	339	431
Number of subassemblies from which taken	7	10
Subassemblies transferred to reactor		
Driver fuel		
From air cell	0	2
From cold line[a]	9	19
Experimental	1	5
Fuel-alloy and Waste Shipments[b]		
Cans to burial ground	1	1
Skull oxide and glass scrap to ICPP	0	0
Recoverable fuel alloy to ICPP		
Fuel elements	0	4 (69.75 kg of alloy)
Subassemblies	7 (37.10 kg of alloy)	14 (75.23 kg of alloy)
Nonspecification material	0	0

[a]Cold-line subassemblies, following fabrication and final tests, are transferred either to the reactor or to the special-materials vaults for interim storage until needed for use in the reactor.

[b]Figure outside parentheses is number of shipments made. Figure inside parentheses is weight of alloy shipped.

Subassembly X077, a Mark-B7A irradiation subassembly, was assembled with three unirradiated structural elements (one PNL and two ORNL) and four dummy elements.

Subassembly X042B, a Mark-B7 irradiation subassembly, was assembled in the air cell with five previously irradiated (calculated total fluence of 2.1×10^{22} nvt) and two unirradiated structural elements containing boron carbide and tantalum samples (all PNL).

PUBLICATIONS

The Manufacture of Vibratorily Compacted Fuel Elements for Doppler-coefficient Measurements
J. E. Ayer, C. F. Konicek, F. E. Soppet, and E. J. Petkus
ANL-7647 (Jan 1970)

Low-Flux Measurements of ^{239}Pu and ^{235}U Capture-to-Fission Ratios in a Fast Reactor Spectrum
M. M. Bretscher and W. C. Redman
Nucl. Sci. Eng. 39, 368-378 (March 1970)

Operating Experience with the EBR-II Rotating-Plug Freeze Seals
L. P. Cooper, B. C. Cerutti, and D. W. Cissel
ANL-7617 (Dec 1969)

An Analysis of the Neutron Capture Cross Section of U^{238} between 1 keV and 15 MeV
W. G. Davey
Nucl. Sci. Eng. 39, 337-360 (March 1970)

Development of Fission Gas Pressure Transducers at Argonne National Laboratory
J. R. Folkrod
Proc. Nat. Symp. on Developments in Irradiation Testing Technology, Sandusky, Ohio, September 9-11, 1969. USAEC Publ. CONF-690910, pp. 267-280

Instrumented-Subassembly System and In-Core Instrument Test Facility for EBR-II
E. Hutter, O. S. Seim, and A. Smaardyk
Proc. Nat. Symp. on Developments in Irradiation Testing Technology, Sandusky, Ohio, September 9-11, 1969. USAEC Publ. CONF-690910, pp. 71-102

EBR-II as a Fast Reactor Irradiation Facility
Frederick S. Kirn
Nucl. News 13(3), 62-68 (March 1970)

Fission Cross-Section Ratio Measurements of ^{239}Pu and ^{233}U to ^{235}U from 0.24 to 24 keV
W. K. Lehto
Nucl. Sci. Eng. 39, 361-367 (March 1970)

Characterization of Advanced Irradiation Testing Vehicles for EBR-II
O. S. Seim, W. R. Ware, and E. Hutter
Proc. Nat. Symp. on Developments in Irradiation Testing Technology, Sandusky, Ohio, September 9-11, 1969. USAEC Publ. CONF-690910, pp. 103-117

Recent Operating Experience with EBR-II
R. R. Smith, R. A. Cushman, R. W. Hyndman, F. S. Kirn, J. K. Long, W. B. Loewenstein, J. T. Madell, T. R. Bump, and P. J. Persiani
The Physics of Fast Reactor Operation and Design, Proc. Int. Conf., London, June 24-26, 1969. British Nuclear Energy Soc., London, 1969, pp. 354-361

Exposed-fuel Calibration Study in EBR-II, Second Series
R. R. Smith, C. B. Doe, and E. R. Ebersole
ANL-7558 (Jan 1970)

Xenon Tagging of Instrumented Fuel Capsules for Use in EBR-II
D. E. Walker, P. J. Halfman, and J. H. Sanecki
Proc. Nat. Symp. on Developments in Irradiation Testing Technology, Sandusky, Ohio, September 9-11, 1969. USAEC Publ. CONF-690910, pp. 59-70

Evaluation of Potential Tube Vibration in EBR-II Steam Superheaters and Evaporators at Full Power
M. W. Wambsganss, Jr.
ANL-7600 (Nov 1969)

II. OTHER FAST REACTORS--OTHER FAST BREEDER REACTORS--FUEL DEVELOPMENT

A. Irradiation Effects, Mechanical Properties and Fabrication

1. Neutron Simulation Experiments by Ion Bombardment (A. Taylor)

Not previously reported.

Preparations are being made to expose samples of stainless steel to ion bombardment in the Dynamitron accelerator. The objective is the simulation of high-fluence, fast-neutron effects on a reduced time scale. Specifically, the effects of materials variables on void formation will be examined.

The basic components for the target chamber and specimen holder have been designed; about one-half have been fabricated and are being tested. The scattering chamber will be ready for installation in the Dynamitron target room by the end of March. Associated electronics and remote monitoring equipment will also be ready for installation at this time. Bench testing of the metal-ion source is in progress, and the equipment to carry out bench and pressure tests has been constructed.

2. Mechanical Properties of Cladding Materials (F. L. Yaggee)

Last Reported: ANL-7669, p. 99 (Feb 1970).

The first creep test to be conducted in the new apparatus was terminated after 440 hr at 550°C and a stress of 25,000 psi. The test was conducted in the absence of cyclotron radiation. The experimental creep curve is shown in Fig. II.A.1. Under these test conditions, the steady-state creep rate ($\dot{\varepsilon}_s$) is established after 50 hr at 2.3% total strain and persists for 350 hr to 3.6% total strain, at which point tertiary creep begins. The measured minimum creep rate is 3.7×10^{-5} hr^{-1}, and the total specimen strain is about 4.2%.

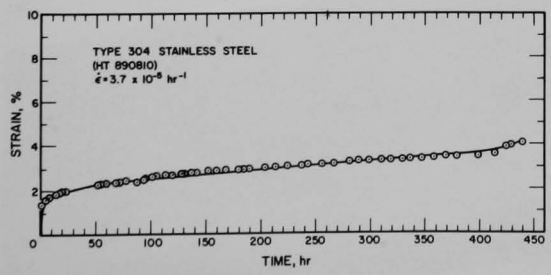

Fig. II.A.1

Creep Curve for Type 304 Stainless Steel Tested at 500°C and a Stress of 25,000 psi

The creep specimen is shown in Fig. II.A.2, before and after testing. All of the recorded strain occurred in the gauge length (1.0 in. long by 0.1997 in. wide by 0.0073 in. thick). The pinholes showed no distortion after testing. The specimen will be examined by electron microscopy to study void density as a function of specimen strain.

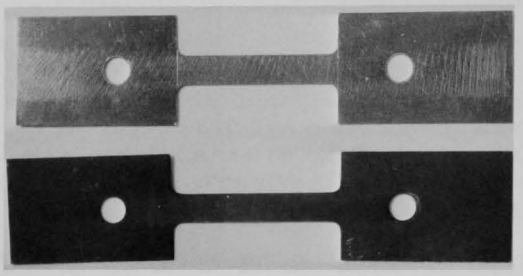

Fig. II.A.2

Type 304 Stainless Steel Sheet Specimen To Be Used in Cyclotron Creep Studies. Top, specimen before testing; bottom, specimen after 4.2% total strain at 550°C and stress of 25,000 psi. Mag. ~1X.

3. Surface Defects as Failure Sites in Type 304 Seamless Stainless Steel Fuel-clad Tubing (F. L. Yaggee)

Last Reported: ANL-7669, pp. 99-100 (Feb 1970).

Biaxial creep tests of artificially defected, thin-wall, Type 304 stainless steel tubes have continued at 650°C and hoop stresses of 7500, 10,000, and 15,000 psi. A pinhole leak was detected in specimen 1AD90 after 200 hr at 15,000 psi. The artificial defect on this specimen is located on the outside surface at midlength, oriented 90° to the longitudinal axis. This defect orientation is considered to have no effect on the straining characteristics of the specimen. The pinhole leak is located near the bottom of the specimen at a point where the diametral strain is 13.8%. A close-up of the specimen surface in the vincinity of the leak is shown in Fig. II.A.3. The leaking specimen will be sectioned by electrical-discharge machining, and examined by optical and electron microscopy.

Fig. II.A.3

Surface Appearance of Type 304 Stainless Steel Tube Specimen in Vicinity of a Pinhole Leak. Mag. ~7X.

Biaxial creep tests of specimens at 7500 and 10,000 psi hoop stress have continued to 700 hr, and the average diametral strains are about 0.7 and 1.3%, respectively.

PUBLICATION

A Method for Reconstructing a Thermal-expansion Graph from Two Values of the Mean Expansion Coefficient
Frank L. Yaggee and Frank G. Foote
ANL-7644 (Dec 1969)

III. GENERAL REACTOR TECHNOLOGY

A. Applied and Reactor Physics Development

1. Theoretical Reactor Physics--Research and Development

a. Theoretical Reactor Physics

(i) Reactor Computation and Code Development (B. J. Toppel)

Last Reported: ANL-7669, pp. 101-104 (Feb 1970).

(a) Reactor Computations (P. H. Kier)

To assess the magnitude of errors introduced into MC^2,* computations of resonance cross sections by the narrow-resonance approximation, MC^2, and RABBLE** utilizing fine-group (1/4 lethargy unit wide) cross sections for Pu-239 and U-238 have been compared. The cell was assumed to be a homogeneous mixture of carbon, U-238, and Pu-239 with atom densities in the respective ratio of 25:5:1. The energy range covered was 2.6 to 300 eV. In the RABBLE computation, the closest ten resonances contribute to the cross sections at each energy point.

The results of the calculations are summarized in Table III.A.1. For Pu-239, there is fairly close agreement between the MC^2 and RABBLE results, with RABBLE yielding cross sections that are

Table III.A.1. Comparison of Fine-group Resonance Cross Sections Computed by MC^2 and RABBLE for a Homogeneous Mixture of C:^{238}U:^{239}Pu = 25:5:1 between 300 and 2.60 eV

	Lower Energy (eV)	σ_a^{28}		σ_a^{49}		σ_f^{49}		Σ_a		Σ_f		Important U Resonances
		MC^2	R	MC^2	R	MC^2	R	MC^2	R	MC^2	R	
1	233.64	1.3885	1.4128	19.867	19.336	12.579	12.069	0.04289	0.04224	0.02013	0.01931	
2	181.96	1.2328	1.5604	16.492	15.515	11.448	10.450	0.03625	0.03731	0.01832	0.01672	189.6
3	141.71	0.8629	0.8581	19.341	19.000	11.037	10.682	0.03785	0.03726	0.01766	0.01709	
4	110.36	1.0555	1.1052	22.606	22.500	15.567	15.350	0.04461	0.04484	0.02491	0.02456	
5	85.95	1.7990	2.5283	24.024	23.214	19.456	18.095	0.05283	0.05737	0.03113	0.02895	102.7
6	66.94	1.6404	1.6123	27.500	25.819	20.940	19.751	0.05712	0.05421	0.03350	0.03160	
7	52.13	2.5432	4.1623	80.954	80.132	61.678	60.981	0.14987	0.16151	0.09868	0.09757	66.3
8	40.60	0.2278	0.1558	37.015	35.287	13.878	12.488	0.06105	0.05771	0.02220	0.01998	
9	31.62	6.3940	8.9392	8.1155	5.9592	4.0695	2.6730	0.06414	0.08105	0.00651	0.00428	36.7
10	24.62	0.4216	0.3806	13.446	12.521	6.0949	5.4203	0.02489	0.02308	0.00975	0.00867	
11	19.17	10.474	9.9988	37.081	42.480	23.348	26.416	0.14312	0.14796	0.03735	0.04227	21.0
12	14.94	0.7972	0.7621	52.893	47.775	38.371	33.940	0.09101	0.08254	0.06139	0.05430	
13	11.63	0.2603	0.1997	86.419	84.938	43.485	43.187	0.14035	0.13750	0.06957	0.06910	
14	9.06	0.6737	0.5538	75.555	72.427	60.144	57.406	0.12628	0.12031	0.09623	0.09185	
15	7.06	3.4897	3.1235	58.270	50.142	30.742	26.416	0.12115	0.10521	0.04918	0.04227	
16	5.49	27.983	40.581	4.7689	4.9034	3.2421	3.1306	0.23149	0.33249	0.00519	0.00501	6.67
17	4.28	1.6340	1.5572	3.6710	3.0718	2.7544	2.2484	0.01895	0.01737	0.00441	0.00360	
18	3.33	0.7349	0.6102	4.1745	3.5010	3.2481	2.6800	0.01256	0.01048	0.00520	0.00429	
19	2.60	0.5431	0.4054	5.5498	4.7693	4.3708	3.7129	0.01322	0.01087	0.00699	0.00594	

*Toppel, B. J., et al., ANL-7318 (June 1967).

**Kier, P. H., and Robba, A. A., ANL-7326 (April 1967).

generally a few percent smaller. For U-238, however, there are large discrepancies between MC^2 and RABBLE results for those groups which contain large uranium resonances, except for the group containing the 21-eV resonance. These large discrepancies can be mainly attributed to the narrow-resonance approximation used in MC^2. For this cell in the energy range covered, the MC^2 computations overestimate fission and underestimate absorption, which should result in an overestimate of the multiplication constant.

In the RABBLE code, the slowing-down source was computed with the formulation developed by Olson.* A resonance escape probability of 0.00015 was reached without appearance of the instabilities that had plagued earlier versions of RABBLE. The RABBLE computation required only 94 sec, which is 10 sec less than the MC^2 computation required.

2. Nuclear Data--Research and Development

a. Cross Section Measurements (N. D. Dudey and C. E. Crouthamel)

(i) Yields of Low-mass Fission Products

Last Reported: ANL-7655, pp. 97-98 (Dec 1969).

Preparations for experiments to measure fast-neutron fission yields of tritium by a radiochemical technique are continuing. In these experiments, gram quantities of fissile material will be irradiated with monoenergetic fast neutrons produced in the Dynamitron. The irradiated samples will be hydrided and dehydrided in a radiochemical separation system in which the hydrogen isotopes (including tritium) will be separated from other volatile fission products. The tritium in the separated gas will be counted in a low-level gas-proportional counter. The number of fissions will be determined by radiochemical analysis of the fissile material for several fission-product monitors. The neutron flux will be measured by means of a fission counter.

The gas-handling system to be used for the tritium separation is nearing completion. Reaction vessels for hydriding and dehydriding both plutonium and uranium samples have been designed and constructed. The furnace and controllers have been calibrated and tested in the system. An oil-diffusion pump for vacuum transfer of the tritium to the sample collector and a silver-palladium membrane for separating the tritium from other fission products are on hand. Upon completion of the sample collector, the entire system will be assembled, tested, and then installed in a glovebox. The necessary modifications to the electrical connections in the glovebox have been made.

*Olson, A. P., RABID, An Integral Transport Theory Code for Neutron Slowing Down in Slab Cells,

Prior to the irradiations by neutrons from the Dynamitron, the entire procedure will be tested by measuring the tritium content of thermally irradiated uranium. In preparation for these tests, samples of fully enriched uranium metal (93.1% ^{235}U) have been irradiated in a thermal flux in the Juggernaut Reactor. The samples have also been counted for ^{99}Mo-^{99m}Tc, the fission products that were chosen to monitor the number of fissions that occurred in the irradiation. Upon completion of the gas-handling system, these samples will be analyzed for their tritium content and fission-yield values calculated. These data on thermal-fission yields of tritium from ^{235}U will be used to assess the capabilities of the experimental apparatus, so that any necessary modifications can be made before the experiments to measure fast-fission yields begin.

b. Burnup Analysis and Fission Yields for Fast Reactors (R. P. Larsen)

(i) Development of Analytical Procedures for Fission-product-burnup Monitors

Last Reported: ANL-7655, pp. 98-99 (Dec 1969).

The manpower normally alotted to this work has, during this reporting period, been assigned to the work described in Sect. (ii), below.

(ii) Development of a New Method for the Determination of the Absolute Fast-fission Yields of Burnup Monitors for Fast Reactor Fuels

Last Reported: ANL-7655, pp. 99-100 (Dec 1969).

A new method has been developed for the determination of the number of fissions that occur in irradiated fast-reactor fuel materials. This method is being applied to the determination of fast-fission yields. Previously, the number of fissions has been established by (1) irradiating the fissile nuclide to a burnup of 20 to 25 at. % and measuring the number of fissions by the change in the actinide-atom content or (2) irradiating the fissile nuclide to a burnup of 1 to 2 at. %, analyzing for all the fission products nuclides in the heavy mass peak, and summing the number of atoms of these nuclides.

In the new method, two irradiations are required: one of about 2-hr duration at a low reactor-power level and one of about 3-month duration at full reactor power. Included in the short irradiation are fission-track detectors (mica disks alternately stacked with platinum disks on which are mounted nanogram amounts of the fissile material) and fission foils (milligram amounts of the fissile material). These samples

provide data for establishing a factor relating the number of fissions that occurred to the count rate of a particular fission product, e.g., ^{95}Zr (65 d). The fission tracks on the mica disks are counted under a microscope; the ^{95}Zr activity of the fission foils is determined by gamma spectrometry. Included in the long irradiation are gram amounts of fissile material, which are subsequently analyzed for the fission product whose yield is being determined and for ^{95}Zr activity. The number of fissions that occurred is established from the ^{95}Zr activity and the previously determined fissions-to-^{95}Zr factor.

With the new method of determining the number of fissions, the time and effort required to measure fission yields will be reduced significantly, and fission yields can be readily measured within a reactor as a function of neutron energy. A unique advantage of the method is that measurements of yields from the fast fission of ^{238}U will be possible. (In large fast reactors fueled with $^{238}UO_2$-$^{239}PuO_2$, it is estimated that 20 to 30% of the fissions will be due to ^{238}U.)

The short calibration experiments, initially planned for EBR-II (see Progress Report for March 1969, ANL-7561, p. 67), would have required special irradiations at low reactor power (50 kW) for 1 to 2 hr. These irradiations are, instead, being conducted in the ZPR-3 mockup experiments of the EBR-II core. The first of the irradiations was carried out on Feb 26, 1970. Samples of ^{235}U, ^{238}U, and ^{239}Pu, contained in each of three irradiation packages of the type shown in Fig. III.A.1, were included. Each package contained 8 fission track detectors of each nuclide (represented by the circles in Fig. III.A.1); each row of detectors was backed with a metal foil strip (1 75 by 0.25 by 0.030 in.) of the same nuclide. The packages were located at positions in ZPR-3 that correspond to the center of the core, the core-blanket interface, and the blanket of EBR-II.

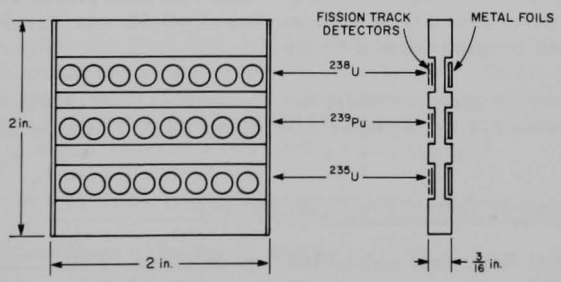

Fig. III.A.1. ZPR-3 Irradiation Package for Fission Track Detectors and Metal Foils (2 by 2 by 1/16 in. face plates not shown)

The irradiated samples were received at Argonne, Ill. on Feb. 27, 1970. Each metal strip was cut into sections corresponding to the positions of the fission track detectors, and these sections are now

being assayed by gamma spectrometry. The preliminary data have shown that there were significant differences in the fission rates of samples within a particular drawer, the largest differences occurring in the samples of ^{238}U. These data should provide useful information on the variation of fission yields and fission rates as a function of position (neutron energy and fluence) within the drawers of the reactor.

Other analytical work on the irradiated samples is proceeding. The mica fission track detectors have been etched, and preliminary examinations* have shown that all except 2 or 3 of the 72 track detectors will provide excellent data. The amount of fissile material in each fission track detector will be determined as follows: ^{239}Pu (20 to 100 ng), by alpha counting; ^{235}U (50 to 150 ng); and ^{238}U (0.3 to 10 μg), by mass-spectrometric isotopic-dilution analysis. The amount of ^{235}U, ^{238}U, or ^{239}Pu in each section of metal foil will be determined by weighing when the gamma-spectrometric assays are completed.

The measurements described above will provide the necessary data for determining the number of fissions (and, hence, the fast-fission yields of selected long-lived and stable burnup monitors) for samples that will subsequently be irradiated in EBR-II.

The gamma-spectrometric measurements of the sections of ^{235}U, ^{238}U, and ^{239}Pu foils have indicated that the experiment in ZPR-3 will provide additional information, namely, values for the fast-fission yields (as functions of neutron energy and fissioning nuclide) of certain short-lived fission products. These nuclides, which were selected on the basis of half-lives, fission yields, gamma energies, and gamma branching ratios, are as follows: ^{95}Zr (65 d), ^{97}Zr (17 hr), ^{99}Mo (67 hr), ^{103}Ru (42 d), ^{106}Ru (265 d), ^{132}Te (77 hr), ^{131}I (8 d), ^{133}I (21 hr), ^{140}Ba (13 d), ^{141}Ce (33 d), and ^{144}Ce (284 d). It is expected that relative fission yields of these nuclides can be determined with an accuracy of $\pm 0.5\%$ and absolute yields with accuracies ranging from 2 to 5%.

Erratum: In the Progress Report for December 1969 (ANL-7655, p. 100, line 10), the value for the number of fissions per 10^9 atoms of ^{239}Pu should be "337 $\pm$ 5."

c. Reactor Code Center (M. Butler)

Last Reported: ANL-7661, p. 94 (Jan 1970).

During February and March thirteen program packages were assimilated into the Code Center collection. These thirteen include seven prepared for the CDC 6600, three for the IBM 360, and one each for the UNIVAC 1108, IBM 7090, and the CDC 3600.

*The fission track detectors are being assayed by R. J. Armani of the Applied Physics Division.

Five of the CDC 6600 programs originated at Bettis Atomic Power Laboratory. These are JITER (ACC #394), a program to compute the statistical parameters measured in reactor fluctuation experiments; WASP (ACC #396), used to calculate thermodynamic properties of water and steam; GAPL3 (ACC #397), an LWBR program for the inelastic large-deflection stress analysis of a thin plate or axially symmetric shell with pressure loading and deflection restraints; BE21 (ACC #398), a few-group, slab-geometry, discrete-ordinate transport approximation; and SUMOR (ACC #399), which calculates S-wave neutron scattering and radiative-capture cross sections, including level-level interference and Doppler broadening.

The Knolls Atomic Power Laboratory submitted a revised CDC 6600 version of their LION program (ACC #299) for studies of three-dimensional temperature distributions.

Argonne National Laboratory contributed both IBM 360 and CDC 6600 versions of the SAS1A program (ACC #400). This program is used for the analysis of fast reactor power and flow transients.

RAFFLE (ACC #392) was supplied by Oak Ridge National Laboratory in two versions, one for the IBM 7090 and the other for the IBM 360. RAFFLE is a Monte Carlo code developed for the calculation of first-flight collision probabilities.

The Kansas State University CORGAM program, designed as a correlation algorithm for gamma-ray spectra and written for the IBM 360, has been incorporated as ACC #390.

Auxiliary programs PROCOP and ENDFB have been added to the UNIVAC 1108 GAND program package (ACC #345).

Supplement 3 of ANL 7411 containing program abstracts number 358 through 384 was distributed in February. In March, two programming notes were issued. The first describing update number 2 for the IBM 360 PDQ7 version (ACC #275) and the second announcing the availability of the revised CDC 6600 LION package.

B. Reactor Fuels and Materials Development

1. Fuels and Claddings--Research and Development

a. Behavior of Reactor Materials

(i) Sinter Pore Migration in UO_2 (R. O. Meyer, J. C. Voglewede, and J. E. Sanecki)

Not previously reported.

The movement in a temperature gradient of intrinsic porosity in sintered uranium dioxide is important to the behavior of fuel material. An attempt to observe such migration was made by annealing a sintered (97.3% theoretical density) uranium dioxide specimen (of 9-mm diameter and 9 mm long) in a temperature gradient of approximately 500°C/cm. The upper 7 mm of the specimen were in a cavity in an induction-heated tungsten heat conductor (see Progress Reports for November 1969, ANL-7640, pp. 96-98, and January 1970, ANL-7661, pp 94-95). The lower face of the cylindrical specimen rested on a stainless steel insert in the water-cooled copper base. The temperature was measured with an optical pyrometer over the exposed lower 2 mm of the specimen. The temperature at the cold end was about 1425°C; 2 mm higher on the specimen (where the specimen went into the tungsten cavity) the temperature was about 1525°C. The temperature of the tungsten was about 1900°C. The anneal lasted 100 hr in a vacuum of approximately 10^{-6} Torr.

The grain size of the material was 10-15 μ, and it was expected that sinter pores could be moved a significant fraction of the grain size. The pores would move toward the hot side of the grain and would be held on the grain boundary. This behavior was not found. There was no accumulation of pores on grain boundaries, and there was no apparent correlation between the position of the pores within a grain and the direction of the temperature gradient. A similar result was reported by Smith et al.[†]

In an attempt to make quantative predictions of pore migration for this specimen, a calculation of pore velocity was made by using an equation[††]

$$V_p = \frac{2\delta D_S^* Q_S^*}{rRT^2} \frac{dT}{dx},$$

which is generally believed to be true if surface diffusion dominates as the mechanism of motion. The depth of the diffusing layer, δ, was assumed to be 3 Å. The surface diffusion coefficient, D_S^*, was given by a preexponential factor of 5.6×10^7 and an activation energy of 120 kcal/mole. Of the four available literature values,[‡] only one gave a value of D* at 1525°C (1.9×10^{-8} cm^2/sec) significantly lower than the value used here (14.5×10^{-8} cm^2/sec). The Wirtz model[‡‡] for thermomigration states roughly that the heat of transport, Q*, is the difference between the energy required to initiate a jump and the energy required to prepare the landing

[†]Smith, J. T., Speidel, E. O., and Kizer, D. E., BMI-1870 (Aug 1969), p. 128.

[††]Nichols, F. A., J. Metals 21, 19 (1969).

[‡]Reynolds, G. L., J. Nucl. Mater. 24, 69 (1967); Marloe, M. O., and Kaznoff, A. I., J. Nucl. Mater. 25, 328 (1968); Henney, J., and Jones, J. W. S., J. Mat. Sci. 3, 158 (1968); Berman, R. M., WAPD-TM-843 (July 1969).

[‡‡]Shewmon, P. G., Diffusion in Solids, McGraw-Hill Book Co. Inc., New York (1963), p. 191.

site for the atom. For surface diffusion, since no lattice vacancy need be available at the landing site, Q_S^* is likely to be close to the former energy, which, in turn, approximates to the activation energy for surface diffusion. Therefore, a value of 100 kcal/mole was chosen for Q_S^*. The pore radius r was taken as 0.5 μ, which was a typical size (range of 0.3-3.5 μ) in our material. R is the gas constant.

This equation predicts a pore movement of 6.5 μ for a 1-μ-dia pore at a position 2 mm from the cold end of the specimen. This is the hottest position where the temperature was actually measured. It is obvious that the temperature in the upper portion of the specimen was higher and that large temperature gradients also would be found. For comparison, at some position where the temperature was 1625°C, instead of 1525°C, the pore movement should be 38.4 μ if all quantities except temperature are unchanged. With the likelihood of such migration distances, we expected to see some evidence of pore migration, but we did not.

Obviously, the quantities used in the equation are not accurately known, and the experimental techniques of this preliminary run can be improved.

Several interesting observations were made in the course of this work. Gross amounts of material were transported from the hot end of the specimen to cooler regions, leaving the top of the 9-mm-dia specimen almost hemispherical. This material collected on the sides of the specimen in a layer about 5 mm long. The surface of the entire upper portion of the specimen appeared metallic. Light microscopy of a cross section of the specimen showed that this transported layer was almost fully dense with only occasional porosity, and was very large grained. There was a well-defined interface (grain boundary) at the original surface of the specimen. Inclusions were found in this grain boundary. Also, inclusions were found at grain boundaries in the interior of the specimen.

Electron-beam microprobe scans across the specimen showed that metallic grains of tungsten cover the outer surface. The inclusions in the grain boundary, between the transported material and the original specimen, were also tungsten. The inclusions in the interior of the specimen contained iron. The transported material was uranium dioxide. No free uranium was found anywhere. All of this indicates that uranium dioxide moved from the hot end, probably by surface diffusion; the surfaces of the specimen picked up tungsten from the heat conductor; and the specimen was contaminated with iron, possibly from the stainless steel specimen support.

The light microscopy also showed that the grain size varied from 10 μ at the cold end to 80 μ at the hot end, and that the pore-size range varied from 0.6 to 7 μ in diameter at the cold end to a diameter of 2-12 μ at the hot end, with a corresponding decrease in pore density.

(ii) Fuel Behavior

(a) Bubble-defect Interactions (R. W. Weeks, R. O. Scattergood, and S. R. Pati)

Last Reported: ANL-7581, pp. 89-90 (June 1969).

In a continued study of interactions between bubbles and dislocations and between bubbles and grain boundaries in nuclear fuels, the effects on bubble-migration velocities due to dragging either a dislocation dipole or a trailing cylinder of grain boundary have been evaluated.*

When a bubble, migrating under the influence of a temperature gradient, becomes pinned on a dislocation or grain boundary, it need not grow to an "escape" size before continuing migration; rather, it is possible for the defect to bow out behind the bubble and then remain attached to the bubble as migration continues. When defect bowing occurs, the bubble can resume migration at a smaller size than the "critical size" usually computed for bubble breakaway from undistorted defects.** Furthermore, the initial velocity of the migrating bubble-defect configuration is reduced in comparison with the free bubble-migration velocity by approximately an order of magnitude. This "defect drag" persists until the bubble has grown about an order of magnitude in volume, whether migrating by surface diffusion, volume diffusion, or by the evaporation-condensation mechanism.

The velocities of both freely migrating bubbles and bubble-defect configurations were determined by using the best data available for UO_2 at a temperature of 2000°C and a temperature gradient of 1000°C/cm, and for UC at a temperature of 1300°C and a temperature gradient of 200°C/cm. As expected, volume diffusion plays no role in bubble migration in UO_2; the crossover point from surface diffusion to evaporation-condensation occurs at a bubble radius of ~16 μ. For UC, however, volume diffusion proves to be the dominant mechanism for bubble migration for all except the very smallest bubbles ($\lesssim$1000 Å), where surface diffusion becomes important. Migration velocities in the UC case chosen were about 7 orders of magnitude less than bubble velocities in the UO_2 case examined. This conclusion supports the evidence that less gas release may be expected from UC fuel elements than from oxide fuel elements under similar temperature conditions.

*Weeks, R. W., Scattergood, R. O., and Pati, S. R., Migration Velocities of Bubble-Defect Configurations in Nuclear Fuels, J. Nucl. Mater. (to be published).

**Weeks, R. W., and Scattergood, R. O., Analysis of Bubble Release from Dislocations in Nuclear Fuels, J. Nucl. Mater. 33, 333 (1969).

(b) Failure Criteria for Fuel Elements (C. Chan and R. W. Weeks)

Not previously reported.

In conjunction with the LIFE code program, a near-term criterion for fuel-element failure is being established that will include the effects of void nucleation and growth, and will account for the thermal and mechanical loading history of the element. It will be assumed that failure is initiated by formation of a pinhole in the cladding. The pinhole may then enlarge, depending on the local loading conditions, producing ductile fracture of the clad.

One of the main mechanisms of ductile fracture involves the expansion, interaction, and coalescence of voids* that are created by the triaxial stress state near the tip of a crack. In addition to these voids, in fuel-element cladding a principal source of voids is from damage by neutron irradiation. A coherent mathematical model for initiation of cladding fracture should include an equation of state for the material, or creep law, that accounts for stress-strain history, void nucleation and growth, thermal history, and strain hardening and softening. Obtaining such an obviously complex equation of state is further complicated by the fact that voids are associated with anisotropic behavior. An excellent discussion and review of the formation of creep laws can be found in Rabotnov.**

A literature survey of ductile failure reveals that most of the available treatments ignore creep, interaction of voids, anisotropy, and nonaxisymmetric three-dimensional problems. A noteworthy publication by Berg† merits comment, since his model accounts for strain hardening and softening from void interaction. Direct application of Berg's method to the problem of fuel-element failure may not be possible due to the assumptions of isotropy and the form of yield locus employed in his analysis, but his concept of singular surfaces of concentrated dilatation may prove useful.

Current rupture tests of irradiated stainless steel specimens (see Progress Report for January 1970, ANL-7661, p. 85) might be correlated by modification of an analysis in Rabotnov. For an unirradiated metal, Rabotnov assumes that the void damage D (e.g., area of voids per unit cross-sectional area) propagates as

*Low, J. R., Jr., "A Review of the Microstructural Aspects of Cleavage Fracture," Fracture, Proc. Intl. Conf. on Atomic Mechanism of Fracture, Swampscott, Mass., 1959; McClintock, F. A., "Crack Growth in Fully Plastic Grooved Tensile Specimens," Physics of Strength and Plasticity, A. Argon, ed., MIT Press (1969).

**Rabotnov, Yu. N., Creep Problems in Structural Members, North-Holland Publishing Company, Amsterdam (1969) (Translated from Russian).

†Berg, C. A., Plastic Dilatation and Void Interaction, MIT Report, 1969.

$$\frac{dD}{dt} = D^{\beta}\dot{\mu}; \qquad 0 \leq \beta \leq \tfrac{1}{2}, \tag{1}$$

where $\dot{\mu}$ is the rate of growth of voids.

If the nominal cross-sectional area is A_0, and the area reduction ratio is $e^{-\nu}$ for viscous failure by creep, where ν is the total strain, then the instantaneous cross-sectional area will be given by

$$A = A_0(1 - D)\, e^{-\nu}. \tag{2}$$

He then assumes that $\dot{\mu}$ is a function of the true stress σ and creep strain ω, so that Eq. (1) may be written as

$$D^{-\beta}\frac{dD}{dt} = \dot{\mu}\left(\frac{\sigma_0 e^{-\nu}}{1 - D}, \omega\right), \tag{3}$$

where σ_0 is the nominal stress.

If one can neglect the creep strain at failure, Eq. (3) becomes

$$D^{-\beta}\frac{dD}{dt} = \dot{\mu}\left(\frac{\sigma_0}{1 - D}\right). \tag{4}$$

Assuming $\dot{\mu}$ to be a power function of the form

$$\dot{\mu} = K\left(\frac{\sigma_0}{1 - D}\right)^n, \tag{5}$$

where K is a constant, continuing with Eq. (4) one finds

$$\int_0^1 (1 - D)^n D^{-\beta}\, dD = \int_0^t K\sigma_0^n\, dt. \tag{6}$$

It can be shown that

$$\int_0^1 (1 - D)^n D^{-\beta}\, dD = \frac{1}{1 + k}, \tag{7}$$

where k is the integral value, and Eq. (6) becomes

$$(1 + k)\int_0^t K\sigma_0^n\, dt = 1, \tag{8}$$

which is another form of the law of linear summation of damage.* If σ_0 is constant, then the time to failure is

$$t = \frac{1}{(1+k)\,K\sigma_0^{n}} \,. \tag{9}$$

The above analysis is based on simplified forms for the creep law and for the rate of growth of the voids, and neglects the creep strain at failure. The analysis can be modified, however, by the incorporation of a creep law for irradiated stainless steel, and by including void nucleation and growth due to irradiation in the damage function. The effect of chemical attack on cladding materials and the stress concentration due to the voids will also be incorporated in the damage parameter.

b. Oxide Fuel Studies

(i) Fuel-swelling Studies (L. C. Michels and G. M. Dragel)

Last Reported: ANL-7655, p. 103 (Dec 1969).

The technique for the preparation of two-stage replicas for electron microscope examination of oxide fuels has been modified (see Progress Report for November 1969, ANL-7640, pp. 106-108). The modification allows the replication of fresh fracture surfaces in the oxide. Replicas of metallographically polished and etched specimens are adequate for detailed observation of general structural features such as grain boundaries and subgrain boundaries, but are not suitable for the determination of distributions of fission-gas bubbles. Polishing and etching of the specimen produces disturbed surface material and enlargement of existing bubbles, as well as inclusion pullout and etch pitting. Bubble-size distributions determined under these conditions are open to serious question. A clean fracture surface provides conditions more suitable for the determination of bubble-size distributions.

To provide fresh fracture surfaces on a specimen previously prepared by standard metallography, a vibrotool was brought into contact with the surface of the specimen at various points. As a result, small pieces were fractured from the surface. Following this operation, two-stage replication was carried out as before. The areas on the replica that correspond to fractured areas on the specimen were located by inspection with a stereomicroscope and selectively cut from the surrounding material. The finished replicas contained areas from the polished and etched surface of the specimen as well as from the fracture surface. This helped to locate the radial position of the areas of interest.

*cf. Miner, M. A., Cumulative Damage in Fatigue, J. Appl. Mech., p. A-159 (Sept 1945).

This technique has been applied to a specimen from mixed-oxide fuel element HOV-15 irradiated in EBR-II. Figure III.B.1 shows a region fairly typical of what is seen in the columnar-grain region. This columnar region of HOV-15 was not molten as were higher temperature columnar regions of the same element. In the photomicrograph, a distribution of fission-gas bubbles is clearly visible in what is probably an area of intergranular fracture. The bubbles range down to about 0.2 μ in size.

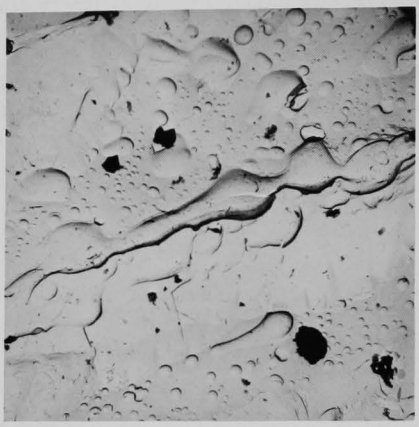

Fig. III.B.1

Fracture Replica from an Area in the Columnar Region of a Specimen from Mixed-oxide Fuel Element HOV-15 Irradiated in EBR-II. Mag. 1340X.

(ii) Fuel-element Performance (L. A. Neimark, W. F. Murphy, and H. V. Rhude)

(a) Irradiation of Group 0-3 Fuel Elements

Last Reported: ANL-7669, pp. 113-114 (Feb 1970).

As of March 12, 1970, Subassembly X072, containing the mixed-oxide fuel elements of Group 0-3, had accumulated 3048 MWd of exposure in EBR-II. This is equivalent to 32% of the first target burnup of 3.5 at. %. A continuation of operation of 50 MW with the current plant factor will result in the achievement of the first target burnup about September 1, 1970.

(b) Out-of-reactor Simulation Experiments

Last Reported: ANL-7661, p. 101 (Jan 1970).

Feasibility tests with the mockup of the high-temperature furnace have been completed, with successful tests of the axial heater to 3000°C. The design of the bottom electrode holder was changed, and the liquid-alloy contact that allows for expansion of the axial heating element was changed from a mercury-indium-thallium alloy to a gallium-indium alloy. These changes eliminated the vaporization that occurred at 1600°C.

The installation of the Centorr high-temperature furnace is proceeding. The furnace chamber, vacuum system, high-pressure air line, helium line, and water lines have all been installed and tested. Only the electrical supply and instrumentation remain to be connected.

A 3/8-in.-dia by 6-in.-long "fuel element" with a 0.069-in. axial hole, and with lavite pellets in place of urania pellets, has been fabricated. This will be used for initial testing of the high-temperature furnace.

Development of an ultrasonic technique for drilling small-diameter axial holes through 1/2-in. urania pellets is proceeding. Both 0.065- and 0.040-in.-dia holes have been drilled through 1/2-in.-long pellets. Refinements in drill design have reduced the drilling time from several hours per pellet to 10 min/pellet. There are still some problems with runout of the drill and with keeping the hole accurately centered. Part of the problem is the slightly irregular shape of the as-sintered urania pellets. This will be corrected by centerless-grinding the pellets.

The first simulation experiments with urania will be to determine the effects of thermal cycling upon the radial and axial ratcheting of fuel and cladding. Of particular interest is the role played by fuel cracking and subsequent healing. These phenomena will be assessed as functions of heating and cooling rates, temperature gradient, and time at temperature.

(c) Analysis of Instrumented Subassembly Data

Not previously reported.

Subassembly XX01 in EBR-II is the initial test of an instrumented fuel subassembly in the reactor. The subassembly was fabricated by the EBR-II Project Group, and the operation of the subassembly in EBR-II has been reported previously by the cognizant EBR-II Project Group (see Progress Reports for November 1969, ANL-7640, pp. 39-40; December 1969, ANL-7655, pp. 57-58; and January 1970, ANL-7661, pp. 36-37). Although the test is principally to check the temperature and pressure sensors and the subassembly hardware, the data from the UO_2 fuel elements are being analyzed to glean any information on fuel-clad gap conductance, closure of the gap, and kinetics of fission-gas release. In addition, the capabilities of the instrumented subassembly are being assessed to assist in planning future experiments with UO_2-PuO_2 fuel. Post-irradiation examination of selected fuel elements will be made to correlate the data from the in-pile measurements with phenomena associated with changes in the fuel elements.

Sixteen encapsulated UO_2 fuel elements are contained in the instrumented subassembly, which is in control-rod position 6 (core location 5F3) of the EBR-II. The maximum linear power rating is ~10 kW/ft. Seven of the elements are provided with W-3Re/W-25Re thermocouples to measure the fuel-center temperatures near the midlength of the fuel column. Four of these seven elements also have Chromel-Alumel thermocouples in the spiral-wire wrapper on the outside of the capsule but at the same relative axial location as the fuel-center thermocouples. Four other fuel elements are equipped with pressure transducers to sense the accumulation of fission gas in the element plenum. Other sensors indicate sodium flow rate and sodium inlet and outlet temperatures. The subassembly has accumulated 3048 MWd exposure, which is equivalent to a burnup of ~0.7 at. %.

Initial maximum fuel-center temperatures ranged from 1170 to 1370°C. Calculated fuel-clad interface conductances ranged from 1000 to 1830 Btu/hr-ft^2-°F. These calculated values are based on measured coolant and fuel-center temperatures; however, they do not correlate with variations in fuel-clad diametral clearance and gas conductance (helium versus helium-15% xenon). The fuel-center thermocouples showed a trend of decreasing temperature with time from startup on December 18, 1969 to February 19, 1970. Thereafter, these temperatures have been relatively constant with time at 50 MW. During the period of decreasing temperature, Element 7 showed the greatest change (1269-1170°C). The thermocouples in the spiral-wire wrap have consistently indicated relatively constant temperatures. The temperature changes indicated by the W-Re thermocouples are, therefore, indicative of either a change in the calibration of the thermocouples or a real change in the fuel element.

There is an indication that the calibration of the W-Re thermocouples has changed with irradiation. When the reactor was shut down from December 30, 1969 to January 1, 1970, temperature differences between the fuel-center thermocouples and the spiral-wire-wrap thermocouples ranged from 2 to 26°C (average 17°C). This is reasonable, since decay heat would be expected to keep the fuel hotter than the capsule wall and coolant. During a shutdown on January 13-15, the same temperature differences ranged from -20 to -3°C (average -11°C). On February 10, temperature differences of -13 and +1°C were noted at zero power, and on March 5, temperature differences of -13 and -2°C were found for the same thermocouples. The only way for the fuel to appear to be colder than the capsule would be an erroneous thermocouple indication. A downward drift in temperature indication due to thermal effects for W-3Re/W-25Re thermocouples is not unknown.* Whether the apparent decrease in fuel-center

*Schwarzer, D. E., High Temperature Thermal Cycling and Drift Test of $W_{95}Re_5$ Versus $W_{74}Re_{26}$ Thermocouples, Nat. Symp. on Developments in Irradiation Testing Technology, CONF-690910, September 9-11, 1969, Append. A, p. 314.

temperature is due entirely to thermocouple drifting is not determinable at present. Closure of the initial 3-4-mil (diametral) fuel-cladding gap could reduce the fuel-center temperature. An improvement in the thermal conductivity of the fuel from sintering also is possible, but in view of the initial high density of the fuel, from 94 to 96% of theoretical, and the low temperatures, it is not probable. Postirradiation examination of some of the fuel elements will be made to examine these possibilities.

Pressure as indicated by the sensors is sensitive to temperature and hence to reactor power. The maximum signal (at full power, 50 MW) has tended to be relatively constant at from 38 to 40 psia for each of the four fuel elements. The fission gas generated would be sufficient to raise the pressure to ~115 psia if all were released from the fuel. Apparently little fission gas is being released at these low fuel temperatures.

2. Radiation Damage on Structural Materials--Research and Development

a. Fracture Studies of Stainless Steel (D. G. Franklin)

Not previously reported.

Voids are expected to have a significant role in determining the nature of the failure of fuel-element cladding. Information is needed on the density, size, and distribution of voids produced both by irradiation and by deformation to determine failure modes as well as when failure will occur. A program is being initiated to study the effect of voids on failure during irradiation.

The scanning electron microscope (SEM) and other metallographic procedures are being employed to determine the mechanisms of failure of irradiated stainless steel. A typical SEM fractograph* of a sample from EBR-II is shown in Fig. III.B.2. The appearance of irradiated specimens is different from that of unirradiated specimens fractured under the same conditions. A systematic study of fractured specimens is now in the initial stages. Specimens fractured at different stresses, strain rates, temperatures, and radiation dosages will be studied. Types 304 and 316 stainless steel will be included in the investigation.

3. Techniques of Fabrication and Testing--Research and Development

a. Nondestructive Testing Research and Development

(i) Ultrasonic Techniques (R. H. Selner)

Last Reported: ANL-7640, pp. 111-112 (Nov 1969).

*Driver fuel-element cladding fractured by Atomics International. Atomics International, AI-68-Memo-94, Sample 12-T-2.

Fig. III.B.2. Scanning Electron Micrograph of Type 304 Stainless Steel Fractured at 1020°F at 0.002 in./in./min. The fuel-element burnup was 1.1% at a flux of 2 x 10^{15} n/cm^2-sec.

Efforts to manufacture an ultrasonic transducer for continuous or periodic monitoring of a Core Components Test Loop (CCTL) butt weld have continued. A shear quartz crystal was successfully soldered to a fused silica wedge with an angle of 58° after silver surfaces had been fired on both the wedge and crystal. When this transducer was coupled to a CCTL weld sample with a grease couplant, shear-wave reflections from the sample end could be detected. Such a transducer could be used to monitor the CCTL weld provided a high-temperature couplant could be found.

Various cements and adhesives including a zirconia-base cement, a silicone rubber, and a muffler cement have been tested. These materials failed at temperatures below 500°C.

Alternative methods for coupling ultrasound from transducers to metal components are under consideration. Two logical methods appear to be welding or brazing of a metal wedge to the component to be tested. At present, attempts are being made to braze ultrasonic crystals to a variety of metal wedges.

b. Nondestructive Testing Measurement of Effective Cold Work in Cladding Tubes (N. J. Carson and C. J. Renken)

Last Reported: ANL-7661, pp. 105-107 (Jan 1970).

Part of the aim of this program is to find parameters that not only correlate well with the degree of cold work, but require only conventional equipment for their measurement. Microhardness has been found to correlate well with percent elongation for tensile specimens elongated up to 40%. Optical strain measurements were also tried as a possible indicator of percent elongation. One assumes that, initially, spherical grains become ellipsoids on working and that the degree of strain can be calculated from the ratios of the axis of the ellipsoids. The number of boundaries that intersect lines both parallel and perpendicular to the direction of elongation were counted, but no high degree of correlation was found. In the samples with the higher elongations, it is increasingly difficult to distinguish between grain boundaries, subgrain boundaries, and twins.

Twin density was another property investigated as a possible indicator of the degree of cold work. Type 316 stainless steel deforms by twinning and by slip, which is unusual for a metal with a face-centered-cubic structure. The number of twins has a cause-and-effect relationship to the degree of work, and twins can be counted with relatively simple equipment.

Samples from elongated rods were prepared and photographed at a magnification of 250X on glass-plate negatives. Surfaces parallel and perpendicular to the direction of elongation were prepared. Line counts were made on the negatives with a Profile Projector, which gave an additional magnification of 20X. The number of boundaries intersected by five, parallel, 2-in. lines were determined for each negative. The results appear in Table III.B.1.

Table III.B.1. Results of Line Counts on Type 316 Stainless Steel Elongated at Room Temperature

	Boundaries Counted on Perpendicular[a] Line				Boundaries Counted on Parallel Line			
Percent Elongation	Total	Grain	Twin	Twins/in. of Sample	Total	Grain	Twin	Twins/in. of Sample
0.0	44	26	18	450	40	26	14	350
2.1	53	33	20	500	43	24	19	475
4.9	59	35	24	600	57	32	25	625
10.1	81	32	49	1225	64	31	33	825
15.2	97	31	66	1650	92	19	73	1825
20.6	128	28	100	2500	116	29	87	2175
25.0	235	30	205	5125	164	29	135	3350
29.8	286	30	256	6400	218	29	189	4725
35.0	242	30	216	5400	252	29	223	5575
40.6	344	30	314	7850	191	29	162	4050

[a]Reference direction is the direction of elongation or the axis of the tensile rod.

A relationship exists between percent elongation and the number of twins produced, but the error is large. The counting of twins does not appear to be an accurate indicator of percent elongation. The error possibly can be reduced simply by increasing the number of counts. The total count recorded is small, particularly at the lower elongations where few deformation twins were present. The number of twins generated on working was influenced by both grain size and precipitate distribution and, therefore, by heat treatment. Small differences in heat treatment or in quenching rate appear to influence significantly the number of twins generated by small amounts of cold work.

One of the more important effects of twins in cold-worked Type 316 stainless steel is that twins, and particularly their intersections, are the favored sites for carbide precipitation on heat treatment. The finest distribution of carbide precipitates should be achieved by heat treating material that has the maximum twin density, i.e., elongations of at least 30%.

Because precipitates are inhibitors of grain growth, the data in Table III.B.1 should provide information important in the design of work schedules that are necessary to produce ultrafine-grain steel.

4. Engineering Properties of Reactor Materials--Research and Development

a. High Temperature Mechanical Properties of Ceramic Fuels

(i) High-temperature Stress Relaxation of UO_2 (J. T. A. Roberts)

Last Reported: ANL-7618, pp. 101-105 (Sept 1969).

The stress dependence of the apparent* activation volume [defined as $-RT\,(\partial \ln \dot{\epsilon}/\partial\sigma)$, where $\dot{\epsilon}$ is the strain rate and σ is the stress] of stoichiometric UO_2 (grain size ~8 μ, 96-97% of theoretical density) was determined in the temperature range 1320-1800°C, and at strain rates of 0.092, 0.37, and 0.92/hr by using the stress-relaxation technique. The conventional method of plotting the stress dependence of the apparent activation volume V' is shown in Fig. III.B.3 for one strain rate, when V' is plotted as V'/b^3, with b the Burgers vector for UO_2 (= 3.86 x 10^{-8} cm). To convert to values obtained in shear, the values are divided by 2, and the shear stress τ is made equal to $\sigma_0/2$. A universal curve can be fitted to data measured in the preyield work-hardening, and steady-state flow stress regions of the flow curve. V' decreases from ~170 b^3 at low σ_0 to 10-15 b^3 at high σ_0. The same trend was observed at the two higher strain rates.

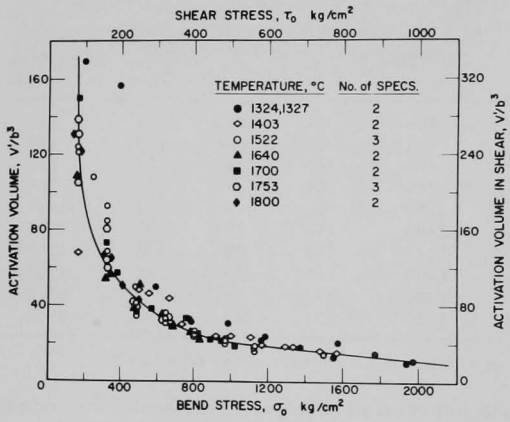

Fig. III.B.3. Stress Dependence of the Activation Volume, V' ($\dot{\epsilon}$ = 0.092/hr)

The data in Fig. III.B.3 show clearly that the activation volume is more sensitive to stress than to temperature, which is similar to the cases of both low- and high-temperature deformation of metals.** The generally observed result that, in metals, the activation volume is

*The word apparent is used to denote that the activation volume is measured by using applied stress σ_0 rather than effective stress σ^*, where $\sigma^* = \sigma_0 - \sigma_\mu$, and σ_μ is the athermal component of the flow stress.

**Li, J. C. M., Dislocation Dynamics, McGraw-Hill Book Co., Inc., New York (1968), p. 87.

approximately inversely proportional to the stress* was checked by plotting V^{-1} versus σ_0. Two types of behavior are illustrated in Fig. III.B.4. Within experimental error, curve (a) is characteristic of all tests at temperatures ≥1400°C. In contrast, the tests at 1324 and 1327°C resulted in a curve similar to (b), where there is a finite intercept on the stress axis.

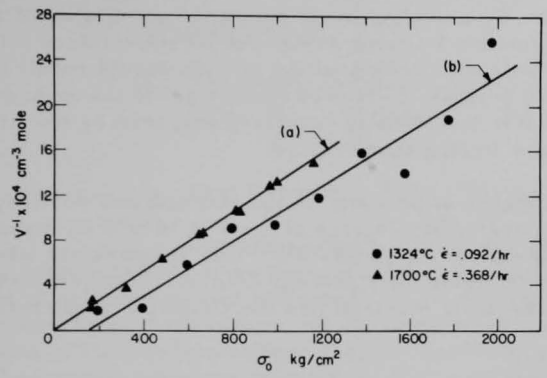

Fig. III.B.4

Plot of V'^{-1} vs σ_0

Curves (a) and (b) can be described, respectively, by the relations $V'\sigma_0 = B$ and $V'(\sigma_0 - \sigma\mu) = B$, where B is a constant, which is equivalent to the "activation work" W, and $\sigma\mu$ is termed the athermal component of the flow stress. When $\sigma\mu$ is measured there is a contribution to the flow stress from long-range interactions. In general, however, $\sigma\mu$ is zero, and the stress dependence of the flow stress is determined by the density of mobile dislocations. Thus, the apparent activation volume V' equals the real activation volume V and $\sigma_0 = \sigma^*$, the effective stress acting on the dislocations. The "activation work" term was approximately independent of temperature (above 1400°C), strain rate, and stress, and equalled 18 ± 1.8 kcal/mole. This amount of energy represents the contribution of the stress to the activated process; approximately twice that normally measured in metals.**

(ii) Plastic Yielding and Fracture of Fuel Oxides
(J. T. A. Roberts and B. J. Wrona)

Last Reported: ANL-7640, pp. 112-115 (Nov 1969).

A preliminary investigation of the plastic yielding and fracture of a sintered UO_2-20 wt % PuO_2 fuel material (density, 90% of theoretical; oxygen-to-metal ratio, 1.98; grain size, 11 μ) indicated a transition from brittle-ductile behavior in the temperature range 1000-1400°C. The

*Li, J. C. M., Dislocation Dynamics, McGraw-Hill Book Co. Inc., New York (1968), p. 87; Luton, M. J., and Jonas, J. J., A Model for High Temperature Deformation Based on Dislocation Dynamics Rate Theory on the Periodical Internal Stress (to be published in Acta Met.).

**Li, J. C. M., Dislocation Dynamics, McGraw-Hill Book Co. Inc., New York (1968), p. 87.

influence of structural variables such as grain size, porosity, and stoichiometry on both brittle and ductile strength is an important part of this program. Preliminary fabrication experiments have indicated that specimen density can be changed in the range 88-94% of theoretical by altering the cold-pressing pressure, but maintaining the same sintering temperature. Therefore, porosity can be changed from 0.06-0.12 volume fraction without changing the grain size. We are also investigating the possibility of attaining even lower specimen densities by using a UO_2-U_3O_8-PuO_2 mixture. The volume change associated with the decomposition of U_3O_8 should result in randomly distributed closed porosity.* This is in contrast to the open, connected porosity that is observed in low-density compacts prepared by low pressing pressures and/or a low sintering temperature.

The influence of porosity on the strength and ductility of the mixed oxide was demonstrated by a series of tests at 1400°C on material with theoretical densities in the range 88-94%. This temperature was suitable because some plastic strain does precede fracture. Conventionally, the strength S of a porous ceramic material has the following empirical relation:**

$$S = S_0 e^{-BP},$$

where S_0 is the strength at zero porosity, B is a constant, and P is the volume fraction porosity. The plot of $\log_e S$ versus P in Fig. III.B.5 shows that this empirical relation is obeyed by the mixed oxide, at least in the theoretical density range 88-94%. The best-fit equation gives $S = 2922\ e^{-13.5P}$ kg/cm², i.e., for a fully dense material, the strength at 1400°C at a strain rate of 0.092/hr should be 2922 kg/cm². The decrease in strength was accompanied by an increase in plastic strain to fracture.

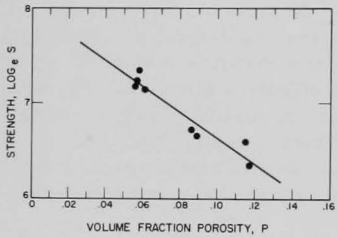

Fig. III.B.5. Plot of $\log_e S$ vs P (T-1400°C; $\dot{\varepsilon}$ = 0.092/hr)

The above empirical relation was used to extrapolate to the strength of the mixed oxide at 96-97% theoretical density (or P = 0.04-0.03). This was the density of the stoichiometric UO_2 material studied by Beals and Canon (see Progress Report for February 1969, ANL-7553, pp. 90-92). The value of S for the mixed oxide lies in the range 1703-1949 kg/cm² for a specimen with a theoretical density of 96-97%. This is ~30% higher than the values of 1300-1400 kg/cm² that were measured for the 8- and 15 μ grain size UO_2, respectively, at the same strain rate. This large discrepancy is being investigated.

*Washburn, T. N., Nucl. Appl. and Tech. 8, 23 (1970).

**Duckworth, W., Discussion of Ryskewitch Paper by W. Duckworth, J. Am. Ceram. Soc. 36(2), 68 (1953).

C. Engineering Development--Research and Development

1. Instrumentation and Control

a. Boiling Detector (T. T. Anderson)

(i) Acoustic Method

(a) Irradiation and Resistance Tests of Piezoelectric and Insulator Materials (S. L. Halverson and T. T. Anderson)

Last Reported: ANL-7669, pp. 123-124 (Feb 1970).

Further analysis of electron-irradiation data has shown lithium niobate to be less affected by ionizing radiation than a first series of calculations had indicated. As previously reported, efficiency of electromechanical conversion can be determined for piezoelectric materials in terms of the electromechanical coupling factor k_t. Additional corrections have been made for stray capacitance of the crystal holder and test leads to bring the measured k_t for lithium niobate into agreement with published values. Corrected values for the relative dielectric constant $\epsilon_{33}^T/\epsilon_0$ are 20% lower than published values. This difference corresponds to a 3-μ air gap between unelectroded crystal and holder, a reasonable value for the optically flat surfaces. The corrected values indicate less damage, i.e., changes of -7% in k_t and -6% in $\epsilon_{33}^T/\epsilon_0$ for a Roentgen-equivalent dose of 3×10^6 R.

Much stronger effects than electromechanical changes of acoustic-signal degradation appear to be electrical conductivity and ionization leakage in vicinity of crystal and insulators. Slight degradation was incurred at 1000°F in the Chemistry Division Gamma Facility, apparently due to increased leakage.

Radiation damage in lithium niobate crystal structure by neutrons is expected to be more severe. Literature on neutron-radiation damage in covalent crystals is being reviewed, and test procedures are being developed for such a study.

(b) Development of High-temperature Detector (A. P. Gavin)

Last Reported: ANL-7669, pp. 124-125 (Feb 1970).

Development of a transducer assembly for operation in high-temperature sodium is being pursued along two lines. The first line is to establish a transducer configuration that will give good response over a wide frequency range. For this purpose, configurations in brass

housings with screwed closures sealed with O-rings are being evaluated by observing the output signal produced when the unit is immersed in a tank of water (3 ft in diameter by 3 ft deep) and excited by sound waves generated by a hydrophone. These tests are qualitative and aimed only at evolving a transducer configuration that can be reproduced in temperature- and corrosion-resistant materials for operation while immersed in sodium at 1200°F. Design optimization will follow the initial proof-of-principle tests.

A brass model which gives a fair response up to 10^5 Hz has been assembled.

The second line of development is aimed at producing a stainless steel "can" which will replace the brass housing. Means of sealing diaphragms to the housing and of making required electrical lead connections have been developed. An assembly containing quartz discs in lieu of lithium niobate crystals has been completely welded and leak tested, including connection of the high-temperature cable lead. After leak test, the unit was opened and examined for damage to the quartz discs, gold foil, and quartz sleeve; none was evident.

Components for the first all-stainless steel-welded model containing lithium niobate crystals are being machined; assembly and testing will follow.

b. Flow Monitor (T. T. Anderson)

(i) Two-thermocouple Method (A. E. Knox and C. W. Michels)

(a) Temperature Variation of Coolant Sodium at the Outlet of the EBR-II Instrumented Subassembly

Last Reported: ANL-7669, pp. 125-126 (Feb 1970).

Data obtained from four coolant thermocouples (ITC 4, OTC 5, OTC 14, and SWTC 17) in the Test XX01 Instrumented Subassembly are being analyzed, using digital methods. Data that have been digitalized are being processed, using the R-111 spectral density, auto-correlation, and cross-correlation program.

A test procedure has been written for obtaining wide-band records of output signals from four coolant thermocouples in the Test XX02 (37-pin) Instrumented Subassembly; these include one inlet, one outlet, and two spacer-wire thermocouples.

c. Vibration Sensor (T. P. Mulcahey)

(i) Out-of-pile Tests of Sodium-immersible Commercial Transducers (T. T. Anderson and A. P. Gavin)

Last Reported: ANL-7655, p. 109 (Dec 1969).

Additional calibrations of three Gulton high-temperature accelerometers with integral 20-ft stainless steel leads were performed at ANL to determine temperature effects on dielectric properties, shunt leakage resistance, and vibration signal level. Each accelerometer was attached to a vibrator-driven rod and was placed in an adapted tube furnace.

In each instance, as furnace temperature was raised, shunt leakage resistance dropped exponentially. Vibration signal level (at 100-1000 Hz), as monitored with a special charge amplifier, remained constant until leakage resistance reached one kilohm at ~1000°F; then it became erratic. At this point, excessive 60-Hz pickup in amplifier output was noted. Transducer admittance (at 10-100 kHz) showed that this effect is not due to internal dielectric losses; therefore surface leakage conditions may be contributory.

A small furnace has been constructed to simplify further testing of high-temperature transducers with right-angle rigid leads. This furnace has a 3-in.-ID, 4-in. heated length, and a slot in the side to accommodate rigid leads; it can be used to test commercial transducers and ANL-developed acoustic sensors.

2. Heat Transfer and Fluid Flow (M. Petrick)

a. LMFBR Burnout Limitations (R. J. Schiltz and R. Rohde)

(i) Preparation of Apparatus

Last Reported: ANL-7669, p. 126 (Feb 1970).

The 1-in.-tubing sections for the suction and discharge of the electromagnetic, helical induction pump were fabricated, hydro tested, and welded to the pump. The 1-in. piping to the dump tank has been welded to the tank. The main $1\frac{1}{2}$-in.-loop piping is 90% complete. Loop enclosure panels, which are made of an insulating material, are being lined with sheet steel; this work is about 20% complete. Variable autotransformers for controlling the electrical trace-heating system have been mounted on the control panel.

(ii) Analytical Prediction of Burnout Limitations

Last Reported: ANL-7632, pp. 115-116 (Oct 1969).

To perform planned experiments with coolant vaporization in a test section simulating LMFBR fuel and blanket regions, it is important to operate with inlet plenum pressures sufficiently high to maintain stable flow. Determination of the required minimum inlet pressure depends upon knowledge of the flow rate-pressure drop characteristics of the test section. Determination of these characteristics, other than by experiment, requires prediction of sodium liquid-vapor pressure distributions along the test section length and of choking conditions at the test-section outlet.

Attempts were made to calculate sodium liquid-vapor pressure distribution along the unheated length of the test section which simulates the upper blanket. Calculations were based on a procedure tested successfully using the low-pressure data and the Lockhart-Martinelli void-fraction correlation (see ANL-7632, pp. 130-131). An important feature of this procedure, in common with those used predominantly in the LMFBR program, is the assumption that void fraction can be obtained from a correlation with fluid properties and quality. This assumption is equivalent to treating void fraction as a thermodynamic property of the fluid.

Calculations were performed by first specifying the simulated outlet plenum pressure, mass flow rate, and stagnation enthalpy, and then numerically integrating appropriate momentum and energy equations in the upstream direction. When choking occurred, the choking pressure, i.e., actual test-section outlet pressure, was determined first. Typical choking conditions are shown in Fig. III.C.1. To ensure accuracy of the numerical integration, especially with choking conditions, length was chosen as the dependent variable and pressure the independent variable (see Progress Report for November 1968, ANL-7518, pp. 97-99).

Attempts to predict pressure distributions with either the MacFarlane* or Wallis** representation of the Lockhart-Martinelli void-fraction correlation were unsuccessful because as the quality approached zero, a point upstream of the test section outlet was always reached where the local momentum change started to increase with decreasing quality and increasing pressure and distance from the outlet (see Fig. III.C.1). In all calculations, the minimum momentum change occurred when the void fraction was about 0.6 to 0.7 (see Fig. III.C.2). This minimum is physically unacceptable since, with sufficiently large flow rates in a constant-area duct, it may result in choking upstream of the outlet. In fact, "upstream choking" was obtained in all computations with quality approaching zero (see Curves (1), (2), and (3), Fig. III.C.1).

---

*MacFarlane, D. R., An Analytical Study of the Transient Boiling of Sodium in Reactor Coolant Channels, ANL-7222 (June 1966), Eq. (16).

**Wallis, G. B., One-dimensional Two-phase Flow, McGraw-Hill Book Co. Inc. (1969), Eq. (3.32).

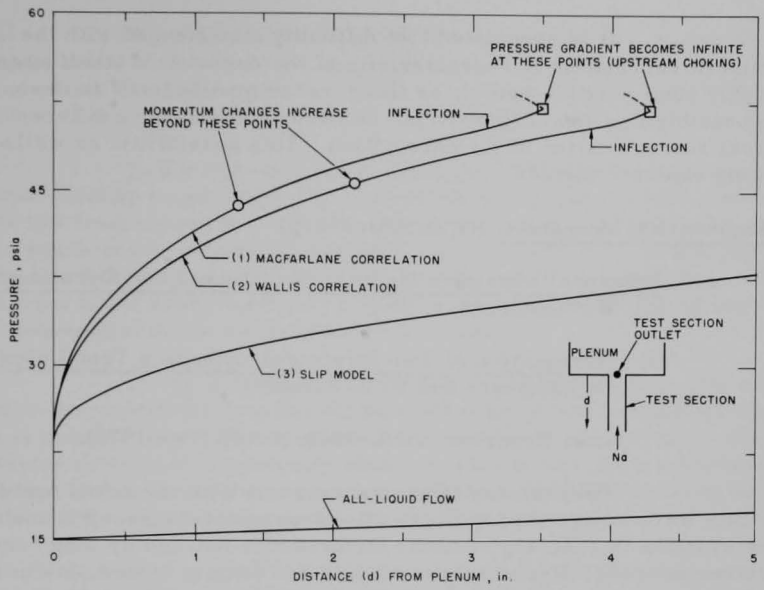

Fig. III.C.1. Illustrative Pressure-distribution Calculations for Adiabatic Sodium Flow through 0.19-in.-dia Tube; Mass Velocity = 2.5×10^6 lb/(ft^2)(hr); Stagnation Temperature = 1900°F; Plenum Outlet Pressure = 15 psia. Curves (1), (2), and (3) are for choked-flow conditions.

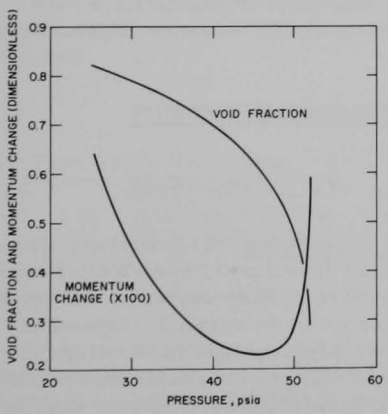

Fig. III.C.2. Local Momentum Change Based on Wallis Correlation for Void Fraction (see Fig. III.C.1, Curve (2))

Existence of "upstream choking" was discovered in earlier computations in the ANL Coolant Dynamics Program.* These computations included a representation of the Lockhart-Martinelli correlation based on an interpolation routine developed from the original Lockhart-Martinelli experimental data.

Alternative computations, also shown in Fig. III.C.1, were performed with void fractions determined on the assumption that the slip ratio (ratio of vapor velocity to liquid velocity) is equal to the square root of the ratio of the liquid to vapor densities. Although this assumption removed the unacceptable momentum changes, it did not allow predictions in agreement with the experimental data plotted in Fig. IV.A.1 of ANL-7632.

*Personal communication, M. A. Grolmes and H. Fauske (RAS) to D. M. France and R. P. Stein (ETD), Feb 1970.

It is speculated that difficulty experienced with the Lockhart-Martinelli correlation is characteristic of the correlation itself when applied to highly compressible two-phase flows as the quality tends to zero. It is also possible that the difficulty may be removed by using a different mathematical representation of the correlation. This possibility, as well as others, is being explored further.

3. Engineering Mechanics (G. S. Rosenberg)

a. Structural Dynamics Studies--Structure-Fluid Dynamics (M. W. Wambsganss, Jr.)

(i) Preparation of Two Structural-dynamics Test Loops (B. L. Boers and P. L. Zaleski)

Last Reported: ANL-7669, p. 128 (Feb 1970).

Preliminary flowtests were run with the small test loop. The data were analyzed to evaluate effectiveness of the recently installed filter systems in reducing acoustic disturbances induced by loop components and other sources. Pressure-power spectral density values obtained indicated an average attenuation of ~11 dB at 30 Hz and ~4 dB at 60 Hz.

Although the filter systems are successful in reducing low-frequency acoustic noise, there is an accompanying variation of the high-frequency turbulent-noise spectrum. The cause or full extent of this variation is not known. Therefore, more extensive flowtests have been initiated to evaluate the filters further and to obtain meaningful pressure data.

b. Structural Dynamics--Flow Noise-Field Dynamics (M. W. Wambsganss, Jr.)

Last Reported: ANL-7661, pp. 115-116 (Jan 1970).

(i) Near-field and Far-field Flow Noise. This activity was last reported under the heading: "Turbulent Boundary-Layer Wall-Pressure Fluctuation." Before installation of the acoustic filter systems, a flowtest was initiated in the small test loop to determine the spatially-dependent characteristics of the pressure field, which are required in the study of parallel-flow-induced vibration of fuel rods. These characteristics, which enter into the equation for the mean-square-value (msv) spectral density of rod displacement, necessitate cross-correlation of signals from closely spaced, miniature pressure transducers. Such transducers were developed; three pairs of diametrically opposite transducers were flush-mounted on a tubular element, and the assembly installed in the loop. However, after several runs, the rubber potting started to peel off the transducers and the test was terminated.

The transducers were resurfaced using a different potting technique, calibrated, and a new series of flowtests were performed. Pressure-time histories were recorded for a range of mean axial flow velocities; these data were processed to give msv spectral densities.

In the high-frequency range ($f > 600$ Hz), the spectra varied with flow velocity as expected; the energy content increased with flow velocity. At low frequencies ($f < 600$ Hz), the spectra exhibited a large energy density which remained nearly invariant with flow velocity. It was postulated that the low-frequency noise might be acoustic noise, masking the contribution from near-field noise and to the msv spectra, making it difficult to obtain meaningful cross-correlation measurements.

It was hypothesized that if the extraneous noise was acoustic in nature, its contribution to the surface pressure would be equal in magnitude and phase at a given section and instant of time. Accordingly, pressure-time histories from diametrically opposite transducers were subtracted in an attempt to cancel out the acoustic contribution, and the resulting differential pressure signals were processed to obtain msv spectra.

It was observed that the subtraction process efficiently cancels the extraneous low-frequency noise, thus supporting the hypothesis that it is acoustic in nature. The resulting spectra are relatively flat out to a cutoff frequency, with the magnitude and cutoff frequency (hence, energy content) increasing with mean flow velocity.

Normalization of the msv spectra is being studied. Another series of flowtests with the acoustic filter system in the loop is being planned.

D. Chemistry and Chemical Separations

1. Fuel Cycle Technology--Research and Development

a. Adaptation of Centrifugal Contactors to LMFBR Processing (G. J. Bernstein)

Last Reported: ANL-7661, p. 116 (Jan 1970).

Centrifugal contactors are being studied to extend the design of the Savannah River centrifugal contactors to a configuration that will be suitable for efficient handling of plutonium in the solvent extraction of LMFBR fuels. The advantages sought are increased nuclear safety through limitation of diameter, reduced radiation damage to the solvent, and increased ease of operation. The restriction on the diameter of the contactor makes it necessary that the unit operate at higher speeds and have a greater length-to-diameter ratio than do the Savannah River contactors in order to achieve high throughput.

Two different designs of centrifugal contactors are being studied. Previous reports described preliminary tests performed with plastic models of a contactor which consisted of a hollow rotor that revolved within a stator. In that design, organic and aqueous phases would be fed into the top of the annular space between rotor and stator, would be mixed as they moved downward, and would flow into an orifice in the bottom of the rotor. The phases would be separated by centrifugal force as they moved upward inside the rotor and would be discharged through ports at the top of the rotor into collecting rings. This design has the advantage of mechanical simplicity over the Savannah River design. However, further development of this unit is being postponed since differences in its design would make difficult correlation of its performance with the operating characteristics of the Savannah River type of contactor.

The design currently being developed, which follows more closely the basic design of the Savannah River contactor, provides for aqueous and organic phases being fed into a mixing chamber located below a hollow cylindrical rotor. The phases are mixed by a paddle attached to the end of the shaft that supports the rotor. The mixed phases are directed into the bottom of the rotor and are separated as they move upward through the rotor to discharge ports at the top. A stainless steel unit with a 4-in.-dia rotor having a separating length of 12 in. is currently being designed.

The rotor is supported only at the top, with no bottom bearing. Operating speeds are limited by the critical speed of the shaft and rotor assembly. A spindle assembly that accommodates a $1\frac{1}{4}$-in.-dia shaft will support the rotor drive shaft. Calculations of critical speeds indicate that operation of this rotor assembly at speeds up to 3600 rpm should be feasible. The length-to-diameter ratio of 3 and the operating speed of 3600 rpm will extend the study of operating characteristics beyond the range covered by the Savannah River units, which have a length-to-diameter ratio of about 1.3 and an operating speed of 1800 rpm.

A facility has been designed that will permit testing of experimental contactors using various organic and aqueous streams. Tanks, pumps, flow meters, and piping have been procured and are being prepared for installation. Initial tests will be made with dilute nitric acid as the aqueous stream and tributyl phosphate in a refined kerosene diluent as the organic stream.

b. Molten Metal Decladding (R. D. Pierce)

Last Reported: ANL-7669, pp. 130-131 (Feb 1970).

Laboratory and engineering work is being done on the development of a molten metal decladding technique to be used as a head-end procedure for aqueous processing of LMFBR fuels. Although molten metal

decladding is being studied in relation to mixed uranium-plutonium oxide fuel clad with stainless steel, this technique can also be used to remove Zircaloy from fuels used in light water reactors.

Information is being organized on the design of a conceptual liquid-metal plant for processing 5 metric tons/day of stainless steel-clad LMFBR oxide fuel (see Progress Report for October 1969, ANL-7632, pp. 122-123).

(i) Process Demonstration Experiments

Last Reported: ANL-7655, pp. 117-118 (Dec 1969).

(a) Hot-fuel Experiments. The Senior Cave of the Chemical Engineering Building (at Argonne, Illinois) is being decontaminated and equipment constructed for a process demonstration using irradiated fuel. The objectives of this study are (1) to determine the degree of fragmentation of irradiated fuel, (2) to demonstrate complete, rapid cladding dissolution using highly irradiated fuel, and (3) to demonstrate a capability for containment of iodine and other fission product gases. Manipulators to be used in the cave have been tested in the mockup area. Stainless steel-clad oxide fuels irradiated at ORNL, Yankee, and Vallecitos are on hand for possible use in these decladding experiments.

(b) Semiworks Experiments. A high-purity helium-atmosphere glovebox containing equipment for handling molten metals and salts is being readied for demonstration of molten metal decladding techniques. Operation of the control panels for furnaces, transfer lines, and valves has been checked. Transfer of molten zinc and salt from one reaction vessel to a receiver by means of a heated Mo-W transfer tube has been demonstrated. Helium has been introduced into the glovebox, and the helium-purification system has been put into operation. In initial experiments, stainless steel tubes (containing unirradiated UO_2 pellets and fines) will be dissolved in molten zinc.

c. Continuous Conversion of U/Pu Nitrates to Oxides (N. M. Levitz)

Last Reported: ANL-7669, pp. 131-132 (Feb 1970).

Denitration of uranium-plutonium nitrate solutions and plutonium nitrate solutions is being studied in scoping runs in preparation for work with fluidized-bed equipment. The major objective is a capability for producing (1) either combined U-Pu oxide or plutonium oxide that could be mechanically mixed with uranium oxide and fabricated into fast reactor fuel and (2) plutonium in powder form (i.e., oxide) which could be shipped more safely and in smaller volumes than the nitrate solutions that are currently being shipped. Fluidized-bed reduction of UO_3-PuO_2 to UO_2-PuO_2 would follow denitration.

Laboratory experiments have been performed on the rate of dissolution in nitric acid of UO_3-20% PuO_2 materials prepared by dropwise denitration. The data are needed for the design of the pilot-plant feed system, since recycle of the fluid-bed denitrator product is planned to minimize plutonium inventory requirements in the pilot plant. The rate of dissolution of the PuO_2 fraction is known to be limiting, so the plutonium content of the solution was monitored (by liquid scintillation counting) as a function of time. Starting materials for the oxide dissolution experiments were mixed oxides prepared by denitration of nitrate solutions at 300, 450, and 600°C (see Progress Report for January 1970, ANL-7661, pp. 118-119). The experimental conditions included the following: nitric acid molarity, 5 to 16; dissolution temperature, 95 to 120°C; and actinide concentrations of the final solutions of 0.35 and 1.5M. Data indicated (1) that oxide prepared at higher temperatures was more difficult to dissolve, (2) that the rate of oxide dissolution was not affected significantly by the dissolution temperatures used, (3) that the dissolution rate was not affected by allowing a higher final actinide concentration for an acid concentration of 16M, and (4) that the fraction of plutonium dissolved is greater at the higher acid concentration. For the 16M acid concentration, 99.5% of the plutonium in an oxide mixture with the higher actinide concentration was dissolved in 5 hr.

For the engineering-scale portion of the program, a fluidized-bed pilot plant is being constructed for denitrating U-Pu nitrate and plutonium nitrate solutions. Approximately one-half of the instrument lines and utility lines outside the pilot-plant alpha box have been installed. Installation of equipment and instruments has begun. The denitrator is being designed.

The merits of batchwise and continuous preparation of nitrate feed solution were compared. Batch preparation, in which the entire batch is prepared before a run, has the following advantages:

1. The overall run time is shorter.
2. The solution composition is known (by analysis) and remains uniform.
3. An operator's time and attention are not diverted during a run to make the feed solution.
4. The equipment is simpler.
5. Fewer analytical samples are required.

Advantages of the continuous preparation method, in which oxide and nitric acid would be added continuously to a 1-hr supply in the feed tank, are as follows:

1. A denitration run may be continued indefinitely.
2. The inventory of plutonium in the box can be smaller than for the batch method.
3. The size of feed tanks is about two-thirds that for batch preparation.

Batch preparation is presently considered the more promising procedure for our experiments.

The use of borosilicate glass or boron-stainless steel Raschig rings in feed-makeup vessels containing concentrated plutonium solutions is being considered for criticality reasons. A vessel containing Raschig rings could have a more convenient geometry for use in a glovebox than a nonpoisoned system (i.e., a larger diameter and shorter length). Nuclear safety applications of Raschig rings in existing plants were reviewed. It was tentatively concluded that vessels of practical size and geometry, filled with boron-containing Raschig rings, would be critically safe for application to the pilot plant.

d. In-Line Analyses in Fabrication (M. J. Steindler)

Last Reported: ANL-7669, pp. 132-133 (Feb 1970).

In-line, nondestructive analytical methods are under development for determining physical and chemical properties of FBR fuel oxide powder and pellets during fabrication in large-capacity plants. An important property affecting the behavior of oxide fuel during irradiation is the ratio of oxygen to metal (O/M) of the fuel material. Compatibility of the fuel with cladding is better for substoichiometric oxide, but thermal conductivity decreases as O/M ratio decreases. The probable desired range of values for the O/M ratio is 1.95 to 1.99. The O/M ratio is presently determined by a thermogravimetric method.

A method being studied for in-line determination of the O/M ratio is based on the change of lattice parameter with O/M ratio at a fixed U/Pu ratio in the single-phase $(Pu_yU_{1-y})O_{2-x}$ region ($0 < y < 0.4$, $0 < x < 0.2$, $x/y \leq 0.5$). Curves have been plotted (see Fig. III.D.1) of data from the literature relating lattice parameter to O/M ratio for ternary materials containing 10 to 40% Pu and of known plutonium and oxygen contents. The data of Markin and Street* for mixed oxide containing 42% Pu give a slope of 0.0024 Å per 0.01 ratio. The data of Gibby** indicate a slope of 0.0030 Å per 0.01 ratio for mixed oxide containing 25% Pu. For other data† that

*Markin, T. L., and Street, R. S., J. Inorg. Nucl. Chem. 29, 2265 (1967).

**Gibby, R. L., The Effect of Oxygen Stoichiometry on Thermal Diffusivity and Conductivity, BNWL-927 (1969).

†Schmitz, F., Structure and Properties of $(U,Pu)O_2$ Containing Fission Products (Inactive), CEA-R-3795 (1969); Baily, W. E., and Lyon, W. L., Some Electrical Properties of the Plutonium-Uranium Mixed Oxide System, GEAP-4675 (1965).

represent measurements over limited ranges, curves were not drawn through the points. Calculated lattice parameters for stoichiometric oxide of several plutonium contents (0, 10, and 30%) also are plotted in Fig. III.D.1.

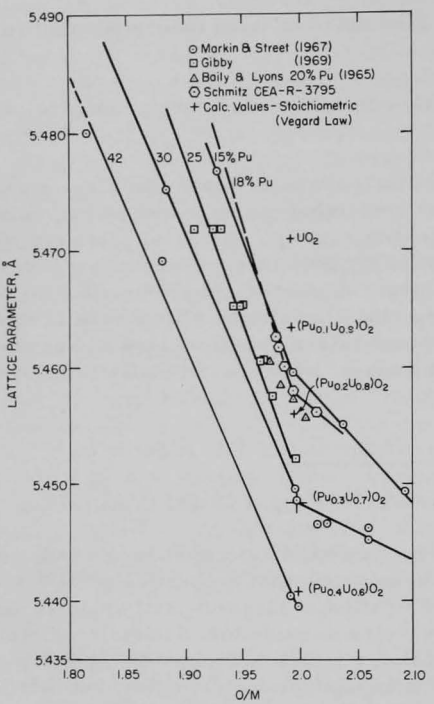

Fig. III.D.1
Lattice Parameter vs O/M for $Pu_yU_{(1-y)}O_{2\pm x}$

The compatibility of the data makes it reasonable to treat them as one relationship. Application of the method to the measurement of the O/M ratio of hypostoichiometric oxide appears to be promising.

2. General Chemistry and Chemical Engineering--Research and Development

a. Thermophysical Properties

(i) Partial Pressures of Vapor Species in the U-Pu-O System and in the U-Pu-O System Containing Fission Products (J. E. Battles and P. E. Blackburn)

Last Reported: ANL-7655, pp. 120-123 (Dec 1969).

Mass-spectrometric studies of the volatilization behavior of the uranium-plutonium-oxygen LMFBR fuel are being made to determine (1) the composition of the vapor phase in equilibrium with the condensed

phase(s), (2) the partial pressures of the vapor species as a function of temperature and oxygen concentration, and (3) the thermodynamic properties of the vapor species. These data are required to establish whether migration occurs within the fuel by vapor transport, and to determine metal and oxygen activities of the fuel. These activities are important in determining the nature of fission products (i.e., their presence as oxides, alloys, or elements), particularly those corrosive to cladding or those contributing to fuel swelling. The data will be used to establish methods for controlling cladding attack and some aspects of fuel swelling. The program will first concentrate on the pure fuel, i.e., $U_{0.8}Pu_{0.2}O_{2\pm x}$, corresponding to zero irradiation. Studies will then be made of simulated irradiated fuel containing fission products.

Studies of the volatilization behavior of the mixed-oxide material ($^{235}UO_2$-20 wt % PuO_2) are continuing, using iridium effusion cells. Experimental data are being obtained for the ion intensities of the vapor species as a function of temperature and the oxygen-to-metal (O/M) atom ratio. Also, the total vapor pressure is being determined from rate-of-effusion measurements at constant temperature (2240°K) as a function of O/M atom ratio. The data have been reported on the first series of experiments (IUP-4A) completed (see ANL-7655, Tables III.D.1 and 2). A second series of experiments (IUP-5A) has been conducted using a larger sample of starting material (~2.5 g initially). The experimental procedures for both the temperature dependency and the rate-of-mass effusion measurements are the same as those employed in the first series. The purpose of the IUP-5A series was primarily to ascertain the reproducibility of the measurements in the first series and to extend the composition range studied to a lower O/M atom ratio.

For the second series of measurements, the partial enthalpies of sublimation are summarized in Table III.D.1; the values agree well

TABLE III.D.1. Mass Spectrometrically Determined Partial Enthalpies of Sublimation for the Vapor Species in the Ternary System U-Pu-O

Run No.	Temperature Range (°K)	Composition of Solid Phase (O/M)[a]	Partial Enthalpy of Sublimation[b] (kcal/mol)				
			PuO	PuO_2	UO	UO_2	UO_3
IUP-5A-2	1905-2298	1.97_9	126.27 ± 1.26	141.49 ± 1.67	-	150.06 ± 1.11	157.41 ± 1.52
IUP-5A-4	1956-2356	1.97_7	126.55 ± 1.23	138.71 ± 1.78	131.18 ± 3.96	148.61 ± 1.44	158.37 ± 1.39
IUP-5A-6	1998-2296	1.95_4	122.19 ± 1.56	137.83 ± 1.60	130.12 ± 4.61	144.09 ± 0.83	160.04 ± 1.43
IUP-5A-8	1992-2374	1.97_7[c]	119.40 ± 1.17	138.80 ± 1.74	130.43 ± 4.67	140.35 ± 1.34	157.72 ± 1.75
IUP-5A-10	1988-2373	1.86_4[d]	124.10 ± 1.14	139.27 ± 1.95	143.75 ± 5.23	146.63 ± 1.19	155.55 ± 1.40
IUP-5A-12	1982-2411	1.93_4	121.88 ± 0.97	138.17 ± 1.62	139.56 ± 3.85	145.00 ± 1.04	158.33 ± 1.70
IUP-5A-14	1988-2370	1.93_0	122.80 ± 0.88	142.79 ± 1.79	143.79 ± 3.59	146.99 ± 0.70	162.05 ± 1.62

[a]The O/M atom ratio was determined from samples taken at the conclusion of the rate-of-effusion experiment and immediately preceding the temperature-dependency experiment.
[b]The errors listed are standard deviations; an ionizing electron energy of 11 eV was used for measurements of PuO^+, UO^+, and UO_2^+, and 15 eV for measurements of PuO_2^+ and UO_3^+.
[c]The oxygen analysis for this sample is believed to be incorrect.
[d]The oxygen analysis is known to be low due to equipment malfunction during analysis.

with those obtained in the first series. As the O/M atom ratio decreased (see Table III.D.1), the partial enthalpies for UO_2 and PuO also appeared to decrease. Whereas this trend of the partial enthalpies with decreasing O/M atom ratio was observed for UO_2 in the first series, the trend was not apparent for PuO. The partial enthalpy data for the other vapor species appear to be independent of composition; however, small changes would probably be obscured by the randomness of the data. The low ion intensity for UO^+ over most of the temperature range (e.g., see ANL-7655, p. 121, Fig. III.D.2) leads to considerable uncertainty in the accuracy of the enthalpy obtained for this vapor species.

The total vapor pressure and preliminary vapor-phase composition data for this second series of measurements are summarized in Table III.D.2. The total vapor pressure was calculated from the rates of mass effusion with the assumption that the vapor phase was entirely $^{235}UO_2(g)$, $UO_2(g)$ is the major species except for O/M atom ratios greater than ~1.98. The results agree reasonably well with those of the IUP-4A experiments.

TABLE III.D.2. Total Vapor Pressures and Ion Intensities for the Vapor Species in the Ternary System U-Pu-O

Run No.	Temperature (°K)	Composition of Solid Phase (O/M)[a]	Pressure (atm)	Ion Intensity[b]				
				PuO^+	PuO_2^+	UO^+	UO_2^+	UO_3^+
IUP-5A-1	2243	1.97_9[c]	3.77×10^{-5}	0.013	0.023	-	0.578	0.386
IUP-5A-3	2240	1.97_7	1.60×10^{-5}	0.049	0.035	0.002	0.758	0.157
IUP-5A-5	2243	1.95_4	1.19×10^{-5}	0.074	0.036	0.003	0.785	0.103
IUP-5A-7	2240	1.97_7[d]	8.28×10^{-6}	0.118	0.031	0.004	0.788	0.059
IUP-5A-9	2242	1.86_4[e]	7.00×10^{-6}	0.168	0.027	0.006	0.767	0.032
IUP-5A-9A	2243	1.97_1[d]	7.70×10^{-6}	0.172	0.026	0.007	0.766	0.029
IUP-5A-9B	2242	2.01_7[d]	7.12×10^{-6}	0.184	0.025	0.007	0.759	0.025
IUP-5A-11	2240	1.93_4	7.57×10^{-6}	0.171	0.024	0.007	0.768	0.031
IUP-5A-13	2242	1.93_0	6.79×10^{-6}	0.209	0.021	0.009	0.742	0.020
IUP-5A-15	2243	1.93_4	7.78×10^{-6}	0.215	0.019	0.009	0.740	0.018
IUP-5A-17	2240	1.92_2	6.8×10^{-6}	0.226	0.019	0.008	0.731	0.016

[a]The O/M atom ratio was determined from samples taken at the conclusion of the experiment.
[b]These values represent the fraction of the total ion current. The ion currents were corrected for isotopic composition. Corrections for ionization cross sections and multiplier efficiency were not made.
[c]The O/M atom ratio was ~2.00_4 at start of experiment.
[d]The oxygen analysis for this sample is believed to be incorrect.
[e]The oxygen analysis is known to be low due to equipment mulfunction during analysis.

Run IUP-5A-1 demonstrates the large change in ion current (and vapor pressure) that occurs with a small change in the O/M atom ratio when the ratio is in the range 1.98 to 2.00. At the start of the run, the O/M atom ratio was 2.00, and the total ion current (sum of the ion intensities for PuO^+, PuO_2^+, UO_2^+, and UO_3^+) was greater by a factor of ~2.3 than at the conclusion of the run. Total vapor pressures of ~5.4×10^{-5} and ~2.3×10^{-5} atm have been estimated from the total ion currents at the start and conclusion of this run, respectively. For the other vapor-pressure runs, the change in total ion current was insignificant.

Preliminary values for the partial pressures of the vapor species were calculated from the rate of effusion and vapor-phase composition data at 2240°K, using the equation for molecular effusion (see Progress Report for October 1968, ANL-7513, p. 129, Eq. 7). The data from both series of measurements (see Table III.D.2 of this report and Table III.D.2 in ANL-7655) were used in these calculations. The partial pressures at 2240°K are shown in Fig. III.D.2 as a function of O/M atom ratio (for the solid). From this figure, it is apparent that the total vapor pressure and vapor-phase composition change significantly with the O/M atom ratio. The vapor phase is predominantly uranium-bearing at the higher O/M atom ratios; at the lower O/M atom ratios, the vapor-phase composition approximates that of the solid phase. Also, it is apparent from Fig. III.D.2 that the total vapor pressure decreased by approximately a factor of 10 as the O/M atom ratio decreased from 2.00 to 1.92. The data indicate that a minimum in the total vapor pressure may exist at an O/M atom ratio of about 1.92.

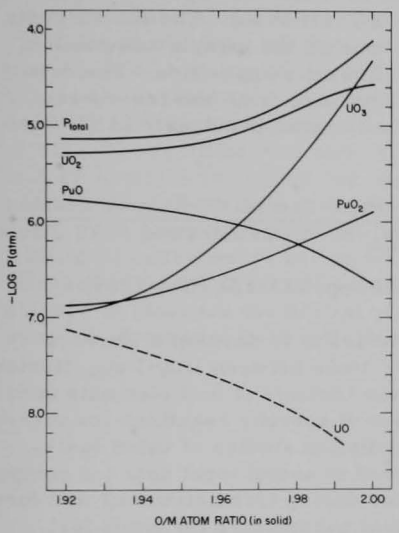

Fig. III.D.2. Partial Pressures of the Vapor Species over $(U_{0.80}Pu_{0.20})O_{2-x}$ at 2240°K

In calculating these partial pressures, the weight loss due to the effusion of oxygen has been neglected. Although the oxygen contribution is significant for O/M atom ratios near or greater than 2.00, it is negligible at the lower O/M ratios.

(ii) Total Effusion of Pu-O and U-Pu-O System (P. E. Blackburn and R. K. Edwards)

Last Reported: ANL-7640, p. 125 (Nov 1969).

The partial pressures of fuel and fission product gases are required to aid in establishing chemical control of cladding corrosion, fuel swelling, and/or fuel-coolant interactions. The partial pressures will be calculated from mass-spectrometric ion intensities measured as a function of temperature and composition. Relative ionization cross sections are necessary to make the calculation.

Experiments are in progress to obtain the relative ionization cross sections of uranium-oxygen vapor species. Satisfactory ionization-efficiency data for U, UO, UO_2, and UO_3 have been measured. Graphical analysis of the data for U^+ and UO^+ show contributions from at least

two ionization processes, but further analysis of these results is required. At the congruently effusing composition for 2185°K, the relative ion currents for UO_2 preliminarily indicate that the relative ionization cross sections might be as low as 1/10, but this is subject to change pending final interpretation of the above ionization-efficiency data.

A "traverse" experiment, in which a sample of $UO_{2.09}$ was held at 2323°K in an effusion cell, has been carried out. The ion currents of UO, UO_2, and UO_3 were recorded with time as the sample composition changed and approached the congruently effusing composition. The data are being treated to obtain the urania composition from the ion-current measurements by the mathematical approach noted previously (ANL-7640, p. 125) to be under development.

(iii) Phase Diagram of the U-Pu-O System Containing Fission Products (Nonradioactive) (C. E. Crouthamel and I. Johnson)

Last Reported: ANL-7655, pp. 123-124 (Dec 1969).

The objective of these studies is to develop a chemical basis for an understanding of those interactions between UO_2-PuO_2, fission products, and cladding which determine the lifetime of fuel elements under reactor irradiation conditions. The choice of specific reactions for investigation is guided by the results of postirradiation studies of oxide fuels. The results of these investigations will lead to useful input data for computer codes for predicting fuel-element behavior during irradiation and will furnish a quantitative basis for specifying chemical parameters for oxide fuel.

As an aid to the definition of the experimental program, theoretical calculations have been made of the dependence on burnup of the solid swelling rate and the average oxygen potential of a mixed urania-plutonia fuel. These calculations highlighted the need for a better understanding of the chemical form of fission product cesium in oxide fuels. For example, if the cesium is assumed to be present in a chemically combined form, the swelling rate is computed to be about 0.26% per atom percent burnup, whereas if metallic cesium is present, the swelling rate could be as large as 0.44% per atom percent burnup. The computed rate of increase of the oxygen potential of the fuel with increasing burnup was also found to be significantly affected by the assumption made concerning the chemical form of the cesium. Additional interest in the chemical form of cesium stems from the results of electron microprobe studies of intergranular corrosion of stainless steel cladding in several specimens of irradiated UO_2-PuO_2 fuel (see Progress Report for April-May 1969, ANL-7577, pp. 144-149). These studies have indicated that cesium is involved in the corrosion reactions. It is believed that the intergranular corrosion is due to an attack of the stainless steel cladding by fission product iodine, cesium oxide, or both. The chemical activity of cesium is an important factor in

controlling, either directly or indirectly, the rate of this attack by iodine, since cesium would be expected to compete with iron, nickel, and chromium of the stainless steel cladding for the iodine.

A series of experiments is under way to determine the extent to which cesium interacts with oxide fuels. In the initial studies, the reaction of cesium with UO_2 is being investigated. In a recent experiment, pellets of UO_2 and cesium metal were heated in a sealed capsule at 725°C for three days. At the end of the thermal treatment, it was found that a partial breakup of the pellet had occurred, i.e., individual grains of UO_2 had separated from the surface of the pellet. X-ray spectrochemical analysis indicated a significant amount of cesium in the separated grains of UO_2. X-ray diffraction analysis indicated UO_2 with a lattice parameter of 5.47 Å, which is normal for nearly stoichiometric oxide. Microscopic examinations of the UO_2 revealed a small amount of a second phase; however, the amount was too small to isolate for study by X-ray diffraction. Additional experiments are under way in which the dependence of the cesium interaction on the O/M ratio of the oxide will be determined. It is also planned to measure the partial vapor pressure of cesium over Cs-UO_2 systems of various O/M ratios using a Knudsen effusion technique.

PUBLICATIONS

Neutron Radiography
J. P. Barton
Isotopes Radiat. Technol. 7(3), 284-285 (Spring 1970) Note

Image Detection Methods for 14.5 MeV Neutrons: Techniques and Applications
Harold Berger
Int. J. Appl. Radiat. Isotopes 21, 59-70 (1970)

Thorium-Uranium-Plutonium Alloys as Potential Fast Power-reactor Fuels. Part II. Properties and Irradiation Behavior of Thorium-Uranium-Plutonium Alloys
B. Blumenthal, J. E. Sanecki, D. E. Busch, and D. R. O'Boyle
ANL-7259 (Oct 1969)

Pulsed-bed Approach to Fluidization
Masaru Kobayashi
ANL-7592 (Oct 1969)

A Numerical Method for the Solution of a Shell Problem
Dusan Krajcinovic
AIAA Journal 7(12), 2350-2353 (1969)

Functionals for Flux Synthesis with Discontinuous Trial Functions
P. Lambropoulos and Victor Luco
ANL-7627 (Oct 1969)

Summary Review of Neutronic Noise Techniques for Incipient Boiling Detection in Liquid Metal Fast Breeder Reactors
T. J. Marciniak, L. J. Habegger, and H. Greenspan
ANL-7652 (Jan 1970)

Fast-neutron Total and Scattering Cross Sections of Bismuth
A. B. Smith, J. F. Whalen, E. Barnard,* J. A. M. de Villiers,* and D. Reitmann*
ANL-7636 (Nov 1969)

Space Time Nuclear Reactor Kinetics
W. M. Stacey
Academic Press, New York, 1969

The Attenuation of a Pulsed Field by a Conducting Sheet
D. L. Waidelich
IEEE Trans. on Instrumentation and Measurement IM-18(4), 326-330 (1970)

An Autographic Dilatometer for Use with Pyrophoric and Alpha-active Materials
F. L. Yaggee and J. W. Styles
ANL-7643 (Dec 1969)

---

*South African Atomic Energy Board.

IV. NUCLEAR SAFETY RESEARCH AND DEVELOPMENT

A. LMFBR Safety--Research and Development

1. Accident Analysis and Safety Evaluation (G. J. Fischer)

a. Sensitivity Studies and Basic Fast Breeder Reactor Safety Studies for Full Range of Accident Events, Including Studies of Parametric Changes

Last Reported: ANL-7618, pp. 120-122 (Sept 1969).

(i) Safety Studies. To understand the mechanism of fast reactor fuel-pin failure during a severe transient, a postrupture analysis of the latest fuel-meltdown experiment (S-4) in a sodium-filled piston autoclave (see Progress Report for October 1969, ANL-7632, pp. 141-142) has been carried out up to the time of first indication of pin failure. The analysis is based on the method used for Experiment S-3 and Mark-II loop Tr-1283 (see Progress Report for June 1969, ANL-7581, pp. 117-118).

The fuel loading and experimental configuration for the S-4 run were identical to those of S-3 experiment (see Progress Report for February 1969, ANL-7553, pp. 113-116). The five fuel rods containing 10%-enriched, nonpreirradiated UO_2 pellets and four helium-filled dummy rods were placed in the autoclave and subjected to the power transient in TREAT shown in Fig. IV.A.1. This experiment involved an integrated TREAT power of 1050 MW-sec with a peak power of 6250 MW. The later value was obtained from the reported value of 6650 MW (see ANL-7632) by requiring the power curve to reproduce the experimentally recorded value of integrated power (520 MW-sec) up to the peak power time. With allowance made for the self-shielding factor, the transient was found to be equivalent to about 3020 J/g of UO_2 for the edge fuel rods and 2810 J/g of UO_2 for the center fuel rod.

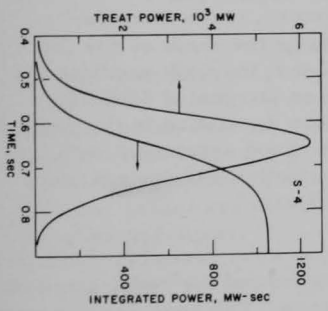

Fig. IV.A.1. TREAT Power Transient for Test S-4

The digital-computer code SAS1A has been used to evaluate the fuel-pin performance, particularly as regards the coolant temperature at the top end of the fuel section and the plastic deformation of the cladding. Results are shown in Fig. IV.A.2, where the thermocouple readings of the coolant temperature (indicated by the filled-in circles) are also included. The SAS1A-predicted values (given by the solid line for coolant temperature) are in good agreement with the measured temperatures. The SAS1A code also predicts that at the time of fuel-pin

rupture (0.68 sec for the edge fuel rod with an equivalent energy deposition of 2020 J/g of UO_2) about 95% of UO_2 was molten and the fuel-centerline temperature was about 4500°C. Furthermore, about 80% of the fuel was predicted to be at a temperature greater than 4000°C. It is realized that the peak fuel temperature should be much less than 4000°C, because UO_2 begins to boil around 3200°C and the heat of vaporization is about 2510 J/g of UO_2. No estimate of true fuel-centerline temperature could be obtained, because the present version of the heat-transfer module in SAS1A does not allow for the fuel vaporization.

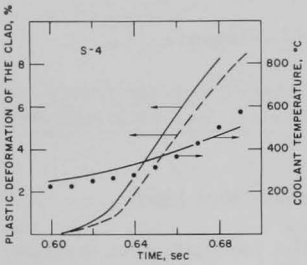

Fig. IV.A.2

Coolant Temperature at the Top End of the Fuel Section and the Plastic Deformation of the Cladding of the Fuel Pin Tested in Experiment S-4

The calculated plastic deformation of the cladding as a function of the transient time for the edge rod is shown (as a solid line) in Fig. IV.A.2. Note that the SAS1A code predicts a threshold plastic deformation of 8.2% at 0.68 sec (30 msec after the peak power), corresponding to an integrated TREAT reactor power of 705 MW-sec, or equivalent to an energy deposition of 2020 J/g of UO_2. The plastic-deformation curve for the center fuel pin (given by the dotted line) differs appreciably from the edge-rod curve because the calibration factor from TREAT power to the central-pin power is about 7% smaller than that of the edge rod. Therefore, one would expect the failure of the central pin to be correspondingly delayed. This prediction is verified by the experimentally observed delay of about 10 msec in the occurrence of the fifth pressure pulse. Furthermore, if the threshold plastic deformation for the center rod is taken to be the same as for the edge rod (i.e., 8.2%), it is seen from Fig. IV.A.2 that the code predicts the central pin to fail at 0.69 sec--corresponding to an integrated TREAT reactor power of 758 MW-sec or equivalent energy deposition in the central pin of 2030 J/g of UO_2. This prediction is also in good agreement with the experimental data. It should be pointed out that similar conclusions were drawn for the failure of the central rod in the S-3 run.*

Present results, like those for previous cases (Tr-1283, S-3), are based on a number of assumptions and limitations of the code, some of which are recalled here for the sake of convenience. The bond gas can cause excessive pressure on the cladding because of the increase in the gas ambient temperature and decrease in the available volume for the gas. Also, the fuel vapor pressure might be an additional source of loading on the unmelted UO_2, which in turn would load the cladding. These factors have been neglected in SAS1A predictions. It seems that both the bond-gas and fuel-vapor-pressure effects could be rather important factors in determining the threshold plastic strain of the cladding, especially for the S-4 run.

---

*Agrawal, A. K., "Analysis of Fuel Meltdown Experiment (S-3) with TREAT," in Reactor Physics Division Annual Report, July 1, 1968 to June 30, 1969, ANL-7410 (to be published).

Finally, in Fig. IV.A.3, we summarize the calculated plastic strain at the time of rupture for the three experiments. This figure is a plot of the SAS1A-calculated threshold plastic strain versus the observed energy deposition in the specimen rod at the time of pin failure. Note that the threshold values for S-3 and Tr-1283 are close to each other, but the threshold value for S-4 is quite high. This observation can perhaps be attributed to the nature of transient (TREAT periods for the Tr-1283, S-3, and S-4 runs were, respectively, 50.4, 53, and 34 msec). It thus seems that perhaps another important parameter to be incorporated in such a unified diagram is the rate of energy deposition, i.e., the TREAT reactor period. However, no attempts were made to include this variable in Fig. IV.A.3 because of lack of enough data points. It is expected that the analysis of rather slow General Electric transient experiments would be of great value in strengthening our understanding of the mechanism of fuel failure.

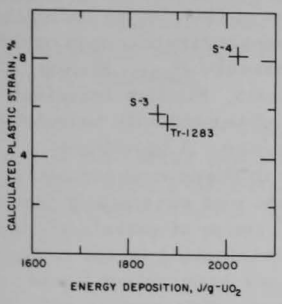

Fig. IV.A.3
Calculated Plastic Strain at the Time of Rupture for Experiments S-3, S-4, and Loop Tr-1283

2. Reactor Control and Stability (W. C. Lipinski)

a. Transfer-Function Techniques to Measure Large Fast Reactor Stability (L. J. Habegger)

Last Reported: ANL-7669, pp. 137-138 (Feb 1970).

A set of parameters was obtained for a realistic two-energy-group, one-delayed-group, two-temperature, multiregion LMFBR system. This set of parameters was used to compute the steady-state solution of the nonlinear reactor model. A linear spatially dependent reactor model was derived from the perturbation of the nonlinear model for the calculation of spatial transfer functions. The parameters being used in the linearized reactor model are modified to include the effects of the steady-state system temperatures.

3. Coolant Dynamics (H. K. Fauske)

a. Liquid-Vapor Dynamics (H. K. Fauske and M. A. Grolmes)

(i) Pressure Drop in Sodium Liquid-Vapor Flows

Last Reported: ANL-7632, pp. 130-131 (Oct 1969).

Experimental data obtained in the Sodium Flashing Facility have been analyzed. These data are pertinent to the understanding of incipient liquid superheat in forced-convection flow, boiling hysteresis, and

equilibration in steady flashing sodium flow. Figure IV.A.4 illustrates sustained liquid superheat up to 79°F at constant system velocity of 5 ft/sec. The system pressure is reduced stepwise until the inception of flashing is indicated by a rapid self-pressurization approaching the saturation pressure P_{sat}. Steady flashing flow follows. Similar incipient superheats were observed with velocities approaching 20 ft/sec. A blowdown facility was used in these experiments, so gas entrainment was essentially non-existent. The presence of entrained inert gas might be a contributing factor to the observed reductions in incipient liquid superheat with increasing system velocity. The so-called boiling hysteresis effect observed with nonmetallic fluids was observed here. Although significant superheating was sustained when the system pressure was decreased from an initial highly subcooled state, negligible superheating was sustained when flashing was ceased as a result of increasing the system pressure.

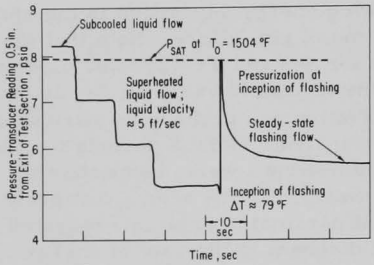

Fig. IV.A.4

Illustration of Incipient Superheat and Pressure Generation in Forced-convection Sodium Flow (for a 0.136-in.-ID, round test section in the Sodium Flashing Facility)

The extent of equilibrium in steady flashing sodium flow was ascertained from simultaneous temperature and pressure measurements (see Fig. IV.A.5) as well as measurements of liquid volume fraction. It is shown that thermodynamic equilibrium can be assumed for annular, annular dispersed flow, but that, for bubble flow at high flowrates, inertia effects must be accounted for in evaluation of vapor production.

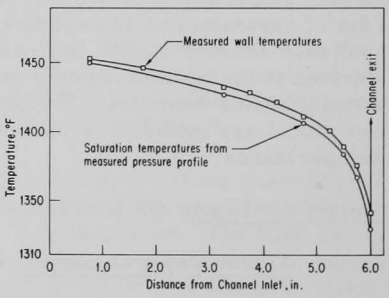

Fig. IV.A.5

Comparison of Measured Temperatures and Converted Temperatures from Pressure Measurements for Forced-convection Sodium Flashing Flow (where G = 180 lb/sec-ft^2 and T_0 = 1503°F)

4. Fuel Meltdown Studies with TREAT

a. Transient In-pile Tests with Ceramic Fuel (C. E. Dickerman)

Last Reported: ANL-7661, pp. 125-127 (Jan 1970).

(i) High-specific-energy UO_2-meltdown Experiment in Flowing Sodium ("Checkout Experiment"). The test section from the Checkout-2 experiment (2,590 J/g of oxide) was removed from the loop, using a glovebox. No difficulty was experienced with the glovebox transfer port or its accessories during the withdrawal operation. The loop was not contaminated or damaged.

No external damage to the test section was visible, but the top of the center (fueled) pin had moved upward about 1.5 in. The spades of all pins were still attached in place at the bottom of the fuel holder, but the top portion of the fuel-pin cladding slid out easily; the center portion had melted.

Some sodium is believed to remain trapped in the fuel holder, which will be slit longitudinally and opened to determine the extent of damage and distribution of meltdown products. This will be done as soon as the slitting machine is received from the decontamination facility.

After the test section was removed, the loop was moved to the sodium scrubber for recovery of the sodium and fuel residues. It had been noted previously that it was not possible to create sodium flow in the loop, so it was thought that the top pump flange was blocked by meltdown products. However, with the test section out, flow in the loop was attained, so it is now believed that the blockage is in the region of the test section.

The sodium drained from the loop contained black powder; the alcohol used as a wash contained noticeable quantities of fines. The sodium, alcohol, and fines have been saved and are available for analysis. No evidence has been found that the loop was damaged during the experiment; after reclamation operations, further inspections will be performed preparatory to reoutfitting the loop.

(ii) Loop Meltdown Experiment with Preirradiated UO_2 Pins. Detailed data from the power-calibration run for the Mark-II-loop meltdown experiment with three preirradiated UO_2 pins have been received and analyzed. The calibration run was made with fresh 10%-enriched UO_2 fuel elements. Radiochemical analysis and gamma counting of the fuel pellets led to an average value for the energy release in the pins during the calibration run of 11.27 J/g UO_2. The best estimate of the TREAT energy release during the calibration run is 5.3 MW-sec, which implies a calibration factor of 2.13 J/g UO_2-MW-sec. This calibration must be corrected for the difference in U-235 content between the calibration pins and the preirradiated pins of the experiment.

Four pins are available for the experiment, having enrichments estimated to be 7.1, 6.9, 8.5, and 8.5%, respectively, after irradiation. If the highest-enrichment pins are chosen for the experiment, the average

enrichment of the assembly will be 8.0%. Using the above data, a calibration factor for the preirradiated pins in the experimental arrangement is estimated to be 1.7 J/g-MW-sec.

The Mark-II-loop earmarked for use in this experiment, No. B-1, has been returned from Idaho, where it was used in TREAT calibration runs. Outfitting of the loop is in progress. Due to lack of a shipping cask suitable for transport of a loop containing preirradiated pins, it will be necessary to ship the loop and the pins to Idaho separately and assemble the experiment there. The test section and bayonet subassembly containing the pins will be shipped in the "T-2" cask borrowed from General Electric. Assembly of the test section into the loop will be done in Idaho.

Design of the specialized test-section parts for use in this experiment has been completed. The design includes provision for extensive coolant-temperature instrumentation, including one inlet and four outlet thermocouples. Most of the assembly work will be done on the bench prior to insertion of the pins in the cave. The test-section design includes many features from a successful test section used with the Mark-I loop.

(iii) TREAT Experiments with Unirradiated Mixed-Oxide Pins. The first TREAT experiment has been performed with an unirradiated mixed-oxide fuel pin, using a pin from the Prototype Fast Reactor fuel-development program. Test data indicate test objectives have been met. Good agreement exists between experimental outlet coolant temperature and the curve calculated by the SAS1A code.

For the second experiment, PNL has supplied a mixed-oxide element, PNL-17-42, of the type designed for use with the Mark-E-37A instrumented EBR-II subassembly. This element is similar enough to the first test element so that no new TREAT calibration or significant fuel-holder modifications are necessary for the second experiment.

The data package for the second experiment, "Requirements for the Second Failure Threshold Test (Series H)," has been submitted to the TREAT staff and to PNL.

b. Experimental Support (C. E. Dickerman)

Last Reported: ANL-7661, pp. 127-128 (Jan 1970).

(i) Shipping Cask. RDT comments on the quality-assurance provisions and the technical content of the cask submittal were received. The comment letter has been reviewed. Design modifications are being made in response to the RDT technical comments. The cask specifications and quality-assurance plans are being revised to conform to RDT Standard F2-2T.

(ii) Fast-neutron Hodoscope

Not previously reported.

Programming and analysis of data from the new digital system of the fast-neutron hodoscope have been advanced sufficiently to draw some initial conclusions about performance. Because of funding limitations, some transients have been run with the hodoscope operating at suboptimum conditions.

Data from Transient 1255 are almost fully processed; these data are being used as a clearcut prototype for purposes of testing the computer program, as well as providing important hodoscope operational information.

The album of transient observations is sufficiently complete to demonstrate clearly evident details of fuel-pin distortion as a function of time with high spatial and time resolution. Detailed analysis is yet to be performed in terms of fuel motion.

Before each transient, either a moving or stationary scan has been carried out to provide a preview of signal-to-background conditions and to ensure that the fuel pin is centered. These scans have been used to indicate quality of response.

As a result of examination of the transient data, it appears that the estimates of response quality for transients have been too conservative by a factor of three; that is, during a transient, the signal-to-background ratio is about three times better than during a steady-state run. This phenomenon appears to arise from several considerations. In early tests of neutron-detection performance, the residual background component was estimated to be due to scattered core and source neutrons, on the basis of indirect evidence provided by the neutron-channel integral bias curves. However, there are two pieces of evidence from the transient data that suggest that the residual "background" effects (in Transient 1255) are dominated by hard gammas from the reactor.

(a) For Transient 1255 to have a signal-to-background ratio of 20:1 (versus the steady-state value of 7:1) requires a delayed-neutron or delayed-gamma type of effect. Delayed neutrons are a small fraction of events, but delayed gammas in fission are approximately 50%, and radioactive-decay gammas from thermal capture are also perhaps 50% or more. The transients last only some few hundred milliseconds, or a matter of seconds at most, so it appears that the delay in issuance of these gammas is sufficient to cut down "background" counts during the transient. Of course, for steady-state runs, an equilibrium condition is reached, which

includes such delayed gammas. These factors were taken into consideration in early analysis of the hodoscope versus the original gamma-scanning system, but we had not previously had quantitative data that would permit establishing this feature.

A preliminary examination of Transient 1283 (Mark-II sodium loop) also suggests a transient signal-to-background ratio larger than the steady-state value.

(b) It has been apparent for some time from previous hodoscope film that there has been an anomalously high "tail" in the data after the cessation of all transients. It is now evident that this confirms the delayed-gamma effect.

Accordingly, the quality of performance of the fast-neutron hodoscope appears to be markedly better than the original steady-state experimental data indicated.

The ratio of signal level at 50 kW for Transient 1255 to the peak power level of 150 MW is 3000; this is also the apparent ratio of count-rates for the hodoscope, which confirms linearity up to 50,000 counts/sec.

A second, but deleterious, aspect of performance that has arisen is apparently due to the high efficiency of the neutron-detection channels; they appear to be too efficient for high-power transients (above a 500-MW peak). Despite earlier estimates taking this into consideration, Transient 1283 indicates that the rates reached greater than 10^6 counts/sec, and that many channels, when faced with rates exceeding 10^5 counts/sec, began to behave in a nonlinear fashion. Because there is more than adequate information at a maximum of 10^5 counts/sec (equivalent to 100 counts/msec), the immediate remedy is simple enough: reduce the system high voltage and recalibrate at a lower efficiency. However, to do this is inconvenient, as it requires one or two technicians for one or two days. Accordingly, investigations are being made of the causes and of possibly more efficient remedies, such as automatic gain adjustment.

Thus, from the limited information available, it can be said that the fast-neutron hodoscope is providing much better performance, quality, and efficiency than the original conservative estimates, although care must be taken not to allow high-power nonlinear effects to distort the data.

c. Postirradiation Examinations (L. A. Neimark)

Last Reported: ANL-7632, pp. 134-137 (Oct 1969).

(i) Examination of Unirradiated PFR Fuel Elements. The nondestructive characterization of 66 unirradiated PF

elements has been completed in preparation for tests in TREAT. The characterization included profilometry, eddy-current inspection, balance-point determinations, length measurements, and radiographs.

(ii) Examination of Irradiated PFR Fuel Elements. The nondestructive examination of seven prototypal PFR fuel elements that were irradiated in the DFR to 5 at. % burnup has been completed. The examination included neutron radiography, visual inspection, profilometry, balance-point determinations, length measurements, volume determinations, eddy-current inspection, and gamma scanning. The destructive examination of one element as a control for the remaining six elements that will be tested in TREAT has been postponed indefinitely.

(iii) Examination of EBR-II Irradiated Fuel Elements. Subassembly X040, the "lead" assembly of unencapsulated oxide pins in EBR-II, contained 19 pins of the same design to provide a source of domestic mixed-oxide pins for safety experiments in TREAT. One pin, 012, was removed at 3 at. % burnup as a lead. The remaining 18 are nearing their specified burnup of 5 at. % in EBR-II.

The nondestructive phase of the examination of Element 012 from Subassembly X040 has been completed. This element achieved a burnup of 3 at. % at a peak linear power rating of 16 kW/ft. The examination has included visual inspection, profilometry, gamma spectrometry, eddy-current inspection, and a measurement of fission-gas release. The element was intact and, from the evidence gathered to date, there were no indications of incipient failures.

A suspected incipient crack was found in the plenum region, about 2 in. above the top of the fuel column, during the interim examination at EBR-II. The "defect" appears to be more of a scratch, an old one, rather than an incipient crack. The area will be examined metallographically.

After removal of the spacer wire, the area covered by the wire in the fuel section was readily discernible. Also visible were shallow scratches where the wire rubbed against the cladding.

The diameter profile of the element was measured at orientations of 0, 45°, 90°, 180°, 225°, and 270° of arc. All scans started 3/4 in. from the bottom of the fuel section. The maximum diameter increase (based on a nominal preirradiation diameter of 0.290 in.) was 1.5 mils and occurred about 5.7 in. above the bottom of the fuel column. The diameter increase was not uniform around the circumference of the element, with a "minimum" maximum of 0.8 mil. The diameter change along the length of the element conformed only generally to the flux profile with a number of peaks and valleys. There was no evidence of "pellet ridging" or "bambooing" along the element.

The gamma activity of the element was scanned using a 3-in. NaI crystal and a 400-channel pulse-height analyzer. The element was scanned for gross activity, Ru-103, Cs-137, and Nb, Zr-95. The gross activity showed a typical profile for EBR-II, with the peak occurring slightly below the reactor midplane and with higher activity at the bottom than at the top of the element. The ruthenium scan indicated what might be small, locally high concentrations of solid fission products. The niobium-zirconium scan was relatively flat and showed no local concentrations of consequence. The cesium scan, however, showed a definite high concentration at the top of the fuel column and a general trend indicating upward migration of this volatile species. There was another high concentration of cesium 3 in. down from the top of the fuel.

The element was inspected by two eddy-current methods. The first method used a pulsed signal and a point probe. The element was scanned every 45° along its length. The point probe has a "window" of about 30°, so complete coverage was not obtained. However, the coverage should be sufficient to detect all but very localized internal defects in the cladding. The instrument was standardized against standard defects of 10, 20 and 40% of the 20-mil cladding wall thickness. In three of the eight orientations, there were indications that defects between 10 and 20% of the wall thickness (2 to 4 mils) might exist in the top half of the fuel section. (This is where ANL has found the most extensive cesium-iodine interaction with the cladding.) In addition, a consistent abnormality, about 3 mils deep, appeared between 1 and 2 in. from the bottom of the fuel. A second eddy-current procedure using a circumferential probe was inconclusive. It should be pointed out that the eddy-current procedures are new and the results have yet to be correlated with metallography or microprobe analysis.

The element was punctured for fission-gas analysis; 37.06 cm^3 of gas were recovered. The free-void volume in the element was measured as 4.69 cm^3, which agrees well with a calculated volume of approximately 5.1 cm^3. The theoretical yield of fission gas for the calculated burnup of 3 at. % would be 30.07 cm^3. This suggests that a considerable amount of adsorbed gas was released from the 83% dense pellets. Samples of the collected gas are being analyzed quantitatively.

d. TREAT Operations (J. F. Boland)

Last Reported: ANL-7661, p. 128 (Jan 1970).

(i) Reactor Operations. Neutron radiographs were made of EBR-II blanket rods, capsules from EBR-II experimental Subassemblies X020 and X012, EBR-II driver-fuel elements, and TREAT experiment GE-FCF-C6B.

Experiment ORNL FRF-2, a cluster of seven Zircaloy-clad, UO_2 fuel rods containing one preirradiated rod, was subjected to two transient

irradiations. The final transient caused failure of one or more of the rods in a flowing steam environment designed to simulate loss-of-coolant conditions. Fission products were collected in a series of traps, which will be analyzed to obtain fission-product-release data.

A Zircaloy-clad UO_2 fuel rod supplied by PNL was irradiated under steady-state conditions in a water tube inside a transparent capsule to determine if flux filters installed around the ends of the rods were effective in preventing flux peaking in the end pellets. Analysis of the pellets after the irradiation showed that the filters had decreased the flux in the end pellets about 20%, which is considered adequate to prevent end effects from influencing failure thresholds during transient tests. Zircaloy-clad pellet-fuel samples PNL-MDF-3 and PNL-MDF-4 and powder-fuel sample PNL-MDF-1 were subsequently subjected to transient irradiations, and end effects noted in previous tests were not observed. One additional sample of each type of fuel remains to be tested in the current series of experiments to establish failure thresholds for these types of fuels. High-speed motion pictures are being obtained during this series of tests.

Experiment GE-FCR-C6B, which contains three stainless steel-clad UO_2 fuel samples, was subjected to a low-energy transient to establish a correlation between reactor energy release and sample energy release. Temperature data obtained during the transient are being analyzed by General Electric to obtain this correlation. When the analysis is completed a test transient will be run on this capsule.

(ii) Development of Automatic Control System for Power Level. Testing of the hydraulic control-rod-drive system continues at the contractor's plant. Although the entire system was operating in January, final testing has been delayed by a number of minor problems that have required disassembly of major components for corrective action. A problem common to a number of components has been the use of materials that are incompatible with the fire-resistant hydraulic fluid. In some cases, replacement parts of the correct material have not been immediately available, and sequential detection of the problems has caused delivery delays to be additive. The contractor now hopes to have the system ready for shipment by April 15.

5. Materials Behavior and Energy Transfer

a. High-temperature Physical Properties (M. G. Chasanov)

Last Reported: ANL-7655, pp. 134-135 (Dec 1969).

(i) Experimental Determination of Enthalpies and Heat Capacities of Molten $(U,Pu)O_2$ Materials. Enthalpy and heat-capacity measurements of fuel materials are used to calculate fuel temperatures

resulting from a reactor accident. This information is needed to evaluate the effects of an accident, such as Doppler shutdown characteristics, extent of fuel melting, and cladding interactions. Our measurements of the enthalpies and heat capacities of fuel materials are based on the method of mixtures, in which a capsule containing a sample of the material for study is equilibrated at the desired temperature and dropped into an adiabatic calorimeter. Heat-loss corrections are made by performing the same experiment using a similarly constructed empty capsule.

In the present work, provisions for capsule fabrication, for sample preparation, and for sealing the capsules by beam welding have been made for measurements with $(U,Pu)O_2$ mixed-oxide fuel. Modifications of the calorimeter system used for liquid UO_2, so as to permit work with $(U,Pu)O_2$, are almost complete. A walk-in hood has been constructed around the equipment, and control of an experiment can now be performed from outside the hood. Several improvements have also been made in the equipment to allow for simpler, more exact operations: it will now be possible to test the temperature-measuring system using a calibrated ribbon lamp during an experiment; in addition, an automatic optical pyrometer will be used, thus reducing the time that the viewing prism is exposed to tungsten vapors from the hot sample.

Two test drops using solid tungsten slugs have been made, and the system appears to be operating satisfactorily. A few minor adjustments will be needed, and then experimental work will be resumed.

Before proceeding to mixed-oxide fuels, an attempt will be made to extend the data on liquid UO_2 to higher temperatures.

b. Facility Definition and Utilization

Last Reported: ANL-7606, pp. 129-132 (Aug 1969).

The review of existing and firmly planned reactor facilities capable of performing safety experiments is continuing. Bases for containment of experimental loops are being studied; parametric design studies of loops are underway to establish vessel size, wall thickness, and explosion-containment capability for safety experiments having from 1 to 217 LMFBR fuel elements. Data are being surveyed and compiled on SEFOR, TREAT, PBF, CDC, ETR, MTR, GETR, other water reactors, FFTF, and EBR-II. The capabilities of these facilities, including reasonable modification, for carrying out LMFBR experiments are being evaluated.

6. Fast Reactor Safety Test Facility Study (L. Baker, Jr.)

a. Programmatic Definition and Justification

Last Reported: ANL-7606, pp. 128-129 (Aug 1969).

Comments from industry, national laboratories, and the AEC on the document "Project Report: Studies of Safety Test Facilities. Volume 1, Program" have been received and have been used as the basis for preparation of a revised document.

A comprehensive basis for experiment priorities and schedules must be based on a delineation of LMFBR accidents. Thus the potential source of LMFBR accidents have been listed, and the likely effects of these initiating events have been considered in detail. These effects were grouped to form a concise list of general accident categories. The general accidents are being reviewed in specific terms--first for FFTF, then for a representative demonstration plant, and finally for a representative 1000-MWe target plant. There are three steps to the review: (1) develop the most likely sequence of events for each potential accident, including an identification of each point in the sequence where accident detection and protective system action might be achieved, (2) develop a favored approach to accommodate each potential accident, and (3) identify key uncertainties and unknowns.

The recommended program of experiments and experiment priorities is derived from an assessment of the optimum means to resolve specific uncertainties through in-pile experimentation. The schedule of experiments is based on the specific needs and key dates for FFTF, demonstration plants, and 1000-MWe target plants.

The accident sequences will be substantiated by calculations using accident-analysis models and codes developed in other activities.

7. 1000-MWe Safety Analysis Studies

a. Contract Management, Technical Review, and Evaluation (L. W. Fromm)

Last Reported: ANL-7661, pp. 129-130 (Jan 1970).

(i) Babcock & Wilcox Co. Subcontract

(a) Phase II: Accident Analysis and Selection of Safety Features. The Phase-II work is approximately two weeks behind schedule. The second quarterly progress report was issued in February. Four technical notes are being prepared.

Sensitivity studies of flow abnormality were extended to determine the effects of reduced rod worths or transients. Preliminary results have been obtained of the reactivity effects of an inadvertent withdrawal of a single control rod.

Studies to identify the possible violent events in a single-pin failure or a chain of pin failures have continued. Major emphasis has been given to developing the models required. The work on sodium-vapor explosion has concentrated on a study of possible conditions and triggering mechanisms.

Work by B&W continued on the identification and review of candidate safety features. A review of the various approaches taken toward protective instrumentation for individual fuel assemblies was made. The differences in approach indicate the uncertainty in functional requirements and capabilities of instruments.

8. Post-accident Heat Removal (R. O. Ivins)

a. Engineering Analyses (J. C. Hesson)

(i) Thermally Stable Fuel-debris Configurations in Sodium

Last Reported: ANL-7661, pp. 134-136 (Jan 1970).

The analysis of heat removal from molten or collapsed core material under sodium is continuing.

In considering heat transfer from and the behavior of a molten pool of fuel, the question arises as to whether a surface crust will form. This depends largely on the depth of the pool, the emissivity, the specific decay heat, and the melting temperature of the fuel debris. Other factors that influence the formation of a surface crust are the temperature of the support on which the pool rests, the boiling temperature, the thermal conductivity of the fuel debris, and whether or not the surface of the pool is covered with liquid sodium or vapor.

If the pool has a large area with respect to depth, most of the decay heat would be removed through the top and bottom surfaces. Due to thermal convection and boiling, the heat removed from the top would be greater than that removed from the bottom, because vapors from the boiling fuel would rise and tend to condense at the pool surface.

The heat-transfer rate through the bottom of the pool, by conduction only in the fuel, to a support surface at T_s would be given by

$$Q_b = \sqrt{(T_b - T_s)\, 2kq}\ (\text{cal/sec-cm}^2),$$

and the thickness of the layer of fuel transferring its heat through the bottom by

$$L_b = \sqrt{(T_b - T_s)(2k/q)}\ (\text{cm}),$$

where T_b is the boiling temperature of fuel debris in °C, T_s is the bottom-surface temperature of fuel debris in °C, k is the thermal conductivity of fuel (solid and liquid) in cal/sec-cm-°C, and q is the specific decay heat in cal/sec-cm^3.

For a pool surface in contact with vapor, radiation would be the major method of heat transfer. The heat radiation from a surface at temperature T_1(°K) to surroundings at temperature T_2(°K), where the emissivities ϵ of the radiating and surrounding surfaces are the same for the two temperatures, is approximately

$$Q_t = 1.37\ E\left[\left(\frac{T_1}{1000}\right)^4 - \left(\frac{T_2}{1000}\right)^4\right] \text{(cal/sec-cm}^2\text{)}.$$

If the areas of the surface and its surroundings are the same (parallel surfaces),

$$E = \frac{\epsilon}{2 - \epsilon},$$

and if the area of the surface is small compared to its surroundings,

$$E = \epsilon.$$

Table IV.A.1 shows values of Q for parallel surfaces and for various values of T_1 and T_2 with $\epsilon = 0.66$.

TABLE IV.A.1. Heat Radiation between Parallel Surfaces (for $\epsilon = 0.66$)

	Q (cal/sec-cm^2)	
T_2 (°K)	T_1 = 3100°K (2827°C)	T_1 = 3000°K (2727°C)
2000	52.3	44.5
1750	56.8	49.1
1500	59.8	52.0
1250	61.6	53.6
1000	62.6	54.8

For a pool surface in contact with boiling sodium at 1 atm, critical heat fluxes of about 5×10^5 to 10^6 Btu/hr-ft^2 (or 38 to 75 cal/sec-cm^2) could be obtained.* Heat fluxes greater than this would cause vapor-film formation (burnout), and heat transfer by radiation would occur. We

*From Fig. 21 in Collier, J. G., and Kosky, P. G., Natural Convective Boiling of the Alkali Metals: A Critical Review, AERE-R5436 (Sept 1967).

would expect the temperature of the surroundings above the pool to be not greater than the melting point of stainless steel (1700°K) and also expect the freezing point of the UO_2 fuel debris to be about 2700 to 2800°C. Thus we could expect that a heat flux of about 50 to 60 cal/sec-cm^2 from the surface of a pool of UO_2 fuel debris, in contact with sodium or a vapor film, would be required to avoid a crust formation.

For fuel debris, melting and boiling temperatures of 2700 and 3180°C, respectively, a thermal conductivity of 0.005 cal/sec-cm-°C, and an emissivity of 0.66, the thickness of a pool resting on a support surface at 1450°C (near the melting temperature of stainless steel) is calculated by

$$L = L_b + L_t = \frac{Q_b + Q_t}{q} = \frac{4.15}{q^{1/2}} + \frac{60}{q},$$

where q is the specific decay heating (in cal/sec-cm^3) of the fuel debris.

Table IV.A.2 shows the approximate minimum thickness of a pool of fuel at which a surface crust would melt for the assumed conditions.

TABLE IV.A.2. Minimum Thickness of Fuel Pool at Which Surface Crust Would Melt

Decay Heat		Minimum Pool Thickness L (cm)
q (cal/sec-cm^3)	Percent of Reactor Power	
1	0.25	64.2
3	0.75	22.4
6	1.50	11.7
12	3.00	6.2
24	6.00	3.3

Because the various factors that affect crust formation, such as melting and boiling temperatures and thermal conductivities of constituents, are not well known, experiments should be conducted to obtain more accurate values for use in calculations.

B. Effluent Control--Environmental Studies--Research and Development

1. Thermal-Plume Transport in the Great Lakes (B. Hoglund and J. J. Roberts)

Not previously reported.

An assessment of the physical and biological consequences of discharges of heated water and low-level radioactivity

generation facilities to be sited on the Great Lakes is necessary if state and federal regulatory officials are to design rational plans for the growth and surveillance of the power industry. The Argonne Great Lakes Research Program will evaluate and, where necessary, develop methods for determining the potential environmental impact of light water and LMFBR systems. Four general areas will be studied:

1. prediction of temperature fields in the vicinity of plant outfalls and on a lake-wide scale;

2. assessment of physical effects of these heated discharges, such as local meteorological influences;

3. assessment of biological consequences of discharges of heated water and low-level radioactivity;

4. determination of regional energy, water, and pollutant budgets to anticipate perturbations in lake-wide temperatures and investigation of the potential for synergistic interactions with other effluent sources.

These research areas contain the principal elements which will influence the design of programs for effective management of the lake environment during a period of expanding demands for electric power.

The Laboratory will endeavor to integrate its program with other research organizations, and to coordinate results in a fashion to optimize their usefulness in assessing the influence of nuclear power stations sited on the Great Lakes. Interlocking with existing programs will be accomplished in several ways: 1) to make appropriate individuals consultants to Argonne, 2) to subcontract certain tasks, and 3) to undertake cooperative investigations where appropriate.

The effort in FY 1970 will be devoted to compiling review or state-of-the-art papers, initiating theoretical modeling studies, and possibly conducting a modest field program at sites near Argonne along with an allied analytical support program.

In FY 1971 a more extensive field program will be undertaken, which will include sites more remote from the Laboratory. Appropriate sampling will also be conducted on the open Lake. Laboratory investigations will be initiated, in part to supplement the field work, to determine reconcentration factors for specific radionuclides; including tritium, and to examine radionuclide uptake as a function of temperature in important aquatic species.

The modeling studies will begin to undergo field verification during FY 1971, and a relatively large analytical effort will be initiated to provide additional input to the mass-energy balance and lake-circulation portions of the program.

Part of the Great Lakes Research Program is funded by the Division of Biology and Medicine (DBM) and part by the Division of Reactor Development and Technology (DRDT). The DBM funding covers radiological aspects, field-measurement studies, and meteorology-climatology effects. The DRDT funding covers thermal-plume dispersion studies of mass-energy balance, and lake-circulation studies. Although the funding arrangement indicates a separation of the programs, they are in fact closely related, and the studies are coordinated to integrate the efforts. In view of the nature of this reporting document, however, only the work funded by DRDT or work funded by DBM that is directly applicable (such as field data) will be reported in these Monthly Progress Reports.

a. State-of-the-Art Paper (J. V. Tokar and D. Miller)

A set of state-of-the-art papers on thermal discharges is being prepared. Visits were made to organizations studying effects of heated discharges to cooling water. Their programs were discussed for contributions to our state-of-the-art study, and reports and papers were collected for documentation and reference. Organizations visited were: Pacific Northwest Laboratory of Battelle Memorial Research Institute, Hydronautics, Inc., Commonwealth Edison Co., the Chesapeake Bay Institute, Johns Hopkins University, St. Anthony Falls Hydraulic Laboratory, University of Minnesota, Illinois Institute of Technology, and University of Illinois-Chicago Circle Campus. In addition, a large number of limited-distribution reports were obtained from the Division of Licensing and Regulation of the AEC for our analysis. A number of major electrical utilities and their consultants were contacted to identify contributions being made to the state-of-the-art by these groups. All of the documents are being logged in and categorized for easy reference.

b. Numerical Modeling of Thermal Plumes (M. Prastein, T. Hughes, and A. Szewczyk)

The following work has been accomplished as part of an overall effort in numerical modeling of the thermal plume produced by heated water effluent:

1. Difference equations for the symmetric semi-infinite jet (x-y plane) with various boundary conditions have been formulated; physical quantities computed include temperature, stream function, velocity, and pressure.

2. Provision has been made for use of varying mesh size in the computations, it having been established that a constant mesh size was not satisfactory.

3. Procedures have been developed for rapidly and efficiently obtaining "initial solutions" for use in starting the computations of unsteady flow; the method used is that of successive overrelaxation (SOR).

4. Graphics for display of streamlines and isotherms, as they evolve in time, have been developed.

The numerical method considers the two-dimensional problem in the vorticity-stream function formulation. The fundamental differential equations for two-dimensional horizontal flow are

$$\frac{\partial\omega}{\partial t} + \frac{\partial(u\omega)}{\partial x} + \frac{\partial(v\omega)}{\partial y} = \frac{1}{R_e}\left\{\frac{\partial^2\omega}{\partial x^2} + \frac{\partial^2\omega}{\partial y^2}\right\}; \tag{1}$$

$$\nabla^2\psi = -\omega; \tag{2}$$

$$\frac{\partial\theta}{\partial t} + \frac{\partial(u\theta)}{\partial x} + \frac{\partial(v\theta)}{\partial y} = \frac{1}{P_R R_e}\left\{\frac{\partial^2\theta}{\partial x^2} + \frac{\partial^2\theta}{\partial y^2}\right\}; \tag{3}$$

$$u = \partial\psi/\partial y; \tag{4}$$

$$v = -\partial\psi/\partial x, \tag{5}$$

where all quantities have been scaled to make them dimensionless; u is the (dimensionless) component of velocity parallel to the jet centerline, v the transverse component of velocity, θ the temperature, ψ the stream function, ω the vorticity, t the time, R_e the Reynolds number and P_R the Prandtl number. The finite difference equations currently being used are as follows: For vorticity and energy transport (explicit, conditionally stable),

$$\frac{S^{k+}_{i,j} - S^k_{i,j}}{\Delta t} + \frac{\delta(uS)^k}{\delta x} + \frac{\delta(vS)^k}{\delta y} = \frac{2\alpha}{a_{i-\frac{1}{2}} + a_{i+\frac{1}{2}}}\left\{\frac{S^k_{i+1,j} - S^k_{i,j}}{a_{i+\frac{1}{2}}} - \frac{S^k_{i,j} - S^k_{i-1,j}}{a_{i-\frac{1}{2}}}\right\}$$
$$+ \frac{2\alpha}{b_{j-\frac{1}{2}} + b_{j+\frac{1}{2}}}\left\{\frac{S^k_{i,j+1} - S^k_{i,j}}{b_{j+\frac{1}{2}}} - \frac{S^k_{i,j} - S^k_{i,j-1}}{b_{j-\frac{1}{2}}}\right\}; \tag{6}$$

$$\frac{\delta(uS)^k}{\partial x} = \left\{\begin{array}{ll} \frac{1}{a_{i-\frac{1}{2}}}\left(u^k_{i,j}S^k_{i,j} - u^k_{i-1,j}S^k_{i-1,j}\right), & u_{i,j} > 0 \\ \\ \frac{1}{a_{i+\frac{1}{2}}}\left(u^k_{i+1,j}S^k_{i+1,j} - u^k_{i,j}S^k_{i,j}\right), & u_{i,j} < 0 \end{array}\right\}; \tag{7}$$

$$\frac{\delta(vS)^k}{\delta x} = \left\{ \begin{array}{ll} \frac{1}{b_{j-\frac{1}{2}}}\left(v^k_{i,j}S^k_{i,j} - v^k_{i,j-1}S^k_{i,j-1}\right), & v_{i,j} > 0 \\ \frac{1}{b_{j+\frac{1}{2}}}\left(v^k_{i,j+1}S^k_{i,j+1} - v^k_{i,j}S_{i,j}\right), & v_{i,j} < 0 \end{array} \right\}, \tag{8}$$

where a and b denote the local mesh dimensions, S stands for ω or θ, and α for either $1/R_e$ or $1/P_R R_e$.

For stream functions,

$$\psi_{i,j} = \frac{1}{d_{i,j}}\left\{\frac{\omega_{i,j}}{2} + \frac{\psi_{i+1,j}}{C^{(1)}_{i,j}} + \frac{\psi_{i-1,j}}{C^{(2)}_{i,j}} + \frac{\psi_{i,j+1}}{C^{(3)}_{i,j}} + \frac{\psi_{i,j-1}}{C^{(4)}_{i,j}}\right\}, \tag{9}$$

where $d_{i,j}$ and the $C_{i,j}$ are functions of the variable mesh;

$$C^{(1)}_{i,j} = a_{i+\frac{1}{2}}(a_{i-\frac{1}{2}} + a_{i+\frac{1}{2}});$$

$$C^{(2)}_{i,j} = a_{i-\frac{1}{2}}(a_{i-\frac{1}{2}} + a_{i+\frac{1}{2}});$$

$$C^{(3)}_{i,j} = b_{j+\frac{1}{2}}(b_{j-\frac{1}{2}} + b_{j+\frac{1}{2}});$$

$$C^{(4)}_{i,j} = b_{j-\frac{1}{2}}(b_{j-\frac{1}{2}} + b_{j+\frac{1}{2}}); \tag{10}$$

and

$$d_{i,j} = \frac{1}{C^{(1)}_{i,j}} + \frac{1}{C^{(2)}_{i,j}} + \frac{1}{C^{(3)}_{i,j}} + \frac{1}{C^{(4)}_{i,j}}. \tag{11}$$

An iterative solution of Eq. (9) by SOR is obtained from

$$\psi^{(\ell+1)}_{i,j} = \frac{\lambda}{d_{i,j}}\left\{\frac{\omega_{i,j}}{2} + \frac{\psi^{(\ell)}_{i+1}}{C^{(1)}_{i,j}} + \frac{\psi^{(\ell+1)}_{i-1,j}}{C^{(2)}_{i,j}} + \frac{\psi^{(\ell)}_{i,j+1}}{C^{(3)}_{i,j}} + \frac{\psi^{(\ell+1)}_{i,j-1}}{C^{(4)}_{i,j}}\right\} + (1-\lambda)\,\psi^{(\ell)}_{i,j},$$

where λ is the relaxation parameter and ℓ the iteration count.

Presently under development are

1. graphics for the display of velocities;
2. unsteady solutions over a region of twenty-five jet diameters;
3. testing of various outflow boundary conditions;

4. provision of a restart facility;

5. models for the variation of eddy viscosity and eddy diffusivity.

Under consideration is the use of implicit, unconditionally stable methods to improve the speed of the computations.

c. Mass-Energy Balance (J. G. Asbury)

A calculation has been made of the average annual increase in Lake Michigan water-surface temperature per gigawatt increase in the rate of advective input. The result, to first order, is independent of lake-water movement patterns and short-term fluctuations in meteorological variables. The average increase in water-surface temperature is probably the single most meaningful parameter for indicating the lake-wide effects of thermal discharges. The accuracy of the calculation (~25%) is limited only by the accuracy with which the annual average of the heat-exchange coefficient can be determined.

The increase in the evaporative water loss associated with the increase in water-surface temperature has also been calculated.

The calculations are based upon the formulation for the rate of heat exchange across a lake surface developed by Edinger and Geyer and subsequently extended by the Cornell Aeronautical Laboratory group in their study of Cayuga Lake.*

From quite general arguments it can be shown that the average annual increase in lake surface temperature can be written as

$$\Delta T = q/\bar{K}, \tag{1}$$

where q is the rate of thermal discharge and $\bar{K}$ the annual average of the heat-exchange coefficient.

The heat-exchange coefficient can be written as the sum of three terms:

$$K = 15.7 + \beta f(w) + C_1 f(w), \tag{2}$$

where the three terms represent, respectively, back radiation, evaporative heat transfer, and sensible heat transfer. The wind speed function f(w) has been parameterized by several authors. The constant C_1 is the Bowen

*Edinger, J. E., and Geyer, J. C., Heat Exchange in the Environment, EEI Publication No. 65-902 (June 1965); Sundaram, T. R., Easterbrook, C. C., Piech, K. R., and Rudinger, R., An Investigation of the Physical Effects of Thermal Discharges into Cayuga Lake, CAL Report No. VT-2616-0-2 (Nov 1969).

coefficient (0.26 mm Hg $°F^{-1}$), and β is the slope of the saturated vapor pressure curve (mm Hg $°F^{-1}$). Units for f(w) are BTU/(ft^2-day-mm Hg); for K, BTU/(ft^2-day-°F).

Meteorological data obtained from the Illinois State Water Survey was used in evaluating K. These data include wind speeds and dew-point temperatures collected from 1950 through 1968 at six weather stations sited around Lake Michigan. The annual average value for the exchange coefficient deduced from these data is K = 152 BTU/(ft^2-day-°F). For a discharge rate of 1 gigawatt--equivalent to 0.13 BTU/(ft^2-day)--the Lake Michigan water-surface temperature rise is 8.5×10^{-4}°F. The associated evaporative water loss is 12 cfs per gigawatt advective input.

C. Engineered Safety Features--Safety Features Technology--Research and Development--Containment

1. Hydrodynamic Response to High-Energy Excursion (Y. W. Chang)

a. Automatic Rezoning of Code to Extend Excursion Treatment into Sodium-momentum Domain

Last Reported: ANL-7669, pp. 141-142 (Feb 1970).

Programming of the rezoning code continues. The scope of the code has been extended to include the treatment of the multimaterial zones. The number of both single and multimaterial zones to be rezoned for each run is limited to 4000; the number of multimaterial zones is limited to 500.

b. System Geometries and Excursion Magnitudes and Durations

Last Reported: ANL-7618, pp. 137-138 (Sept 1969).

The REXCO-H code can give the reactor designer some insight into the phenomena occurring in a reactor excursion. The purpose of this study is to show the difference between a chemical explosion and a nuclear excursion, as obtained from computer calculations, and to demonstrate the usefulness of the computer code. The mathematical model used to simulate a TNT explosion is shown in Fig. IV.C.1, which was the same experimental model selected for comparison of the computer code with existing experiments (see Sect. IV.C.1.c below), except that the mesh size was increased. As a result, the mesh distortion was reduced and computation was able to proceed to a much longer time without rezoning. In the nuclear-excursion model, the TNT charge is replaced by vaporized oxide fuel, which has a work-energy equivalent to that released in the TNT charge. Figure IV.C.2 shows that the pressure loading on the containment wall is much larger for the TNT charge, and so is the radial displacement of the fluid.

The other major difference as observed from the computer results is the energy partition. In the TNT charge, virtually all the energy

released in the detonation is transferred to the surrounding medium as compression and kinetic energy; for example, 0.230 msec after detonation, the energy transferred from the core is about 98%, but in the nuclear excursion, only 50% of the energy is transferred to the surroundings. This study shows that the REXCO-H code can play an important part in understanding of problems of reactor safety. Results can be obtained quickly and at reasonable cost. The effects of design modifications can be assessed rapidly.

c. Comparison of Codes with Existing Experiments

Not previously reported.

Available data on simulated and real excursions have been collected, and have been compared with code predictions. The purpose of the

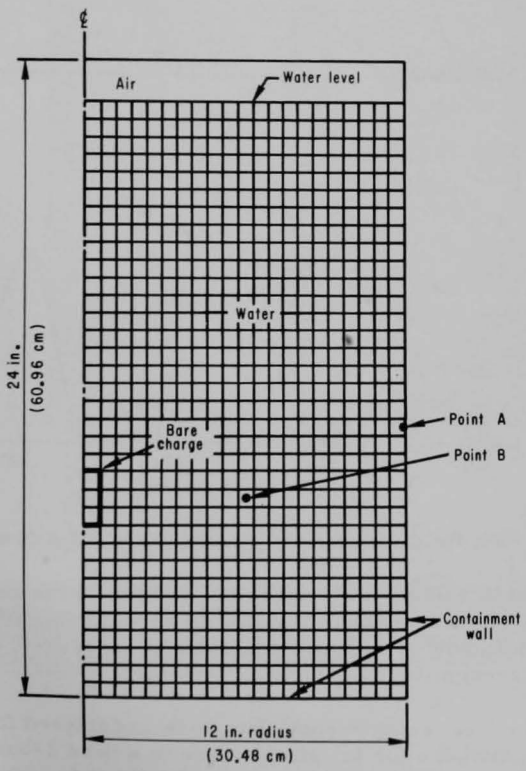

Fig. IV.C.1. Mathematical Model

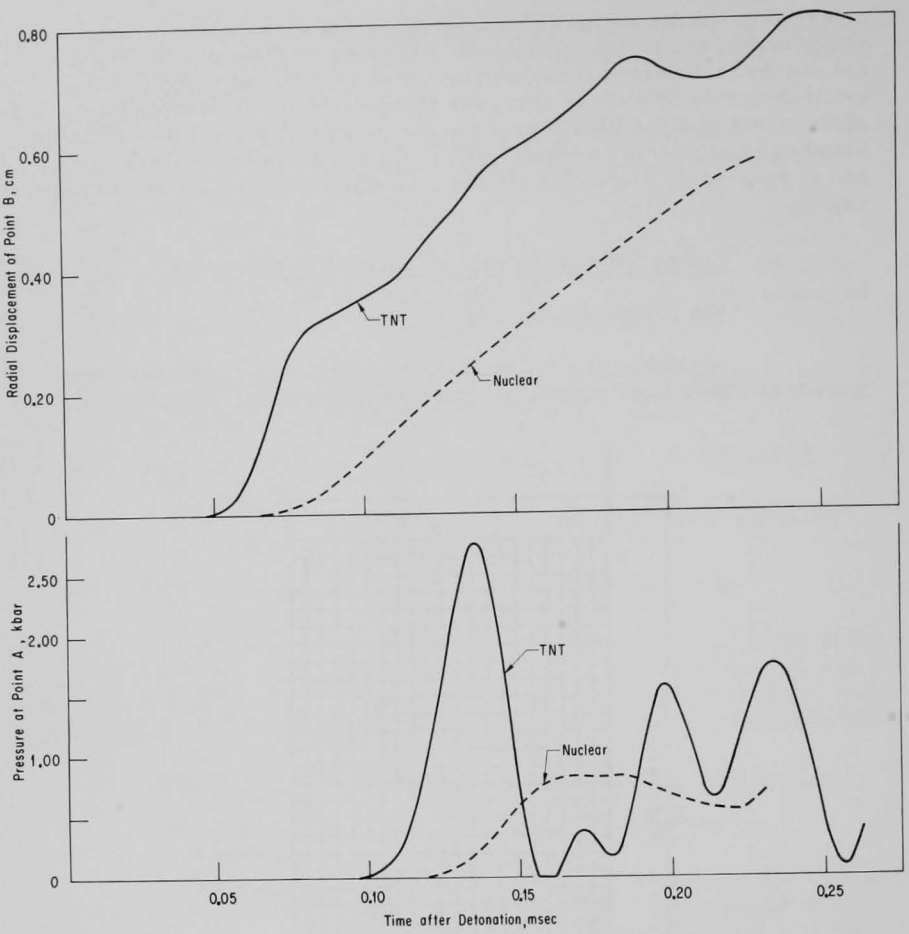

Fig. IV.C.2. Comparison on TNT Explosion and Nuclear Excursion

comparisons is to establish the degree of validity of the code performance and to support the development of full code capabilities; if vital measurements are insufficient or inconsistent, then, if necessary, additional experiments will be recommended.

The first experimental data to be considered for comparison with the code prediction are for the simple case of a bare 2-ounce charge of RDX/TNT 60/40 immersed in water (see Fig. IV.C.3). The recorded pressure trace at Position 3 was measured in this UKAEA experiment with a quartz-crystal pressure transducer (Type M020). The pressure recorded at Gage 3 is compared in Fig. IV.C.4 with our code prediction. Successive

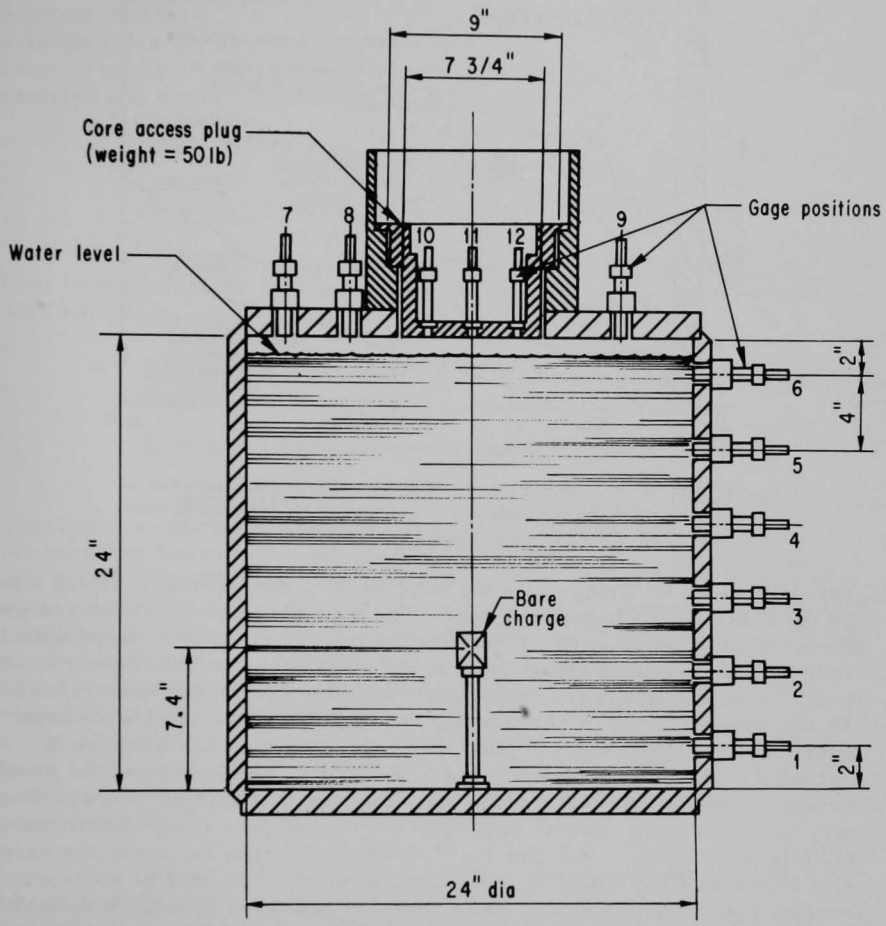

Fig. IV.C.3. Cross Section of Model Reactor Tank, Showing Positions of Pressure Gages and the Bare Charge [from A Model Investigation of Explosion Containment in Single Tank Fast Reactors, by N. J. M. Rees (UKAEA), pp. 692-719, in ANL-7120, Proceedings of the Conference on Safety, Fuel, and Core Design in Large Fast Power Reactors, held at ANL October 11-14, 1965].

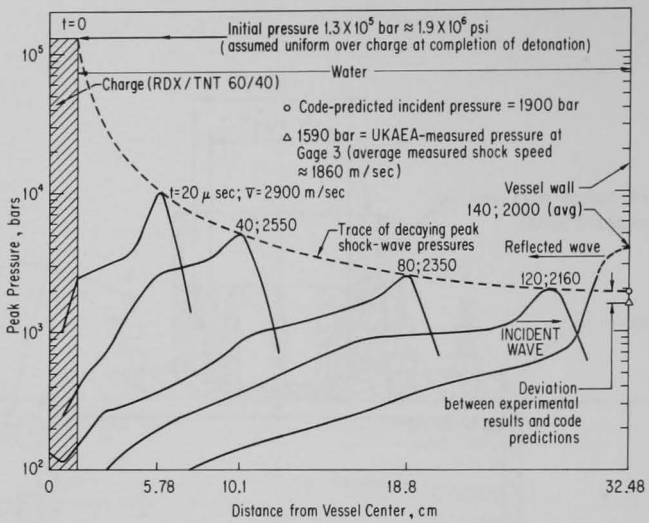

Fig. IV.C.4. Preliminary Computer-code Computation of Successive Pressure Profiles for Detonation of 2-ounce Cylindrical Charge in Water (fixed Δt = 20 μsec, possible numerical instability)

positions of the decaying pressure wave as computed by our code are shown as the wave travels toward the gage. The computed results shown are preliminary and may be in error because the time interval was forced upon the code rather than being determined by the stability criterion. Distortion of the cells at the ends of the cylindrical explosive charge becomes excessive, 35 μsec after detonation, diminishing the allowable time interval between numerical iterations to an impractically small value. At this point, a rezoning of the computational grid is required. The rezoning of the problem by hand computations is a tedious and time-consuming task, so a supplementary computer code is being developed for this purpose. The distortion of cells is much more severe for the TNT explosion than for a nuclear excursion because of the initial high pressure gradient. The initial pressure, energy, and velocity distributions within the explosive have been refined through analysis of the detonation process. A spherical charge has been substituted for the cylindrical shape to reduce cell deformation; the rezoning is near completion.

The reflected peak pressure exists as only a very brief spike and is missed in the experiment because of the comparatively slow response of the recording system in which the time sweep is provided by a rotating-drum camera (the cited system frequency response is 20 kc/sec). For this reason, also, the peak of the incident pressure can be expected to be shaved off. It might be found that further experimental data are required to establish reliable code predictions. In particular, special tests might be required

to reveal intermediate and internal features of the processes, and to provide more detailed and accurate equations of state, especially for multicomponent-material mixtures. At present, it appears that the primary function of the existing tests has been to determine the end effects of excursions for specific reactor configurations. As such, the model configurations have been too complex and internal measurements are lacking.

d. Selections of Temperature-Dependent Equation of State

Last Reported: ANL-7640, pp. 139-140 (Nov 1969).

Various types of equations of state pertinent to core excursions have been inserted in the REXCO-H code, as has the equation of state of TNT explosive.

e. Transformation of Code Coordinates from Lagrangian to Eulerian Systems

Last Reported: ANL-7669, pp. 142-143 (Feb 1970).

A quantitative comparison of Lagrangian- and Eulerian-coordinate solutions of a simplified problem has been started. For this purpose, the Lagrangian REXCO-H code was modified by incorporating into it the TRANSF code. The TRANSF code converted the Lagrangian results into the form of the Eulerian output without changing the Lagrangian method of solution. In effect, this modification superimposed the Eulerian mesh over that of the Lagrangian at given time intervals. Then the average of the Lagrangian properties within each Eulerian cell was calculated, providing a convenient method for comparing the Lagrangian and Eulerian solutions. The results of the already established Lagrangian solution were used as a basis for the evaluation. The comparison should help to point out any remaining errors in the Eulerian program and also should provide the specific characteristics of the new program.

Not all the results obtained in this way are truly equivalent, because of the nonlinear characteristics of some of the quantities. An example of such would be the pressure of the core material, where the equation of state is an exponential function. As a result, the average of the individual pressures would not be equivalent to a single pressure calculated from the average of the individual internal energies. However, if the nonlinearity is not excessive, comparison of both quantities should yield close results.

The comparison is based on a simplified reactor model that consists only of core and coolant. With the TRANSF routine transforming the input conditions of the Lagrangian code for the Eulerian code, one Eulerian particle was assigned to each of the Lagrangian cells of the coolant and

four particles to that of the core. The size of the Eulerian cells was made exactly four times larger than that of the undeformed Lagrangian cells. Consequently, at the beginning, each Eulerian coolant cell contains four symmetrically positioned particles and each core cell contains 16 particles.

Table IV.C.1 shows some results of the sample problems compiled from computer output. Each number refers to an Eulerian cell. Because of symmetry of the problem, the results in the axial and radial directions are similar, so only those in the axial direction are given. Thus, Table IV.C.1 lists the quantities for the innermost axial Eulerian cells. The comparison of Eulerian with the Lagrangian solution is of primary interest here, so the scale factor of the quantities is unimportant and is not included. The values at 0 μsec are the input quantities. The calculated values start at 8 μsec. The change in pressure of the Eulerian value of the first cell is attributed to nonlinearity. For all the results, the conservation of mass the total energy was maintained in both methods of solution.

TABLE IV.C.1. Results of Sample Problem Comparing Lagrangian- and Eulerian-coordinate Solutions

	Pressure[a]		Specific Internal Energy[a]		Mass[a]	
Time (μsec)	Lagrangian Cells	Eulerian Cells	Lagrangian Cells	Eulerian Cells	Lagrangian Cells	Eulerian Cells
0	3300	3300	1834	1834	353	353
	0	0	757	757	58	58
8	3296	3081	1833	1834	353	353
	4	0	757	757	58	58
	0					
80	2992	2963	1776	1807	353	353
	423	15	772	778	58	58
	5	6	757	766		
	0	0		757		
88	3188	2939	1827	1803	309	353
	739	20	1020	784	102	58
	13	8	757	769	58	
	0	0		757		
96	3120	2915	1814	1798	309	309
	811	25	1025	1178	102	102
	27	11	757	771	58	58
	0	0		757		
144	2866	2773	1792	1771	264	309
	1300	2611	1164	1291	146	87
	315	19	767	794	58	72
	2	3	757	762		58
	0	0		757		
200	2317	2607	1684	1739	220	309
	1828	2477	1365	1261	176	87
	911	2018	814	847	72	58
	150	17	760	812	58	72
	0	2	757	762		58
		0		757		

[a]All numbers are relative.

Mass transfer to adjacent cells is first noticed at 88 μsec according to the Lagrangian solution, and at 96 μsec according to the Eulerian solution. The corresponding change in pressure and internal energy is quite large, more than was expected. It is believed that this large jump is due to relatively large mass transfer during one time increment. For two core particles, one-eighth of the mass of the first zone transfers to the second zone, so pressures and internal energies increase appreciably.

At 144 μsec, the Lagrangian solution predicts that two additional particles from the first zone cross over to the second zone. On the other hand, the Eulerian solution indicates one particle crossing from the second to the third zone. At 200 μsec, mass transfer from the second to the third cell is predicted by Lagrangian solution, but the Eulerian method predicts mass transfer from the third to the fourth cell. Although this seems to be consistent, the peculiar mass transfer according to the Eulerian method is of concern. This will be investigated by examining the effect of different particle distributions inside the Lagrangian cells.

Although this preliminary comparison does not lead to firm conclusions, trends can be observed so that their causes can be investigated. Later extension of the time scale will produce better and more meaningful results.

PUBLICATIONS

Observation of Fuel Failure Behavior during In-Pile Meltdown Tests Using High-Speed Photography and a Transparent Autoclave
J. J. Barghusen, L. J. Harrison, R. O. Ivins, and L. E. Robinson
Proc. Nat. Symp. on Developments in Irradiation Testing Technology, Sandusky, Ohio, September 9-11, 1969. USAEC Publ. CONF-690910, pp. 378-400

Inelastic Response of Primary Reactor Containment to High-Energy Excursions
G. Cinelli, Jr., J. Gvildys, and S. H. Fistedis
ANL-7499 (Nov 1969)

Use of the Thermal TREAT Reactor for Fast Reactor Safety Studies
C. E. Dickerman, R. O. Ivins, A. B. Rothman, and J. F. Boland
Proc. Nat. Symp. on Developments in Irradiation Testing Technology, Sandusky, Ohio, September 9-11, 1969. USAEC Publ. CONF-690910, pp. 52-58

Capsules and Sodium Loops Used in Argonne National Laboratory Safety Experiments in the TREAT Reactor
L. E. Robinson, R. O. Ivins, and C. E. Dickerman
Proc. Nat. Symp. on Developments in Irradiation Testing Technology, Sandusky, Ohio, September 9-11, 1969. USAEC Publ. CONF-690910,

PUBLICATION--General

Annual Progress Report for 1967, Metallurgy Division
ANL-7417

ARGONNE NATIONAL LAB WEST
3 4444 00007921 0